Aerial sensor for wind turbines Design, implementation and demonstration of the technology

Schmidt Paulsen, Uwe; Moñux, Oscar

Publication date:
2016

Document Version
Publisher's PDF, also known as Version of record

DTU Wind Energy

Aerial sensor for wind turbines

Design, implementation and demonstration of the technology

Report DTU Wind Energy E-0128 (EN)

Oscar Moñux
Uwe Schmidt Paulsen

June 2016

Aerial sensor for wind turbines
Design, implementation and demonstration of the technology

Report DTU Wind Energy E-0128 (EN)
2016

By
Oscar Moñux
Uwe Schmidt Paulsen

Cover photo: Photo of inflow aerial sensor system with NI DAQ board on 500 kW wind turbine
Published by: Department of Wind Energy, Frederiksborgvej 399
Request report from: www.dtu.dk
ISSN: [0000-0000] (electronic version)
ISBN: [000-00-0000-000-0] (electronic version)

ISSN: [0000-0000] (printed version)
ISBN: [978-87-93278-91-2] (printed version)

Preface

The EUDP-2012 proposal, “Improved wind turbine efficiency using synchronized sensors” is a project which focuses on improving the efficiency of energy production, primarily for wind turbines, but as a spinoff, also traditional power plants. It builds on the experience and proven technology from three previous wind turbine projects:
-A wing mounted inflow sensor for wind turbines. This system has gone through multiple stages of development, and will be greatly enhanced by the synchronization technology from this project.

-A synchronized system for measurement of electrical transients in the Nysted offshore wind turbine farm (Christensen, 2007). This system had a weight of over 30 kg and required over 300 Watts of power.

-A second generation synchronized system for creating airborne instrumentation demonstration in trial flights at Nøjsomhed (Giebel,G. 2010). Technology advances reduced the weight of the project to about 1 kg with a corresponding reduction in power consumption from about 300 Watts to 8 W thus making battery operations possible.

-With the current state of the art it will be possible to develop a third generation system (“SyncBoard”) as defined by this project, which reduces power and weight by an additional factor 5 by shrinking the electronics to a CD size circuit board, for turbine wing mounting. The measurements from this system give high quality, multi-channel synchronized data (with 100 ns accuracy) as input to wind turbine manufacturers that contributes to innovations in design for greater efficiency, for example by dynamic control of wing loading, and design of lighter wings due to better real time operational control.”

The present report focus on the different aspects for making the aerial sensor a basic instrument measuring inflow on wind turbines, and the hardware(e.g. SyncBoard) as data acquisition unit converting raw signals into calibrated -and proper derived signals, for the interpretation of the measured inflow.

DTU campus Risø, June 2016

Uwe Schmidt Paulsen
Senior Scientist

Content

Summary

This report describes the efforts initiated within the EUDP demonstration project “Improved wind turbine efficiency using synchronized sensors” to improve wind turbine efficiency by using synchronized sensors on wind turbines. The main objective with this report is to convey experiences gained with this technology and to provide our results using a measurement system, which consists of a sensor mounted in front of the leading edge of the wind turbine for inflow measurement, and a recording system capable to handle this information (the synch board).
The first chapter introduces this project on the ideas and the background of the use of the aerial sensor for wind turbine, and why such an instrument is beneficial for the wind industry.
The second chapter explains the technicalities to achieve the inflow and other signals provided by the aerial sensor as a measurement unit. The wind tunnel is described on how to achieve this in the laboratory.
The Third chapter deals with how to calibrate the 5-hole pitot sensor on achieving a calibrated inflow as vector, and to provide a description of uncertainties characterising the output at the present.
The fourth chapter describes the measurement campaigns with the aerial sensor mounted on the 500 kW wind turbine rotor blade, and the results.
Chapter five evaluates on the obtained results for the present campaigns, under the given constraints and challenges.

The conclusion summarises the results and the following recommendations are made:
Several milestones mentioned in chapter 1 are achieved, and results from the wind tunnel tests and the implementation of the aerial sensor board are reported on few campaign measurements. The board is feasible for further refinement/development. Recommendations include added functionalities such as monitoring tube position and orientation with blade, acceleration sensors orientation add on and motion reference(INS) would improve the functionality and ease the use of the boards technology. The data analysed in this report inflow shows a good correlation with wind turbine electrical power, even though the analyses are limited to limited number of time series.

1. Project outline

1.1 Introduction

The inflow in front of the wind turbine is a very important issue for wind turbine performance, loads and operation. Even in the planning phase before operating the wind turbine the knowledge of the wind characteristics is a key factor for getting the best out of the cost of energy from the particular turbine when it is sited, or in a more large scale application for many wind turbines, representing a wind energy power plant.

The details of the wind, in particular in connection with presence of turbulence and variation of wind over the rotor disk area, are key input variables for design of an efficient wind turbine. This form of information is needed as input for rotor design programs used in the industry. Designing the turbine without these details leaves a design prone to higher rotor loads and to less generated kWh. One of the areas where this gives a measurable impact can be explained by looking at the way a wind turbine operates at conditions with horizontal and vertical flow differences. For differences between the flow direction and the alignment of the rotor, this kind of error occurs at typically 10 Degrees wind turbine misalignment and accounts with 5-10% of the annual energy output (AEP). The rotor loads will increase about 6%, with a reduction of generated power in the order of 1-3%. In the vertical plane similar happens for variation of the flow. In flat terrain this difference with typical wind turbine design is typically 6% of AEP.

Vertical shear, with a typical profile exponent of 0.2- gives for best wind turbine efficiency operation a power reduction of 2%. On pitch regulated wind turbines, we would be able to counterbalance these variations and avoid stress differences in the blade with appropriate inflow measurement devices, and ideally we could develop lighter rotors. The power reduction correlates un-linear with wind speed, and compared to optimum wind conditions, this effect is more significant at lower winds than at higher wind speeds.
The above considerations are evident when analysing for site planning, and important when considering load penalties on the turbine due to wind loads.

Why to measure with an inflow instrument?

The three inflow velocity components in a position in front of the leading edge of the blade shall be measured. In the experiments conducted so far, a five-hole pitot tube has been used, but other types of sensor could be used, such as e.g. a sonic.

The aerial measurement transducer is a device built on a proven technology. It is used by aerospace industry for determining relative wind speeds.

The aerial/pitot transducer has a 5-hole pitot device in front with dynamic pressure transducers capable of detecting the varying wind speed in three dimensions at hundreds times faster than the actual standard cup anemometers. The system involves a careful calibration of the 5-hole pitot's tube and it is installed at a fixed position on one of the rotor blades. The induction effects are compensated by

adjustment via a code. The measurement device has as a data acquisition unit which shall be capable through an integrated GPS to synchronize and detect events on different locations keeping timing with a resolution of milliseconds; besides the measurement devices shall contain an acceleration measurement enabling to derive the position of the system in the blade itself. The data acquisition unit is powered by a battery system which shall provide sufficient power for electronics for lasting at least 3 days

Along with this document different stages are shown to give the recommended steps to assess the original requirements described in the project's original scope. In order to conform with the scope, several components and tests have been realized, from the characteristics of the pitot head to the development of different synchronized boards, development of wind tunnel as a tool to calibrate the 5-hole pitot, algorithms to understand the measured signals within given constraints, applying different energy harvesting systems capable of giving additional autonomy for such a device, and last but not end the results will be shown deriving final conclusions.

1.2 Background

Potential use of the sensor was suggested for different experimental wind turbine applications, such as for power curve measurements, in this case for referencing with measured power from the wind turbine with a free wind speed. Another application is to use the inflow sensor signals with characterizing the flap loads on the blade segment and in this way to estimate to rotor flap loads.

The basic idea to use a 5-port pitot tube refers to work carried out in the 90 'ties at Risø, mainly on a 100 kW horizontal wind turbine for the investigation of inflow relevant, aerodynamically loads, on a blade segment (H, 1988). A photo of the sensor mounted on the rotor blade close to the load cell (black) is shown in Figure 1

Figure 1 Pitot sensor on 100 kW wind turbine blade

The sensor was pneumatically connected with separate, rather big and weighty pressure transducers which were mounted in the interior of the blade void close to the sensor. The signals were transmitted via the slip ring mounted on the drivetrain shaft to a central data acquisition system which synchronously collected Meteorological and, as well, status signals for the wind turbine system.

As a development in design of the sensory system, a more compact, robust and integrated design was investigated, with potential to operate/synchronise on a time autonomous basis with other units. Later this technique has been developed further and used with good experience in different research projects (Bak, 2010). A correlation of the angle of attack (AoA) and the electrical power is shown in the Figure 2

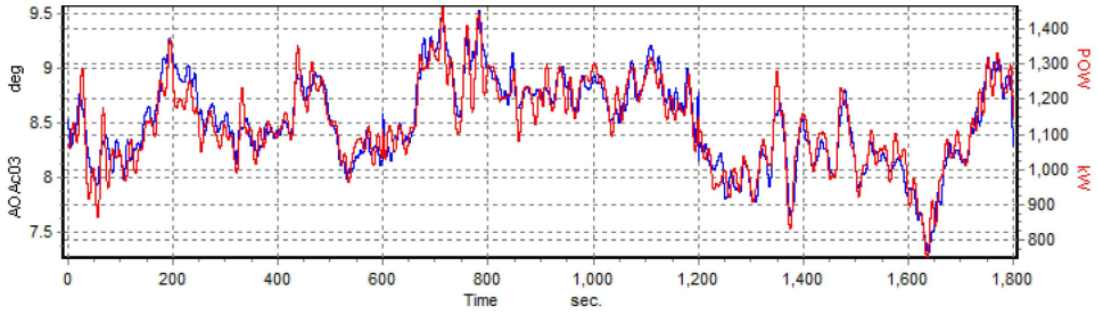

Figure 2 Pitot sensor angle of attack (blue), and electrical power signal from the wind turbine (red)

The idea and development of nanoseconds-synchronized data loggers, "Nanosync-board" datalogger was fostered within this project from studying electrical transients in the very end of the grid transmission, and generated within the cut-in control sequence of wind turbines in a windfarm (Leif S. Christensen, 2007). The prototype data loggers filled an enclosure of 1m x 1m x 0.5m, see Figure 3.

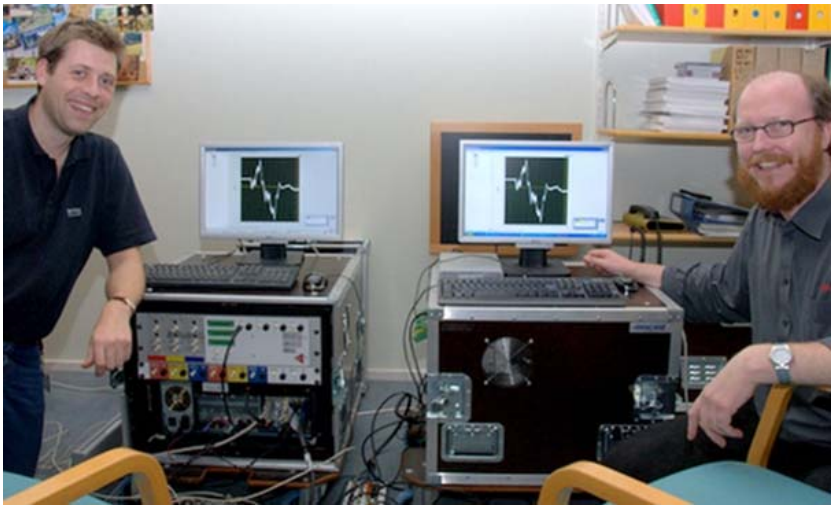

Figure 3 Realisation of first generation Nano-synch system

The next Nanosync version (see Figure 4), was 10-30 times smaller in dimensions, and the total weight was around 2 kg. This made the application useful for installation on measurement platform and carried by a tethered (Gregor Giebel, May 2009).

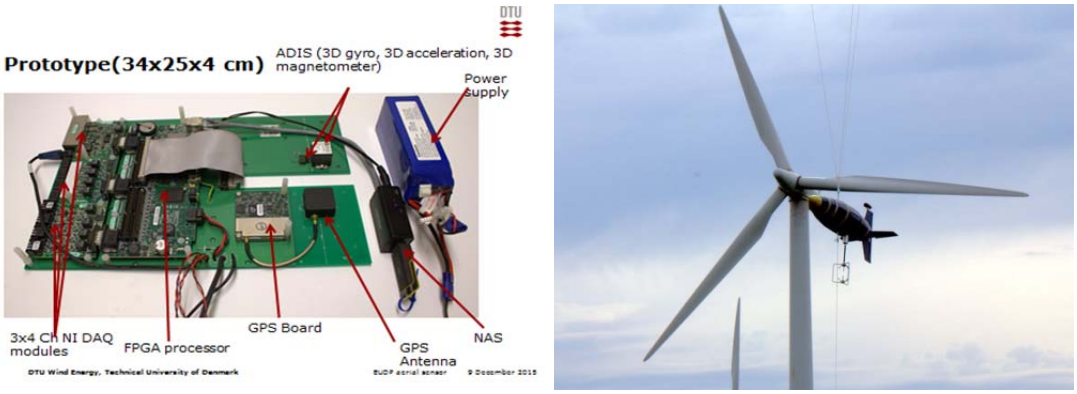

Figure 4 Left Nano synch-boards, second generation. Right: platform mounted board

For this realisation, we need to solve some evident challenges for applications on wind turbines:

- Vulnerable for pneumatic blockage of ports by rain drops, heavy dust etc.

- Limited operational duration with battery power supply
- Pitot tube obstructs the flow and determination of velocities needs calibration. Calibration of pitot tube needs a high speed calibration wind tunnel facility
- Adjustment of inflow properties with angle of attack and side slip angle sensitivity
- Acoustic damping occurs in tubes connecting ports and pressure transducers. Damping of pressure fluctuations increases with the length of these tubes and limits the measurements to mean values

In particular the sensitivity of the device with variation of angle is of important for use with wind turbines, which partially or to full extend are subjected to variations of the angle of attack from non-stall to full stall conditions. The flow angle can be detected with pitot tubes of different geometry and number of ports, and the range of angles can be extended considerably in measurement. A supplemental challenge is that the airfoil will divide the flow and in this sense create a potential blockage, depending on how much loading the wind turbine is subjected to. In summary, the challenge is to place the sensor at a position which is not affected by the presence of the blade, and that the wind vector incorporates representative speeds and angles (e.g. angle of attack, side slip angle). The positioning of the probe is solved by using flow simulations over the airfoil segment, as shown qualitatively in Figure 5 positioning the probe outside the domain of speed and angle interference, the 5-hole pitot's tube senses the aerodynamic variations of flow. For the determination of flow derived uncertainties, the accurate position has to be known.

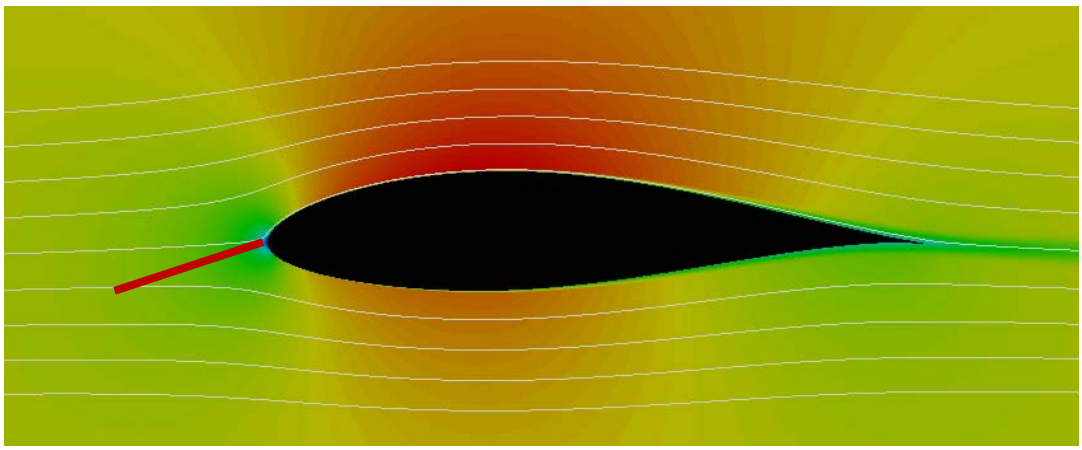

Figure 5 Contour plot of 2-d flow representation, together with probe indication (stick) angle of attack is zero.

2. Aerial sensor

In order to create and test the sensor several components have to be developed. This section will start naming and explaining not only the different components that allows the sensor to fulfil the requirements but also the test bench created to derive the behaviour and check whenever the requirements have being accomplished.

2.1 Main parts description

As described in the first section the sensor development has different stages that varies from each component. The physical and logical parts that are inherent in any electronic device are:

- **5-hole pitot head sensor**: capable of quantifying a physical quantity
- **Tubes** connecting the pneumatic ports with pressure transducers. Too long tubes will reduce the ability to measure inflow with frequency content.
- **Hardware**:
  - **A/D module**: an analogue to digital converter capable of balancing two characteristics of the measurement: resolution and accuracy. Aiming to have more than the enough resolution held on the sensor but not exceeding in certain manner the real accuracy of the device
  - **DAQ**: a data acquisition module capable of saving or either communicating in real time the information provided by the data acquisition module.
  - **Power supply**: Module capable of giving enough energy for the estimated highest peaks of processing and reaching the desired capacity in time
- **Software**: capable of acquiring , monitor and save the signals

In addition of described components and the sensor itself, the following contributions make this project interesting:

- **Synchronization module**: extra module needed for the goal of this project which has the characteristics of being able to write the correct timestamp on a certain sample under harsh environmental conditions.
- **Energy harvester**: extra module that under certain circumstances whenever not feasible to have the power supply will be present make the measurement longer. The capability of this device shall not interfere the timing capable of saving data of the data acquisition system.
- The post processing **software** analysis is a special purpose made development

2.2 Measurement of the instantaneous wind vector

It all depends on the fact that the highest pressure occurs at the point of stagnation and the pressure on the surface of the probe tip decreases with distance from this point. For a sphere, one can derive unique mathematical relations that connect the pressure at the pressure taps with the direction and the magnitude of the velocity as functions of the location of the pressure taps. In practice, there are no analytical solutions for tip geometries other than the sphere, and therefore these relationships should be determined only by calibration.

In order to interpret the sensor measurements and derive them into the instantaneous speeds, several steps have to be accomplished, see Figure 6.

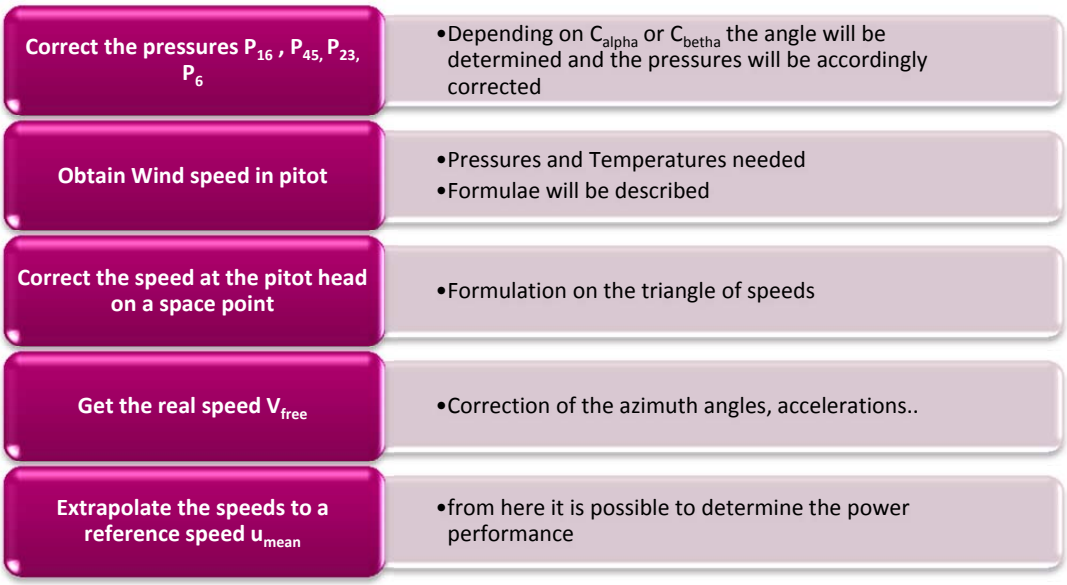

Figure 6 steps to perform an adequate measurement

2.2.1 Formulae on the pitot, translation from Pressures into Wind speeds

The pressure and the speed for compressible fluids have a relation (Bernoulli) where the pressure in a point and the speed remains constant among a volume of fluid. This in other words, considering the flow following a stream line filament at position (index '0', '1' and '2')::

$$\frac{\gamma \cdot P_2}{(\gamma-1)\cdot \rho_2} + \frac{1}{2}\cdot V_2^2 = \frac{\gamma \cdot P_1}{(\gamma-1)\cdot \rho_1} + \frac{1}{2}\cdot V_1^2 = \frac{\gamma}{(\gamma-1)}\cdot\frac{P_0}{\rho_0}$$

Being ρ the density of the fluid and index '$_0$' designing the stagnation condition (V=0) in the incompressible case ($\rho_2 = \rho_1 = \rho$[1]= constant), we can neglect the term γ/(γ-1)

[1] since the air, here assumed to be dry, can contain moist, it is important to remark that an increment of moisture can reduce the density of the air, as expressed in the IEC 61400-12

$$\rho = \frac{1}{T}\cdot\left(\frac{B}{R_0} - \emptyset \cdot 0.0000205 \cdot e^{0.0631846\cdot T}\right)\cdot\left(\frac{1}{R_0} - \frac{1}{R_w}\right)$$

Being B the barometric pressure [Pa], T is the absolute temperature[K], Ø the relative humidity, R_0 the gas constant of dry air [287,95 J/Kg·K], R_w the gas constant of water vapour [461,5 J/Kg·K]

$$\rho_i = \frac{P_{total}}{R \cdot T_s} = \frac{P_{static} + P_{dynamic}}{R \cdot T_s} = \frac{P_{static} + q}{R \cdot T_s}$$

$P_{dynamic}$ is usually being renamed as q in the bibliography; P_{static} is the static pressure of the fluid. P_{static} at 0 level is the barometric pressure of the fluid P_{baro} measured at the stagnation point, i.e. speed of the flow = 0. When mounted on the wind turbine blade, as explained later, the hydrostatic air pressure P_{static} is equal to the gauge pressure for the air parcel at the vertical position z(t) of the 5-hole pitot head: ρz(t)g, and where t indicates the time dependency with the rotational speed. In the wind tunnel laboratory, this static pressure only changes according to the air barometric/atmospheric conditions. The blower is in our case located close to sea level so P_{baro} is equivalent to P_{atm} .The dynamic pressure is described by q, equivalent to the pressure at the stagnation point

$$\frac{\Delta P}{\frac{P_{static} + q}{R \cdot T_s}} = \frac{1}{2} \cdot (V_1^2)$$

This model changes when the speed of the flow reaches values close to a Mach 0.3, and thereby exceeding the limit where to neglect compressibility. In this case the Bernoulli equations derive with a Mach number, Ma, of

$$Ma = \sqrt{\frac{2}{\gamma - 1} \cdot \left[\left(\frac{P_{static} + q}{P_{static}} \right)^{\frac{\gamma - 1}{\gamma}} - 1 \right]}$$

Also the flow temperature will decrease whenever Ma increases

$$T_s = \frac{T_{measured}}{1 + \left[\frac{1}{2} \cdot (\gamma - 1) \cdot K \cdot Ma^2 \right]}$$

There must be distinguished between the outside ambient temperature, T_a, which is the temperature measured when undisturbed or when the flow is at rest, and the total air temperature which is the temperature measured at stagnation point. T_s is the absolute temperature

The speed of sound depends on the temperature, and the thermodynamic gas properties (ratio of C_P, C_V). As mentioned in (Gracey, 1980) , K is expressing the recovery factor for the temperature probe in a high speed flowing gas:

$$K = \frac{T_{flow,probe} - T_s}{T_{Flow} - T_s}$$

The speed of sound c is defined via the universal gas law as

$$c = \sqrt{\gamma \cdot R \cdot T_s} = \sqrt{\frac{\gamma \cdot P_{static}}{\rho}}$$

Thought there are some other approaches[2], however here the standard equation will be used

$$u = c \cdot Ma = Ma \cdot \sqrt{\gamma \cdot R \cdot \frac{T_{measured}}{1 + \left[\frac{1}{2} \cdot (\gamma - 1) \cdot K \cdot Ma^2\right]}} = \sqrt{\gamma \cdot R \cdot \frac{T_{measured} \cdot Ma^2}{1 + \left[\frac{1}{2} \cdot (\gamma - 1) \cdot K \cdot Ma^2\right]}}$$

$$u = \sqrt{\gamma \cdot R \cdot \frac{T_{measured}}{\frac{1}{Ma^2}\left[1 + \left[\frac{1}{2} \cdot (\gamma - 1) \cdot K \cdot Ma^2\right]\right]}} = \sqrt{\gamma \cdot R \cdot \frac{T_{measured}}{\frac{1}{Ma^2} + \left[\frac{1}{2} \cdot (\gamma - 1) \cdot K\right]}}$$

There is a substantial difference between true speed and the calibrated probe wind speed. The calibrated speed in aviation nomenclature is the speed measured at sea level and the true speed is the speed at the actual height. In these measurements, the height cannot be higher than the blade tip height which is approximately maximum 300 meters. Where 0 is the compressibility factor at the reference at sea level '0'; for the range studied this speed formula gives:

$$\frac{V}{V_c} = \frac{f}{f_0}\sqrt{\frac{\rho_0}{\rho}}$$

Where the compressibility factor is

$$f = \sqrt{\frac{\gamma}{\gamma - 1} \cdot \frac{P_{static}}{q} \cdot \left[\left(\frac{q}{P_{static}} + 1\right)^{\frac{\gamma - 1}{\gamma}} - 1\right]},$$

And q is the dynamic pressure

2.2.2 Normalization of pressures. Blower calibration factors

The pressures will be corrected according to applied dimensionless coefficients obtained during the calibration in the wind tunnel. The dynamic pressure is proportional to ~½·ρ·V², and is defined as the differential pressure between port 1 and 6. This dynamic pressure at the position of the 5-hole pitot head (e.g. P_1) is defined as q_{pitot}, being:

$$q_{pitot} = P_1 - P_6$$

The reason for this is that the pressure correlation with q_{pitot} depends on the positioning of the pitot head and determined by flow blockage of the pitot arrangement. In order to resolve this, the functional speed dependency between contraction and flow at various positions are calibrated with the Prandtl

---

[2] With Ma<0.2 for instance

$$P_{total} - P_{static} = q = \frac{1}{2} \cdot \rho_{air} \cdot u^2 \cdot \left[1 + \frac{1}{4} \cdot Ma^2 + \frac{2 - \gamma}{24} \cdot Ma^4 \ldots\right] \cdot Ma^4 + \cdots.\Big]$$

tube, $q_{prandtl}$, which in this connection is used as an instrument being not capable to detect misalignment between flow transducer and flow direction[3].

In order to derive a functional between the measured pressure drop over the contraction $q_{contraction}$ and the wind speed obtained at the particular spot where the 5-hole pitot head will be positioned, a correlation will be set up and used to calibrate the speed of the 5-hole pitot transducer. Furthermore, in this document and understanding the equations it cannot be derived any expression that relates the speed and the contraction pressure with the position, though the speed depends on two parameters, that they cannot be controlled in the actual circumstances: the atmospheric pressure and the ambient temperature. Thereby the ratio that will be the contraction pressure versus the incremental pressure in any position in space versus speeds.

$$\zeta_{x,y,z,frequency} = \frac{q_{prandtl}}{q_{contraction}}(x, y, z, frequency)$$

Here it can be also extracted that $\zeta_{x,y,z,frequency}$ is an a-dimensional term normalized that can be decomposed in two different terms

$$\zeta_{x,y,z,frequency} = \zeta_{x,y,z} \cdot \zeta_{frequency}$$

Functional coefficients were derived by normalisation with dynamic pressure:

$$C_\alpha(\alpha) = \frac{P_2 - P_3}{q_{pitot}}$$

$$C_\beta(\beta) = \frac{P_4 - P_5}{q_{pitot}}$$

Being

β: angle of slip
α: angle of attack

From $C_\alpha$and $C_\beta$the angles will be obtained. Those angles will give the correction to be applied on

$$C_q(\alpha, \beta) = \frac{q_{pitot}}{q_{prandtl}}$$

i.e. the measured pressure on that position. This can be rewritten as

$$C_q(\alpha, \beta) = \frac{q_{pitot}}{\zeta_{x,y,z} \cdot \zeta_{frequency} \cdot q_{contraction}}$$

The determination of the static coefficient depends on the configuration and connections realized[4] they might slightly vary due to the precision and number of sensors. In the case that the pitot does not

[3] The misalignment should not exceed a range of ±15 degrees, otherwise the Prandtl tube will not work properly
[4] The different configurations can be found in the annexure

provide a pneumatic option of the static pressure then this coefficient shall not be applied at all. Whenever a differential pressure between the P6 and the absolute sensor then

$$C_s = \frac{P_{6\_diff}}{q_{pitot}}$$

This option nevertheless will not be applied. Therefore the static pressure will be defined as

$$C_s = \frac{\Delta P_s}{q_{pitot}}$$

under some different configurations P_6 is not existing as standalone measurement, so if

$$C_t(\alpha, \beta) = \frac{q_{pitot}}{q_{prandtl}}$$

and the suffixes α,β refer to the AoA and the sideslip plane.

Therefore the speed stablished via the pitot during calibration, thought this is not the goal, can be expressed as

$$u = \sqrt{\gamma \cdot R \cdot \frac{T_{measured}}{\frac{1}{\frac{2}{\gamma - 1} \cdot \left[\left(1 + \frac{\zeta_{x,y,z} \cdot \zeta_{frequency} \cdot q_{contraction}}{P_{static}}\right)^{\frac{\gamma-1}{\gamma}} - 1\right]} + \left[\frac{1}{2} \cdot (\gamma - 1) \cdot K\right]}}$$

2.2.3 Application of correction factors from the blower

To obtain the speeds, first the static pressures must be determined this varies depending on how the static pressure has being measured. In our case

$$Ps_M = \frac{P_{s\alpha} + P_{s\beta}}{2}$$

Where as previously being described:

$$C_{s\alpha} = f(C_\alpha)$$

$$C_{s\beta} = f(C_\beta)$$

And

$$P_{s\alpha} = P_s - C_{s\alpha} \cdot q_{pitot}$$

$$P_{s\beta} = P_{s-} C_{s\beta} \cdot q_{pitot}$$

$$P_{t\alpha} = P_{s\alpha} + \frac{q_{pitot}}{C_{t\alpha}}$$

$$P_{t\beta} = P_{s\beta} + \frac{q_{pitot}}{C_{t\beta}}$$

In overall combining the previous equations, considering index 'i' as either 'α' or'β'

$$P_{ti} = P_{si} + \frac{q_{pitot}}{C_{ti}} = P_{si\_}C_{si} \cdot q_{pitot} + \frac{q_{pitot}}{C_{ti}} = P_{si} + q_{pitot} \cdot \left(\frac{1 - C_{ti} \cdot C_{si}}{C_{ti}}\right)$$

2.2.4 Formulae on a point triangle of speeds, space point

At the wind turbine blade segment, the speed (V_M in the sketch) can be defined as the 5-hole pitot head follow a periodic cycle on that blade section circular path in the rotor plane:

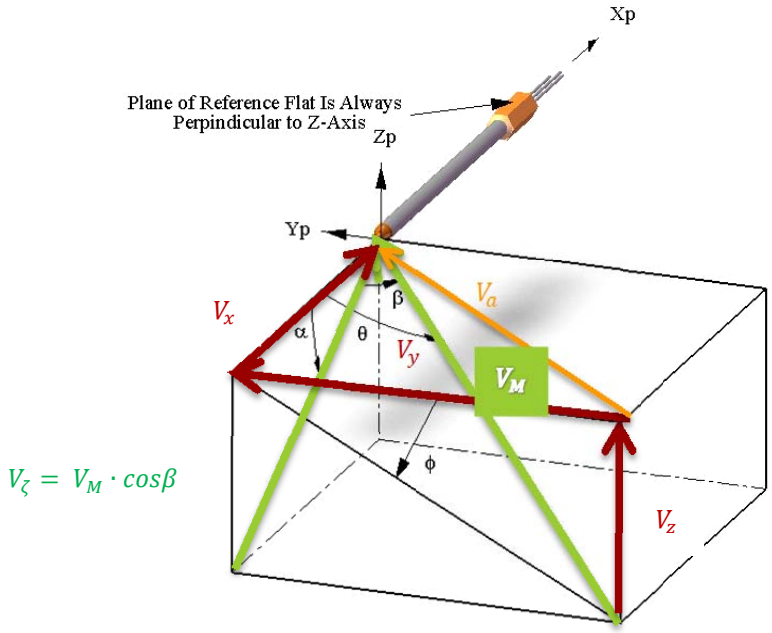

Figure 7 Values of the coordinate system from Aeroprobe™

The set of equations set in the DANAERO were defined as:

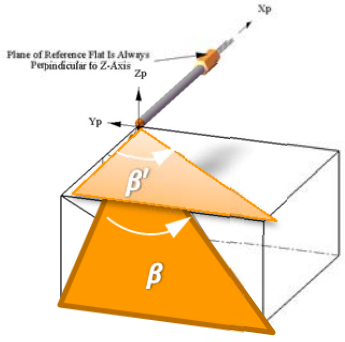

Figure 8 β and β'

$$V_x = V_M \cdot \cos\beta \cdot cos\alpha$$

$$V_y = V_M \cdot sin\,\beta$$

$$V_z = V_M \cdot \cos\beta \cdot sin\alpha$$

This is not coherently defined, thus the β angle measured by the pitot tube is different on what is stated in Figure 7, indeed the pitot´s head gets the pressure β'.

If β' is the real angle the relation between them is

$$V_a = \sqrt{V_M^2 - V_z^2}$$

$$(sin\,\beta)^2 = \left(\frac{V_y}{V_M}\right)^2 = \left(\frac{V_y^2}{V_z^2 + V_a^2}\right)$$

$$\left(\frac{1}{sin\,\beta}\right)^2 = \left(\frac{V_z^2 + V_a^2}{V_y^2}\right) = \frac{V_z^2 + V_a^2}{V_y^2} = \frac{V_z^2}{V_y^2} + \frac{V_a^2}{V_y^2}$$

$$\left(\frac{V_z}{V_y}\right)^2 + \left(\frac{1}{sin\beta'}\right)^2 = \left(\frac{1}{sin\beta}\right)^2 = \left(\frac{\cos\beta \cdot sin\alpha}{sin\,\beta}\right)^2 + \left(\frac{1}{sin\beta'}\right)^2$$

Then

$$\frac{1 - \cos^2\beta \cdot sin^2\alpha}{sin^2\beta} = \left(\frac{1}{sin\beta'}\right)^2$$

Is equal than

$$sin\beta' = \left(\frac{sin\beta}{\sqrt{1 - \cos^2\beta \cdot sin^2\alpha}}\right)$$

There is another faster equivalence found, if:

$$V_y = V_M \cdot sin\,\beta$$

$$V_x = V_M \cdot \cos\beta \cdot cos\alpha$$

Then

$$\frac{V_y}{sin\,\beta} = \frac{V_x}{\cos\beta \cdot cos\alpha}$$

$$V_y = \frac{V_x}{cos\alpha} \cdot \mathrm{tg}\,\beta$$

$$\mathrm{tg}\,\beta' = \frac{1}{cos\alpha} \cdot \mathrm{tg}\,\beta$$

Expressions valid when $\forall\beta, \alpha > 0$

The corrected angle, asin(sinβ') and atan(tgβ') are shown is shown in Figure 9, whereas The difference between the apparent angle β and β' is shown in Figure 10. The deviation will be for practical sideslip around ±1 degrees when α and β are 20 degrees.

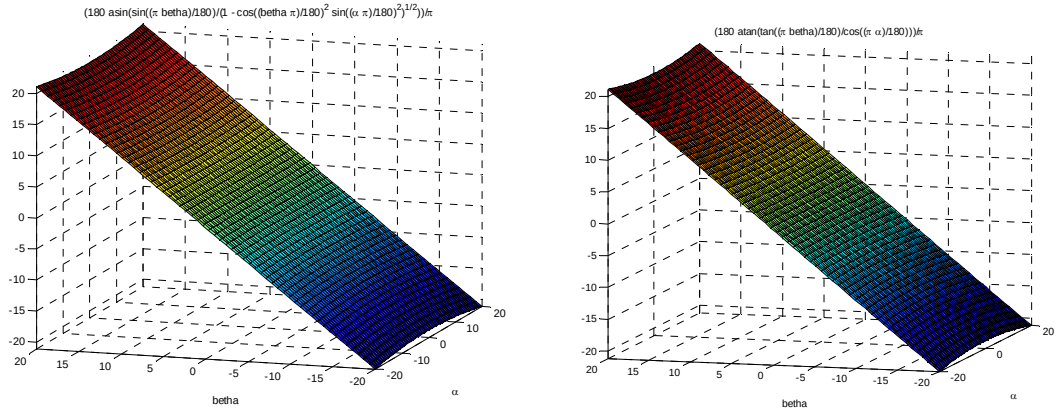

Figure 9. Variation of the angle when α and β vary applying the first and second formula

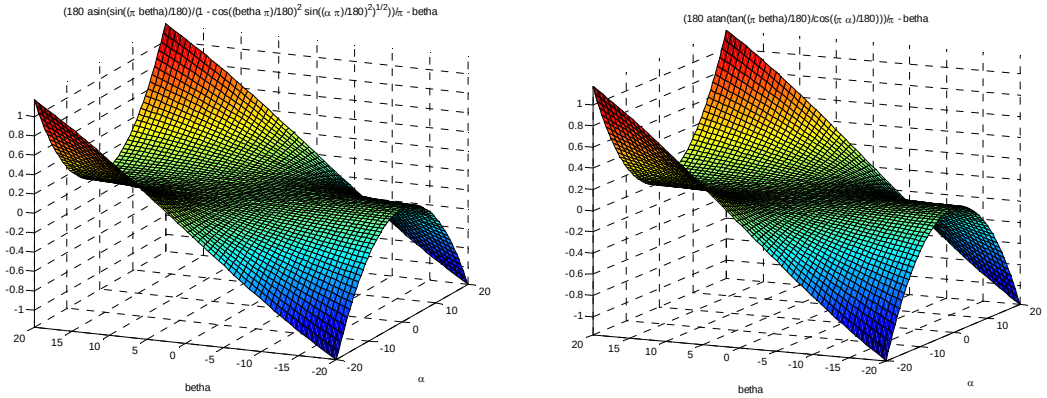

Figure 10.- Error in degrees β' – β, applying first and second formula

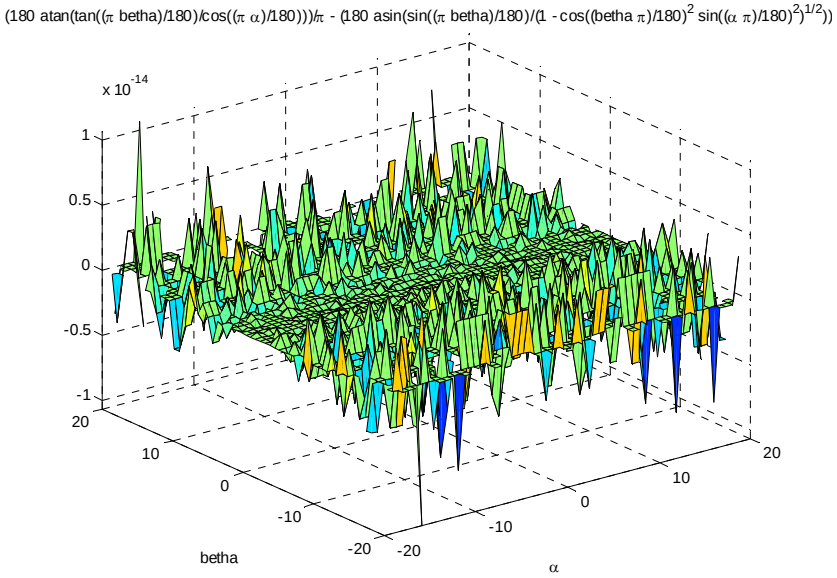

Figure 11.- Error between first and second formula

Combining both expressions

$$\frac{\left(\frac{1}{\sqrt{1-\cos^2\beta\cdot sin^2\alpha}}\right)}{\cos\beta'}=\frac{1}{cos\alpha}\cdot\frac{1}{\cos\beta}$$

$$\cos\beta'=\frac{cos\alpha}{\sqrt{1-\cos^2\beta\cdot sin^2\alpha}}\cdot\cos\beta$$

In overall the error can reach 1 degree at 20 degrees, this gives a maximum relative error of 0.6%

$$V_{total}=V_M=\sqrt{V_x^2+V_y^2+V_z^2}$$

$$\emptyset=atan\frac{V_z}{V_y}$$

The wind perpendicular to the rotor plane, here as V_{free} is:

$$V_{free}\approx V_M\cdot\cos\alpha\cdot\sin(\beta+Pitch')=V_M\cdot\cos\alpha\cdot\sin(\beta+Pitot_{orientation}-Twist+Pitch)$$

expressing, that $(+Pitot_{orientation}-Twist+Pitch)$ is the algebraic sum of angles[5] measured from the base of the rotor plane to the chord of the airfoil, hereby Vfree is a measure of the wind in the direction of thrust. Not to mention that the pitot tube itself could be not well aligned in the rotor plane with respect to the tangential direction ,and with respect to a misalignment of the ports.

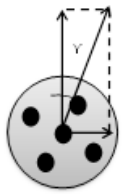

The equations hereafter are simply derived by taking in account, that the orientation is perfect, which is not the case. This angle indeed will be called ϒ and will clearly have a priori not known effect on the output. This can be seen as an angular offset which can be determined with simulations or

In order to reduce the expressions the plane will be taken as 2D and then the solutions will be expressed afterwards as 3D

Figure 12 angle

Being

$$V_M=\frac{V_{M\alpha}+V_{M\beta}}{2}$$

[5] The sign of positive angle may depend on a different definition

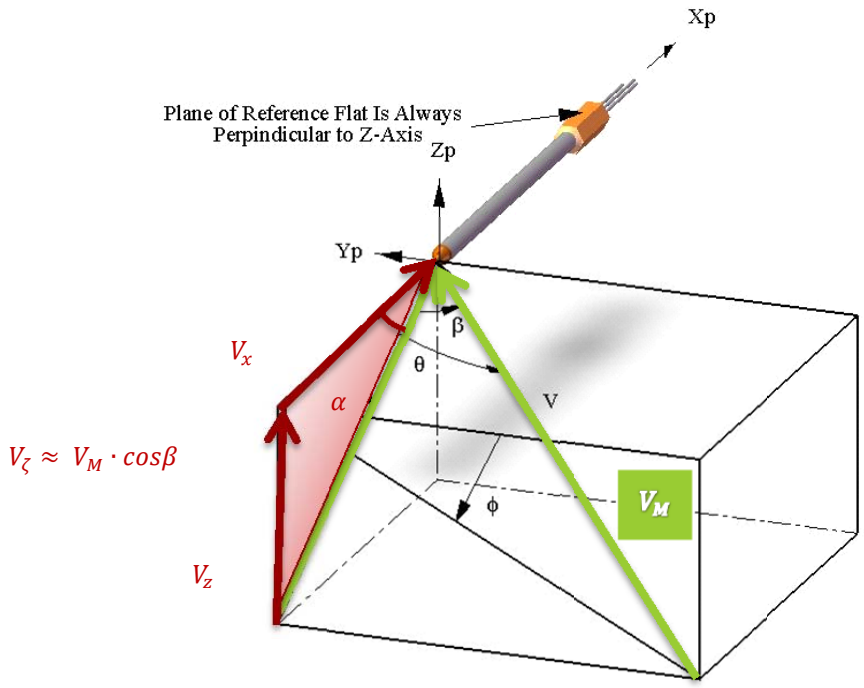

Figure 13 Projected used speed 2D plane from Aeroprobe™

$V_{free} = V_\zeta \cdot \sin(\alpha + Pitch') = V_\zeta \cdot \sin(\alpha + Pitot_{orientation} - Twist + Pitch) = V_\zeta \cdot \cos(90 - (\alpha + Pitot_{orientation} - Twist + Pitch))$

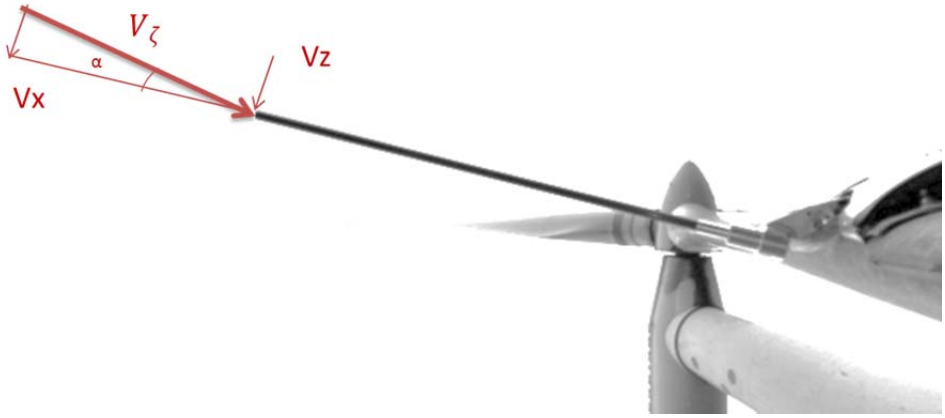

Figure 14 Decomposition of the relative speed, Vx and Vz being components inline and perpendicular to the pitot tube in the AoA plane

In the angle of attack plane, assigning and assuming the local vectors V_ζ, v_{wind} induction is included:

$$\overline{V_\zeta} = \overline{v_{wind}} + \overline{\omega R}$$

On the different speeds and angles definition:

v_{wind}: *wind speed*
$\omega * R$: *rotational speed*
V_ζ: relative speed

From the Figure 15 it is clear that the angle of V_ζ will depend on the orientation of the blade

$$V_x = V_\zeta \cdot \cos(\alpha) = -v_{wind} * \cos(90 - \mu + \vartheta) + \omega * R * \cos(\vartheta)$$

$$V_z = V_\zeta \cdot \sin(\alpha) = v_{wind} * \sin(90 - \mu + \vartheta) - \omega * R * \sin(\vartheta)$$

$$V_\zeta \cdot \sin(\alpha + \vartheta) = v_{wind} * \cos(\mu)$$

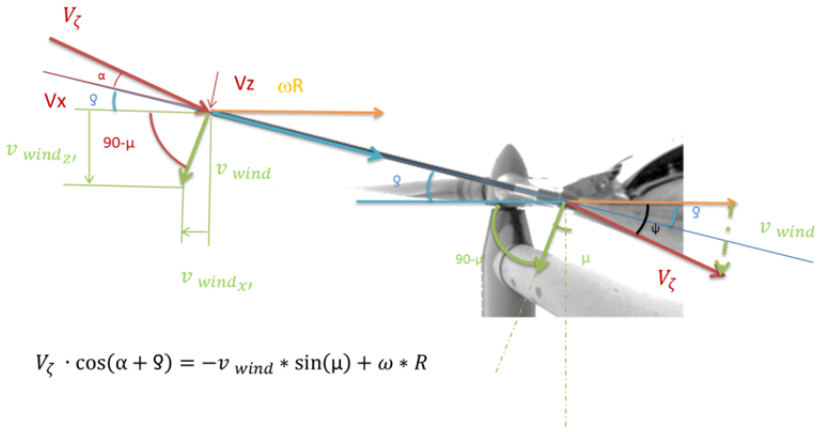

$$V_\zeta \cdot \cos(\alpha + \vartheta) = -v_{wind} * \sin(\mu) + \omega * R$$

Figure 15 Schematics of the triangle of speeds

$$V_x = V_\zeta * \cos(\alpha) = V_\zeta * \cos(\psi - \vartheta)$$

$$V_z = V_\zeta * \sin(\alpha) = V_\zeta * \sin(\psi - \vartheta)$$

Where $V_\zeta, V_x, V_y, \alpha$ are determined from the dynamics of the pitot tube

$$V_x = V_\zeta \cdot \cos(\alpha) = -v_{wind} * \cos(90 - \mu + \vartheta) + \omega * R * \cos(\vartheta)$$

$$V_z = V_\zeta \cdot \sin(\alpha) = v_{wind} * \sin(90 - \mu + \vartheta) - \omega * R * \sin(\vartheta)$$

$$V_\zeta \cdot \sin(\alpha + \vartheta) = v_{wind} * \cos(\mu)$$

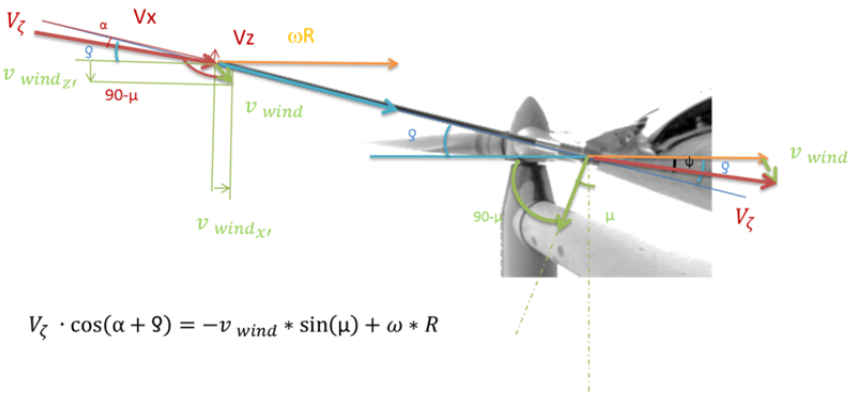

$$V_\zeta \cdot \cos(\alpha + \vartheta) = -v_{wind} * \sin(\mu) + \omega * R$$

Figure 16 Representation of the angles when negative alpha

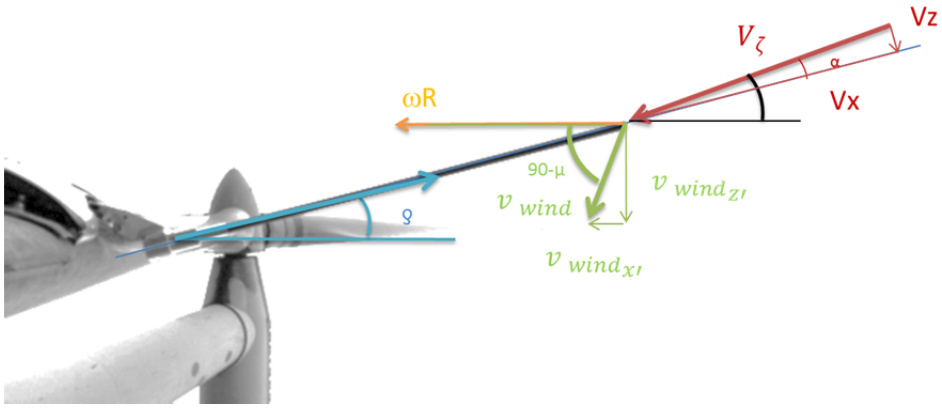

Figure 17 Representation of the angles in the other turbine cycle

$$V_x = V_\zeta \cdot \cos(\alpha) = -v_{wind} * \cos(90 - \mu + \varrho) + \omega * R * \cos(\varrho)$$

$$V_z = V_\zeta \cdot \sin(\alpha) = v_{wind} * \sin(90 - \mu + \varrho) - \omega * R * \sin(\varrho)$$

If

$$\alpha = \psi - \varrho$$

Then

$$\varrho = \psi - \alpha$$

$$\begin{aligned} V_x = V_\zeta \cdot \cos(\alpha) &= -v_{wind} * \cos(90 - \mu + \varrho) + \omega * R * \cos(\varrho) = \\ &= -v_{wind} * \cos(90 - (\mu - \psi + \alpha)) + \omega * R * \cos(\psi - \alpha) = \\ &= -v_{wind} * \sin(\mu - \psi + \alpha) + \omega * R * \cos(\psi - \alpha) \end{aligned}$$

$$V_z = V_\zeta \cdot \sin(\alpha) = v_{wind} * \sin(90 - \mu + \varrho) - \omega * R * \sin(\varrho) = v_{wind} * \cos(\mu - \varrho) - \omega * R * \sin(\varrho)$$

And

$$V_\zeta \cdot \sin(\alpha + \varrho) = v_{wind} * \cos(\mu)$$

$$V_\zeta \cdot \cos(\alpha + \varrho) = -v_{wind} * \sin(\mu) + \omega * R$$

Then

$$v_{wind} * \cos(\mu) \cdot \frac{\cos(\alpha + \varrho)}{\sin(\alpha + \varrho)} = -v_{wind} * \sin(\mu) + \omega * R$$

$$\frac{v_{wind} * \cos(\mu)}{\mathrm{tg}(\alpha + \varrho)} = -v_{wind} * \sin(\mu) + \omega * R$$

$$v_{wind} \cdot \left[\frac{\cos(\mu)}{\mathrm{tg}(\alpha + \varrho)} + \sin(\mu)\right] = \omega * R$$

$$v_{wind} \cdot \cos(\mu) \cdot \left[\frac{1}{\mathrm{tg}(\alpha + \varrho)} + \frac{1}{\mathrm{tg}(\mu)}\right] = \omega * R$$

Rearranging the expression

$$v_{wind} \cdot sin(\mu - \psi + \alpha) = \omega * R * \cos(\psi - \alpha) - V_x$$

Then

$$\mathrm{v}_{\mathrm{wind}} = \frac{\omega * \mathrm{R} * \cos(\psi - \alpha) - \mathrm{V_x}}{\sin(\mu - \psi + \alpha)} = \frac{\omega * R * \cos(\varrho) - V_x}{sin(\mu - \varrho)}$$

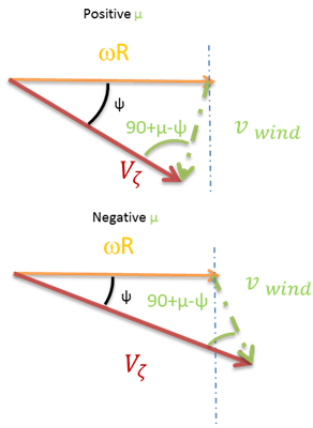

Figure 18 Triangle of speeds

The cosine and sine expressions also plays a role here to determine the relation between v_{wind} and ψ. Therefore

$$v_{wind}^2 = (\omega * R)^2 + V_\zeta^2 - 2 \cdot V_\zeta \cdot \omega * R \cdot \cos(\psi)$$
$$= (\omega * R)^2 + V_\zeta^2 - 2 \cdot V_\zeta \cdot \omega * R \cdot \cos(\alpha + \varrho)$$

$$\frac{v_{wind}}{\sin(\psi)} = \frac{\omega * R}{\sin(90 + \mu - \psi)} = \frac{V_\zeta}{\sin(90 - \mu)}$$

Considering that in this case μ is negative when the angles are obtuse, and positive when acute.

This is equivalent to

$$\frac{v_{wind}}{\sin(\varrho + \alpha)} = \frac{\omega * R}{\sin(90 - (\psi - \mu))} = \frac{\omega * R}{\cos(\psi - \mu)} = \frac{V_\zeta}{\sin(90 - \mu)} = \frac{V_\zeta}{\cos(\mu)}$$

This means that if we have the speed and the radius and the angle, the wind speed can be obtained

$$v_{wind} = \sqrt{(\omega * R)^2 + V_\zeta^2 - 2 \cdot V_\zeta \cdot \omega * R \cdot \cos(\alpha + \varrho)}$$

The orientation can be obtained with

$$v_{wind} = \frac{\omega * R * \cos(\varrho) - V_x}{sin(\mu - \varrho)}$$

Then

$$v_{wind} = \frac{V_z + \omega * R * \sin(\varrho)}{\cos(\mu - \varrho)}$$

$$v_{wind} = \frac{V_\zeta \cdot \sin(\alpha + \varrho)}{\cos(\mu)}$$

$$\mu = \varrho + \operatorname{asin}\left(\frac{\omega * R * \cos(\varrho) - V_x}{v_{wind}}\right)$$

Corroboration formulae

In order to satisfy and confirm the prior formulas, a formal mathematical derivation is provided. There are several ways to reduce the uncertainty. One way is to apply different formulas on different values and derive results. These results must somehow fit statistically

$$v_{wind} \cdot \cos(\mu) \cdot \left[\frac{1}{\operatorname{tg}(\alpha + \varrho)} + \frac{1}{\operatorname{tg}(\mu)}\right] = \omega * R$$

The derivate when assuming that $\mu = cte$

$$\frac{dv_{wind}}{dt} \cdot \cos(\mu) \cdot \left[\frac{1}{\operatorname{tg}(\alpha + \varrho)} + \frac{1}{\operatorname{tg}(\mu)}\right] - v_{wind} \cdot \frac{\cos(\mu)}{\sin^2(\alpha + \varrho)} = 0$$

$$\frac{dv_{wind}}{dt} \cdot \left[\frac{1}{\operatorname{tg}(\alpha + \varrho)} + \frac{1}{\operatorname{tg}(\mu)}\right] = \frac{v_{wind}}{\sin^2(\alpha + \varrho)}$$

$$\frac{dv_{wind}}{dt} \cdot \left[\frac{\sin(\mu) * \cos(\alpha + \varrho) + \sin(\alpha + \varrho) * \cos(\mu)}{\sin(\alpha + \varrho) * \sin(\mu)}\right] = \frac{v_{wind}}{\sin^2(\alpha + \varrho)}$$

$$\frac{dv_{wind}}{dt} \cdot \left[\frac{\sin(\mu) * \cos(\alpha + \varrho) + \sin(\alpha + \varrho) * \cos(\mu)}{\sin(\mu)}\right] = \frac{v_{wind}}{\sin(\alpha + \varrho)}$$

$$\frac{dv_{wind}}{dt} \cdot \left[\frac{\sin(\mu + \alpha + \varrho)}{\sin(\mu)}\right] = \frac{v_{wind}}{\sin(\alpha + \varrho)}$$

$$\frac{dv_{wind}}{v_{wind}} = \frac{\sin(\mu) \cdot dt}{\sin(\mu + \alpha + \varrho) \cdot \sin(\alpha + \varrho)} = \frac{\sin(\mu) \cdot dt}{\sin(\mu + \psi) \cdot \sin(\psi)}$$

Then

$$\int \frac{dv_{wind}}{v_{wind}} = \int \frac{\sin(\mu) \cdot dt}{\sin(\mu + \psi) \cdot \sin(\psi)}$$

It will be assumed that $\mu \approx cte$ in one cycle

$$\int \frac{dv_{wind}}{v_{wind}} = \sin(\mu) \cdot \int \frac{dt}{\sin(\mu + \psi) \cdot \sin(\psi)}$$

If we know ϱ then

$$\frac{V_z + \omega * R * \sin(\varsigma)}{\cos(\mu - \varsigma)} = v_{wind}$$

$$v_{wind} = \sqrt{(\omega * R)^2 + {V_\zeta}^2 - 2 \cdot V_\zeta \cdot \omega * R \cdot \cos(\alpha + \varsigma)}$$

$$v_{wind} * cos(90 - \mu + \varsigma) = v_{wind} * cos(90 - \mu) * \cos(\varsigma) - v_{wind} * sin(90 - \mu) * \sin(\varsigma) = -V_x + \omega * R$$
$$* cos(\varsigma) = v_{wind} * sin(\mu) * \cos(\varsigma) - v_{wind} * cos(\mu) * \sin(\varsigma)$$
$$= v_{wind} * sin(\mu - \varsigma) = -V_\zeta \cdot \cos(\alpha) + \omega * R$$

And

$$v_{wind} * \cos(\mu) = V_\zeta \cdot \sin(\alpha + \varsigma)$$

$$v_{wind} * sin(\mu) * \cos(\varsigma) - v_{wind} * cos(\mu) * \sin(\varsigma) = v_{wind} * sin(\mu - \varsigma) = -V_\zeta \cdot \cos(\alpha) + \omega * R$$

Then

$$v_{wind} * sin(\mu) * \cos(\varsigma) - V_\zeta \cdot \sin(\alpha + \varsigma) * \sin(\varsigma) = -V_\zeta \cdot \cos(\alpha) + \omega * R$$

$$v_{wind} * sin(\mu) * \cos(\varsigma) = V_\zeta \cdot \big(\sin(\alpha + \varsigma) * \sin(\varsigma) - \cos(\alpha)\big) + \omega * R$$

$$\frac{V_\zeta \cdot \sin(\alpha + \varsigma)}{\cos(\mu)} = v_{wind}$$

$$\frac{V_\zeta \cdot \sin(\alpha + \varsigma)}{\cos(\mu)} * sin(\mu) * \cos(\varsigma) = V_\zeta \cdot \big(\sin(\alpha + \varsigma) * \sin(\varsigma) - \cos(\alpha)\big) + \omega * R$$

$$V_\zeta \cdot \sin(\alpha + \varsigma) * tg(\mu) * \cos(\varsigma) = V_\zeta \cdot \big(\sin(\alpha + \varsigma) * \sin(\varsigma) - \cos(\alpha)\big) + \omega * R$$

$$V_\zeta \cdot [\cos(\alpha) + \sin(\alpha + \varsigma) * tg(\mu) * \cos(\varsigma) - \sin(\alpha + \varsigma) * \sin(\varsigma)] = \omega * R$$

$$V_\zeta \cdot [\cos(\alpha) + \sin(\alpha + \varsigma) * (tg(\mu) * \cos(\varsigma) - \sin(\varsigma))] = \omega * R$$

$$V_x \cdot \left[\frac{\cos(\alpha) + \sin(\alpha + \varsigma) * (tg(\mu) * \cos(\varsigma) - \sin(\varsigma))}{\cos(\alpha)}\right] = \omega * R$$

$$\omega * R = V_x \cdot \left[1 + \frac{\sin(\alpha + \varsigma) * (tg(\mu) * \cos(\varsigma) - \sin(\varsigma))}{\cos(\alpha)}\right]$$

Whenever no yaw misalignment the expression will be reduced to an estimate of the position of the sensor as:

$$R \approx \frac{V_x \cdot \left[1 - \frac{\sin(\alpha + \varsigma) * \sin(\varsigma)}{\cos(\alpha)}\right]}{\omega}$$

As in principle R is constant, some generic properties of this formula can be generated. However a validation of this hypothesis must be carried out on the real wind turbine.

2.2.5 Correction of the speed

In order to get the speed in a good basis several algorithms have being developed. There are two main procedures:

- procedures which directly determine the speed
- procedures required to determine different parameters and functions to estimate the position and speed

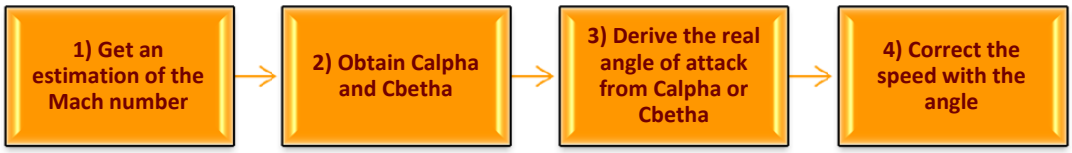

Figure 19 Diagram showing the sequence of operations

The Mach number is estimated taking in account the pressure as it is without any correction. This value will be use to get the applicable correlation needed to get the angle of attack depending on the $C\alpha$ or $C\beta$. After obtaining the belonging value the pressure is corrected applying Cq and afterwards the speed is obtained.

The steps taken can lead to a better understanding of the behavior of the azimuth speed variation occurring at the blade section. The methodology is shown in the next block diagrams A) to L) and is explained in the subsections.

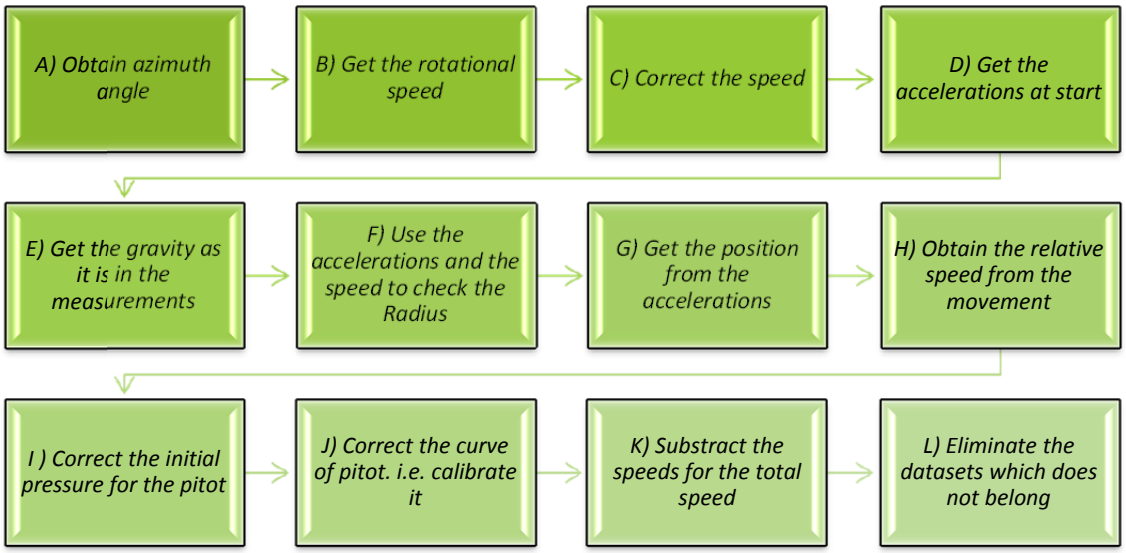

Figure 20 Methodology to correct the speed

Obtain the azimuth angle

There are two signals that potentially can give the azimuth position (i.e. acceleration and absolute pressure). For both signals there are several approaches that were checked. The first approach used it

helped in the first measurement campaign uses a vectorial approach, where the normalization of the local maximum and minimum defined the complete variation of the angle. Nevertheless this logic-array approach has its limitations derived from the variation of speed which inherently depends on the time. This leads that in the end the second approach was used, i.e. getting the azimuth angle from the signal per se. Here it is convenient to describe the used hypothesis and a methodology

a) The acceleration is useless as long as the position is not known and even if known the other direction movements or vibrations, will provoke big variations in the derived azimuth. A correction in the value assuming the big inertia of the rotor is a useful approach, but for this it is needed first to get accurately the value of the position of the accelerometer in a global coordinate system. Instead it has being used the barometric pressure which is the most stable value on a cycle, though the atmospheric pressure is not varying substantially on a pressure range and on a small variation of the angle of attack

b) In order to get the best of the cycle two approaches has being tested, the conclusion is that a mixed between them is the best option, i.e. Get the frequency per cycle, make a bin analysis or not taking in account the signal, interpolate the signal using sinusoidal approach and compare the signal with the original. If the moving average of the signal is different in a 2% it will try again to create the signal starting from the deviation of 2%, in case the 2% is on the starting point it will ignore that part and move to the next point. After all of this the phase and signal is known and the azimuth angle is created

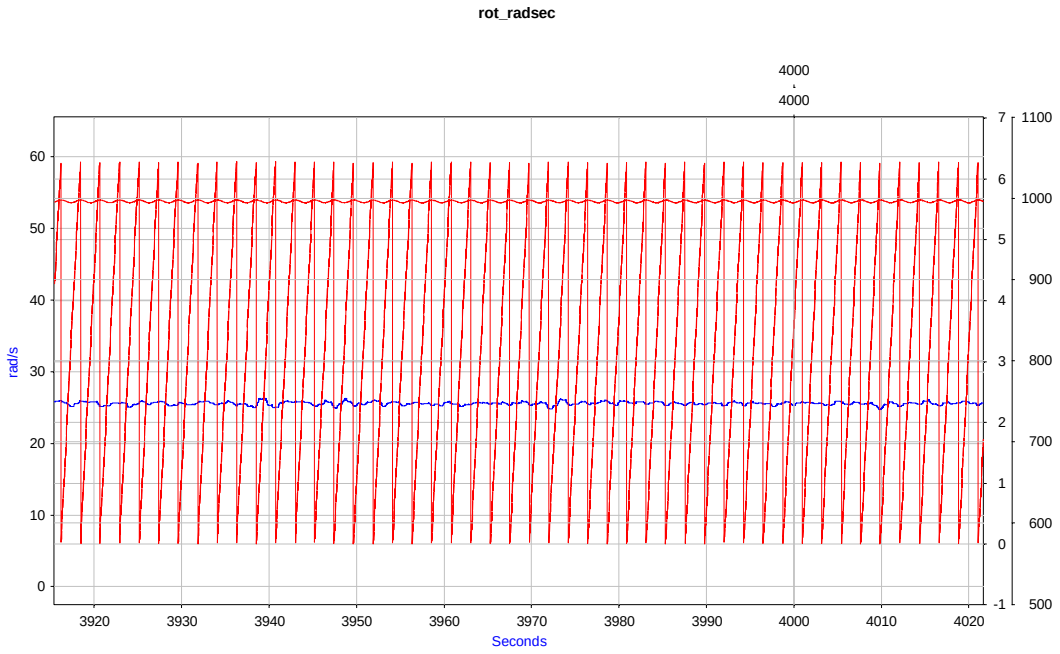

Figure 21 Final result of the algorithm using the barometric pressure.

As mention the previous array based fast algorithm (or low requirements algorithm) to determine the azimuth position did not work properly. One of the reasons for the differences among other algorithms comes from the change of speed in the rotor which alters the time-weighted averaged/enveloped signal used to normalize the azimuth angle. This can be corrected backwards but there will be always a slight

unreal variation in the angle which it is difficult to determine up to which extend comes from the blade itself. The results from the first measurement campaign with this “old” methodology can be found in the next section.

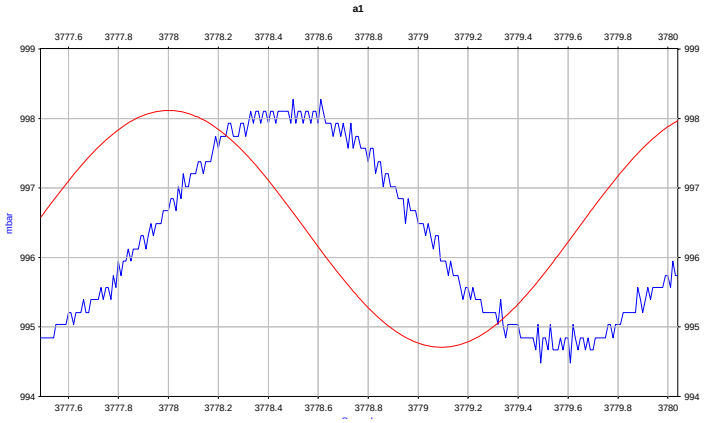

Figure 22 Comparison of the "old" signal in blue against the new one in red

A FFT decomposition gave after a generation of a new signal from the barometric pressure see Figure 22, a visible difference in frequency. As it might be seen though the phase is different this is irrelevant. Nevertheless the blue signal does not reach 1.25 periods and the red one seems to reach that level, i.e. the red is faster than the blue signal, this is due to the resolution of the FFT. Another visual comparison can be done, getting the slopes of both signals

The next approach was to use the FFT to get the best time from the period and then interpolate the signal itself making a bin analysis. The result is shown in Figure 23

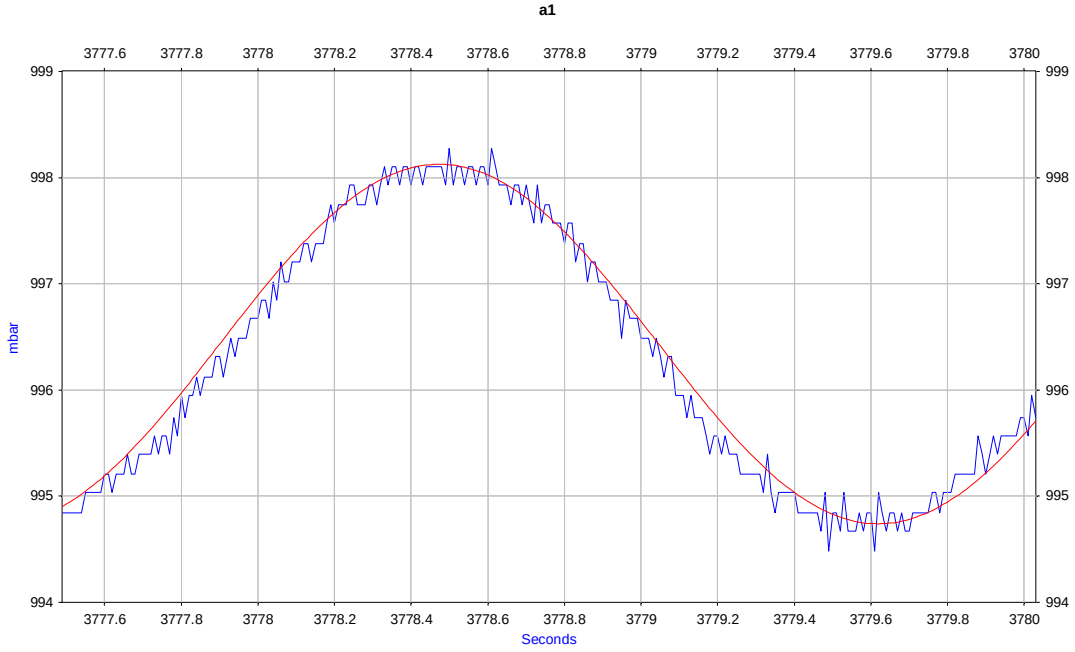

Figure 23 the frequency and the initial phase shift is not yet perfect

A change in the speed of the rotor slowing down the speed will create an initial phase gap which will differ from the original waveform; additionally the frequency will be also not correct.

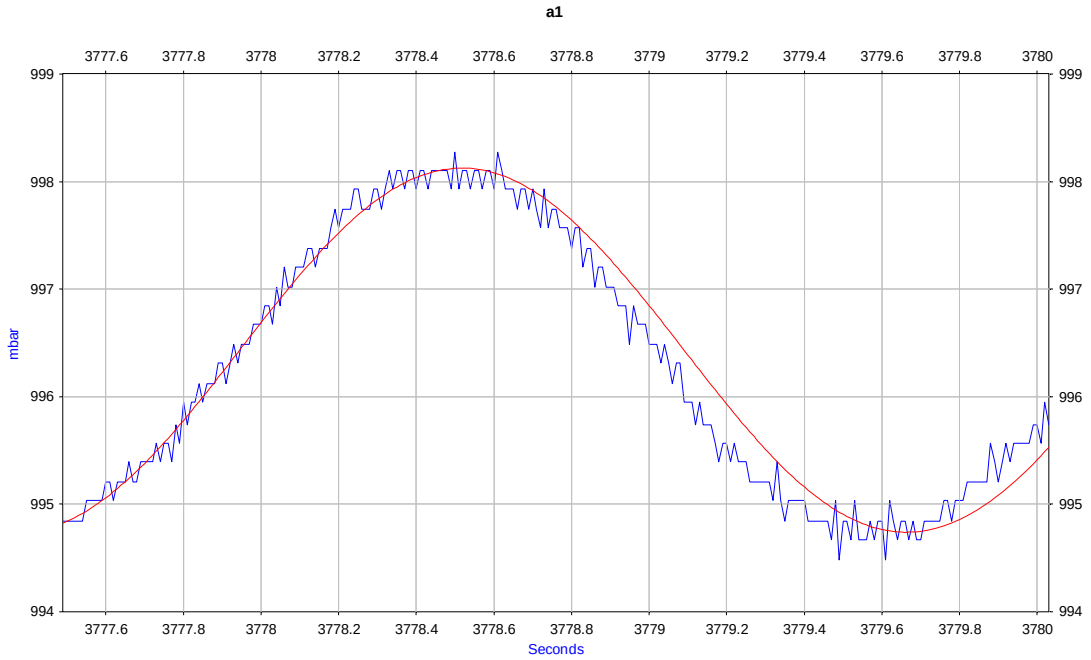

Figure 24 "Manual" correction on the sinusoidal wave

Therefore two steps have been created to re-correct the frequency and phase changes, the first checks “manually” the error from -10 to +10 degrees (i.e. depending on the sampling rate this amount should be changed, in this case the bin analysis is performed in 20 bins, i.e. 360/20 = 18 degrees) and get the value when the first ¼ cycle has a minimum. This change of phase can be seen for the same signal in Figure 24

In order to reduce the final offset, a barometric pressure correction is applied. Here is not used for the azimuth but for the absolute pressure itself. The resulting value can be seen in Figure 25.

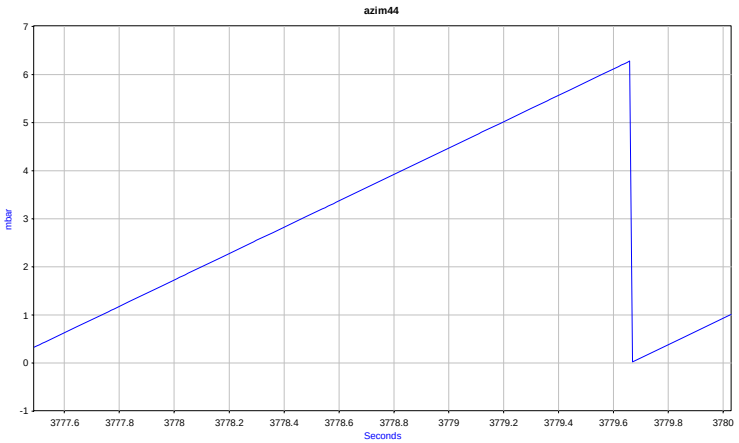

Figure 25 Obtained azimuth position

Nevertheless whenever this approach is used the signal shakes due to the corrections, for this approach and taking into account that the resolution is fairly nothing comparing with the estimation done, this approach will be used just when the error is higher than an estimated value

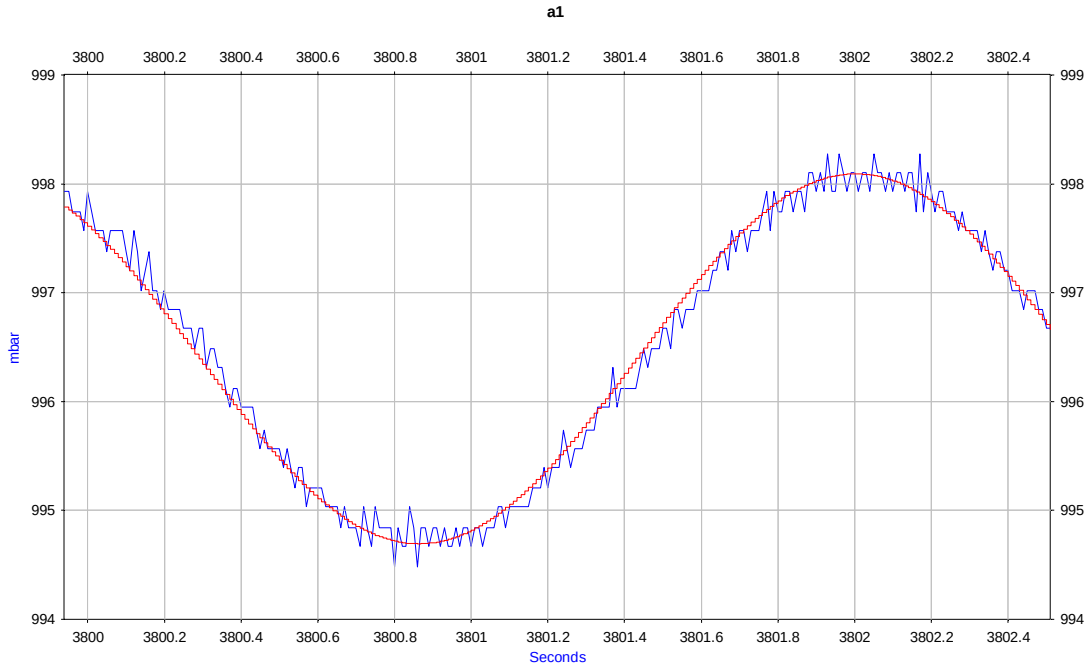

Figure 26 Another example of the deviation in the signal.

An instantaneous accuracy in the angle smaller than 1 degree be reached because the peaks caused by the uncertainty are already bigger, nevertheless the mean value can vary up to 0.02 mBar, which in mean value will be approx. 0.8 degrees.

$$\frac{\Delta p}{4.5} = \frac{0.8}{180}$$

$$\Delta p = \frac{0.8 * 4.5}{180} = 0.02\ mbar$$

In this specific case the total number of points per cycle is 250 points. The maximum errors in position are in the highest values of the sinus, i.e. from 5 to -5 degrees or depending on the deviation in the maximum slope itself (4 to 5 degrees). Whenever consider as a minimum 3 degrees. The equivalent will be 4*250/180 ~ 5 points, which are the minimum considered to get a sinusoidal approximation. It cannot go lower due that it will be completely unstable.

Nevertheless as computational effects, the error will be considered as 5% for the correction in the phase gap and a maximum of +-5 degrees in the correction.

The binning analysis indeed gave better approach in the signal itself. If not done a bin the frequency obtained could vary in +/- 0.05 Hz but the signal has being always resulting as having a lower frequency from the original, producing that the rotational speed thereof lower. In order to correct those behaviors a recurrent loop with a break control has being introduced. The result can be here foreseen as total (though this example has a tolerance of 5%). A proper representation of the results on the second measurement campaign can be found in Figure 27

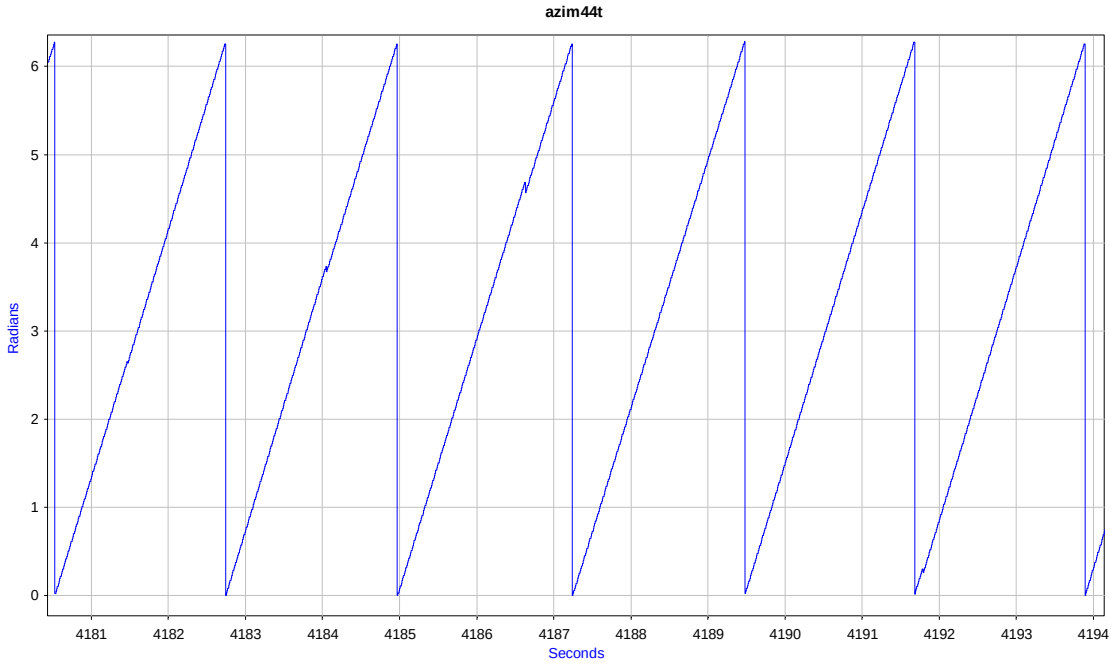

Figure 27 Azimuth angle in radians

Difference whenever using acceleration instead of pressure

There are several methodologies to use also the acceleration as input for the angle. One is explained above which is the most usual, nevertheless, it does exist another way as for example getting the integration of the acceleration caused by gravity. The signal scaled looks like Figure 28

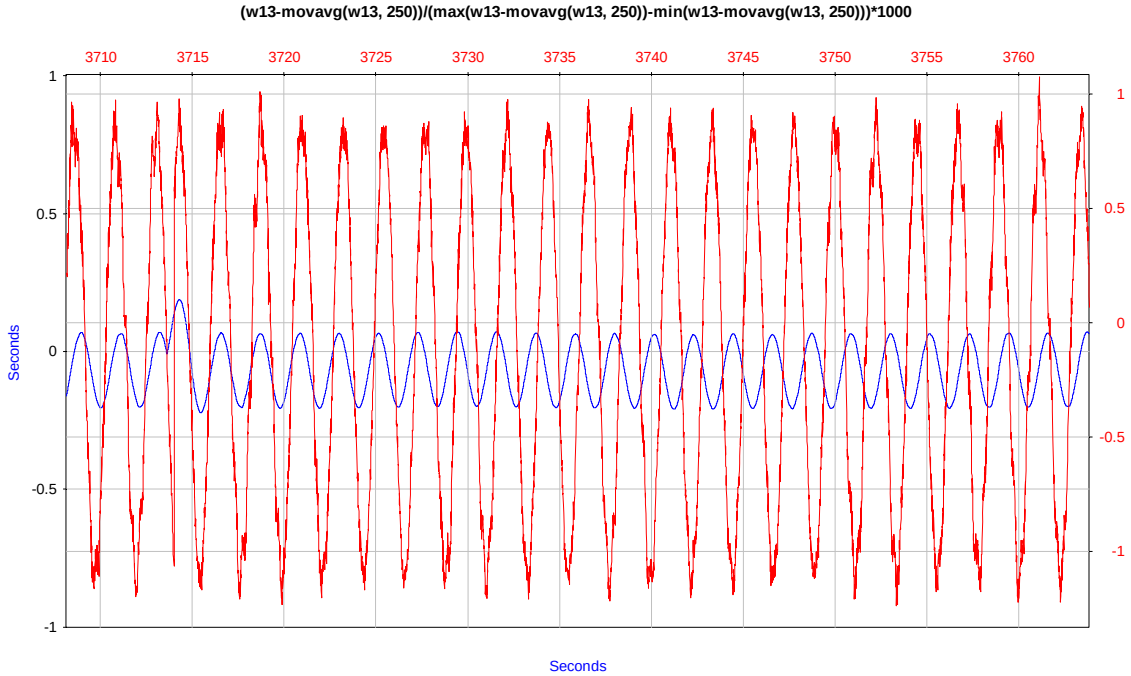

Figure 28 in red the acceleration in blue the integration

$$t = \int g * \sin(wt + \alpha)\, dt = -gcos(wt + \alpha)$$

And the idea behind is to use as it is a sinusoidal signal the gravity cycle, whenever noise is found thought is a discrete integral it simply gets reduced. The change of phase is of 90 degrees. The frequency as it can be seen belongs to the same value as the acceleration itself

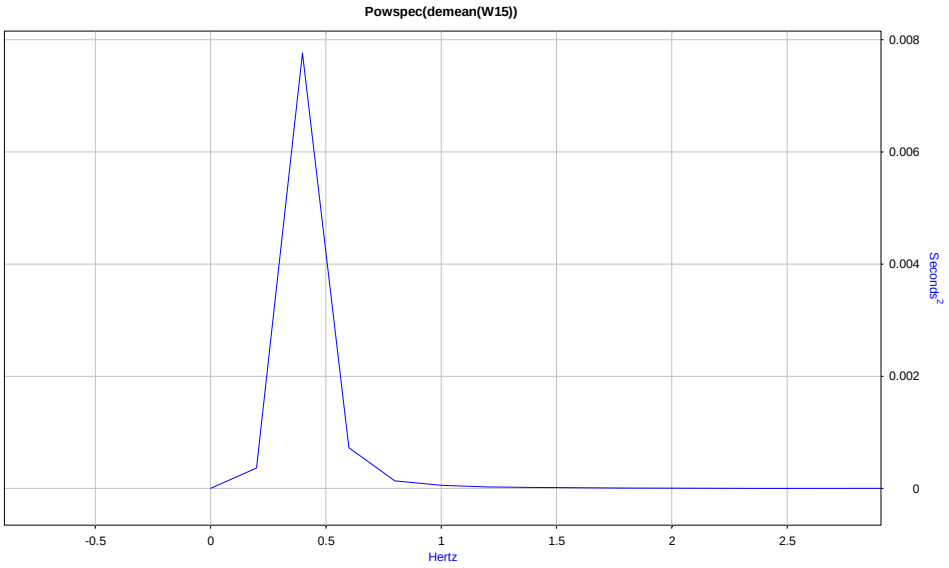

Figure 29.- Peak at approx. 0.4 Hertz

But the inconvenient of this methodology is that the signals are not reproduced perfectly and whenever any noise or missing single involved the phase between the signals can change significantly. So there is not an easy way to correct that, therefore the best that can be done is to use the barometric pressure or the gravity itself and as shown in Figure 31 the values have magnitude influence on higher frequency regime the rotor is working.

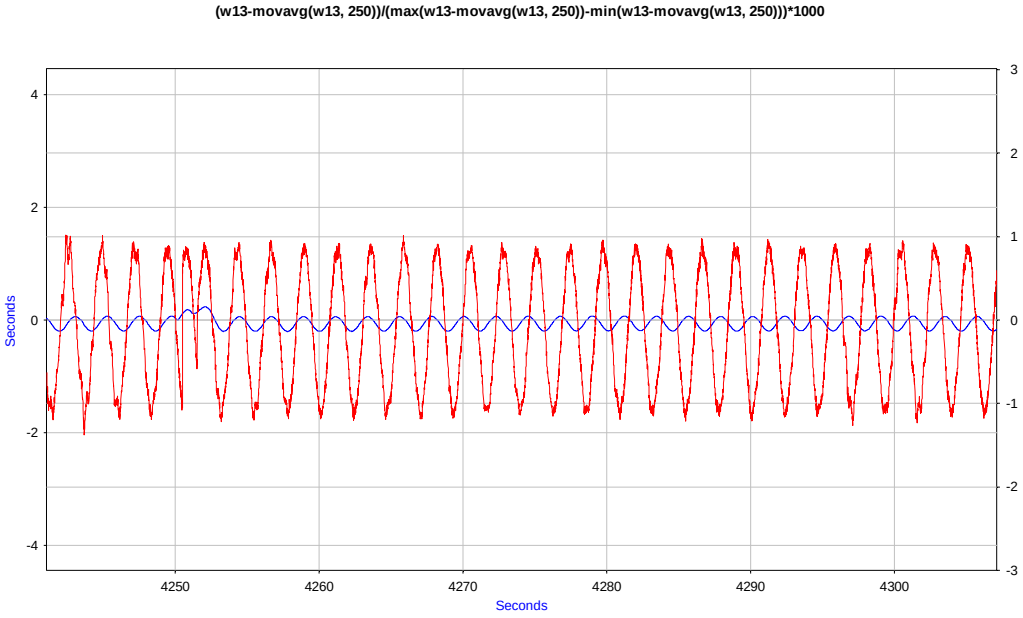

Figure 30.- Change of phase between signals

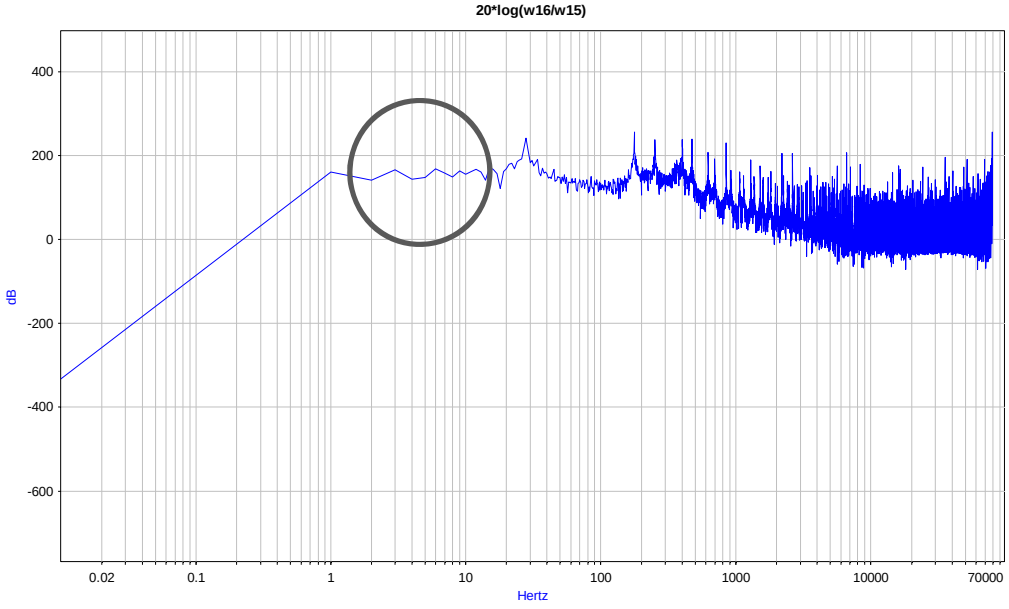

Figure 31. Gain change between output and input

Get the rotational speed

Once obtained the azimuth angle, the derivation of the summed angle will give the speed. The next figures show how initially is given the speed and afterwards the real one

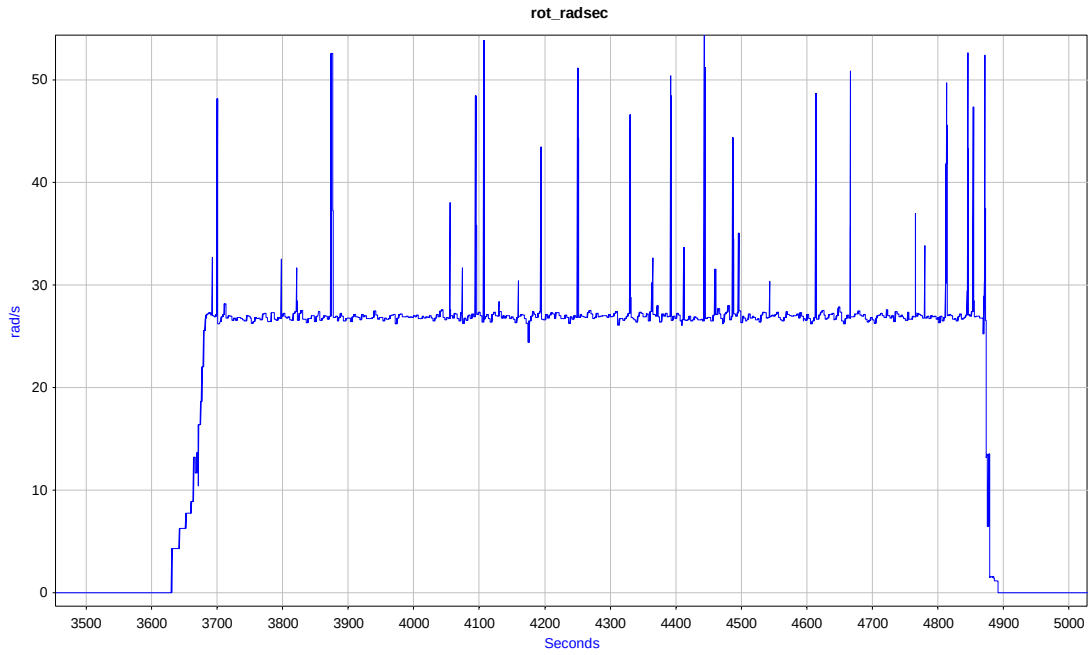

Figure 32.- Rotational speed from the resulting corrected signal from the not-binned signal

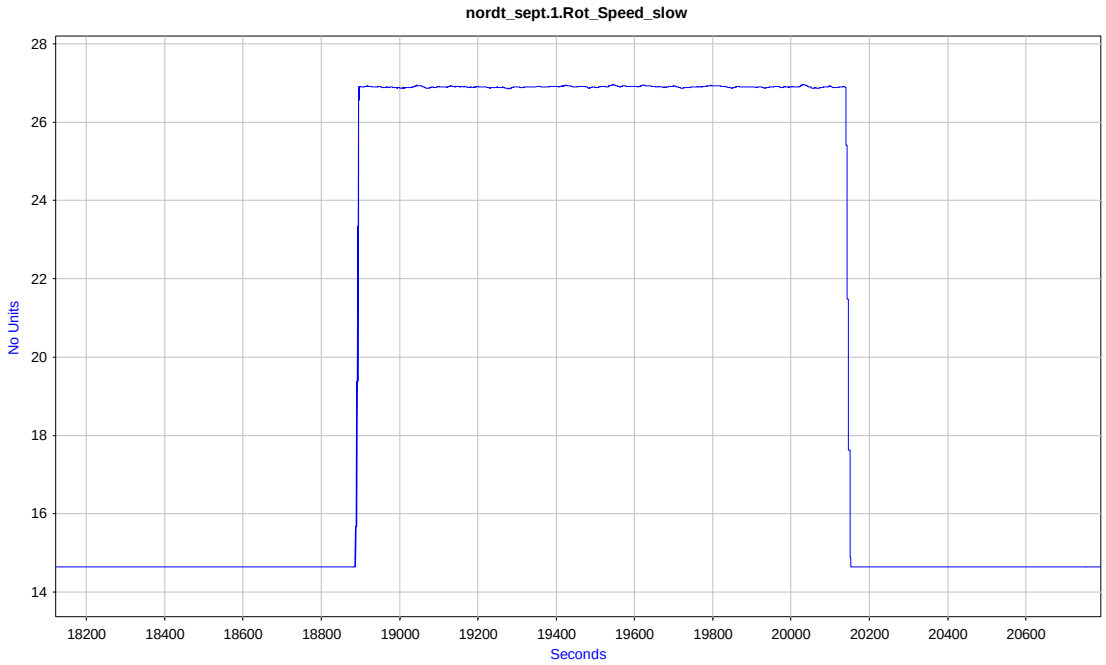

Figure 33. Rotor shaft speed, Nordtank

As described in the previous section there could be a potential source of error in the speed whenever the frequency has not enough accuracy, and this is mainly why a correction of the speed is usually here needed.

Correction of the speed

Due to the losses in the GPS signal in the second measurement campaign, peaks are a side effect when obtaining the rotational speed. –The raw signal is shown in Figure 32. There are two steps to clean the noise, the first reduce the bigger peaks naturally impossible in physical terms derived by the angle. The second makes sense in terms of speed itself.

Another side effect is the correction of the frequency whenever is needed. The signal in Figure 34 is cleaned for peak occurrences. The final, corrected signal is shown in Figure 35.

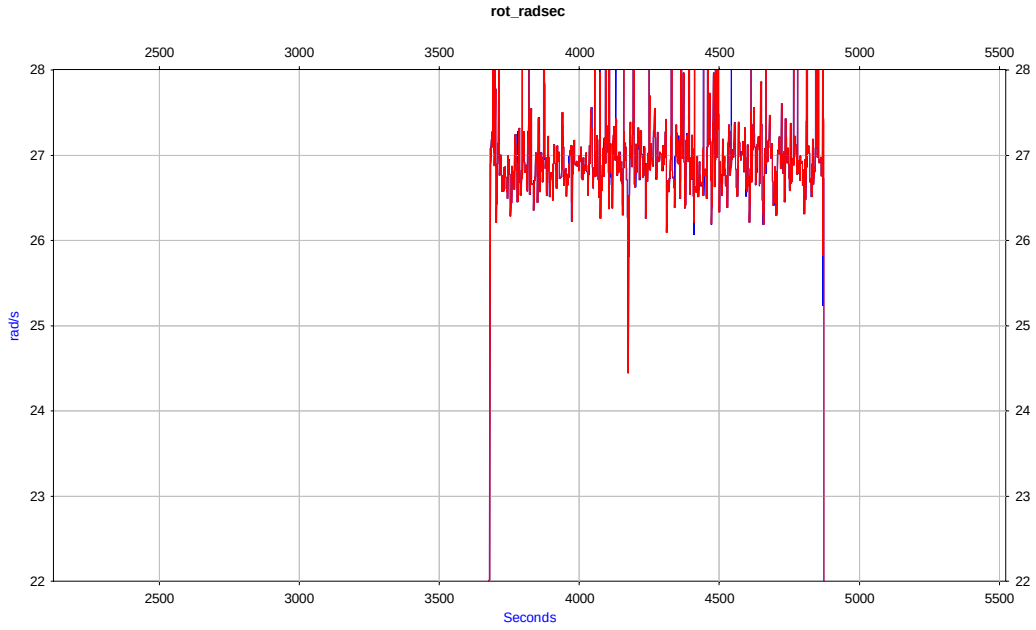

Figure 34.- Correction of the signal at 30 rpm

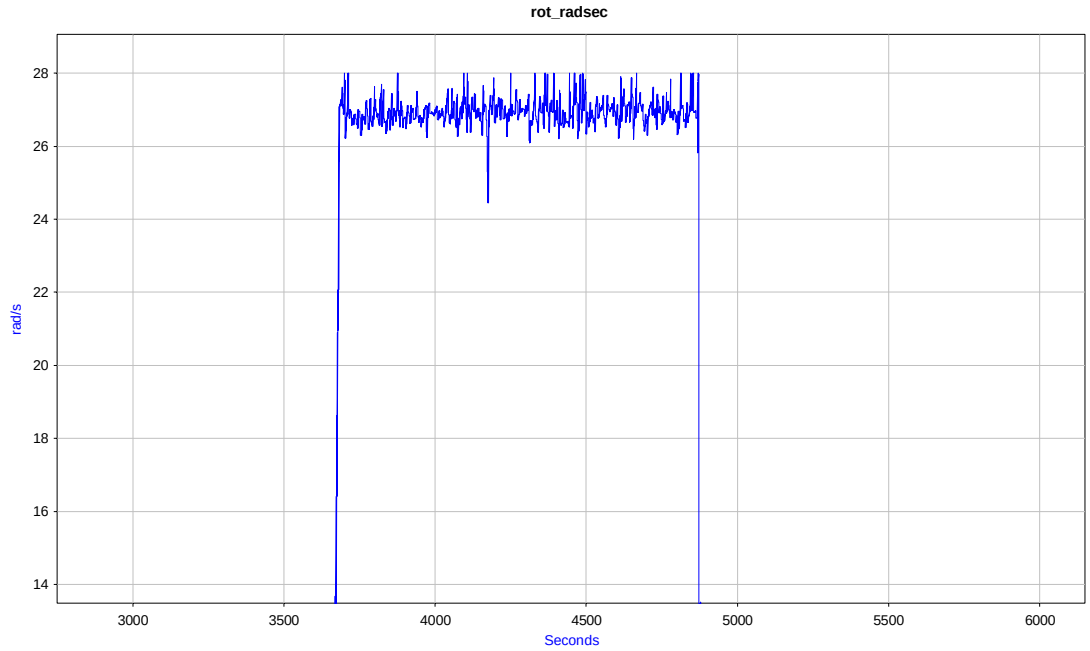

Figure 35.- Final signal corrected

Though it is not the same timeframe it can be seen that the speed belongs to what was expected

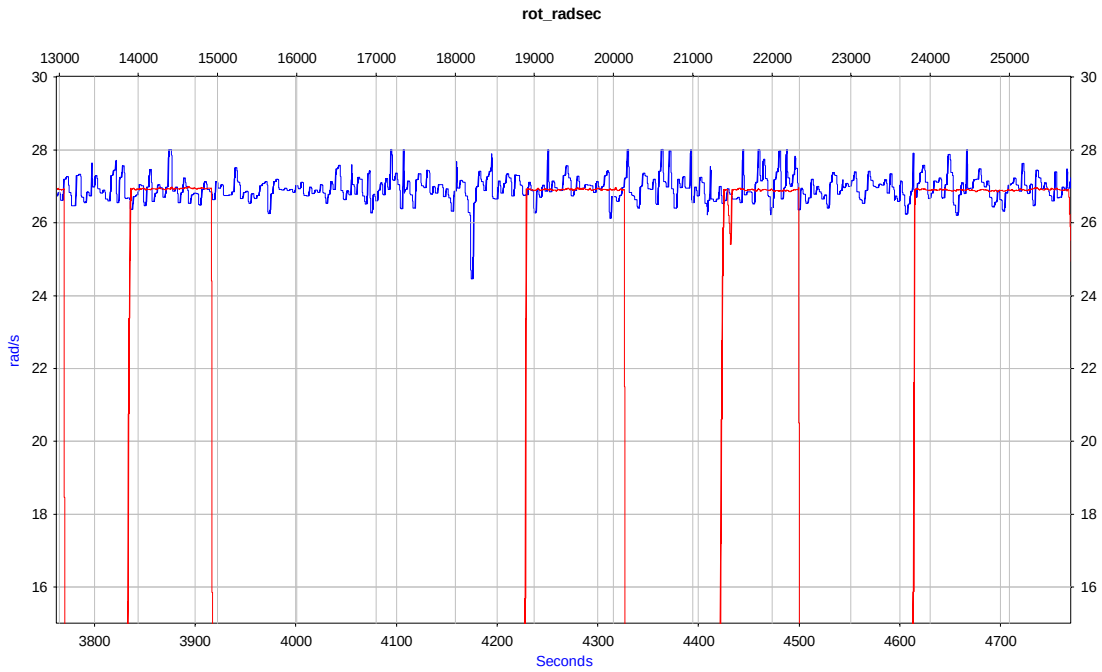

Figure 36.- red signal is the rotational speed in Nordtank for long period. In blue, the obtained speed is shown for a short period

Nevertheless the variability is much higher than the real variation in the rotor signal. The median for random periods of time seemed to be quite close ~26.9 rpm although the standard deviation is about 15 times bigger.

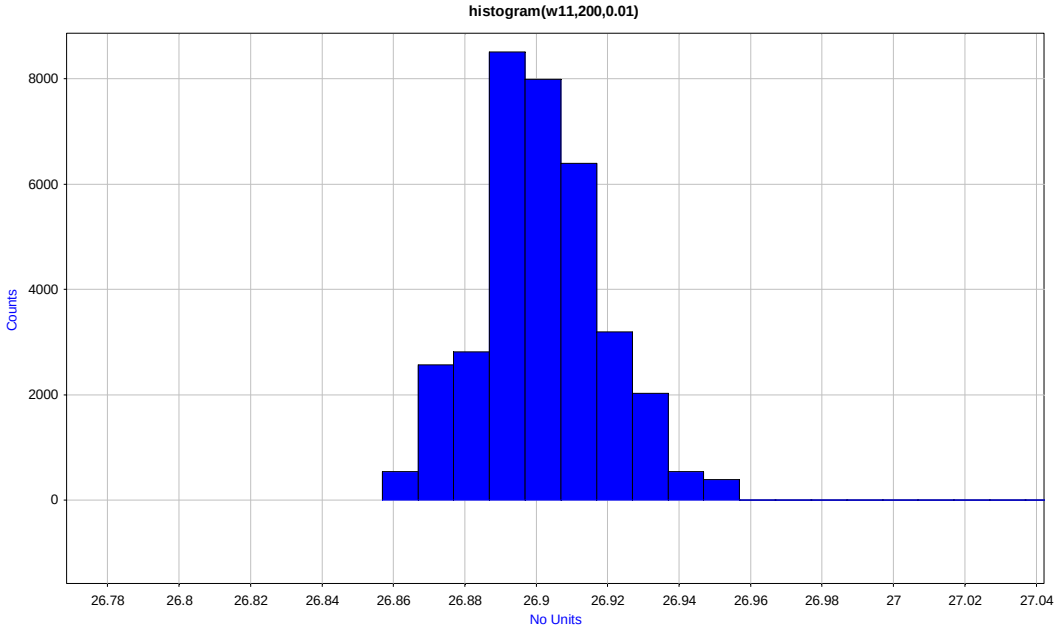

Figure 37histogram of the rotor speed. Median 26.90 rpm. Stdev 0.017 rpm

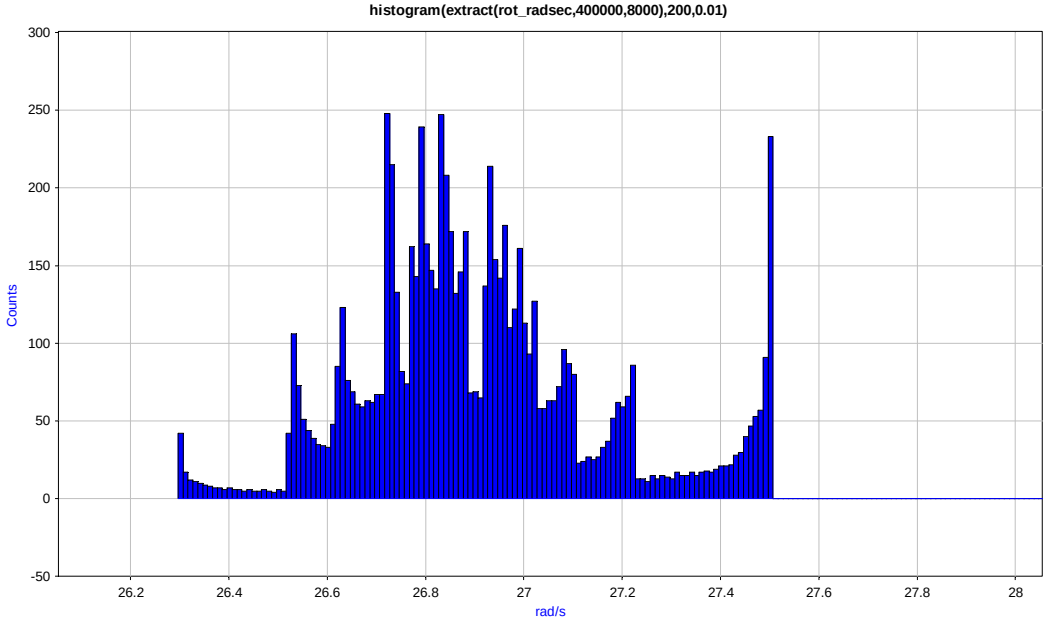

Figure 38. Histogram of the obtained values. Median 26.87 rpm. Stdev 0.254 rpm

Get the accelerations at the cut-in/start of the turbine

The algorithms used to determine the position of the accelerometers whenever starting and the deflection caused in the blade when the turbine is moving. These algorithms are also used in this case to determine the initial and final angles of the position of the sensors and afterwards the position of the pitot to the turbine. The problem here is that this turbine, in the installed position, that excess the usual limit on normal turbines in terms of centripetal acceleration. This limit can be derived on onshore turbines as:

Horizontal Wind turbines

The maximum speed allowed in a turbine in onshore for reasons of noise would not exceed 100m/s. Assuming that as a reference the maximum speed it is clear that on a radius of a 70% the speed will not be higher than 70m/s. On big turbines (>3MW) the maximum diameter up to nowadays 180 meters it is clear than the acceleration will not be bigger than 70^2/90 < 7g in as the small value and 70^2/50 < 10g as the maximum. On the other hand on the small turbines the maximum increases, thought in this specific case reaches the maximum of 12.2g. So, it is clear that on turbines with a size lower than 1MW a limit in the acceleration of 16g is needed.

Vertical Wind turbines

There are not many vertical wind turbines but applying some theoretical background it is clear that expecting three different ranges of turbines, then the maximum linear speed will not exceed 50m/s whenever talking to turbines >2MW, and 80 m/s in turbines >50KW in and thought in overall shall not exceed 16g

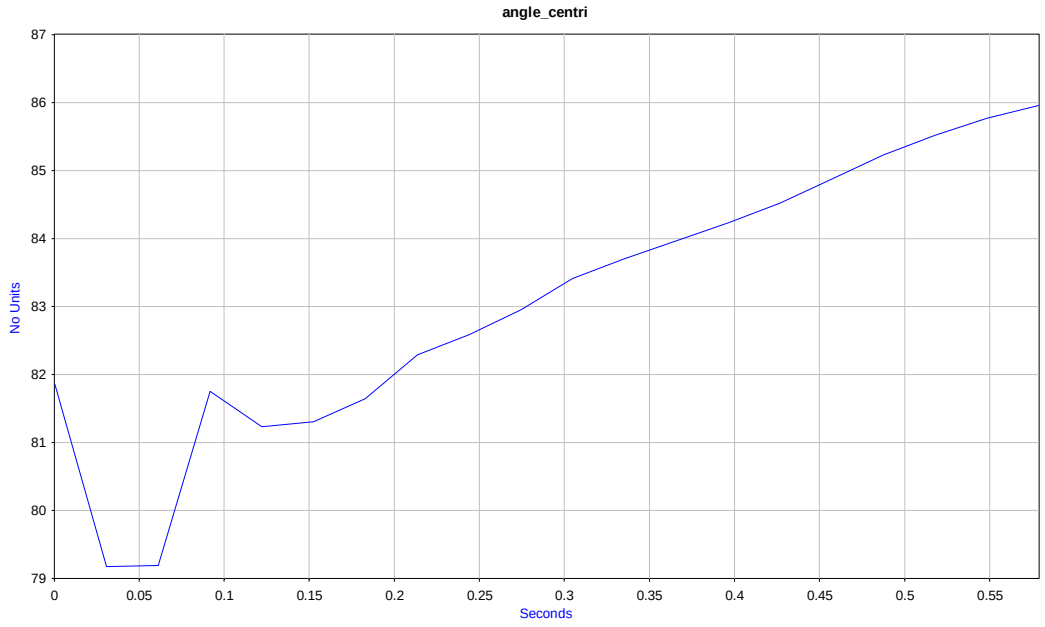

Figure 39.- Centripetal angle at the starting of the turbine

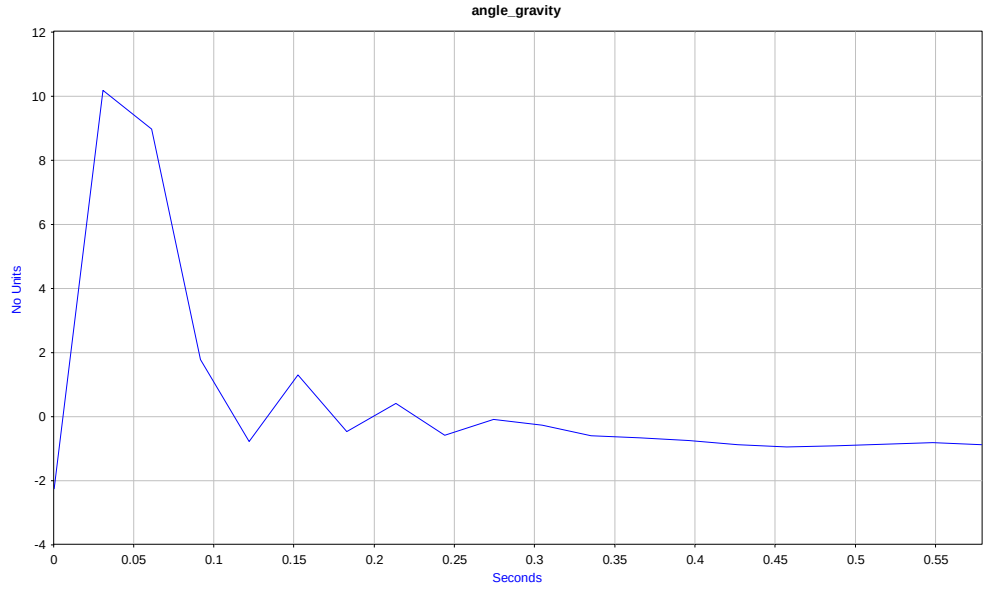

Figure 40.- Gravity angle

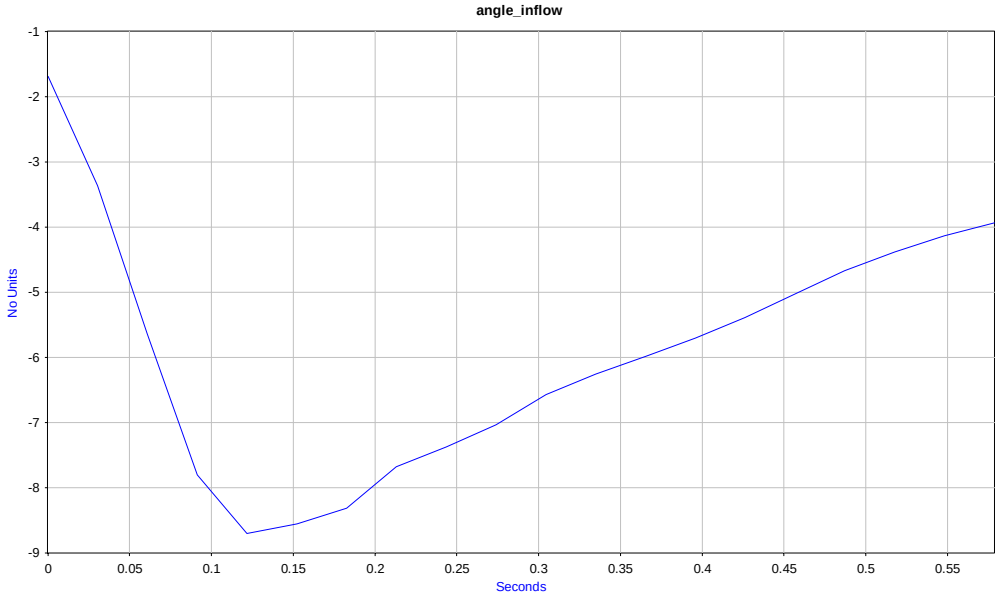

Figure 41. Inflow angle

Get the gravity as it is in the measurements

The gravity gave on the evaluation 9.692656 m/s2, which is way below what is normal for this location. Usually this step would have never being evaluated, but it has being noticed that the value did not fit reality. The maximum acceleration where the accelerometer saturates is 78.52m/s2; the theory says to be 78.48m/s2. The mean value of the gravity is taken; possible reasons for this could be that the uncertainty gives a negative impact on the value itself, or something in the calibration chain is wrong[6].

[6] This has being actually proven by the value per se1, and the resulting component gives actually less than 1 as in the results, thought the complete acceleration value has being taken 9.81 m/s2

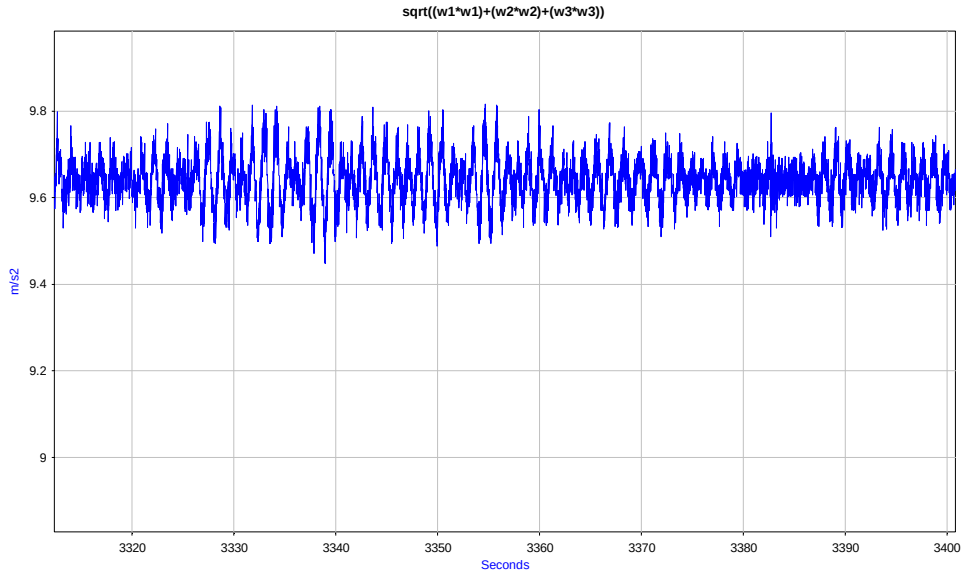

Figure 42.- Value of the three axis quadratic component at turbine stopped ($\sqrt{acc_x^2 + acc_y^2 + acc_z^2}$)

Use the accelerations to check the radius

There are several ways to check the radius itself. From the formulas described in "Formulae on a point triangle of speeds, space point" if the turbine does not have a huge misalignment it can be committed that then β is approximately 90 degrees and therefore

$$R \approx \frac{V_x \cdot \left[1 - \frac{\sin(\alpha + \varrho) * \sin(\varrho)}{\cos(\alpha)}\right]}{\omega}$$

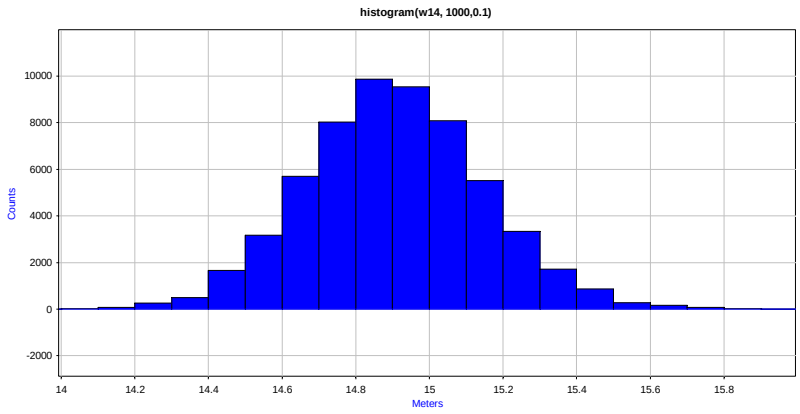

Figure 43 Results of the radius assuming $\varrho = 15$ degrees on the second measurement campaign (14.91m)

Assuming that the wind speed is close to 26.8 rpm in average, though the data was not present. It can be derived with some binning the Radius. In this case the p_{attack} has being considered to be negative.

Nevertheless in the whole assumptions the angle ϱ seems to be assumed constant and this is simply not true:

$$\varrho = \varrho(t) = \varrho_{fixed} + \sigma_{tilt} * \sin(wt + \varphi)$$

at 90 degrees ϱ is positive and the tilt angle will be added and at 270 degrees substracted. This belongs to whenever compared to the barometric pressure as reference, the maximum will appear when the turbine pass from minimum pressure to maximum (in red), which is equivalent to move from 0 degrees to 180.

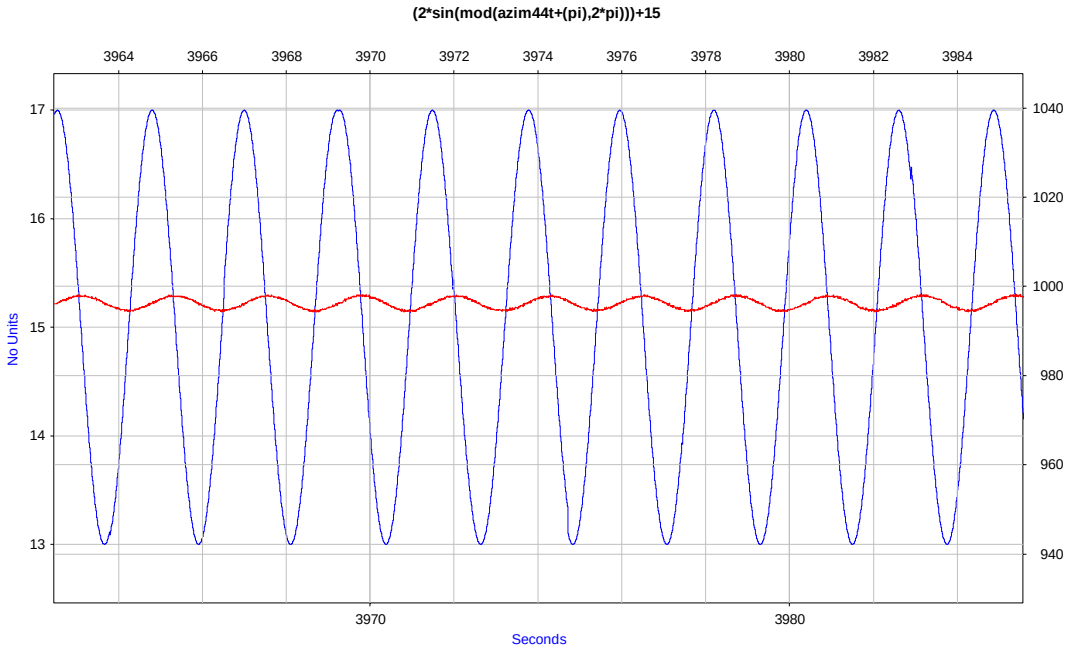

Figure 44 Variation of the angle

Nevertheless the variation of the angle does not contribute much to the final angle.

The correlation of the inflow angle with the electrical power signal was evaluated for the first campaign runs, and the angle are shown in the following as a moving average over one revolution:

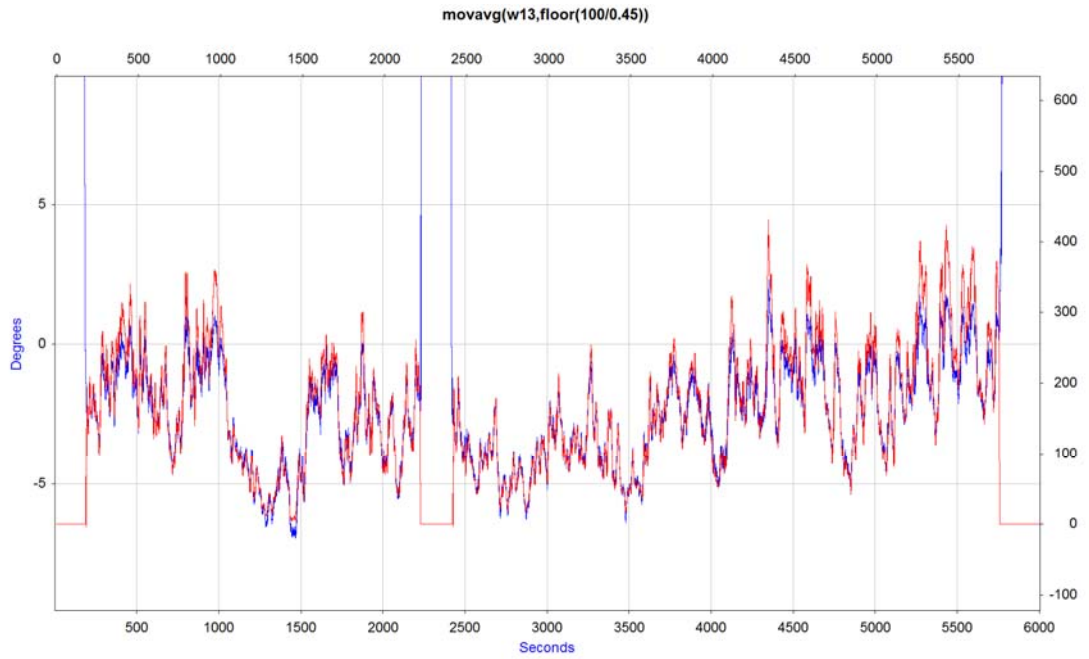

Figure 45 Inflow angle(blue) and electrical power(red) correlation

2.3 Components

2.3.1 Sensor: 5-hole Pitot measurement

For the blade sensor, following definitions for the channels can be found on the appendix. The port and signal nomenclature was configured as shown in the two next figures.

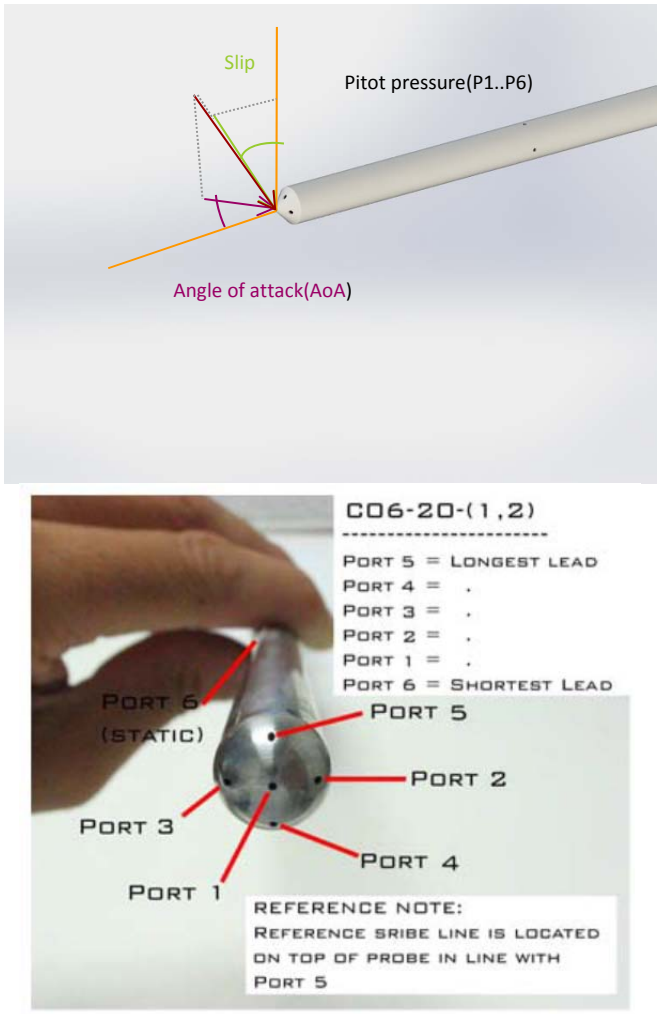

Figure 46 Definition of the pitot ports

- The SLIP was defined from the difference of pressure between the ports 3 and 2
- The AoA was defined from measuring the difference of the pressure between the ports 4 and 5
- The barometric pressure was measured in the port 6
- The dynamic pressure was measured as difference between port 1 and port 6

Nevertheless though there has being several developments for the head of the pitot the works comprises here are centred in the conical head. The behaviour will be shown in “Evaluation and Calibration of the system”

2.3.2 Hardware components

The requirements of the bard have being described as follows:

Specifications SyncBoard:

Function:	A battery-operated unit. Logs data from sensors on a globally synchronized time axis. Data may be stored locally or transmitted via an external wireless communication unit.
Signal input.	A shielded flat cable connects the SyncBoard to an external connection box. Connection box may be built by an end user.
Low speed analog inputs:	8 channels 24 bit 1024 S/s analog to digital converter. Unipolar/bipolar. FSD 5 V. Programmable gain 1,2,3,4, 6 8 or 12.
High Speed Analog Inputs:	4 channels 24 bit 48 kS/s. Analog to digital converter. 10 V RMS FSD. Microphone bias programmable 5 V – 9 V. EIPE requires external unit.
On board sensors:	3 axis accelerometer 1048 S/s. Full-scale range of ±2g, ±4g, ±8g, and ±16g, 16 bit converter.
DIO ports:	4 pins from µController.
Timing:	Medium accuracy: 1 ms global sync: 3 weeks battery life (no mics.) High accuracy: 200 ns global sync: XX% battery life
Data Storage:	Slot for Micro SD card with up to 32 GBytes. Time domain waveforms stored with global time stamp.
Data Communication:	Bluetooth 4.0, low power for communication to external Smart Phone which can be used to monitor Data Acquisition Process.
External Switches and status:	Power On/off/Reset Status/error/battery indicators Timing Mode switch High speed A/D converter switch (on/off) (power saving).
Battery connection:	Permits connection to various size external batteries. A 1400mAH, 11,1 V battery could provide continuous operation for: Medium accuracy timing: 21 days High accuracy timing: 7 days High accuracy timing, High Speed Analog Input: 1 day.
Physical Enclosure:	Approximately 10 x 10 x 1 cm. Weight less than 250 g, incl. battery, as above. Clamshell giving moderate environmental protection. Should there be mounting holes or is "gaffer tape" OK?

Figure 47 Description of the requirements for the Syncboard

As explained in the first section the development of the board has being completed in different stages:

Stage 1:

This concept was developed as a lightweight system for the purpose of measuring ambient wind speed and- direction with a 5-hole pitot, air temperature, air barometric pressure and 3D-turbulence with a sonic anemometer and carried by a balloon. The challenge was mainly in design the board and accessories so light to be carried by the Lighter-Than-Air(LTA) balloon (Gregor Giebel, May 2009). The board was realized by design criteria of:

- GPS assisted synchronisation
- Data storage on RAM of data link modem(NAS)
- Inertial system(INS) for accelerations, Euler angles determination and magnetometer(ADIS)
- Battery power supply
- Weight not exceeding the balloon pay load capacity of 10 kg

NI universal boards for 24-Bit OEM applications were used along with a NI sbRIO-9601/9602 OEM device, and with a high energy LIPO battery power supply. The different components are visible in **Error! Reference source not found.**. The pitot tube support was made in carbon and the head was manufactured in Aluminium, with drilled straight ports (P1, P2, P3, P4, P5, see **Error! Reference source not found.**) aligned with the main support axis. The platform containing the board and pitot system is shown in Figure 4.

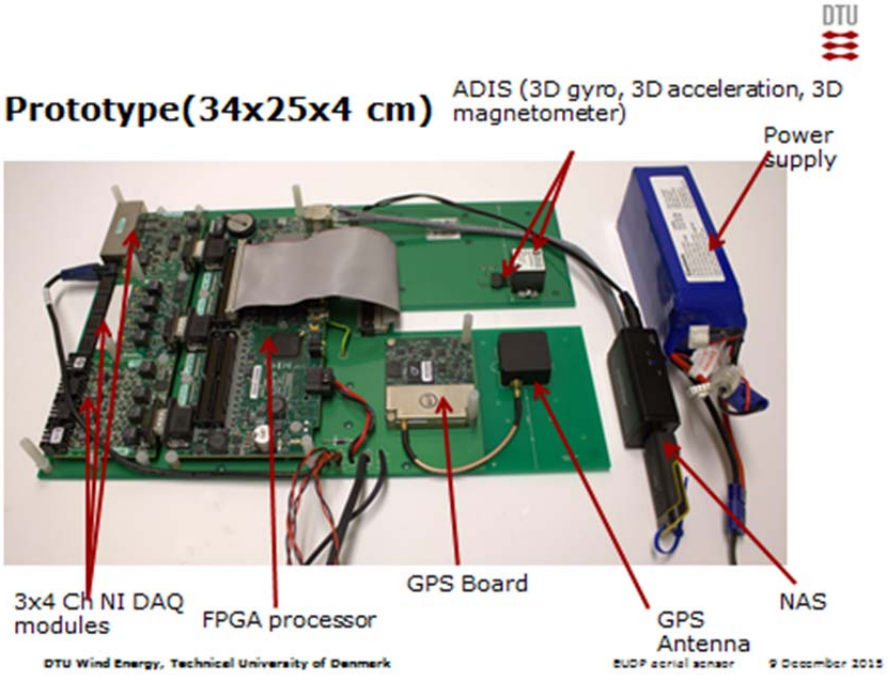

Figure 48 Second system developed by Delta

Stage 2:

This is a setup realized in order to be able to take the measurements in parallel with the delta development. In order to do not create a load for delta and get a delay in the project itself, Risø decided to get a commercial product and test a part of the components that are independent of the overall system. For this proposes DTU acquired a commercial system from National Instruments, MyRio 1900, which was able to get the basic requirements of the required board.

As briefly explained the overall system was composed by

- A data logger and transducer system: Data logger series MyRio [7]National instruments which has an internal field programmable gate array.
- A Small printed Circuit board with 3 Pressure manometric transducers HCLA00xx…Band one absolute pressure transducer, both capable of converting the signals in a digital I2C protocol.
- A GPS
- Battery system

All the external hardware is connected to the FPGA. The i2c elements needed to have separate addresses and hereby the liens were configured defining the logic.

The hardware is composed by several elements, as shown in the overview Figure 3:

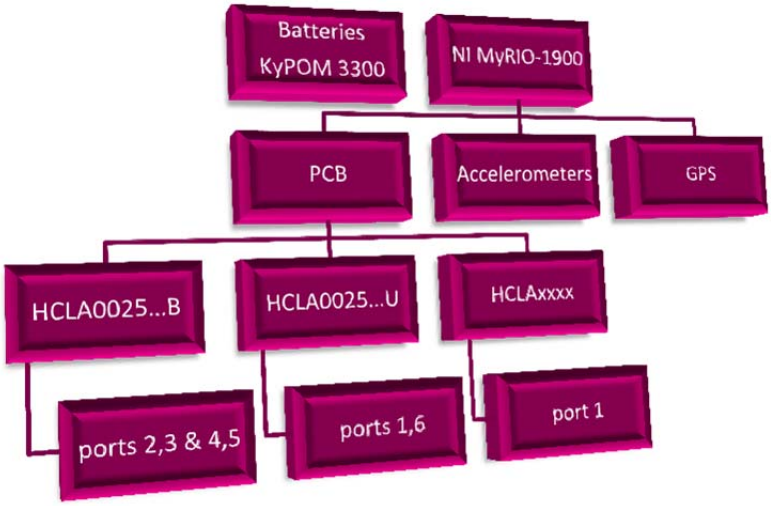

Figure 49 Scheme/overview of the hardware

The power supply independent battery supply systems consists of two 3.3Ah, 11.1 V LiPo, see Figure 4. The power supply circuit and circuit board with miniature pressure transducers is shown together with the myRio data logger (including accelerometer, and GPS), see Figure 50

[7] The specifications of this device and the pressure transducers as well can be found in the appendix

Figure 50 System batteries

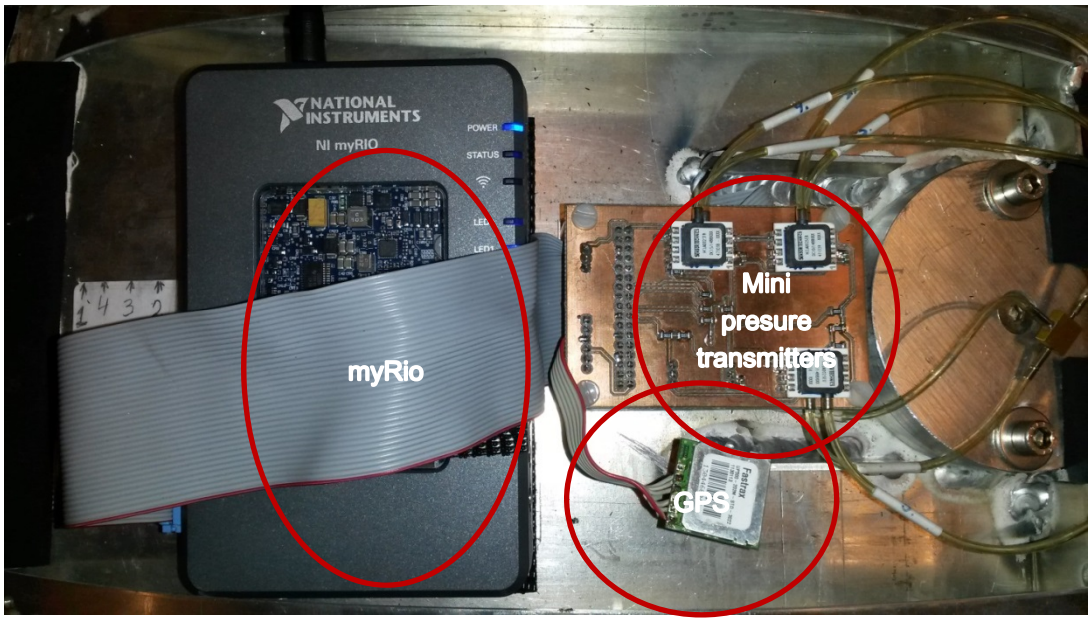

Figure 51 Pitot's hardware components (excluding batteries)

Stage 3:

Measurements with ..

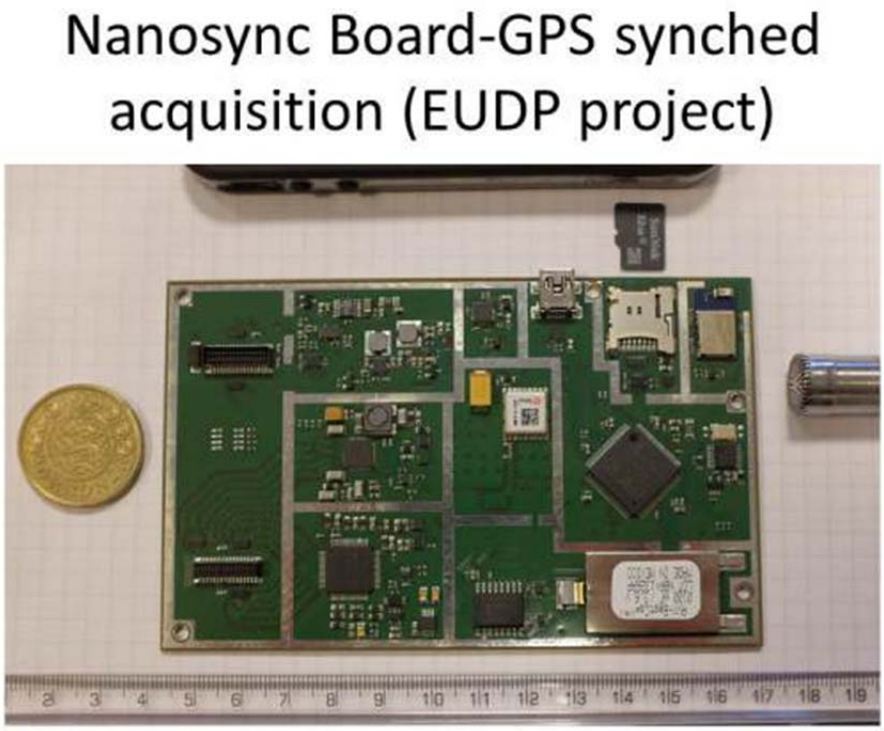

Figure 52 Prototype board of the new generation type of DAQ as per specs(see Figure 46)

2.3.3 Energy harvester

The setup will be located on a blade and as described in the previous sections. the batteries lasts for maximum of 2 to 3 days. This is a major problem and this is mainly why an energy harvester is here needed for longer measurement periods. Other solutions as drilling the blade and passing power supply could lead to major problems for instance with the humidity on the blade

Requirements

The power consumption of the board with sensors has being estimated to be 2 to 10 watts, having the breakdown consumption shown in Table 1.The main objective is to produce the energy on the blade in Denmark and these limits the usage due to the sunlight in winter

Table 1 Breakdown comsuption

Device	Number	Max Consumption	Total
Pressure transducers	4	0.01 W	0.05 W
Temperature	1	0.01 W	0.01 W

MyRio	1	14 W	15 W
Acoustic	1	0.2 W	0.2 W
Total			16 W

Proposals

There are in the market several typologies for energy harvesting, to cite some

- Solar panels
- Piezoelectric
- Propellers
- Flywheel

For the consumption rate and the weight of the final prototype seems that the piezoelectric and flywheel does not fit our constraints. So from here on the solar panel and the propeller will be commented

Solar Panel

A low cost, flexible polymer solar cell technology developed at Risø was investigated on how much area there was needed to cover a wind turbine blade for sufficient power backup. It was realized, that applying this foil on the blades of the Nordtank wind turbine would not cause any technical problem within the power supply requirements to feed a backup system. A unit representing 15x15 cm delivers typically 0.5V at 4A, and connecting several cells multiplying to-25 V power supply will represent with 10% efficiency about 10m^2 of panel area(the area of 1 rotor blade is approximately 30 m^2).

Propellers

The first idea was to get a propeller and input in a motor, using it as a generator. We used different propellers, and one more in plastic with the Archimedes form. The main problem on the original propellers was the noise and afterwards the power generation. It can be seen in **Error! Reference source not found.** that the Archimedes gave much more power than the normal propellers and was quite silent.

Figure 53.- Propeller prototype

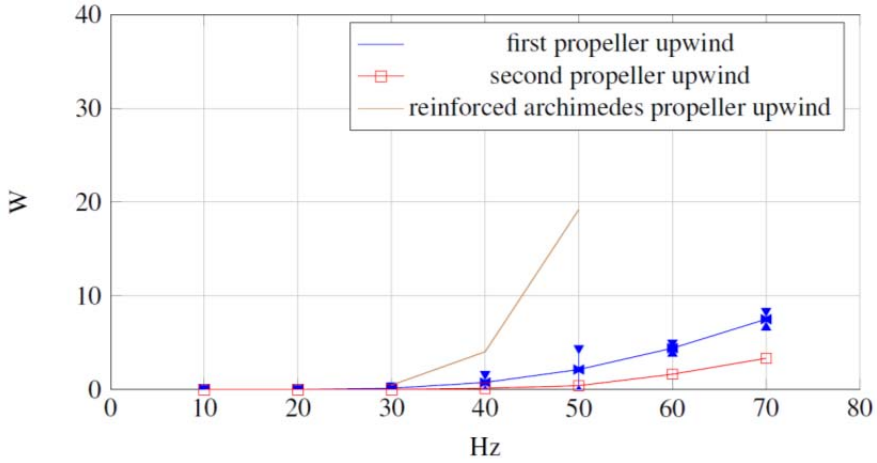

Figure 54 Upwind prototypes power production in front of the blower. In x-axis the frequency of the blower is represented

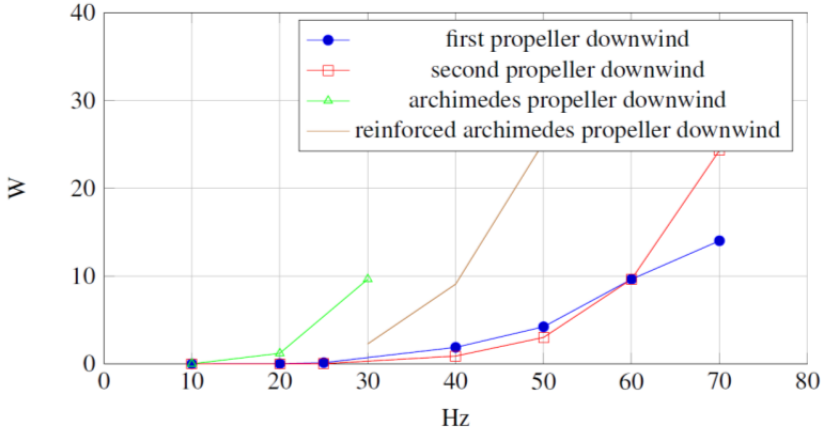

Figure 55 Downwind prototypes power production in front of the blower. In x-axis the frequency of the blower is represented

Estimating that the position of the Archimedes and orientation was not varying during the test, and assuming that the resulting Mach wont vary much more than 1.5% in Mach number (belonging to a minimal dynamic pressure and a maximum variation in absolute pressure of +-3%), from the results obtained in Figure 55 and taking in account that the variability of the measurement was high the minimum power should look like Figure 56 and Figure 57

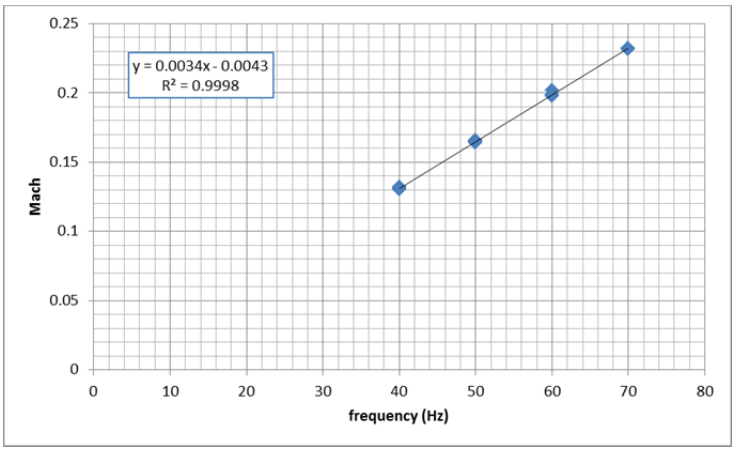

Figure 56 Mach number versus speed on a specific date

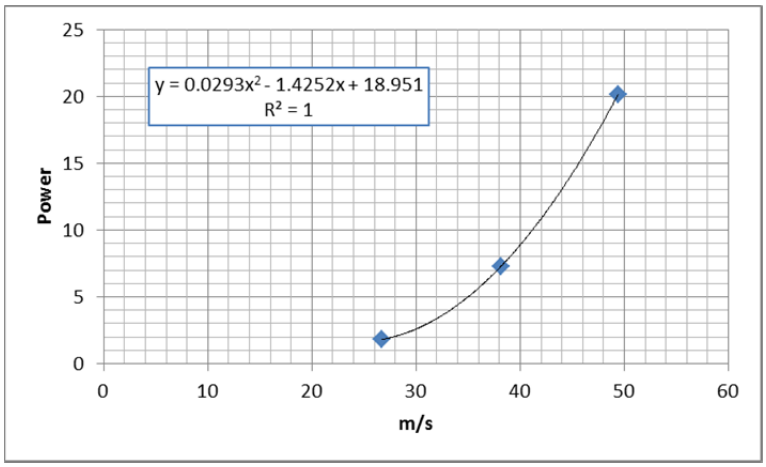

Figure 57. Possible Power versus speed

Figure 58.- First design

The power at 30 Hz should belong to ca. 30 m/s which will be our range of speeds as minimum. Therefore the Archimedes is recommended to be used.

There has being 2 different designs. The first one, shown in Figure 58 due to the light concept and aerodynamic forces broke up above 40Hz. The second, shown in Figure 59, has being shown to be robust up to 50 Hz (i.e. 55 m/s)

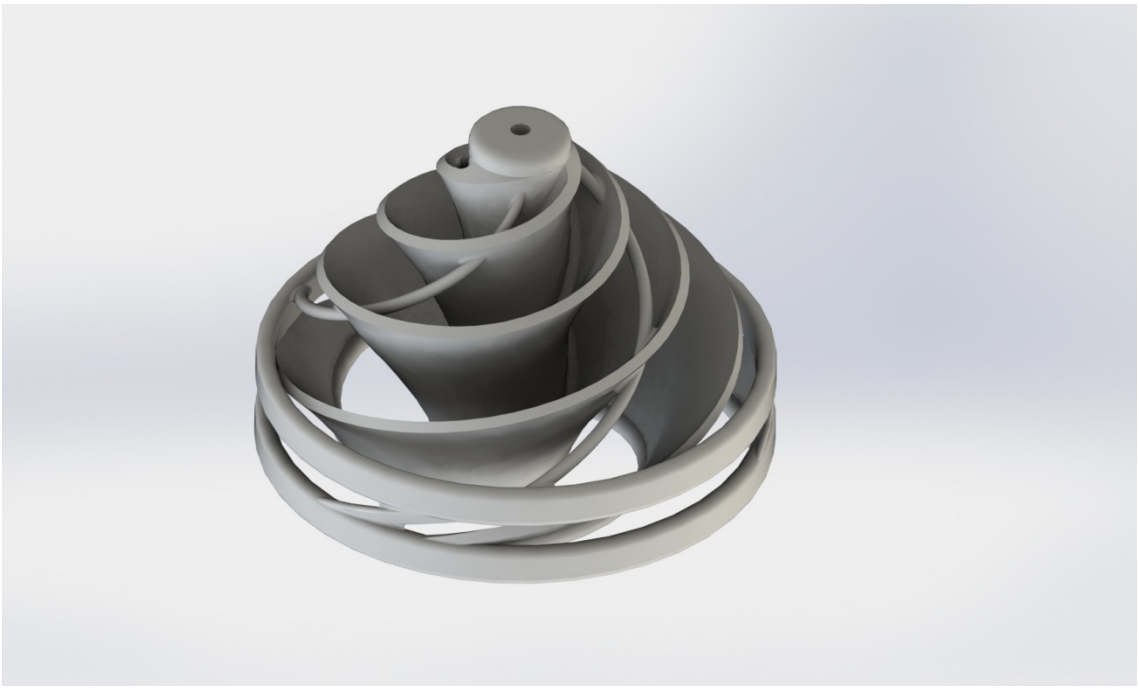

Figure 59 Second design

The difference between the first and second design are:

- Reinforcement of the junctions between faces
- 3 spiral rods crossing the blades penetrating them at angles between 45 to 90 degrees to the tangent of the blade surface being higher when smaller swept area
- Lateral outside cylinders that hold the structural integrity of the screw
- 3 extra blades between both cylinders that keep the spacing between cylinders

2.4 Test plan

On the testing it has being performed several tasks related to each of its subcomponents. As previously described the design had several characteristics that needed to be checked. In overall:

- Pitot's head
- Board
- System as standalone

A sketch scheme of what comes first is shown here.

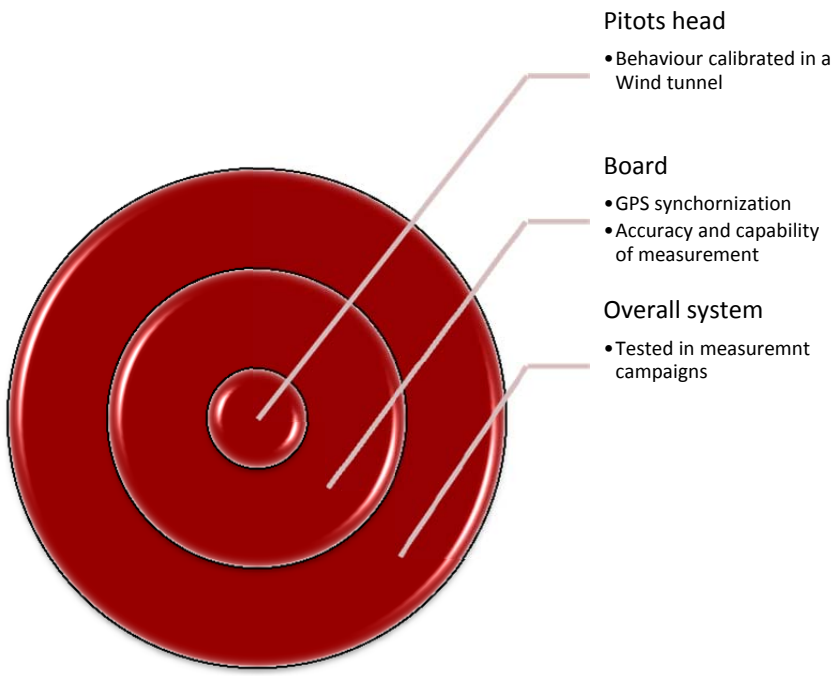

Figure 60 Test scheme

2.4.1 Wind tunnel

The functional description of the wind tunnel is made (including the design of the air flow treatment section), and main results of the flow quality for the setup is made. Flow quality, calibration functions and results are shown as well as the results important for the aerial sensor calibration, and difficulties. The calibration of the sensor is of outmost importance for the accurate determination of the speed-measured as the pressure difference between the port at head (P0), and static (P6). Since the relative speed at the blade is about 40-100 m/s for larger wind turbines, the impeller has to produce sufficient rate of volumetric air flow at a sufficient pressure. In a subsequent station downstream, without major pressure losses, the airflow has to be aligned and turbulence has to be remedied before the section with a contraction increases the flow to wind speeds up to 100 m/s.

Within this understanding, the design task has been to integrate the radial blower with a section that improves(straightens) the flow into laminar flow, and a section which increases the flow to 100 m/s and decrease turbulence intensity in the order of less than 0.1. Further requirement is that the maintenance effort (e.g. interior part dust removal) intended is easy.

Wind tunnel specifications

The list of requirements to be fulfilled in order to get the requirements for the nozzle

- The blower shall be capable to generate enough airflow in the output
- Shall be an economic solution

These conditions are met when Risø consulted the company NOVENCO which gave a solution with a motor and a coupled fan. The specifications can be found in **Error! Reference source not found.**. The radial fan has several components in order to achieve high laminar wind speeds:

- **Fan.** Impeller that on rotation generates a volume flow which goes from the inlet of the impeller to the outlet of the fan housing. In order to move the impeller a motor is needed.
- **Motor.** Drives the blades up to a maximum rotational speed of 4509 rpm generating the blowing airflow. The control of the rotational speed in the motor comes from the change of frequency
- **Frequency converter.** Used to change the frequency of the motor and hence the volume flow and air speed of the outlet.

The frequency converter needed an special adaptation phase to be built

- **Grid fuse**. In order to use the frequency converter a grid fuse has being adapted
- **Adapter**. Set of different pieces created to adequate that the outlet stream into a higher laminar and pressurized flow with a contraction area ratio of 2.4.

Lastly but not last, the fan must have a measurement system that can get the pressure measurements. In order to accomplish this task a ***P2858 Data Acquisition Unit*** connected with several pressure

transducers, temperature measurements have being provided and installed. A further description of the full equipment can be seen on 0, Wind tunnel measurement system section.

As shown in **Error! Reference source not found.** the motor is embedded in the fan and on the outlet of the fan there are several pieces. The next subsections the different components will be described

Fan:

CAL-400/70-DSR RD/90

Volume flow	1.57 m³/s
Fan total pressure	4600 Pa
Fan dynamic pressure	241 Pa
Fan static pressure	4359 Pa
Casing material	HDG
Shaft sealing	Double lip sealing
Impeller Material	HDG
Efficiency	81 %
Power	8.9 kW
Speed	4509 rpm
Max. speed	5696 rpm
Altitude of installation	0.0 m
Temperature	20.0 °C
Humidity	50.0 %RH
Inlet	Duct
Outlet	Duct
Total weight of installation	258 kg
Master product ID	mp-l01
Total Efficiency	71.9 %
Measurement category (A-D)	D
Efficiency category	Total
Optimum Efficiency grade	73.7 %
Target Efficiency grade (N)	58(2015)
Specific ratio	1.02

Motor:

WEG 2P ET-22-160M 11.0kW B3 400D/690YV 50Hz

Motor requires frequency converter

Vendor	WEG
Product code	ET-22-160M
Rated power	11.0 kW
Max Power	11.0 kW
Rated speed	2935 rpm
Current	16.5 A
Rated current	20.4 A
Supply voltage	3x400 V
Rated voltage	400D/690Y V
Frequency	50 Hz
Actual motor frequency	77 Hz
Enclosure	IP55
Efficiency class	IE2
Efficiency	91 %
Mounting arrangement	B3
Start-up	Direct starting
Windings type	1 speed (1 Winding)
Motor weight	104 kg
Power input	10.0 kW

Figure 61 Original specifications of the motor and fan.

Fan

The overall settings for the fan are described in the table where the model CAL-400/70-DSR RD/90, 5 is characterized. The impeller has backward curved blades. The maximum pressure that can be reached with this device is 8000 Pascals

Motor

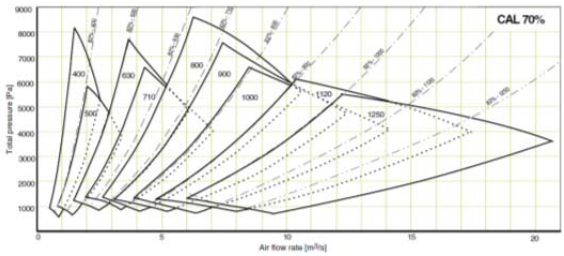

Figure 62. Flow characteristics

The motor is capable as specified in the description, to reach 85 Hz. Nevertheless, as a remark: whenever the frequency converter gets over 20 Hz the ear protective aids shall be used.

The flow and speed are represented on the horizontal axis. The values here annexed are for the motor without the adapter, i.e. max 3m^3/s

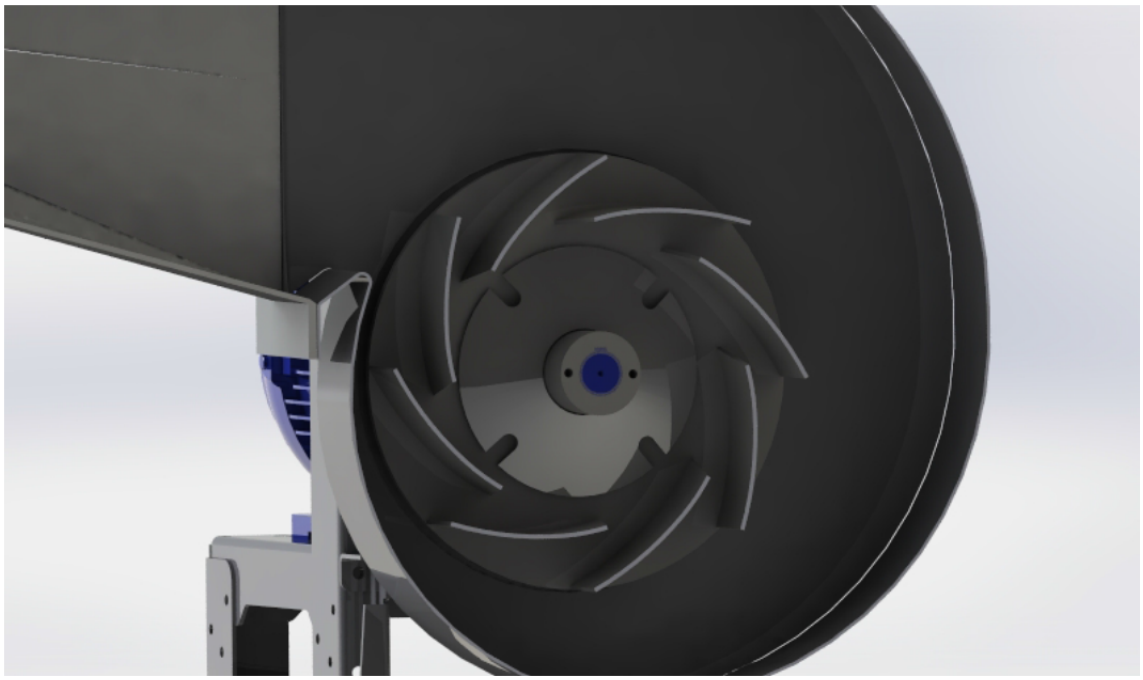

Figure 63 Backward curved blades of the Impeller. Section view

Frequency converter

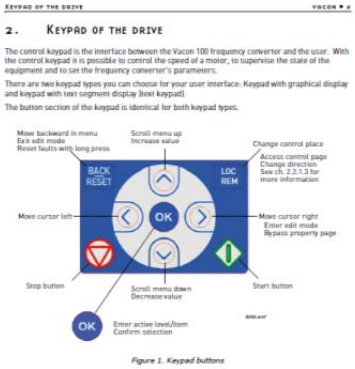

The frequency converter brand VACON 100 HVAC is capable of reaching frequencies up to 320Hz. In this case it is not recommended to go more than 85Hz as because of the safety issues described before. In order to set up the converter it is needed to change the maximum frequency of the converter, do not confuse this with the motor rated frequency. Figure 64 shows the keypad control symbols.

Use the LOC bottom to go to the properties and allocated in the menu, on the manual section P3.3.2.The limit for the maximum frequency can be set.

Figure 64 keypad

Grid fuse

The motor of the fan is controlled by a frequency converter which operates with a tri-phasic voltage of 400V with a maximum of 24 Amperes. This kind of frequency converter uses high chopping frequencies that cause unbalance which usually is derived through the earthing. The level of the current on the earthing is higher than the allowed in the installation. Therefore it was needed to readapt the circuit breaker in order to allow that this high leak current could let operate the motor without triggering.

Figure 65 Switch

The circuit breaker type B at 32 A with tripped 300 mA was used for this purposes

Adapter

The adapter has being the more complex part to be built. Indeed the first step is to create more requirements on this component

- non expensive solution
- easy to clean, reuse and readapt
- it should contain a nozzle and a meshing phase
- good tolerances

In the following table a list of requisites are made

Figure 66 Scheme of the requirements that the components of the wind tunnel has to fulfil

In order to first check the compliance of the flow and make it circular, the first step was to create an adapter made of aluminum which will be here called the transition piece

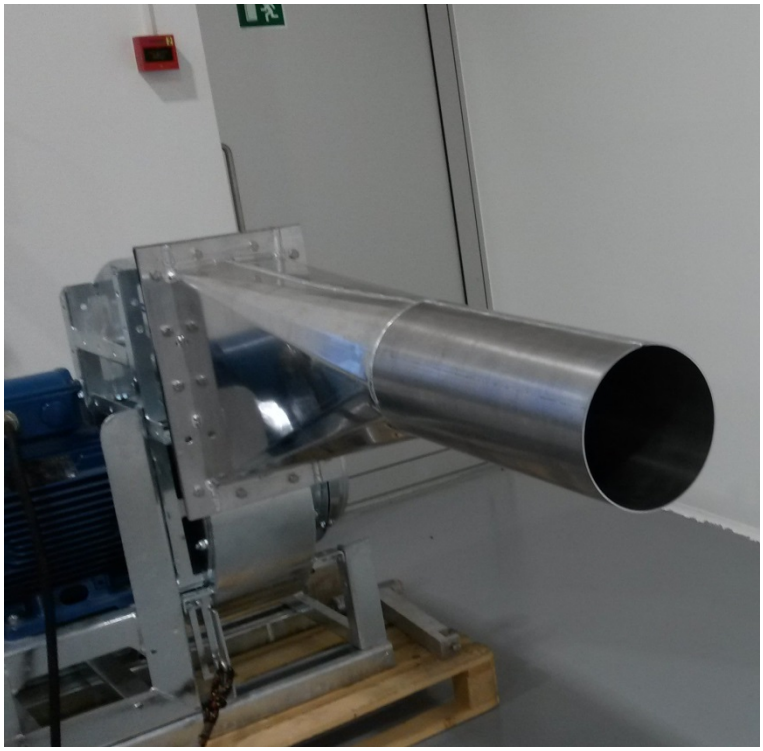

Figure 67 Adaptation piece

Wind tunnel adaptation piece tests

The aim of this section is to describe the calibration of the aerial sensor and the fan itself. The calibration trials have being realized in different steps. Each step is related with the objective of learning and building the fan under optimal circumstances.

- **Assessment of the wind profile on the fan per se.** Calibration with the laser.

- *Calibration with the Aluminum transition piece.* Main objective is to determine the distribution of the speeds along the Aluminum piece.

- *Calibration without the Aluminum transition piece.* The goal was to assess the gain with, and without this piece, to check the turbulence, asses a background noise found in the laser measurements and get the wind speed distribution.

- **Assessment of the construction.** Calibration with the hot wire.

- *Calibration with the complete adapter and straws*. On the first calibration trial the set-up was intended to check the functionality and ratio on the frequency and speeds.

- *Calibration with the complete adapter without straws.* That trial pretend to estimate the influence of the pressure loss on the speeds.

- *Calibration with the complete adapter,* with straws and applied silicon on the rubber. This was the final setup where the leakage of two sections were corrected and the fan was set up to 50Hz.

Assessment of the wind profile on the fan

Prior to build any adapter the first objective is to know if with the already built setup was sufficient to get the speeds. For that reason it was decided to check the speeds of the fan with a laser (Lidic, see Figure 68)

The laser provides the ability to measure on several positions of the fan adjusting the focal point. This capability has being used to get the distribution of speeds among the built Aluminum transition piece. As shown, the laser was placed on a truck in front of the fan.

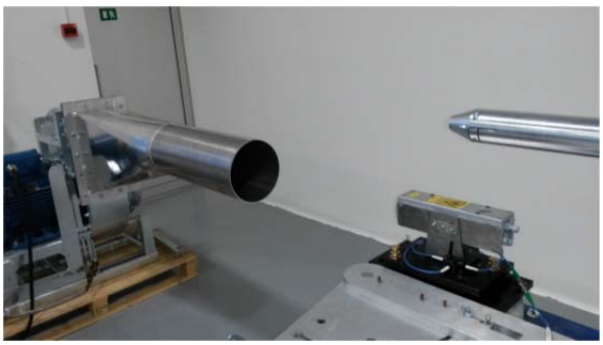

Figure 68 Laser in front of the fan

Calibration test performed with a laser scanner

On this section it will be shown the different tests realized with the laser. The methodology to place the laser in the desired position was to allocate a target in front of the laser and measure the location where it was placed. The vertical displacement was corrected with the truck itself, which has the possibility to heave and lower with the height with the use of two levelers.

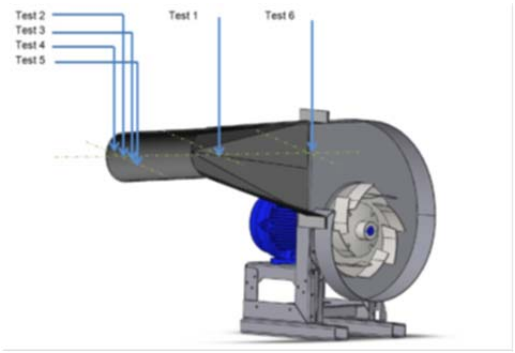

Figure 69 Tests positions with laser

Figure 70 Checking the centre

As being a photograph the laser cannot be seen on 3. As an important remark, this was a trial to check the capabilities of the fan, therefore it was not needed to check the alignment with better assessment

Test 1. 85 cm from the outlet

The first test was performed with the laser in front of the fan but having the focus at 110 cm from the laser at a mark on the adapter at 65 cm to the flange.

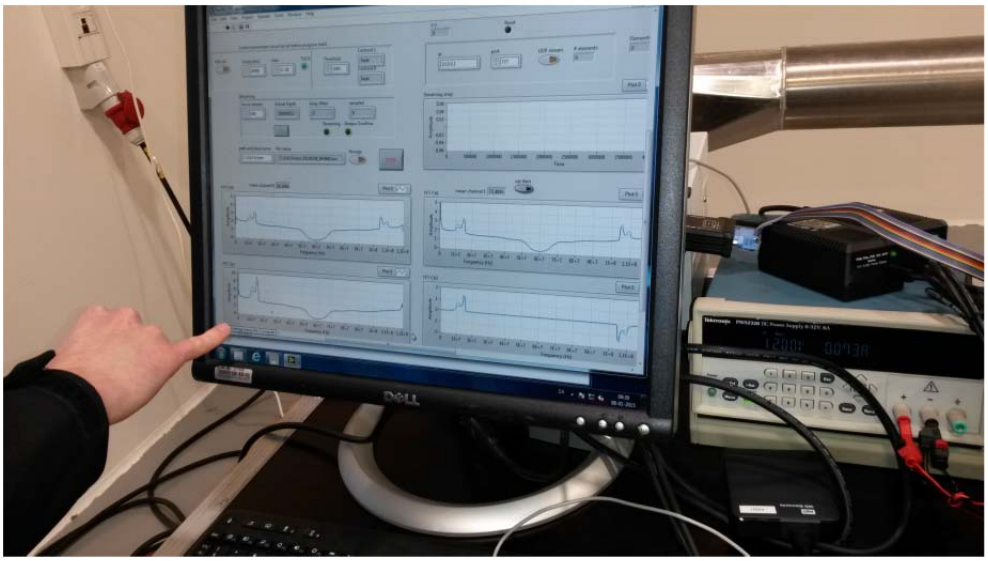

Figure 71 Laser results on the screen

The turbulence level is diminishing due to the fact that the mean increases, but the standard deviation of the measurement remained almost constant, from 2.7 to 2.2 m/s.

The resulting linear interpolation between frequency and wind speed gave as result

$$speed_{85cm} = 1.3309 * f_{motor} - 0.6103$$

Test 2. Center and adapters outlet

The importance to get the actual speed on the outlet is given by the fact in terms of design what kind of adapter was required. There was taken few measurements that will be compared against several sections and positions of the adapter

The resulting linear interpolation between frequency and wind speed gave as result

$$speed_{150cm} = 1.3357 * f_{motor} - 0.1071$$

Test 3 to 5. Profiles at the adapters outlet

The test 3 to 5 intended to check the wind profile at the outlet.

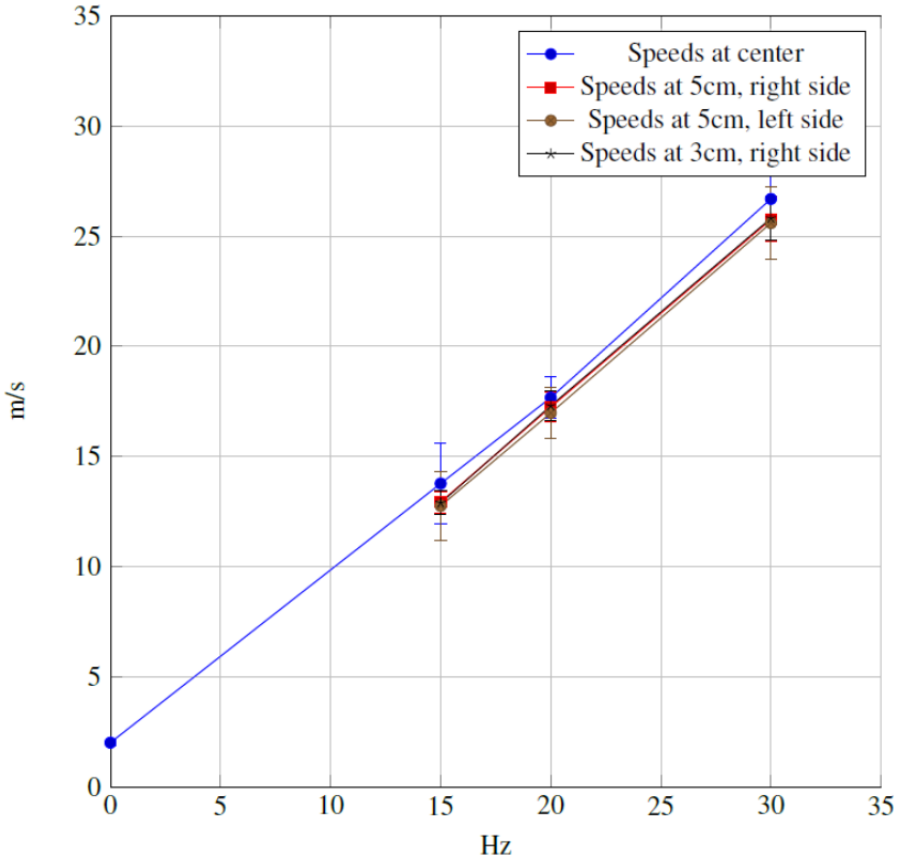

Figure 72 speeds at different positions measured with the laser versus frequency

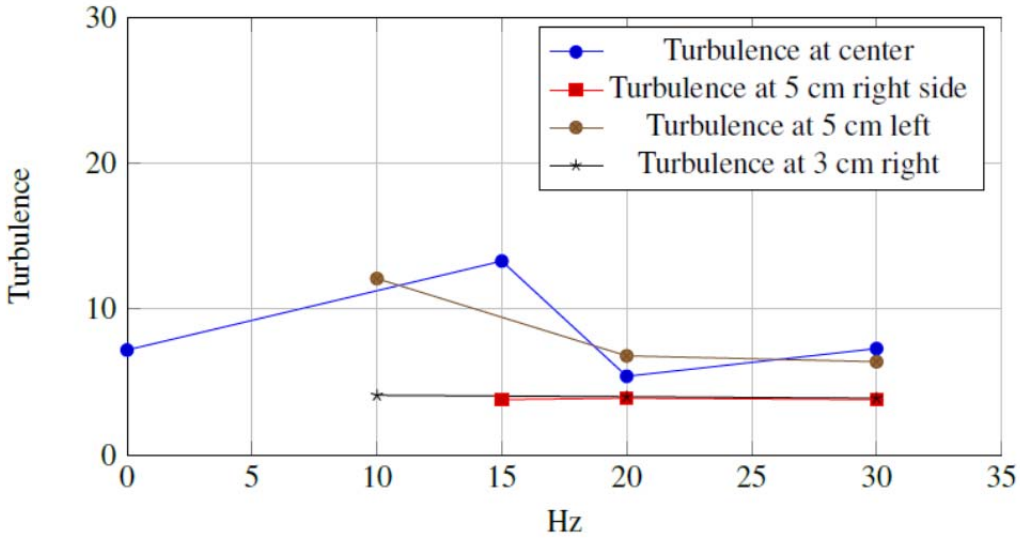

Figure 73 Standard deviation versus mean value, this could be interpreted as the"Turbulence" thought actually there are huge discussions on this particular term whenever is measured with lasers.

Calibration without the aluminium transition piece

As previously discussed the objective of this section was to get an idea of the reasoning behind the effects found on a peak in the laser results, plus assessing the measurement at 0 and comparing the turbulence effects with and without the adapter.

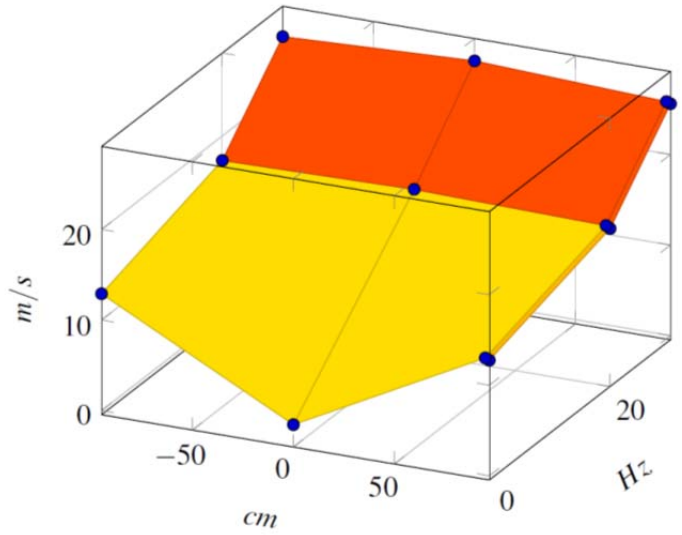

Figure 74 3d plot at different positions versus frequency of the fan

$$speed_{0cm} = 1.2303 * f_{motor} - 0.6047$$

Comparison of the results

As result of the calibration the gain in speed among the distance to the fan outlet has being represented. From 85 cm to 150 cm the gain is minimal thought the profile remain almost constant and the pressure losses and non linearities seems to be shown more for instance in the turbulence levels which increase substantially at higher frequencies when comparing 85 cm to 150 cm.

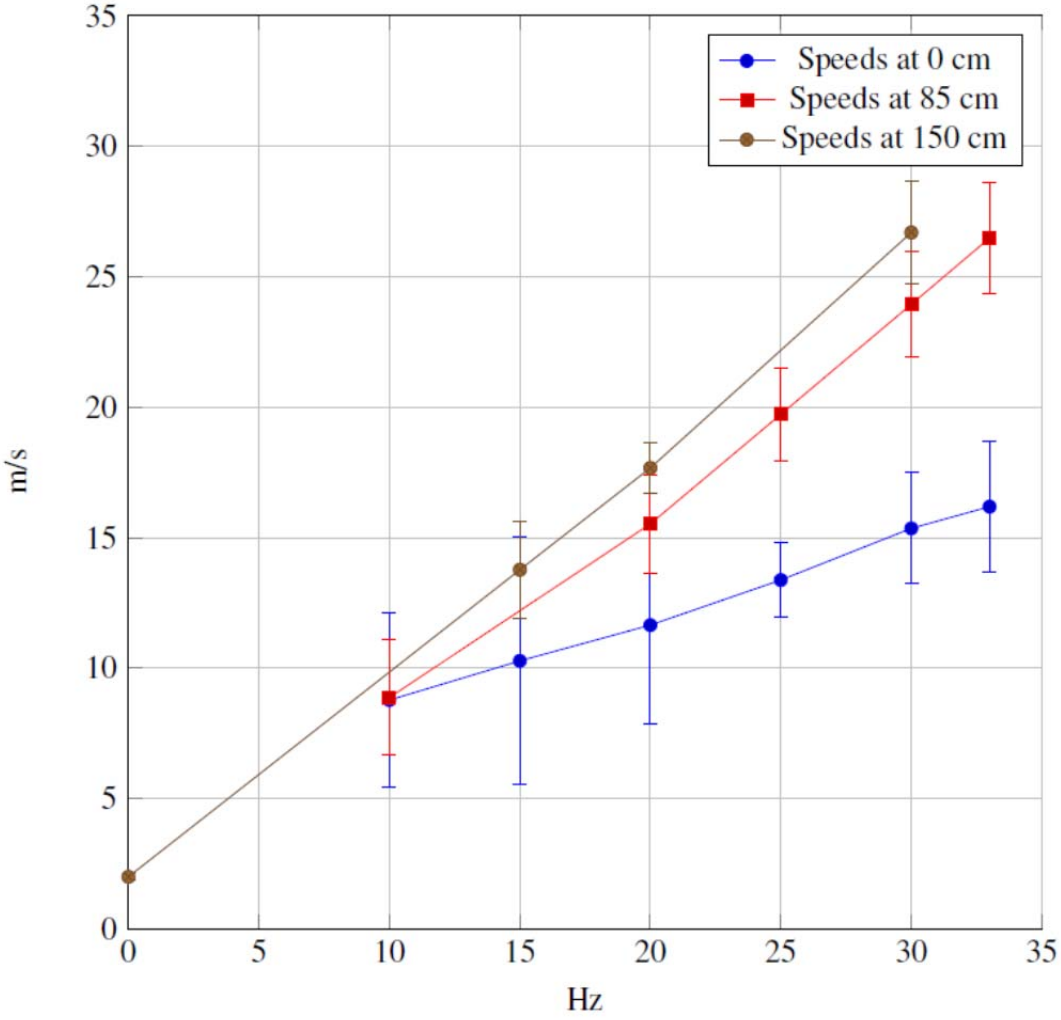

Figure 75 Wind speeds versus frequency at different positions

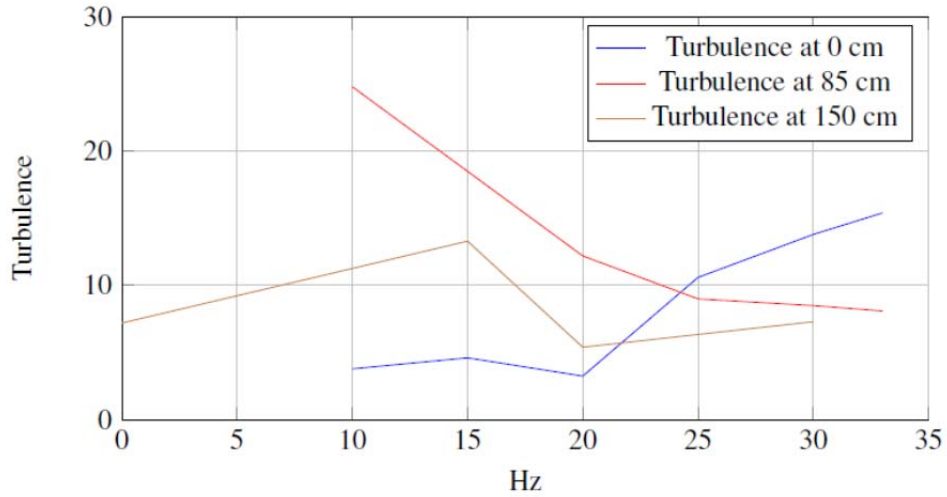

Figure 76 "Turbulence" versus frequency at different ranges and among different distances to the outlet

Assessment of the construction

The final construction and elements will be shown in detail in the section 0. and final construction can be seen in a 3d image on Figure 77. Nevertheless the construction has being a loop method where some assessments have being realized after testing the blower. For this reason in this chapter will be shown resulting tests

Figure 77 Rendered view of the fan, housing and motor with the in-house built adapter

The assessment of the construction ideally is a phase whereas it is tested the most

Checking the complete adapter with straws

There was performed a small check up with the straws inserted and the rubbers fixed without silicon. In this case the ratio between speeds and frequency was below 1.1. It was noticed a leakage before and after the straw phase. This forced to demount the complete setup and make two trials:

testing without straws checking:

- pressure leakage
- ratio of wind speeds versus frequencies
- consistency of the flow
- testing with silicon in case that the previous test was not satisfactory

Checking the complete adapter without straws

The complete adapter was demounted, it has being removed the straws and checked if something could obstruct the flow but nothing was found. Then all the setup was made again and the tests showed a

light improvement thought still was present a leakage of the pressure in the same section. The flow it seemed to have the same consistency as the previous. So after those trials it has being decided to apply silicon on:

- the rubber on the octogonal to circular transition piece
- one of the Aluminium grids

and increment the limit of the frequency of the motor up to where possible.

In order to check the improvement in the flow, it was taken the worst case scenario, i.e. the straws were introduced again in the PVC adapter. So with these conditions the blower was tested and it was found that the leakage was drastically reduced, and on these conditions the first calibration of the blower was performed.

Wind tunnel Nozzle components and final manufacturing

Below a list of the pieces for the nozzle is made, and shown in overview in Figure 78.

1. **Transition piece from fan outlet.** The function of the first adapter is to take the dimensions of the fan outlet into a circular shape.

2. **Polygonal to circular transition piece**. This part has two different functions:

Transform the octagonal shape of the previous adapter into a circular
allocate a mesh grid which will be used to mesh the air flow and/or straws (flow straightened)

3. **Ring with meshing grid frontal.** The function of this piece is to mesh the air flow in small streams and hold the straws if used

4. **Meshing tube adapter/Flow conditioner.** The function of this piece is to mesh the air flow in small streams. It can hold straws inside

5. **Meshing transition piece.** It will hold the meshing tube adapter, straws and the set of rings mesh for turbulence reduction

6. **Set of rings with meshing rings back.** The function of this grids is to hold 1 to 3 rings capable to create more meshes if needed

7. **Ring holder and adapter.** The function of this piece is to hold and align the rings and hold the next piece

8. **Tube.** The function of this piece is prepare the flow for equilibrium before entering

9. **Nozzle.** The function of this piece is to compress the air flow and laminarize it according to contraction ratio

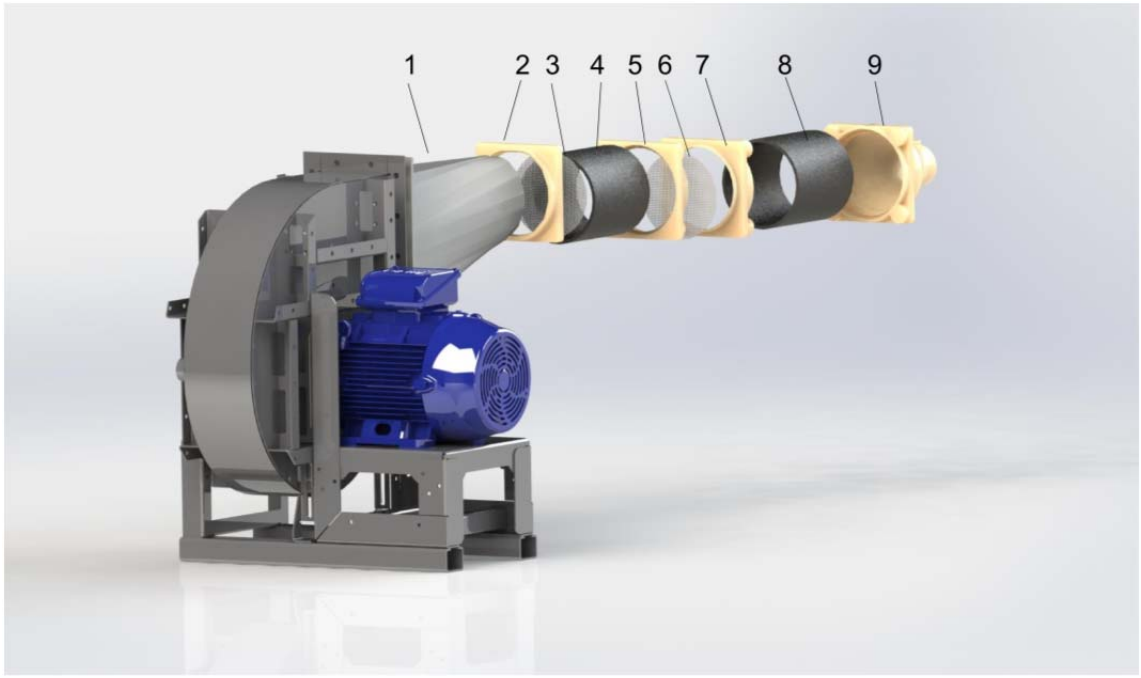

Figure 78 Section view of the adapter with the different components

Transition piece from fan outlet.

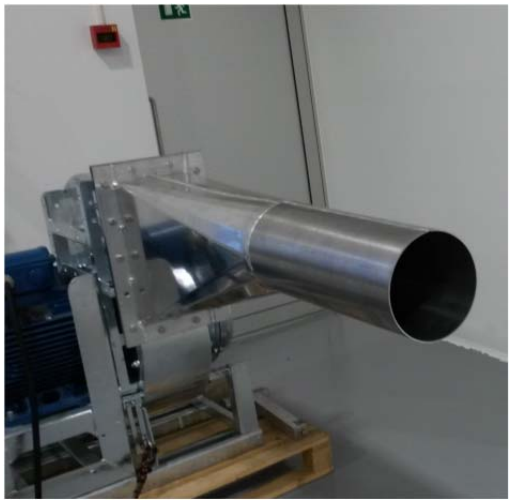

The transition piece from the fan to the outlet has the function as explained before, to adapt the flow to a circular shape.

Of the max min the outlet has a rectangular shape, whereas the smaller rectangular shape side measures 200mm, see Figure 79.

This was taken as the driving dimension to create the new adapter. On 2014 it was made an adapter on aluminum with diameter about 200mm.

After several tests it was decided to cut the piece at a distance of 85cm leaving the section of the piece in a polygonal shape from the rectangular shape.

Figure 79 Old transition piece

The reasons behind had considered several facts:

- As being manufactured from an Aluminum piece, the closing flange was perform with soldering, this could create big flow distortion
- As being a manual process, the shape was not circular but ellipsoidal. The difference was not more than 5 mm but was easily seen.

- The need to have flexible part with other sectional properties than just one.

Octagonal to circular transition piece.

The multi-faceted transition piece has being manufactured in a 3D printer with thermoplastic material. This piece adapts the air flow from the outlet of the fan to a circular flow.

In the designed piece it was allocated a holder capable of fitting the cut transition piece.

Nevertheless, as it was fit an Aluminum ring in front of the transition piece, this adapt had to be cut. On the rear back side of this plastic piece can be found a place to allocate an Aluminum ring and a big holder for the meshing tube adapter. The ring is sealed with a rubber ring.

Prior to install the multi-faceted transition, it is allocated a 2mm rubber which seals the flow.

The rubber is glued with silicon.

Figure 80 Photograph of the polygonal to circular

The interior of the parts is designed to allow that the flow adapts to 207.8 mm in diameter along the tube

Ring with meshing grid frontal.

The meshing ring is used to hold the straws and helps meshing the air stream. The tightness of this meshing ring with the other pieces comes from the pressure exerted by the other materials and the rubber. The ring has being made by Aluminum and the filter meshed by a light metal (unknown). In order to keep the planarity of the meshing grid, this has being welded to the Aluminum ring on the external diameter

Meshing tube adapter.

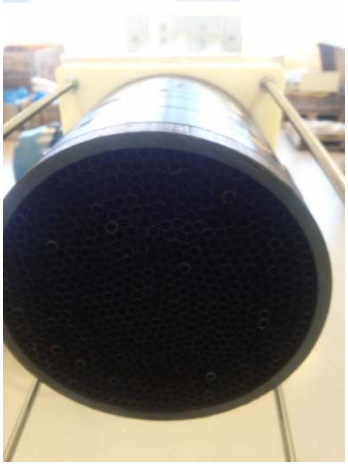

The tube part can hold multiple straws in the inside. The straws help aligning the flow upstream.

The length of this section is 250mm and the number of straws inside of this tube is less than 800.

The method used to hold the straws was done in several steps:

1. allocate the straws in a line on the bottom of a box, letting the gravity align them
2. allocate a weight on the bottom of the straws helping to block any movement

Figure 81 Photograph of the meshing tube adapter

3. holding the perpendicularity making that the straws covered the full length of the box
4. fix tape over the bundle periphery at the middle of the straw section
5. grab the layer of straws
6. roll the layer of straws making a spiral
7. repeat the previous operation adding more layers of straws

It is experienced that this in the end allows for a good perpendicularity and assure a proper setup of straws at a cost of large axial displacement.

Meshing transition piece.

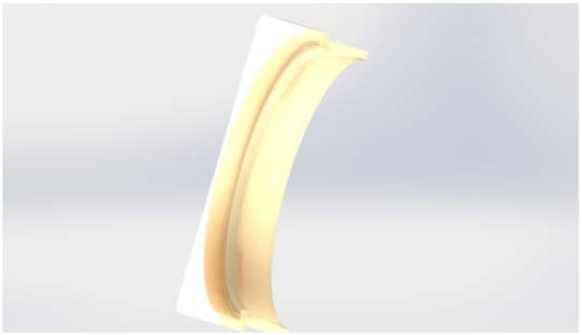

The meshing transition piece is capable to hold the rear and front pieces, allowing that one of the walls of the ring holder adapter slides against this piece, allowing the tightness of the Montage with the set of rings

Figure 82 Photograph of the meshing tube

Set of rings with meshing grid

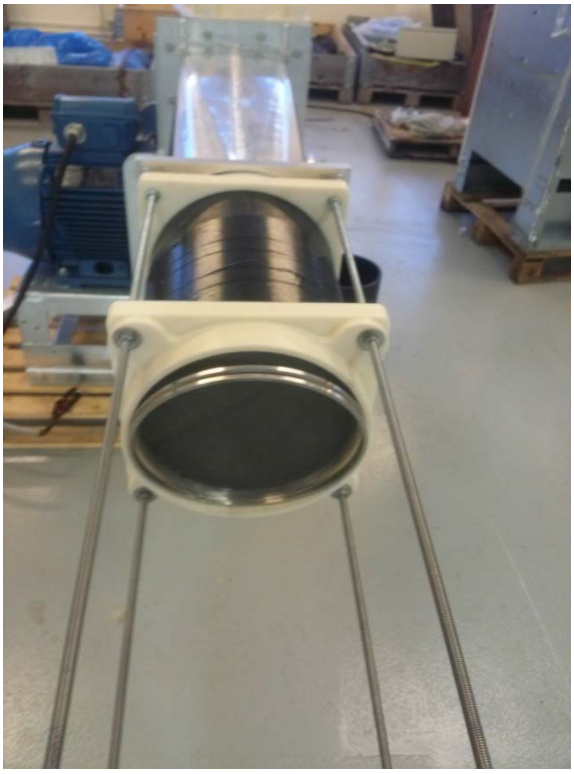

It has being produced a set of 3 rings, where one of them has a bigger dimension that the rest. This ring though can be demounted it is not recommended.

The other set of two rings are made with Aluminium and up to day they do not have a mesh. A rubber with silicon has being glued to the ring in order to prevent pressure losses

Figure 83 Photograph of the set of meshing rings

Ring holder and adapter.

The ring holder and adapter forms the opposite direction of the part subjected to the flow with the meshing rings. The devices blocks and holds the straws in a correct position. In the other side holds the tube that will connect afterwards the nozzle

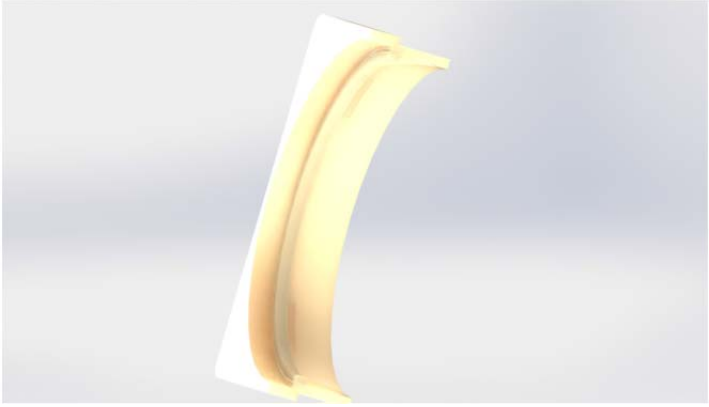

Figure 84 Section of the ring holder

Tube.

The tube is made of PVC, with an external diameter of 225 mm and a thickness of 8.7 mm. The length can freely be chosen, but for the first prototype it was decided to be 250 mm long

Nozzle.

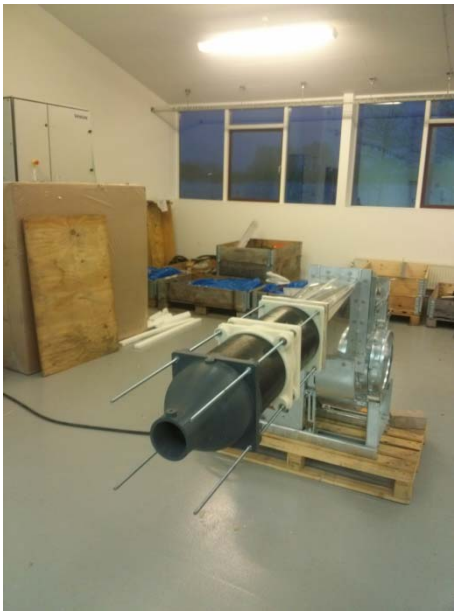

Figure 85 Photograph of the final montage

The nozzle was manufactured in plastics with a different color. The properties are the same. The rear part contains a small groove designed to hold a rubber of 1.5 to 2.5 mm in diameter. The rubber creates a tight connection with the PVC. Then the shape of the nozzle follows the equation described in 3.4.9 being x the distance along the axis in mm from 0 to 173. This equation has being modified to adapt the dimension of the PVC and get a ratio between diameters of 2.4 times. On the upwind part of the nozzle are existing two holes that allows to get the pressures over the contraction

The polynomial fit of the contraction is shown below, with x as the variable distance with base at the cylinder section with the largest diameter, which indeed follows $f(\xi) = 1$ (Doolan, 2007)

$$103.8 - 60.55 \cdot \left(6 \cdot \left(\frac{x}{173}\right)^5 - 15 \cdot \left(\frac{x}{173}\right)^4 + 10 \cdot \left(\frac{x}{173}\right)^3\right)$$

The final contraction piece with outlets for the measurement of the contraction pressure difference, is shown in **Error! Reference source not found.**

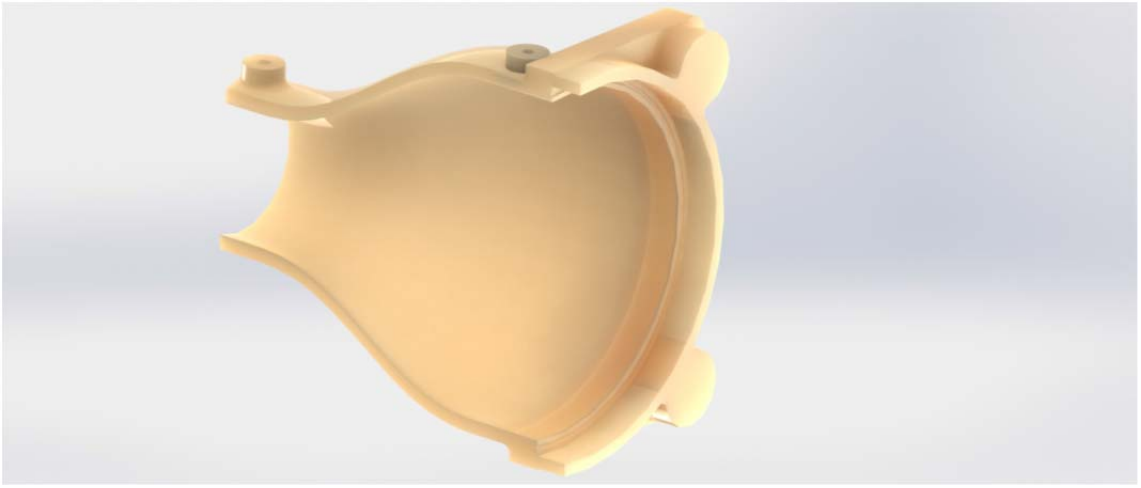

Figure 86 Section of the nozzle

Wind tunnel measurement system

The measurement system is composed by different systems:

- Sensors:
    - 2 Pressure transducers: absolute PMP 4010
    - 1 Vaisala pressure transducer
    - 4 Pressure transducers: dynamic PMP 4110
    - 3 Temperature sensors with power supply and voltage output adapted to the DAU. P2426B
- Computer with DAQWIN software
- Power supply for the pressure transducers and voltage supply
- Data acquisition System P2858B with Voltage inputs

The calibration of the sensors and other specifications can be found in the annexes

The scheme is as shown in Figure 81

Wind tunnel positioning system

In front of the wind tunnel is allocated a moving chariot where the pitot is placed. This system has 3 degrees of freedom and this is mainly why a system of lasers has being placed in order to

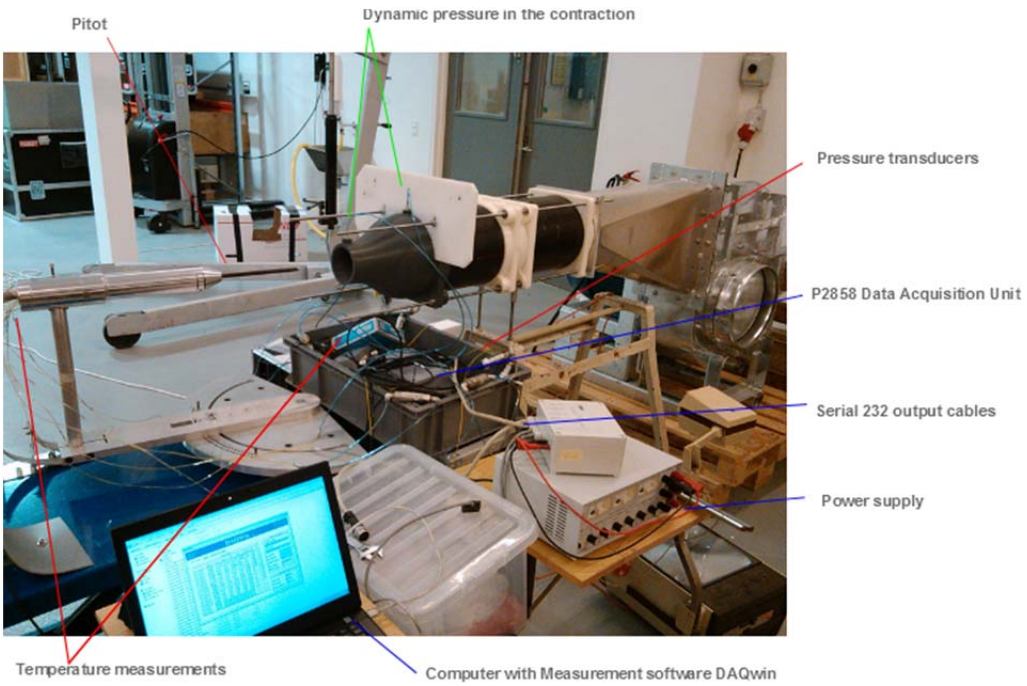

Figure 87 Measurement system of the blower

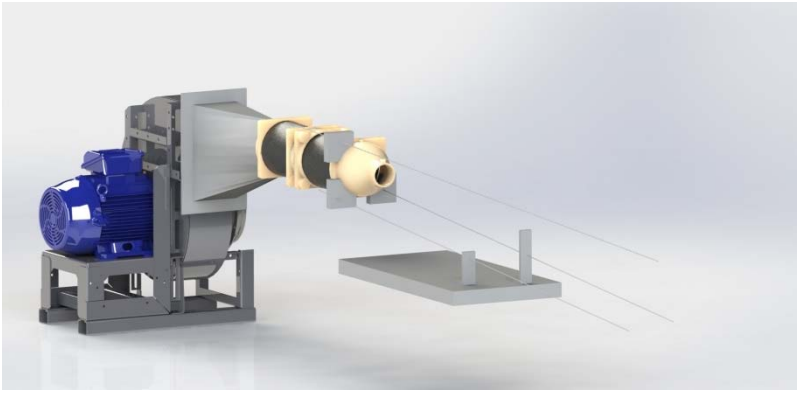

Wind speed calibration

The wind speed calibration of the 5-hole pitot is performed by carrying out a measurement of the dynamic pressure with the reference of the pressure obtained over the contraction. The sensor with sensor head is installed at the position in the symmetry line of the flow 1.5 D behind the nozzle exit.

The speed obtained at this point is assumed to be the same as measured with the Prandtl tube at the same position at the different contraction pressure differences, providing a linear function equivalent to

$$\zeta_{x,y,z,frequency} = \frac{q_{prandtl}}{q_{contraction}}(x, y, z, frequency) + \zeta_{offset}$$

Here it can be also extracted that $\zeta_{x,y,z,frequency}$ is a dimensionless term normalized that can be decomposed in two different terms

$$\zeta_{x,y,z,frequency} = \zeta_{x,y,z} * \zeta_{frequency} + \zeta_{offset}$$

Setups

Several setups have being performed among 2015. On this report it will be shown just 3 of the different setups. For traceability purposes the numbering shown will belong to the performed tests. In overall the next characteristics will be checked and assessed:

- Output Flow characteristics positioning and flux symmetries
- Stability of the flow
- Temperature distributions and recovery factor

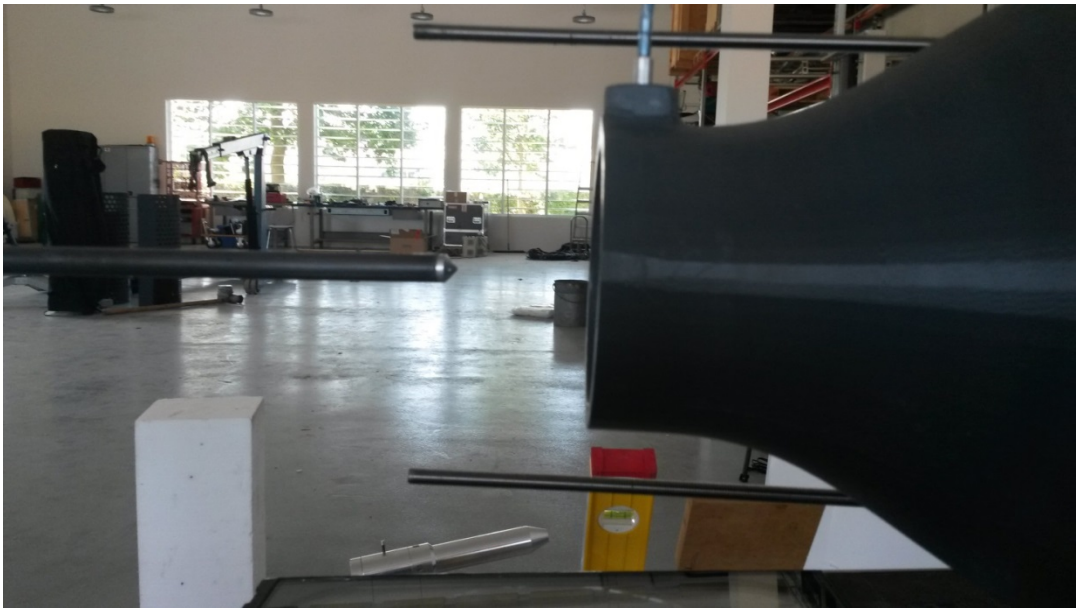

Figure 88 Pitot position when the second test started

The numbering of the

- **Second setup:** the pitot tube was put ahead removing the effects of the Prandtl. The stability of the flow has being checked.
    - 06-Aug-2015
- **Third setup:** Temperature sensors have being introduced and pretested
    - 18-Aug-2015
- **Fourth setup:** Prandtl measuring
    - 20-Aug-2015
    - 19-Sept-2015

For not extending much the report there will be only shown the relevant setups (2nd and 4th).

Second Setup: Test on 6-August-2015. 3.5 cm of the flow at different speeds

Description of the test

The main goal of the test is to check the stability of the flow when the pitot is in front of the blower. This entails to allocate the pitot tube in front of the blower and hold it until the variation in the pressure keeps stable, i.e., it does not move within an empirical determined limits.

Figure 90. Pitot and prandtl not aligned

The pitot tube was settled in front of the blower at a distance of 4.5 cm, which is equivalent to approximately ~0.5 Diameters of the blower. To hold the pitot a bedplate and some extenders were used. The bedplate had marks in inches and cm. As an internal reference longitudinally inches were used to place the system.

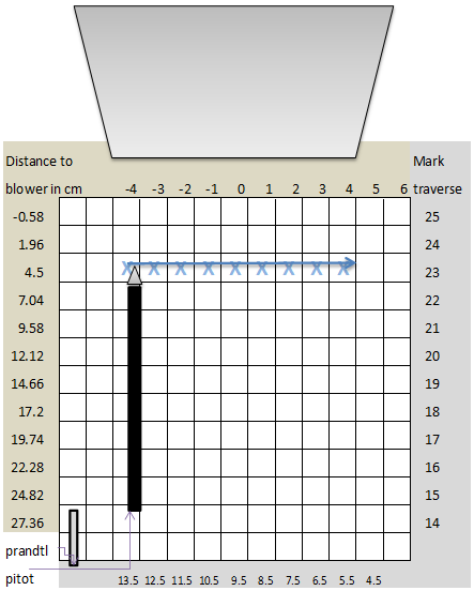

Figure 89. Pitot Static positions carried during the test viewed from the vertical plane

The test was realized along different positions moving the bedplate along the traverse axis each cm. In each position the system was left for some minutes.

The calibration values applied in this setup had a multiplying factor used to check the stability of the measurements during the monitoring of the test.

Table 2 Calibration factors for the setup

channel	serial number	offset	factor	Units	Sensitivity
1	2377	-1999260	10^4	MBar	305.0630849
2	2379	-1999260	10^4	MBar	305.0630849
3	2392	-479.82	10^0	MBar	0.01220704
4	2390	-480.29	10^0	MBar	0.01220704
5	2387	-17346.5	10^{-2}	MBar	0.525970836
6	2388	-17347.5	10^{-2}	MBar	0.525970836

Logbook

The test lasted for 1 hour

Table 3.-Logbook for the test

hour	mBar	lateral distance[cm]	distance longitudinal [inches]
15:30	0	Stopped	
15:40	39.45	center, i.e. 9.5	4.5 to the center
15:50	39.38	1cm to the right, i.e 8.5	4.5 to the center
15:55	39.3	2 cm to the right i.e 7.5	4.5 to the center
16:01	39.32	3 cm to the right 6.5	4.5 to the center
16:06	39.32	4 cm to the right 5.5	4.5 to the center
16:10	39.3	center, i.e. 9.5	4.5 to the center
16:11	39.3	left 10.5	4.5 to the center
16:14	39.34	left 11.5	4.5 to the center
16:17	39.3	left 12.5	4.5 to the center
16:20	39.31	left 13.5	4.5 to the center
16.23	39.3	left 14	4.5 to the center
16:33	0	Stopped	

Results: Speed and pressure stability

The stability in this case has being defined using the next formula, where x_j are bins of the desired quantity

$$Error_{x_i} = 100 * \frac{\frac{\sum_{j=1}^{i} x_j}{n}}{x_n}$$

This assumes that the last measured bin x_n is the real value. In terms of pressure the centre measurements they reach faster the stability region thus they do not depend on the temperature. The problematic that the temperature was not in the same pitot itself affects to the final speed measurements. Nevertheless as it is measured the dynamic pressure and the pitot due to the high winds, it does shake, the measurement of 1 pressure is not so stable as the static pressure (needs to be proven)

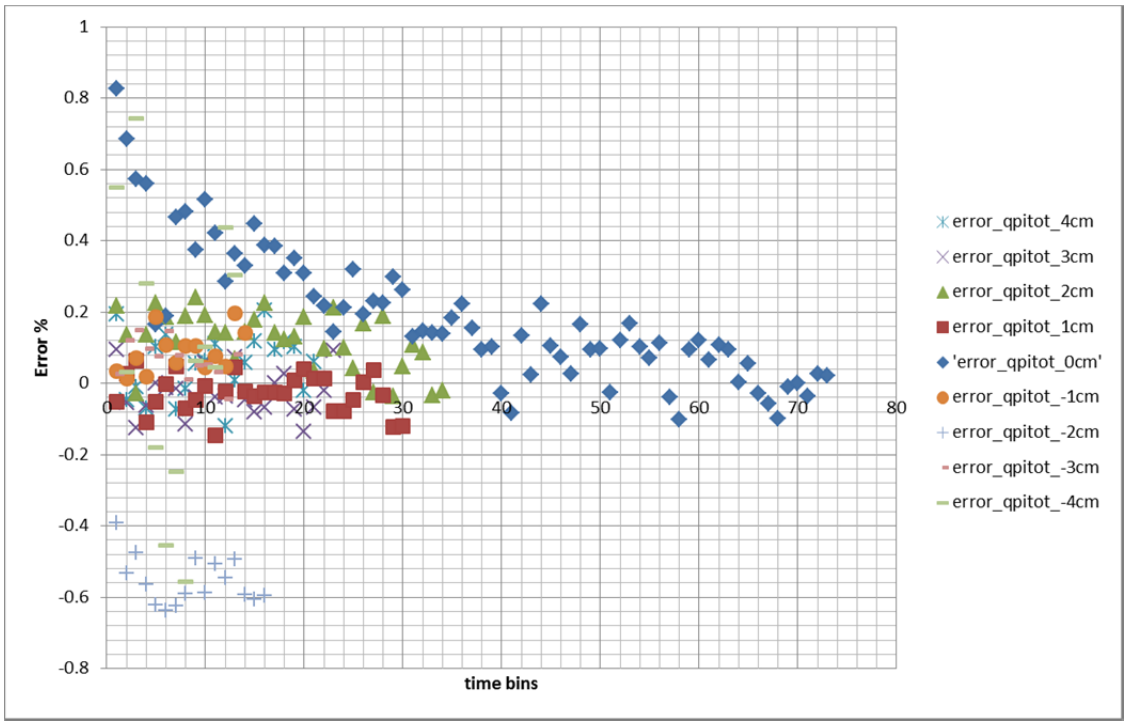

Figure 91 % Error in the measurements $Error_{qi}$

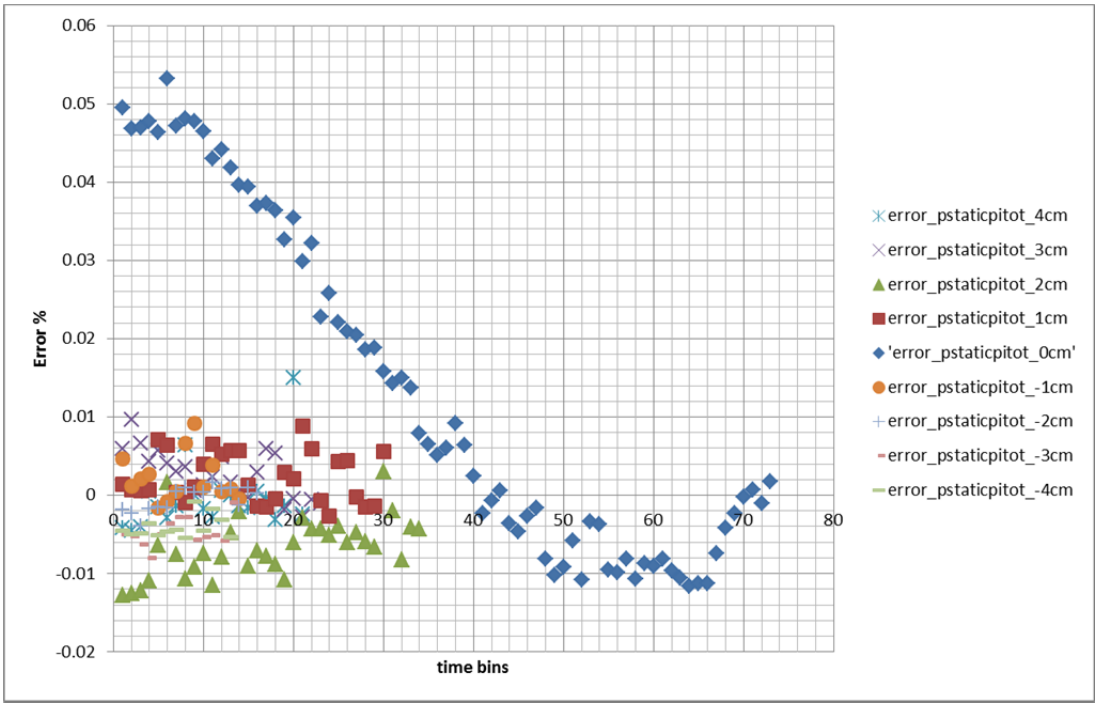

Figure 92 % Error in the measurements $Error_{psi}$

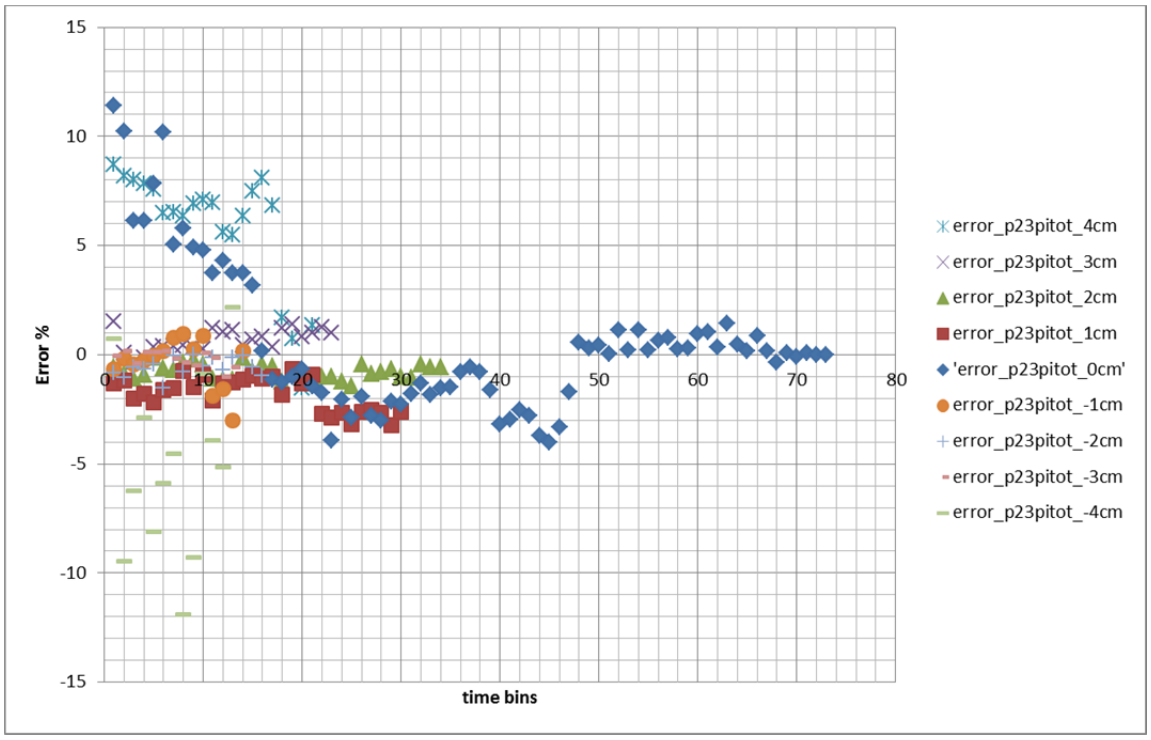

Figure 93 % Error in the measurements $Error_{p23i}$

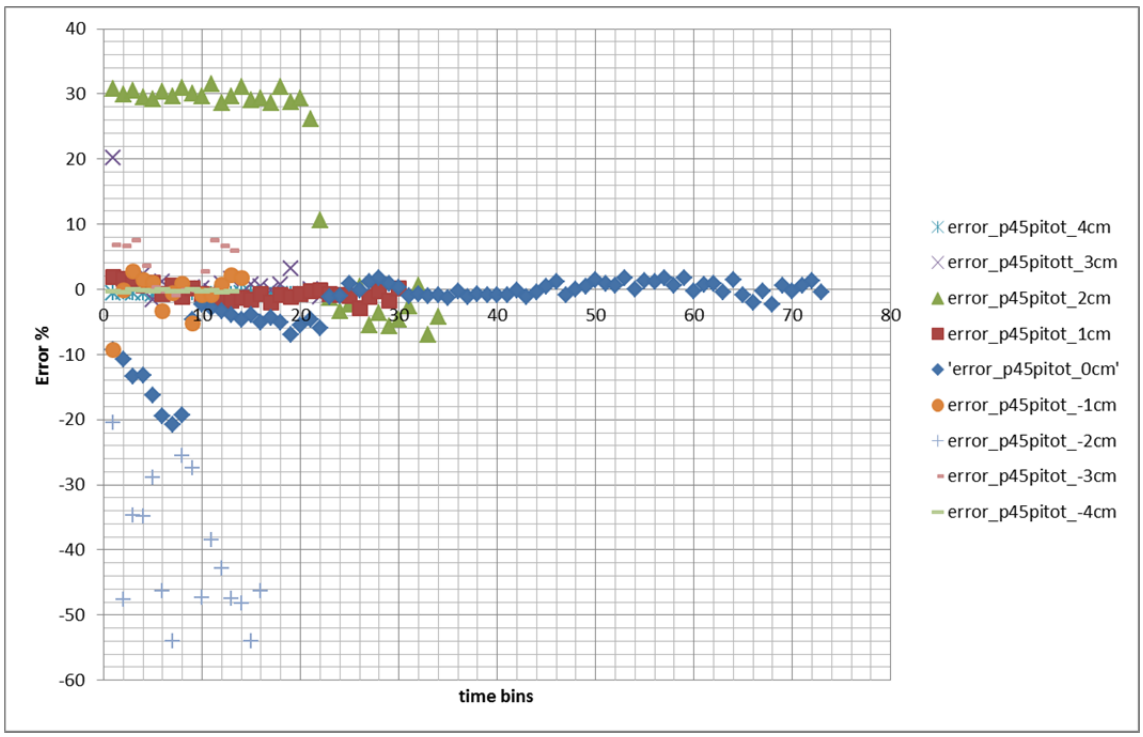

Figure 94% Error in the measurements $Error_{p45i}$

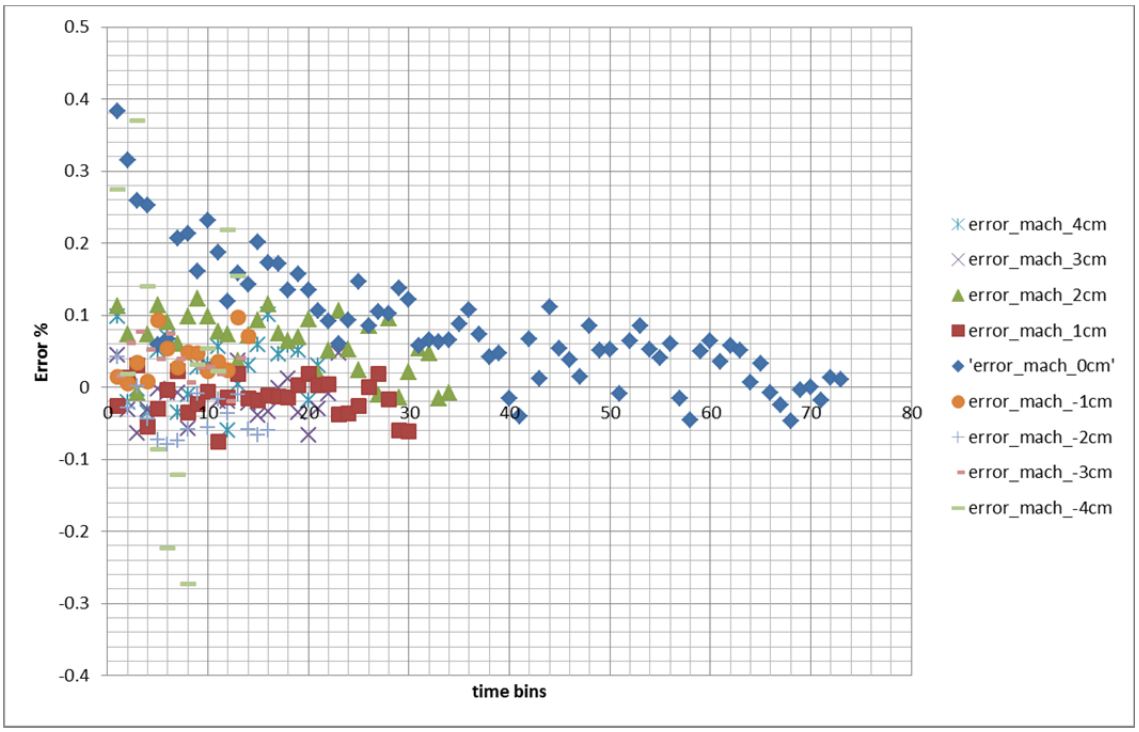

Figure 95 percentual error in the measurements $Error_{Machi}$

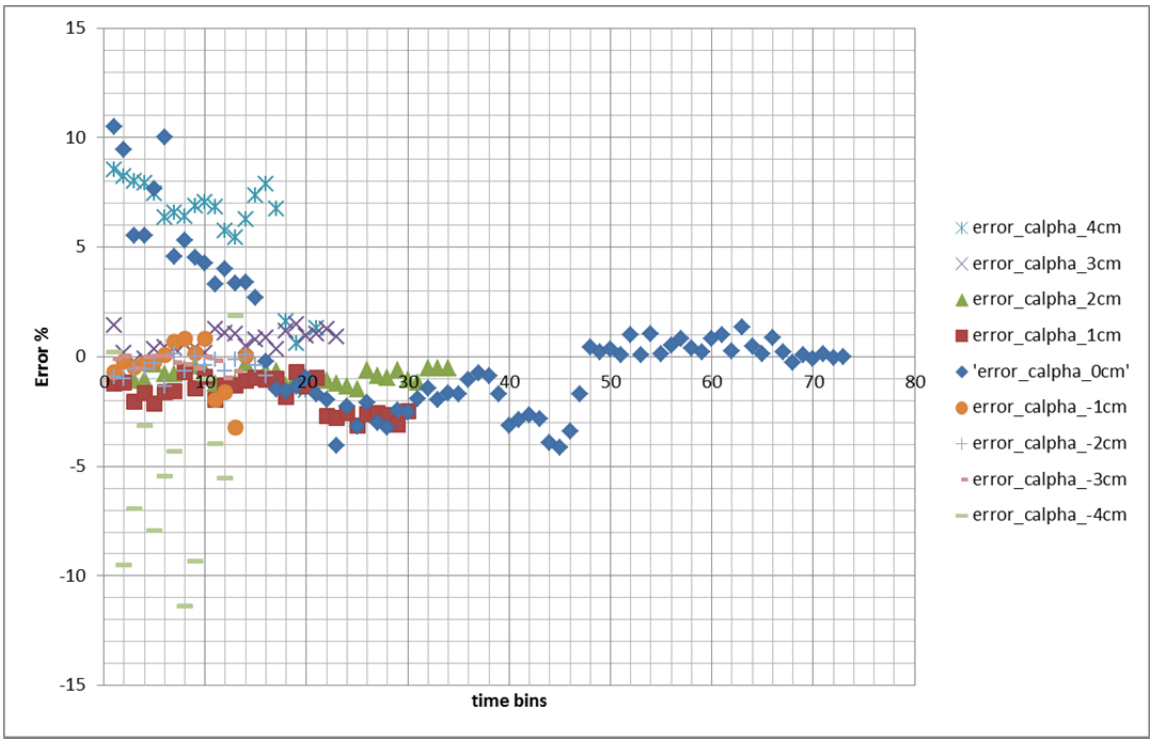

Figure 96 percentual error in the measurements $Error_{calphai}$

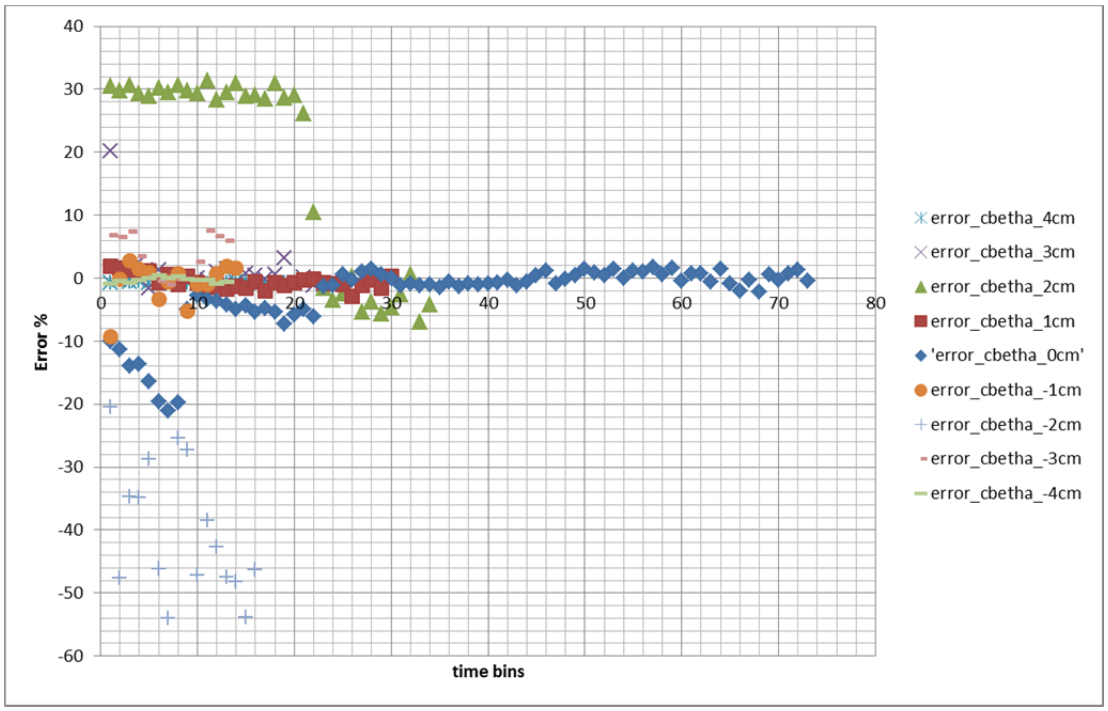

Figure 97 percentual error in the measurements $Error_{cbethai}$

Conclusions

For stable measurements it will be needed to get at least 2 minutes. The higher dispersion seems to appear at ±2cm of the centre. This can be due to the flow profile at that distance. Nevertheless the error is in any case small after that period of time. It is also obvious that the on the 0 measurement the time to stabilize the pressure in the blower did influenced the error. The pressure on p45 port has a deviation on the first minutes, this can be solely derived by an adjustment of the pitot, i.e. the pitot moved after some time caused by the effect of the thrust.

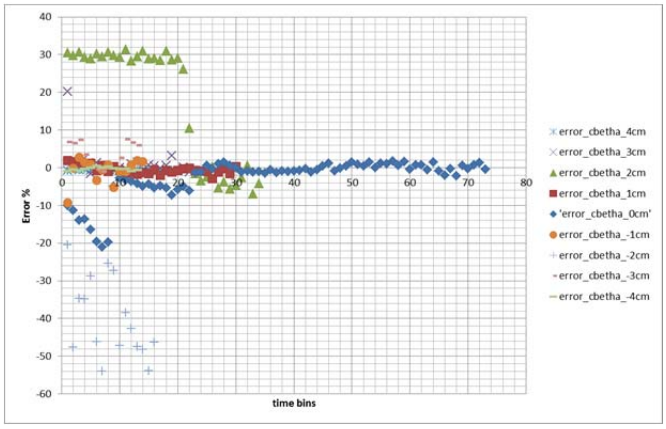

Figure 98.- Change of the level at 2cm and -2cm

Test on 20-August-2015. Prandtl measurement, different positions, measuring the flow

The pitot tube was removed from the flow. The position of the pitot was replaced with the Prandtl tube where behind a couple of temperature sensors were accordingly placed. A metallic pitot tube covered the temperature sensor at ~15cm from the Prandtl head. The front holes were partially covered in order to let the flow mixed in the internal chamber of the pitot tube and change the temperature of the chamber. Due to the heat exchange rate the system had a thermic inertia that will be seen afterwards.

Figure 99 Prandtl tube placing after the blower

Description of the test

The test realized has the aim to determine the factor $\zeta_{x,y,z}$ among different positions in the space. The averages taken are considered in bins of 10 seconds each and afterwards combined in the final binning.

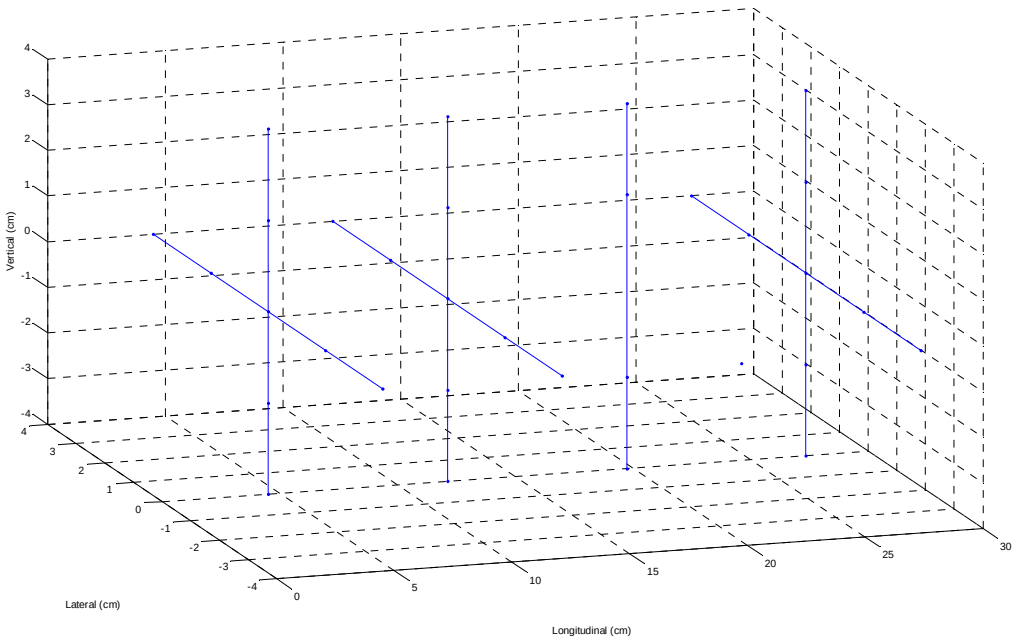

Figure 100 Points measured in space

To get the Mach number in the contraction side, the absolute pressure used came from the vaisala

Logbook

Table 4.- Logbook for the test

	Rpm		center at 10		equivalent to 4.5
Hour		Trasversal[cm]	Trasversal note	Lateral[cm]	Vertical[cm]
16:00	0	-4	14	4.5	0
16:26	70	-4	14	4.5	0
16:33	70	-2	12	4.5	0
16:41	70	0	10	4.5	0
16:46	70	2	8	4.5	0
16:51	70	4	6	4.5	0
16:56	70				0
16:58	70	-4	14	12.12	0
17:03	70	-2	12	12.12	0
17:08	70	0	10	12.12	0
17:13	70	2	8	12.12	0
17:19	70	4	6	12.12	0
17:24	70				0
17:25	70	-4	14	19.74	0
17:28	70				
17:29	70	-4	14	27.36	0
17:34	70	-2	12	27.36	0
17:39	70	0	10	27.36	0

17:43	70	2	8	27.36	0
17:50	70	4	6	27.36	0
17:55	70	0			2
17:57	70	0	10	27.36	2
18:02	70	0	10	27.36	4
18:07	70	0	10	27.36	-2
18:12	70	0	10	27.36	-4
	70				
18:18	70	0	10	19.74	-4
18:23	70	0	10	19.74	-2
18:28	70	0	10	19.74	2
18:33	70	0	10	19.74	4
				19.74	
18:40	70	0	10	12.12	4
18:43	70	0	10	12.12	2
18:46	70	0	10	12.12	-2
18:48	70	0	10	12.12	-4
				12.12	
18:51	70	0	10	4.5	-4
18:53	70	0	10	4.5	-2
18:55	70	0	10	4.5	2
18:57	70	0	10	4.5	4

On this particular day there has being a discordance in the atmospheric pressure. As safety redundancy sensor, there were a couple of sensors saving the same pressure. The Vaisala had a different pressure than the other sensors on the start-up within a difference of 0.39% taking as reference the absolute pressure from the Vaisala. So in order to get the total pressure the offset of the pressure transducers have being corrected.

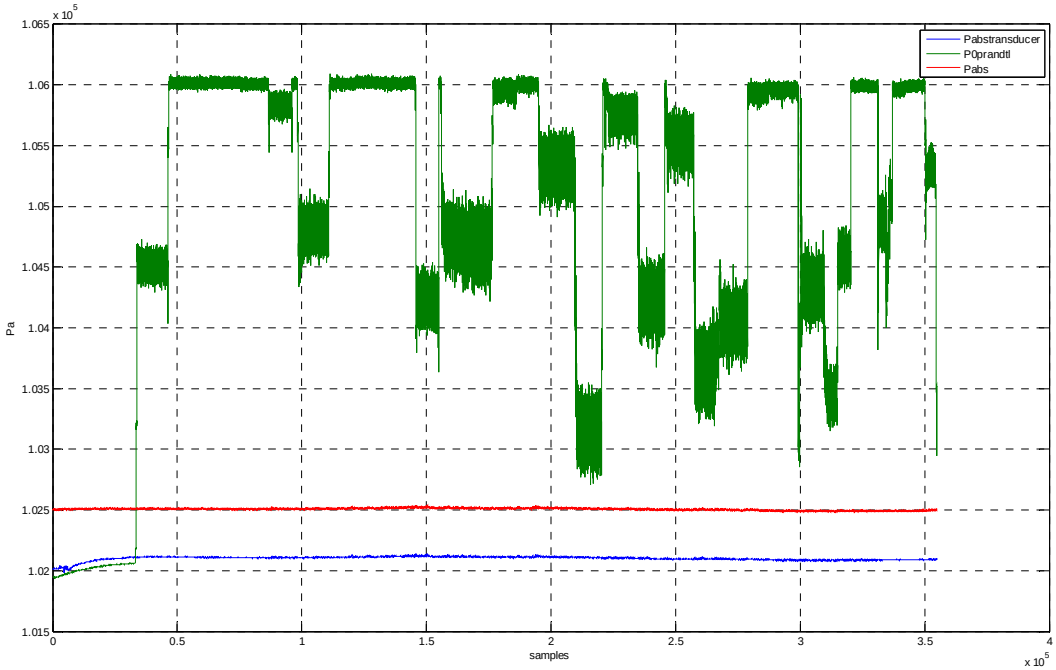

Figure 101 difference of absolute pressures of 0.39%

Correction of the offsets

Table 5.- Corrected offsets used in the test

	Signal	Value
$\overline{-q_{contraction}}]_{f=0}$	*mean dynamic pressure contraction*	0.000269 mBar
$\overline{-q_{prandtl}}]_{f=0}$	*Mean dynamic presure prandtl*	0.14912 mBar
$\overline{-P_{atm}+P_{0_{prandtl}}}]_{f=0}$	*Pressure absolute prandtl*	-4.93812 mBar

The sign in the original values of the contraction were negative but they have being converted to the positive side. Therefore it must be taking in account that the offset it has being also corrected, thus the maximum and the minimum found in the original values.

The mean value of the atmospheric pressure during the experiment was of 1025.10403 mBar

Results

On this section the results are obtained in different directions:

- Line among the flow: i.e. the correlation from the center of the blower to different positions when distancing $\zeta_{0,0,xD}$

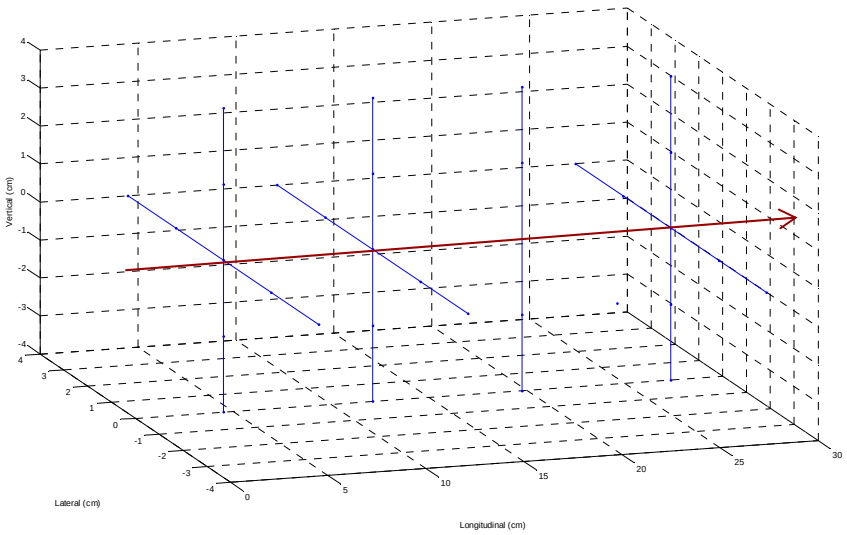

Figure 102 line among the flow

- Perpendicular plane: describes the perpendicular plane on several positions among the flow $\zeta_{x,y,z}$

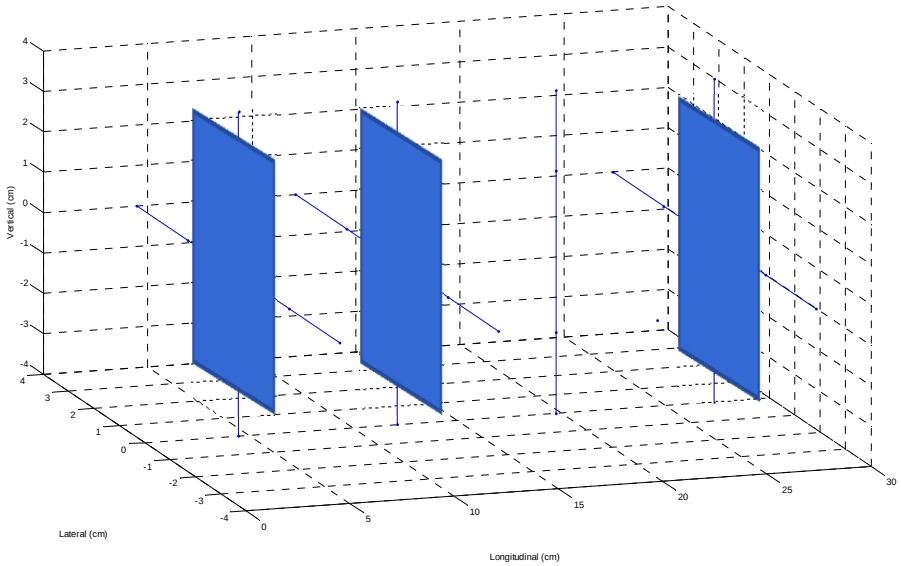

Figure 103 perpendicular plane

Line among the flow

The ratio $\zeta_{0,0,\mathrm{xD}}$ among the flow from distances 0.5 to 3.5D is shown in Figure 104

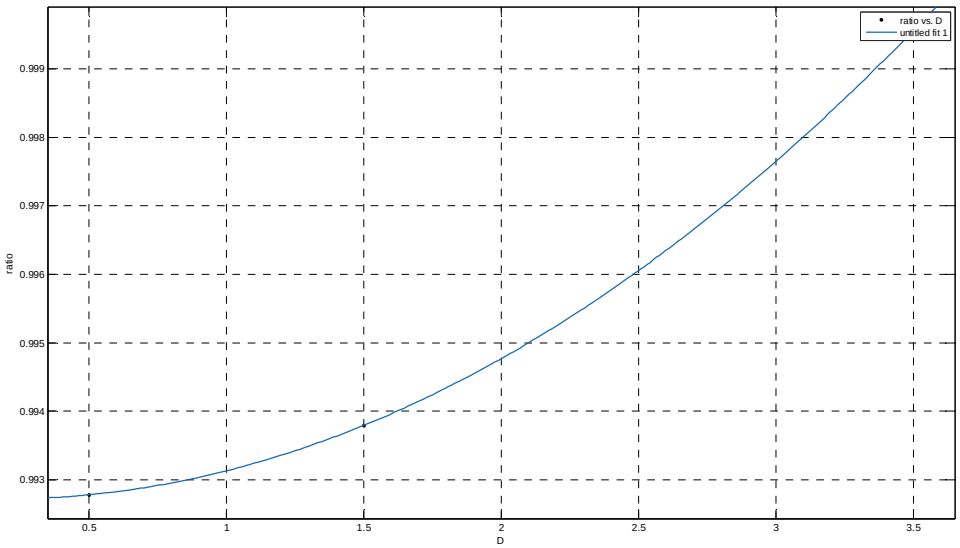

Figure 104 Manometric pressure ratios against the number of diameters of the nozzle

Which gave the next equation and correlation (being x the number of times the diameter):

$$\zeta_{0,0,xD} = 0.9927 - 0.0002327x + 0.0006238 \cdot x^2$$

$$R^2 = 1$$

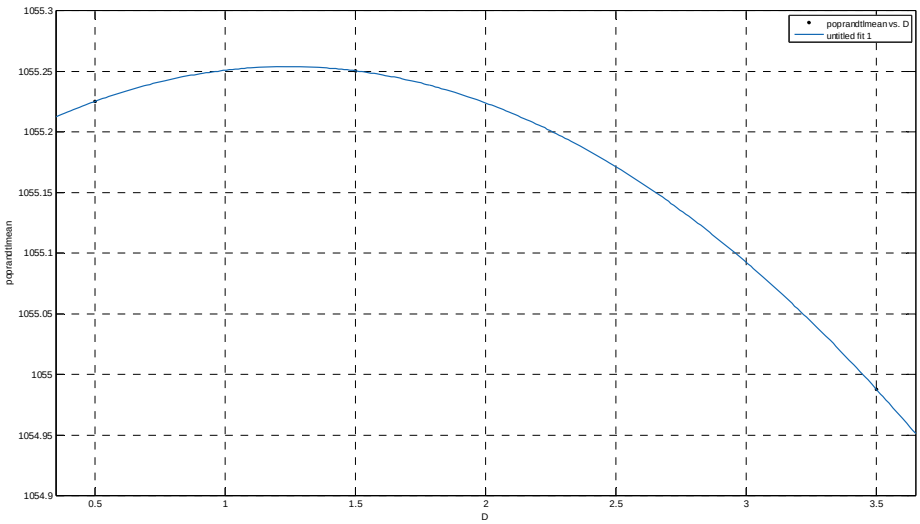

Figure 105 Absolute pressure in the Prandtl tube against the number of diameters of the nozzle

$$P_{0,0,xD} = 1055 + 0.1295 \cdot x - 0.1295 \cdot x^2$$

$$R^2 = 1$$

N	D	ζmean	qprandtlmean	qprandtlstd	qprandtlmax	qprandtlmin	qcontractionmean	qcontractionstd	qcontractionmax	qcontractionmin	poprandtlmean	poprandtlstd	poprandtlmax	poprandtlmin
13650	0.5	0.992776881	39.19740389	0.175214243	39.84853338	38.48134238	39.48259135	0.169283101	40.21427038	38.88370338	1055.225352	0.179600579	1055.751208	1054.728862
11550	1.5	0.993791785	39.15906807	0.175732891	39.88515438	38.51796338	39.40369468	0.166808053	40.06778538	38.73721988	1055.250543	0.168583197	1055.761944	1054.74415
8400	3.5	0.999564499	39.39327954	0.391783715	40.27577938	38.42567438	39.41044283	0.16783684	40.11661338	38.78604738	1054.987875	0.416402806	1055.671817	1054.037163

Figure 106 Table with the results of the measurements

Results at 0.5D perpendicular plane

On the next figures are represented the isovalues, or colored graph with the same value for the pressures and ratio. The distance to the blower was of 4.2 cm to the output

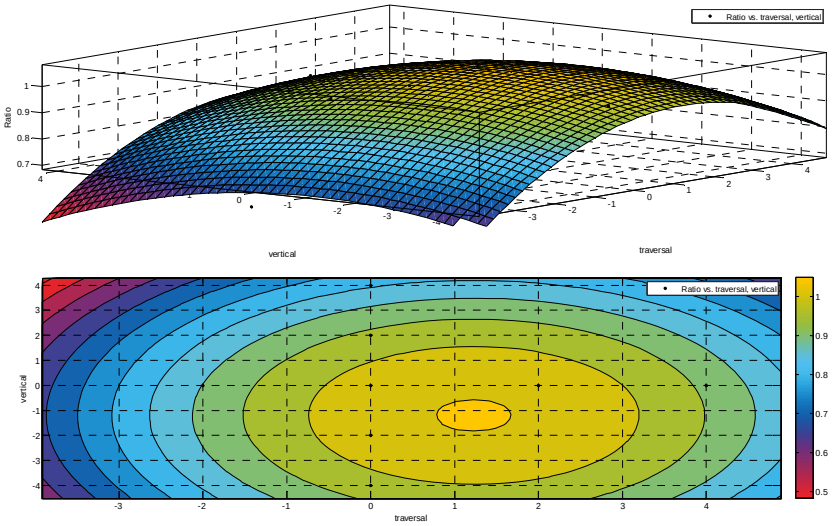

Figure 107 3D scheme of the ratio of the dynamic pressure in a perpendicular plane to the nozzle output at 0.5 diameters from the nozzle

Which gave the next equation and correlation:

$$\zeta_{x,y,0.5D} = 1.022 + 0.03336 \cdot x - 0.01358 \cdot x^2 - 0.01672 \cdot y - 0.006963 \cdot y^2$$

$$R^2 = 0.75$$

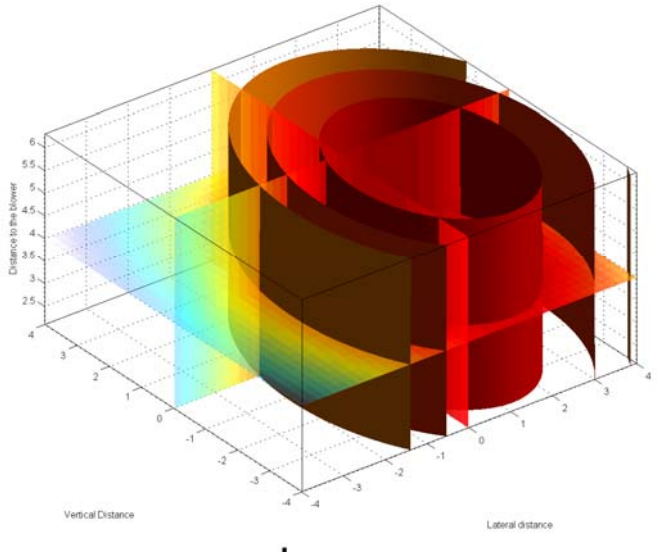

Figure 108 Flow with the isovalues for the ratio between dynamic pressures

Table 6.- Mean and standard deviation for the obtained values

N	traversal	vertical	ζmean	qprandtlmean	qprandtlstd	qprandtlmax	qprandtlmin	qcontractionmean	qcontractionstd	qcontractionmax	qcontractionmin
				mbar	mbar	mbar	mbar	mbar	mbar	mbar	mbar
12250	-4	0	0.632612	25.05509012	0.406899559	27.36072938	22.85633238	39.60580372	0.168924466	40.29971938	38.93253138
16100	-2	0	0.990992	39.15605051	0.184410289	40.17812338	37.79774838	39.51195488	0.171899999	40.27530538	38.83487538
13650	0	0	0.992777	39.19740389	0.175214243	39.84853338	38.48134238	39.48259135	0.169283101	40.21427038	38.88370338
9450	2	0	0.992235	39.1367913	0.179708843	39.79970538	38.46913538	39.44307249	0.16930603	40.05557838	38.76163338
9100	4	0	0.965611	38.07203768	0.403889573	39.44569738	35.33192838	39.42792538	0.169724563	40.20206338	38.66397738
2450	0	-2	0.991607	39.10592338	0.527714	39.89736138	36.02772938	39.43692638	0.159067	39.87247338	38.94473838
4550	0	-4	0.994841	39.20226538	0.383755713	40.14150238	35.57606838	39.40555838	0.173025751	40.07999238	38.79825438
3150	0	2	0.989206	38.96977071	0.176206587	39.67763538	38.23720138	39.39500382	0.168552324	40.06778538	38.73721938
3500	0	4	0.828871	32.65749978	0.773679504	35.03895938	24.45545338	39.39998418	0.171332505	39.99454338	38.77384038

Table 7.- Mean and standard deviation for the period

N	traversal	vertical	ζmean	poprandtlmea	poprandtlstd	poprandtlmax	poporandtlmin
				mbar	mbar	mbar	mbar
12250	-4	0	0.632611581	1040.132106	0.539766225	1041.711671	1038.578243
16100	-2	0	0.990992489	1055.179914	0.191479304	1055.740123	1054.647867
13650	0	0	0.992776881	1055.225352	0.179600579	1055.751208	1054.728862
9450	2	0	0.992234855	1055.096906	0.180408688	1055.629447	1054.598991
9100	4	0	0.965610981	1053.435924	0.401682909	1054.491426	1052.167103
2450	0	-2	0.991606775	1054.531824	0.558480772	1055.41248	1051.38568
4550	0	-4	0.994841007	1054.70396	0.214503298	1055.313941	1054.079588
3150	0	2	0.989205913	1054.997753	0.177741972	1055.510769	1054.470169
3500	0	4	0.828870886	1048.041894	0.662899857	1049.89697	1046.14773

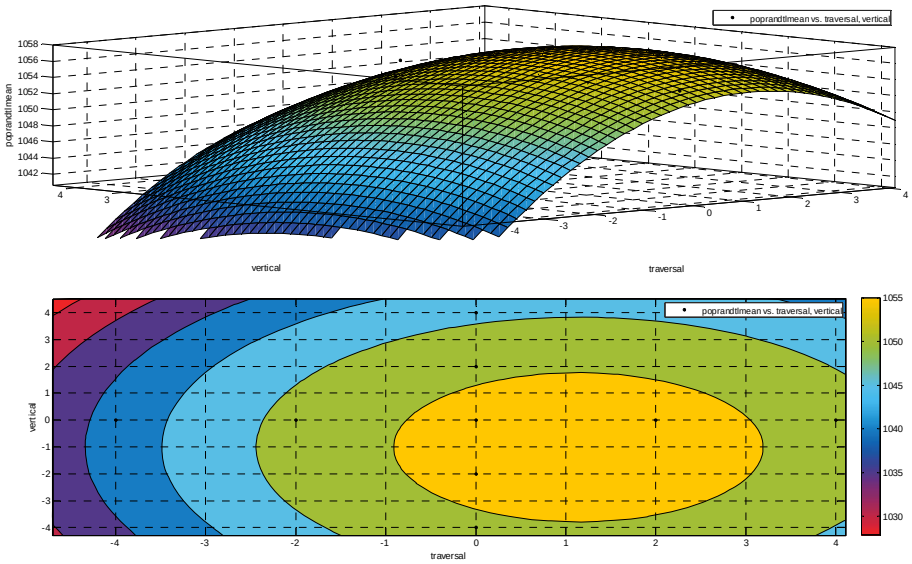

Figure 109 3D scheme of the absolute pressure in a perpendicular plane to the nozzle output at 0.5 diameters from the nozzle

Which gave the next equation and correlation:

$$P_{x,y,0.5D} = 1056 + 1.326 \cdot x - 0.5819 \cdot x^2 - 0.6429 \cdot y - 0.3175 \cdot y^2$$

$$R^2 = 0.73$$

Results at 1.5D perpendicular plane

The distance to the blower was of 12.6 cm to the output

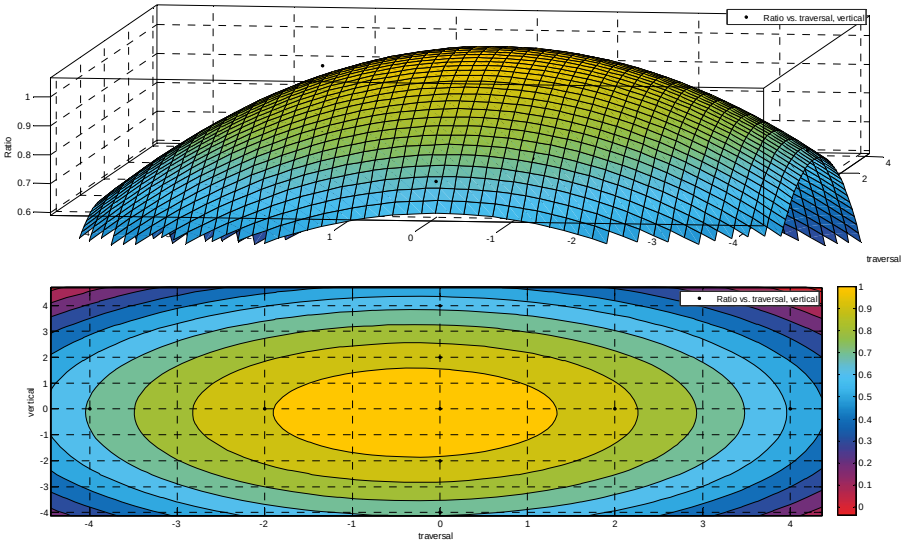

Figure 110 3D scheme of the ratio of the dynamic pressure in a perpendicular plane to the nozzle output at 1.5 diameters from the nozzle

Which gave the next equation and correlation:

$$\zeta_{x,y,1.5D} = 1.066 - 0.01466 \cdot x - 0.026 \cdot x^2 - 0.006584 \cdot y - 0.0232 \cdot y^2$$

$$R^2 = 0.91$$

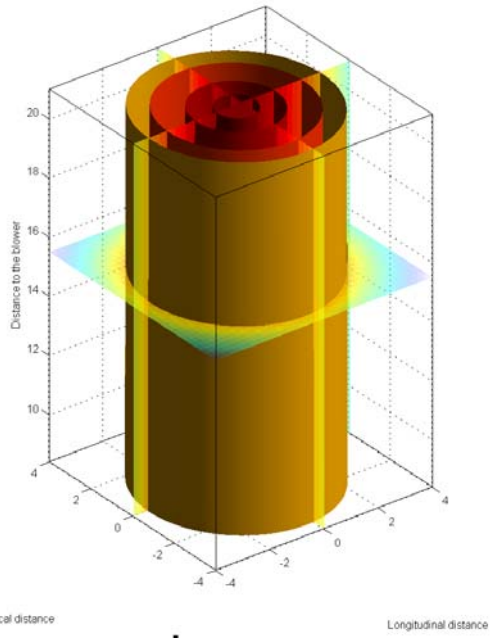

Figure 111 Flow with the isovalues for the ratio between dynamic pressures

Table 8.- Mean, max, min and standard deviation for the measured period

N	traversal	vertical	ζmean	qprandtlmean	qprandtlstd	qprandtlmax	qprandtlmin	qcontractionmean	qcontractionstd	qcontractionmax	qcontractionmin
				mbar	mbar	mbar	mbar	mbar	mbar	mbar	mbar
11550	-4	0	0.715650591	28.22223301	0.924614885	36.76015038	23.75965338	39.43577126	0.169732722	40.15323538	38.73721938
10150	-2	0	0.993146655	39.13344538	0.17850517	40.15370938	38.46913538	39.4034911	0.167723318	40.10440638	38.74942638
11550	0	0	0.993791785	39.15906807	0.175732891	39.88515438	38.51796338	39.40369468	0.166806953	40.06778538	38.73721938
11900	2	0	0.995157167	39.21187358	0.182795136	39.89736138	38.49354938	39.40269426	0.168915019	40.14102838	38.79825438
7700	4	0	0.567997025	22.37253065	0.825379235	25.59070938	19.25525438	39.38846447	0.168722484	40.07999238	38.78604738
3850	0	4	0.655365447	25.83452965	0.801434281	28.56922738	23.11268038	39.42003619	0.169914086	40.04337138	38.82266838
6300	0	2	0.993698219	39.16012488	0.223756703	39.87294738	36.71132238	39.40846843	0.167367109	40.07999238	38.83487538
3150	0	-2	0.98405851	38.76545582	0.616999608	39.79970538	33.39100638	39.39344604	0.165524837	40.03116438	38.88370338
3150	0	-4	0.72602437	28.60855293	1.503626643	32.84169038	20.42713138	39.4043976	0.170258373	39.99454338	38.74942638

Table 9.- Mean, max, min and standard deviation for the measurements

N	traversal	vertical	ζmean	poprandtl	poprandtlstd	poprandtlmax	poprandtlmin
				mbar	mbar	mbar	mbar
11550	-4	0	0.715650591	1043.170319	0.928608742	1045.73275	1040.713077
10150	-2	0	0.993146655	1055.138389	0.172101317	1055.671294	1054.623549
11550	0	0	0.993791785	1055.250543	0.168583197	1055.761944	1054.74415
11900	2	0	0.995157167	1055.163959	0.177105452	1055.69335	1054.633709
7700	4	0	0.567997025	1037.302847	0.820445366	1039.80298	1034.895625
3850	0	4	0.655365447	1040.737616	0.796750743	1043.096253	1038.353934
6300	0	2	0.993698219	1054.987188	0.175871576	1055.488747	1054.485419
3150	0	-2	0.98405851	1054.920317	0.17904654	1055.405702	1054.409169
3150	0	-4	0.72602437	1043.451457	1.462880629	1046.314847	1040.650847

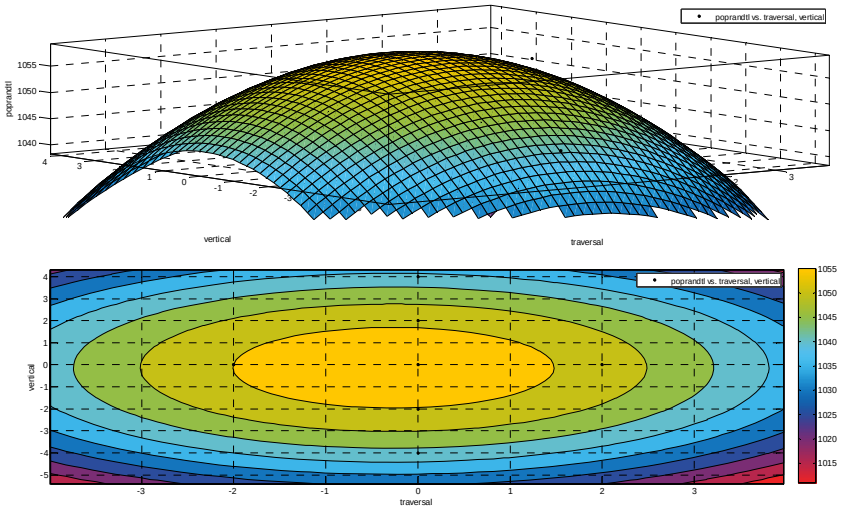

Figure 112 3D scheme of the absolute pressure in a perpendicular plane to the nozzle output at 1.5 diameters from the nozzle

$$P_{x,y,1.5D} = 1058 - 0.5855 \cdot x - 1.106 \cdot x^2 - 0.268 \cdot y - 0.9995 \cdot y^2$$

$$R^2 = 0.92$$

Results at 3.5D perpendicular plane

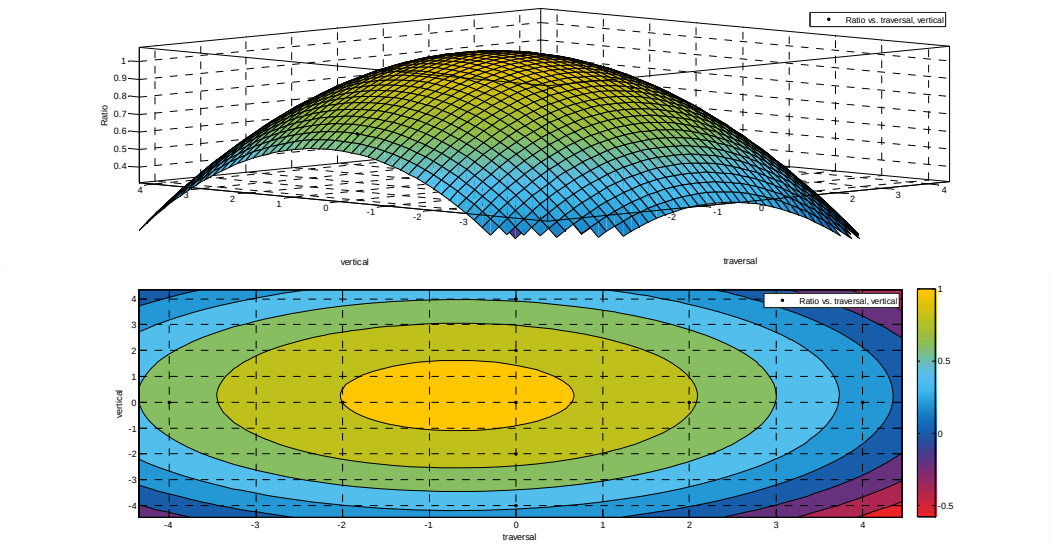

Figure 113 3D scheme of the ratio of the dynamic pressure in a perpendicular plane to the nozzle output at 3.5 diameters from the nozzle

$$\zeta_{x,y,3.5D} = 1.044 - 0.04628 \cdot x - 0.03407 \cdot x^2 + 0.01706 \cdot y - 0.03343 \cdot y^2$$

$$R^2 = 0.98$$

Being x traversal and y vertical

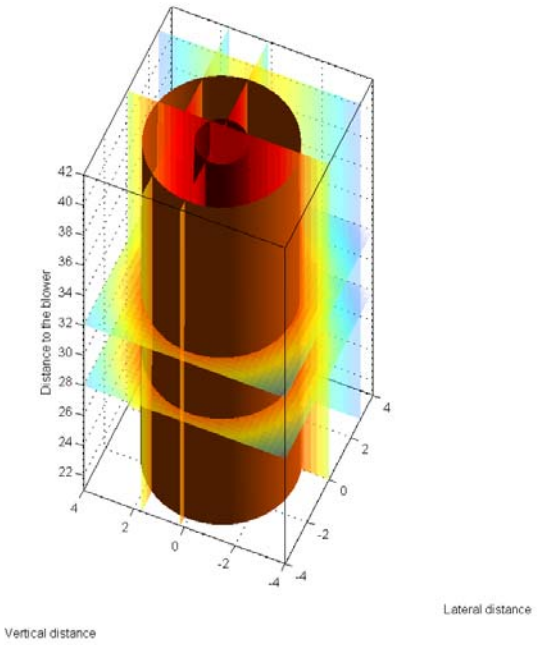

Figure 114 Flow with the isovalues for the ratio between dynamic pressures

Table 10.- mean, max, min and standard deviation of the measurements

N	traversal	vertical	ζmean	qprandtlmean	qprandtlstd	qprandtlmax	qprandtlmin	qcontractionmean	qcontractionstd	qcontractionmax	qcontractionmin	poprandtlmean
	cm	cm		mbar	mbar	mbar	mbar	mbar	mbar	mbar	mbar	mbar
10150	-4	0	0.69007555	27.20480076	1.141851544	31.14491238	22.62439938	39.42293096	0.169899559	40.09219938	38.74942638	1041.953753
10150	-2	0	0.995476781	39.22548079	0.423459807	40.26357238	32.76844738	39.40371241	0.168597553	40.14102838	38.76163338	1054.70246
8400	0	0	0.999564499	39.39327954	0.391783715	40.27577938	31.42567438	39.41044283	0.16783684	40.11661338	38.78604738	1054.987875
13650	2	0	0.847846736	33.41377653	1.006240542	36.78456438	29.47254738	39.4101612	0.169165534	40.07999238	38.65177038	1048.332416
9450	4	0	0.301070757	11.86659623	1.171640175	15.92273338	7.487668377	39.41464238	0.169203032	40.11661338	38.78604738	1026.590074
11200	0	2	0.950740612	37.4709205	0.634832966	39.25038538	34.68495538	39.41234866	0.167295211	40.04337138	38.83487538	1052.741274
9800	0	4	0.578422217	22.79935881	1.249004295	32.80506838	17.64392638	39.41646456	0.16840911	40.15323538	38.71280538	1037.505639
10150	0	-2	0.901874087	35.54206917	0.889274036	38.60341238	30.00965638	39.40912562	0.168286155	40.06778538	38.79825438	1050.501348
6300	0	-4	0.432256223	17.0395031	1.23060129	21.55017838	12.62683238	39.41991388	0.167778432	40.07999238	38.84708238	1031.621929

Table 11.- Mean, max, min and standard deviation of the emasurements

N	traversal	vertical	ζmean	poprandtlmean	poprandtlstd	poprandtlmax	poprandtlmin
0	cm	cm	0	mbar	mbar	mbar	mbar
10150	-4	0	0.69007555	1041.953753	1.158690165	1045.230752	1038.458363
10150	-2	0	0.995476781	1054.70246	0.457813405	1055.549249	1053.34647
8400	0	0	0.999564499	1054.987875	0.416402806	1055.671817	1054.037163
13650	2	0	0.847846736	1048.332416	1.035852004	1051.1072	1045.253895
9450	4	0	0.301070757	1026.590074	1.176546536	1029.875317	1023.200095
11200	0	2	0.950740612	1052.741274	0.660080365	1054.338108	1050.557224
9800	0	4	0.578422217	1037.505639	1.253615494	1040.817416	1033.895741
10150	0	-2	0.901874087	1050.501348	0.891930865	1052.828932	1047.643914
6300	0	-4	0.432256223	1031.621929	1.243411191	1035.125802	1027.921241

There is a loss in the absolute pressure that can be seen in the next interpolation

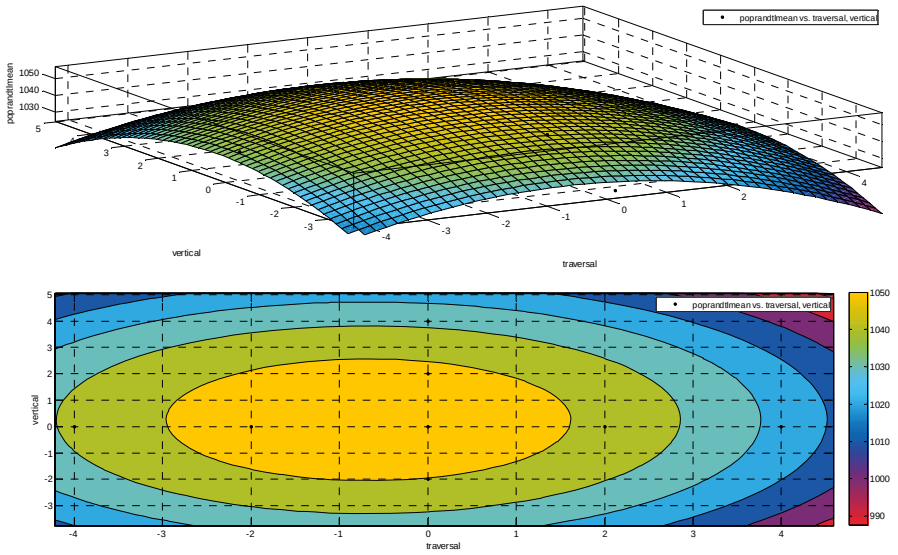

Figure 115 3D scheme of the absolute pressure in a perpendicular plane to the nozzle output at 3.5 diameters from the nozzle

$$P_{x,y,3.5D} = 1057 - 1.855 \cdot x - 1.384 \cdot x^2 + 0.7004 \cdot y - 1.366 \cdot y^2$$

$$R^2 = 0.99$$

Final Results

As long as the prandtl is far away from the blower the correlation becomes bigger, this will reverse for longer distances. Nevertheless in the perpendicular directions becomes smaller then the influence of

the lateral and vertical displacements become higher when moving far away thought the different is minimal. This is mainly why the point at 1.5 diameters seemed to be more stable in terms of direction. On the next table it can be seen the reults on different points for each coefficient.

Table 12.- Distribution of the coefficients among the longitudinal and vertical plane

Distance	Longitudinal	Ratio	Distance	Longitudinal	Ratio	Longitudinal	vertical	Ratio	Longitudinal	Ratio	Longitudinal	Ratio
cm	cm		cm	cm		cm	cm		cm			
						0	4	0.828870886				
						0	2	0.989205913				
4.2	-4	0.632611581	4.2	-2	0.990992489	0	0	0.992776881	2	0.992234855	4	0.965610981
						0	-2	0.991606775				
						0	-4	0.994841007				
						0	4	0.655365447				
						0	2	0.993698219				
12.6	-4	0.715650591	12.6	-2	0.993146655	0	0	0.993791785	2	0.995157167	4	0.567997025
						0	-2	0.98405851				
						0	-4	0.72602437				
						0	4	0.578422217				
						0	2	0.950740612				
29.4	-4	0.69007555	29.4	-2	0.995476781	0	0	0.999564499	2	0.847846736	4	0.301070757
						0	-2	0.901874087				
						0	-4	0.432256223				

Conclusions

Though the flow seems not to be centred this is corrected from 1.5D, which seems to be an optimal distance to perform the measurements.

Test on 15-September-2015.

Description of the test

The test realized has the aim to determine the factor $\zeta_{frequency}$ among different positions in the space.

Table 13.- logbook for the measurement period

channel	sensor	serial number	offset	factor	units	sensitivity
1		2377	-1999260	10^4	mBar	305.0630849
2		2379	-1999260	10^4	mBar	305.0630849
3		2392	-479.82	10^0	mBar	0.01220704
4		2390	-480.29	10^0	mBar	0.01220704
5		2387	-17346.5	10^{-2}	mBar	0.525970836
6		2388	-17347.5	10^{-2}	mBar	0.525970836
7			-5	10^0	V	0.000152588
8	P_{atm}		-5	10^0	V	0.000152588
9			-5	10^0	V	0.000152588
10	$T_{prandtl}$		-200.088	10^0	C	0.0038180541992188
11	$T_{downstream}$		-199.872	10^0	C	0.0038117980957031
12	T_{amb}		-199.916	10^0	C	0.0038136291503906

Correction of the offsets

The offsets for the Qcontraction and Qprandtl were respectively -0.16139 mBar and -0.102261 mBar respectively

Table 14.- Offset correction for the measurment period

	Signal	Value
$\overline{-q_{contraction}}]_{f=0}$	*mean dynamic pressure contraction*	-0.16139 mBar
$\overline{-q_{prandtl}}]_{f=0}$	*Mean dynamic presure prandtl*	-0.102261 mBar
$\overline{-P_{atm} + P_{0_{prandtl}}}]_{f=0}$	*Pressure absolute prandtl*	-32.32551 mBar

Logbook

Table 15.- Loogbook for the measurement period

hour	Frequency	Trasversal Note [cm]	trasversal	lateral	lateral note
15:09	20	10	0	27.7	4.5
15:09	40	10	0	27.7	4.5
15:19	60	10	0	27.7	4.5
15:44	70	10	0	27.7	4.5
15:55	85	10	0	27.7	4.5
16:03	85	13	-3	27.7	4.5
16:15	70	13	-3	27.7	4.5
16:23	70	12.5	-2.5	27.7	4.5
16:34	70	12	-2	27.7	4.5
16:40	70	13.5	-3.5	27.7	4.5
16:45	70	13.5	-3.5	24.7	12.12
16:50	70	13	-3	24.7	12.12
16:55	70	12.5	-2.5	24.7	12.12
17:00	70	11.5	-1.5	24.7	12.12
17:07	85	10	0	24.7	12.12
17:17	85	10	0	21.7	19.74

Results

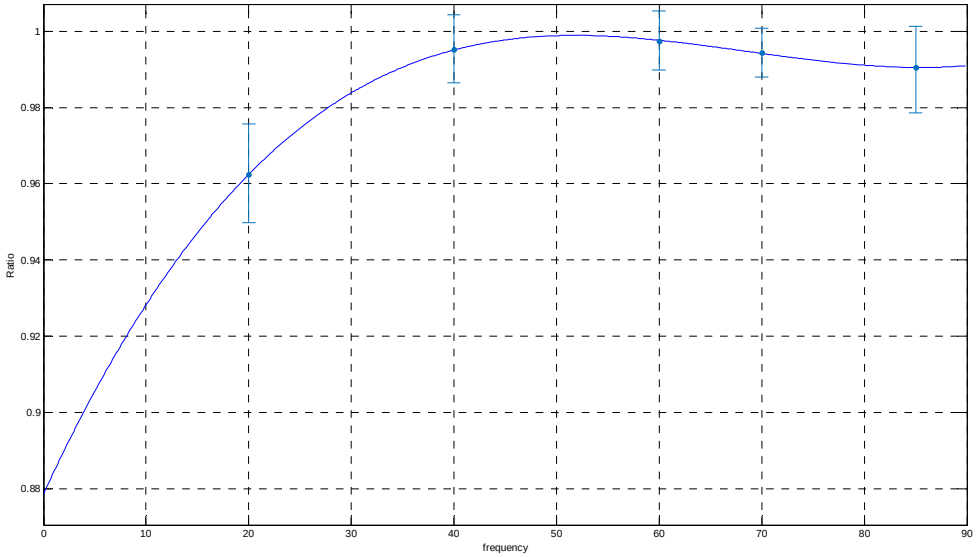

Figure 116 Maximum and Minimum

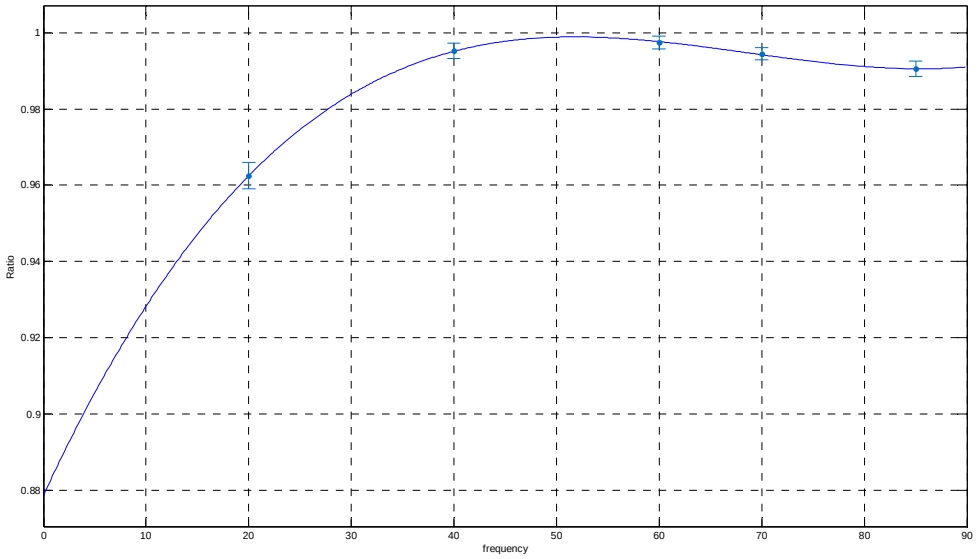

Figure 117 standard deviation

$$\zeta_{frequency} = 4.378 \cdot 10^{-7} \cdot x^3 - 9.016 \cdot 10^{-5} \cdot x^2 + 0.005816 \cdot x + 0.8787$$

$$R^2 = 0.9994$$

Table 16 results

frequency	Ratio	stdev	Ratio_max	Ratio_min
20	0.962477	0.003453	0.975782	0.949866
40	0.995236	0.002061	1.00434	0.986447

60	0.997434	0.001743	1.005311	0.989824
70	0.994453	0.00164	1.000733	0.988012
85	0.990488	0.002001	1.001355	0.978515

This approach nevertheless is quadratic though from 20 Hz and 40 there are some non linearities. This nevertheless does not happens in the last part of the curve

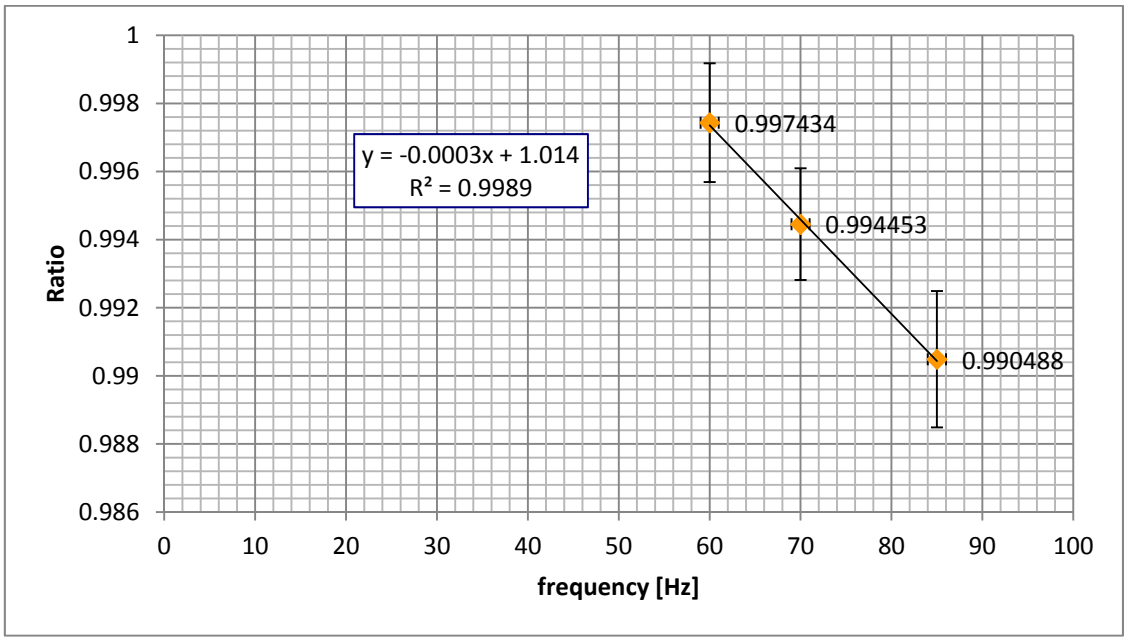

Figure 118 Plotted the standard deviation

Conclusions

The correlation is more adequate for “higher” Mach numbers.

3. Evaluation and Calibration of the system

The overall system has several components that had to be tested in different environments. The task of synchronization needed to analyse several facts where the GPS and timing had to be accurate enough and response adequately under satellite signal losses, starting of the system or power loss. On the other hand the pitot head needed to be assessed in order to find the real angle of attack and pressure on the system itself.

3.1 Hardware performance

In terms of synchronization on the boards have being checked the performance under three regimes:

- Start of the board
- Loss of GPS satellite signals.
- Power loss

In the other hand the duration of the measurement is being analysed getting the power consumption on the maximum peak.

3.2 5-hole pitot head calibration

The pitot head calibration for the last design has being performed in what for traceability purposes is called the fifth and last setup. This was held on winter 2015.

- **Fifth setup:** Calibration of the pitot and different angles
  - 12-Nov-2015: part calibration up to +/- 20 degrees
  - 02-December-2015: full angle calibration with different speeds and angles.

The results on the pressure calibration belongs to the test on December and the results on the flow angle calibration will presented on the results of both test, in November and December.

3.2.1 Instrumentation and measurement conditions

Instruments

Table 17.- Instrument serial numbers and channel naming

Tube Mark	Pressure transducer	PCB location	serial number dynamic pressure	serial number absolute pressure sensor
6	HCLA0050EU	Down	2392	2377
5	HCLA0050EU	Up	2392	
1	HLB far away to the pitot	Up	2387	
4	HLB far away to the pitot	Down	2387	

3	HLB closer	Up	2388
2		down	2388

Table 18.- Offset correction and range of magnitude in the measurements

channel	Sensor	serial number	offset	factor	units	sensitivity
1		2377	-1999260	10^4	mBar	305.0630849
2		2379	-1999260	10^4	mBar	305.0630849
3		2392	-479.82	10^0	mBar	0.01220704
4		2390	-480.29	10^0	mBar	0.01220704
5		2387	-17346.5	10^{-2}	mBar	0.525970836
6		2388	-17347.5	10^{-2}	mBar	0.525970836
7			-5	10^0	V	0.000152588
8	P_{atm}		-5	10^0	V	0.000152588
9			-5	10^0	V	0.000152588
10	$T_{prandtl}$		-200.088	10^0	C	0.0038180541992188
11	$T_{downstream}$		-199.872	10^0	C	0.0038117980957031
12	T_{amb}		-199.916	10^0	C	0.0038136291503906

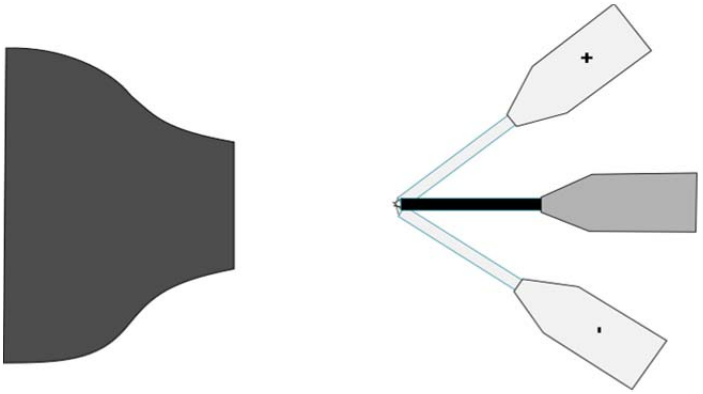

Figure 119.- Sign convention

3.2.2 Pressure calibration

As mentioned in the previous sections the first evaluation to perform is the determination of Cq at different Mach numbers. The next plots show the values for different Mach numbers and orientation.

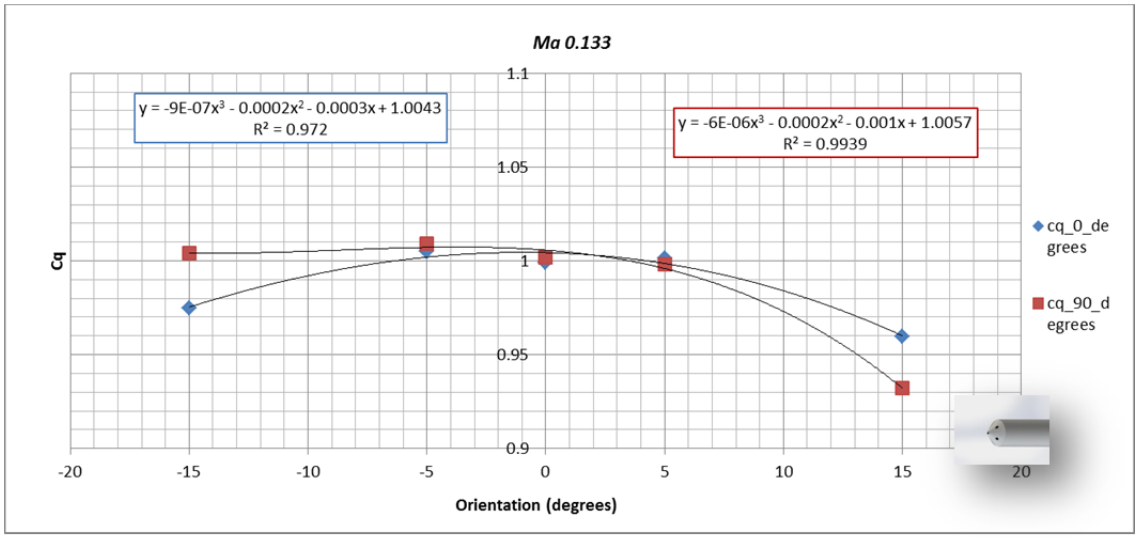

Figure 120.- Cq versus orientation at Mach 0.133

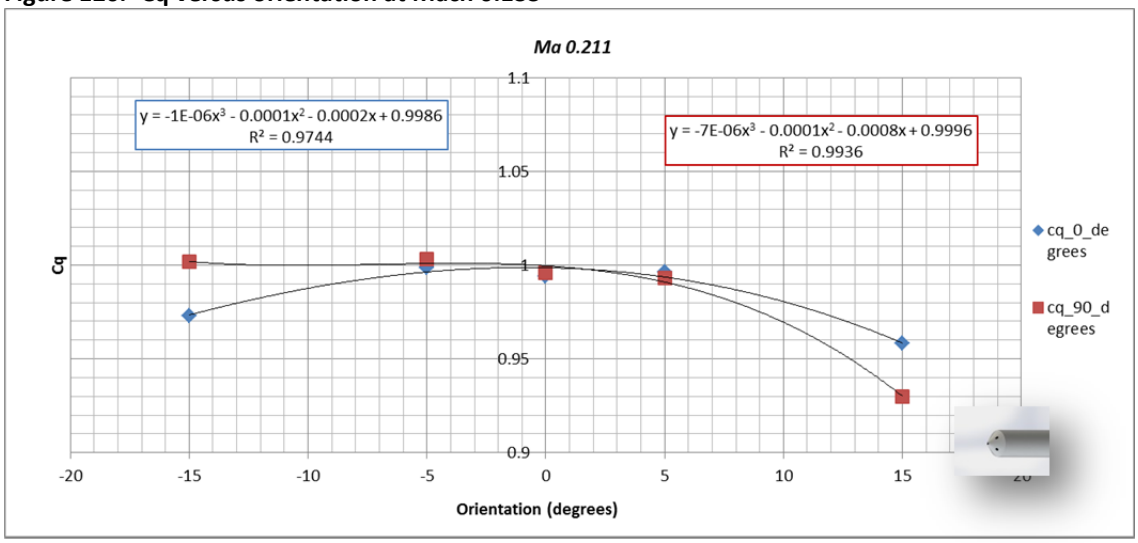

Figure 121.- Cq versus orientation at Mach 0.211

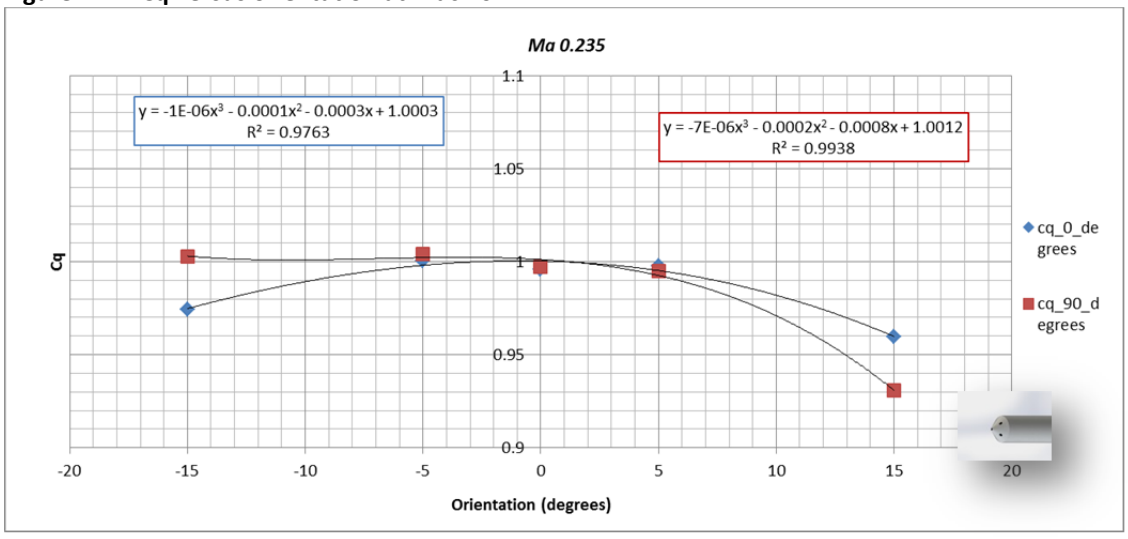

Figure 122.- Cq versus orientation at Mach 0.235

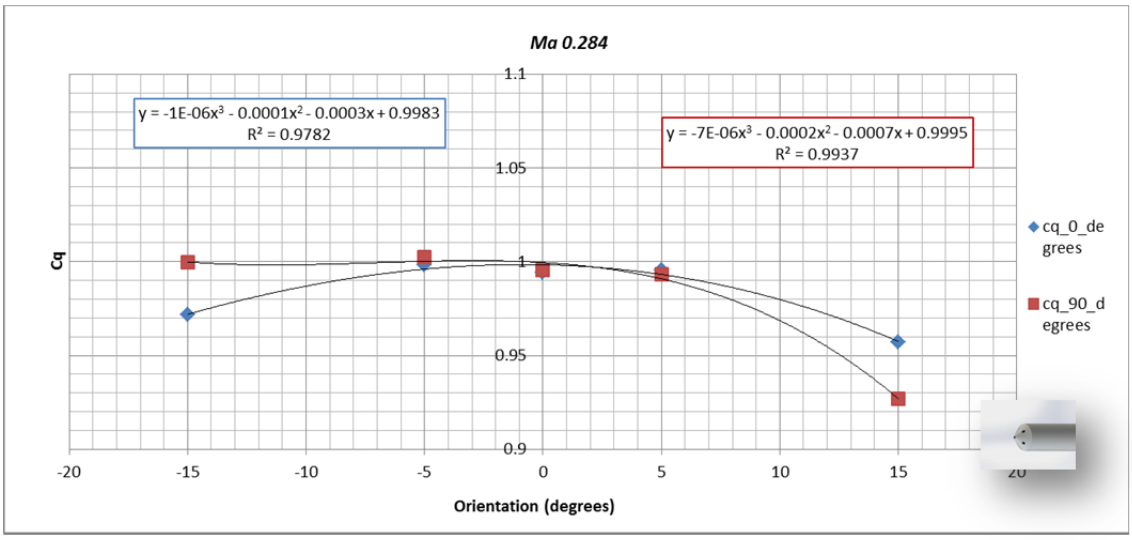

Figure 123.- Cq versus orientation at Mach 0.284

3.2.3 Flow angle calibration

Description

The offsets on the starting have being corrected as usual. In some points the values have exceed the usual offset points as shown here.

Logbook

Table 19.- Logbook

Logbook with the set of setups				
Day 2nd december 2015.				
Distance 1.5D. Vertical position 0 cm. Horizontal position 0 cm				
Hour	converter frequency [Hz]		Horizontal angle	Pitot holes angle
13:20	40		0 degrees	0
13:22	60		0 degrees	0
13:25	70		0 degrees	0
13:28	85		0 degrees	0
13:29	85		5 degrees	0
13:31	70		5 degrees	0
13:33	60		5 degrees	0
13:35	40		5 degrees	0

	13:37	40	15 degrees	0
	13:39	60	15 degrees	0
	13:41	70	15 degrees	0
	13:43	85	15 degrees	0
	13:45	85	-5 degrees	0
	13:47	70	-5 degrees	0
	13:49	60	-5 degrees	0
	13:51	40	-5 degrees	0
	13:53	40	-15 degrees	0
	13:55	60	-15 degrees	0
	13:57	70	-15 degrees	0
	13:59	85	-15 degrees	0
	14:01	85	-15 degrees	90
	14:03	70	-15 degrees	90
	14:05	60	-15 degrees	90
	14:07	40	-15 degrees	90
	14:09	40	-5 degrees	90
	14:11	60	-5 degrees	90
	14:13	70	-5 degrees	90
	14:15	85	-5 degrees	90
	14:17	85	0 degrees	90
	14:19	70	0 degrees	90
	14:21	60	0 degrees	90
	14:23	40	0 degrees	90
	14:25	40	5 degrees	90
	14:27	60	5 degrees	90
	14:29	70	5 degrees	90
	14:31	85	5 degrees	90
	14:33	85	15 degrees	90
	14:35	70	15 degrees	90
	14:37	60	15 degrees	90
	14:39	40	15 degrees	90
	14:41	0		

There has being taken several points for the calculation of the Mach number

Relation between Calpha, Cbetha and the angle

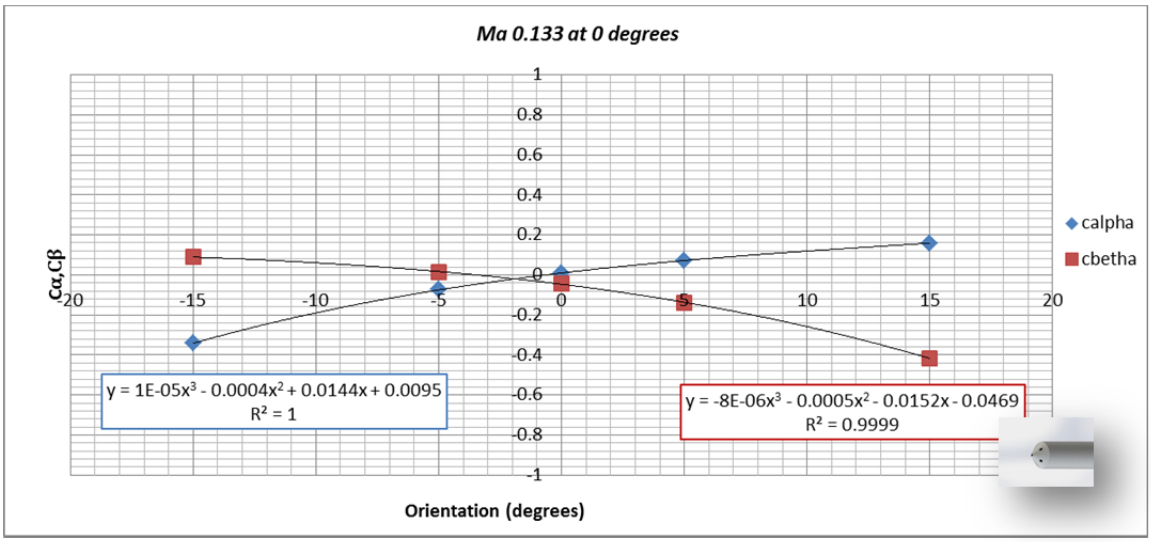

Figure 124. Calpha and Cbetha versus orientation at Mach 0.133 and 0 degrees

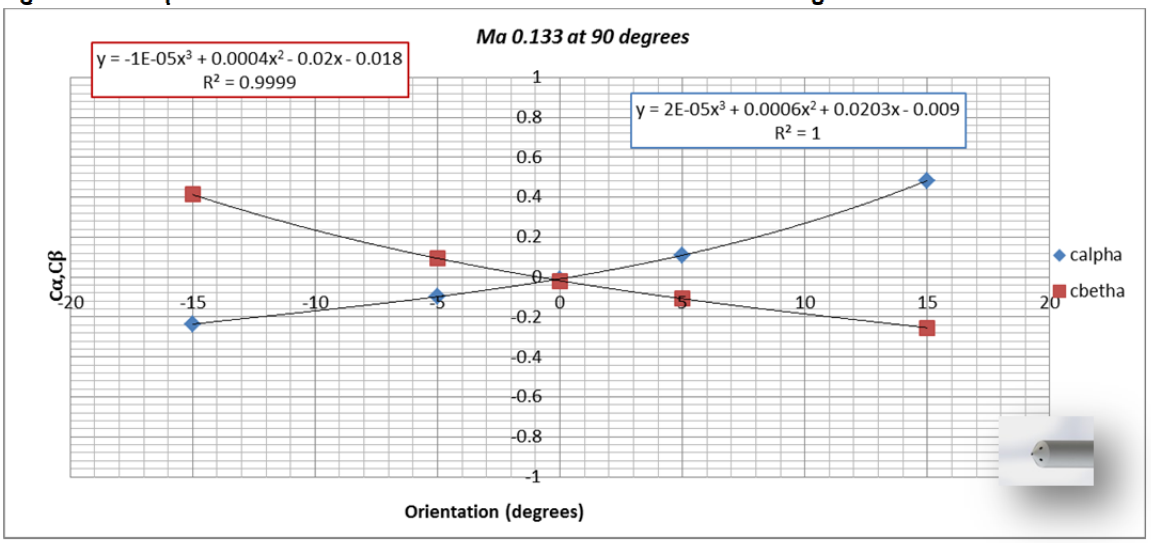

Figure 125. Calpha and Cbetha versus orientation at Mach 0.133 and 90 degrees

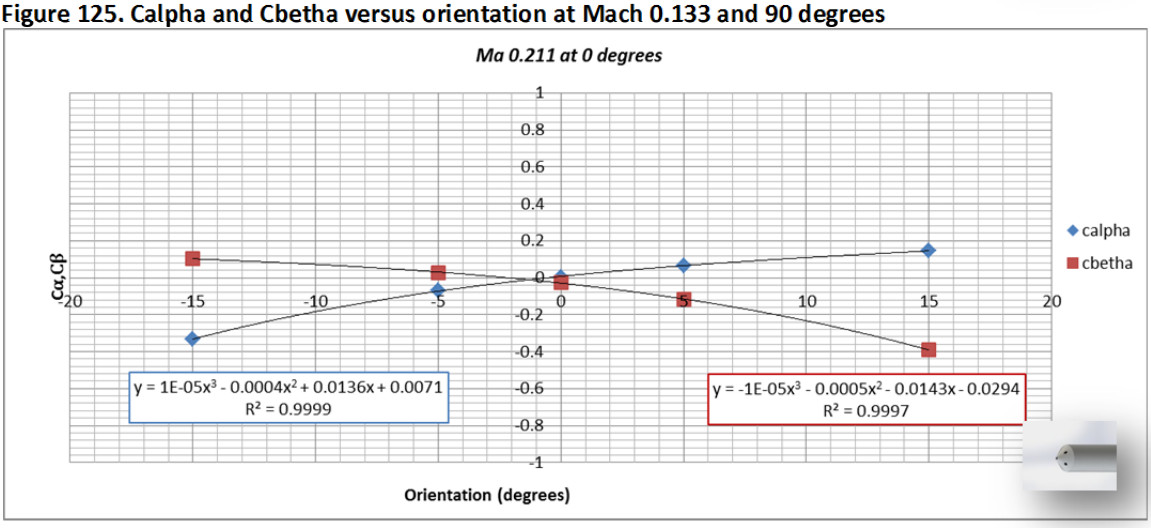

Figure 126. Calpha and Cbetha versus orientation at Mach 0.211 and 0 degrees

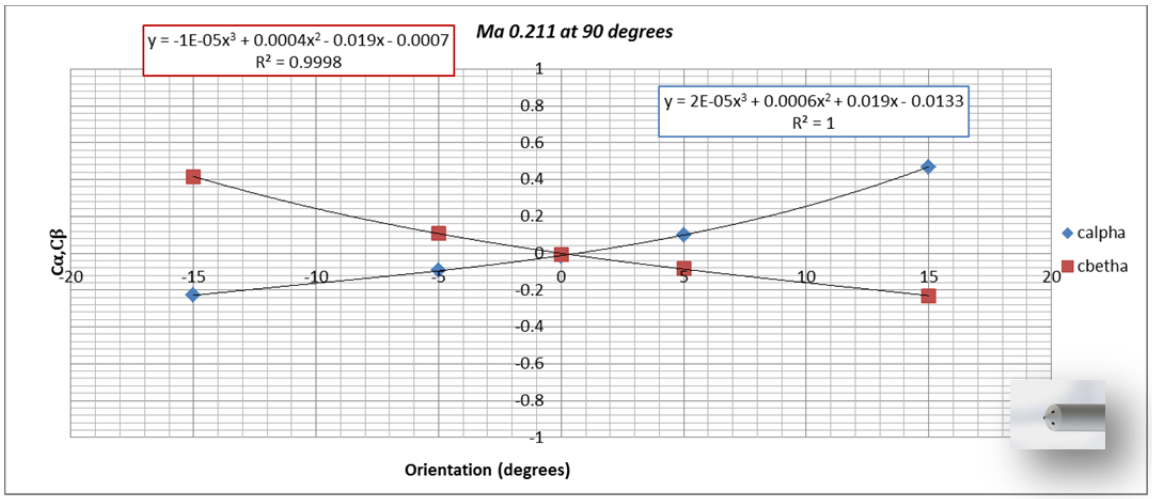

Figure 127. Calpha and Cbetha versus orientation at Mach 0.211 and 90 degrees

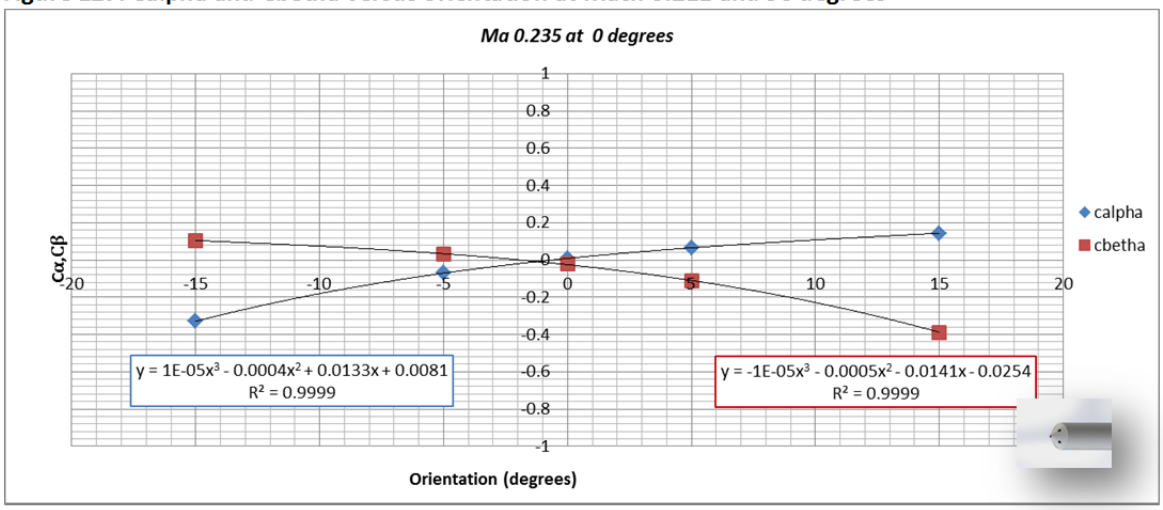

Figure 128. Calpha and Cbetha versus orientation at Mach 0.211 and 0 degrees

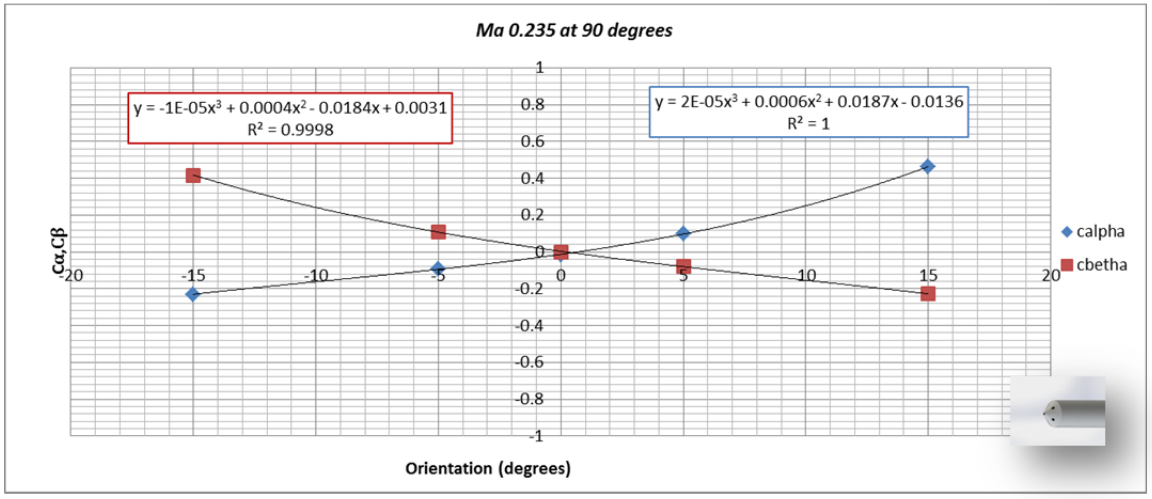

Figure 129. Calpha and Cbetha versus orientation at Mach 0.235 and 0 degrees

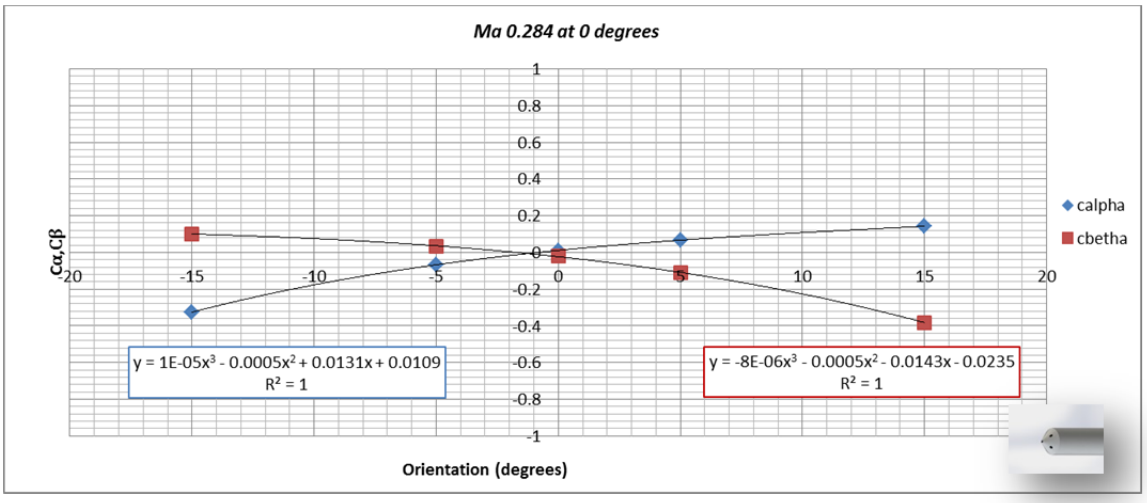

Figure 130. Calpha and Cbetha versus orientation at Mach 0.284 and 0 degrees

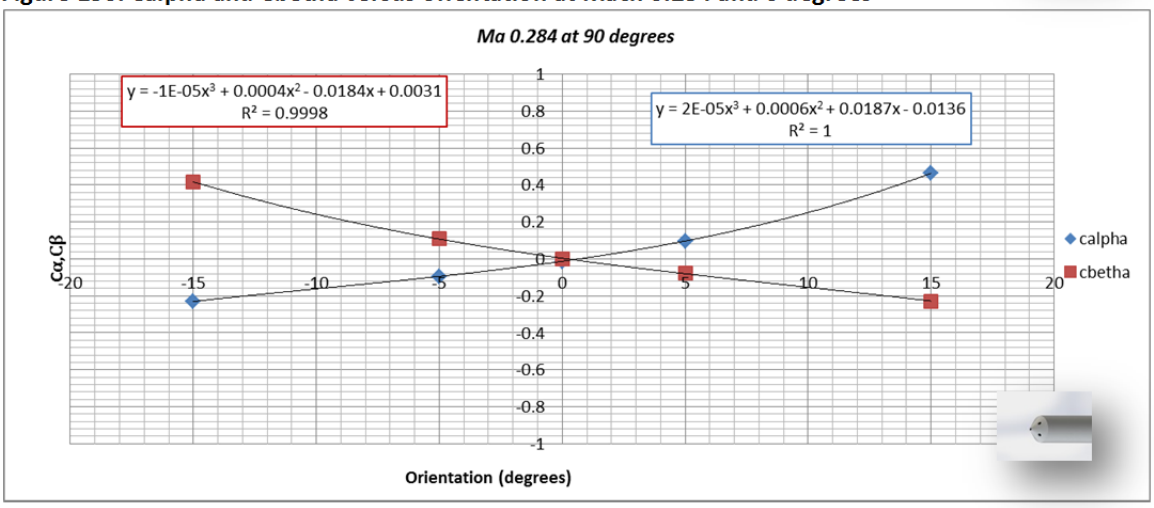

Figure 131. Calpha and Cbetha versus orientation at Mach 0.284 and 90 degrees

Representing in the opposite direction, i.e.. Having Calpha and getting as result the orientation the equations gave

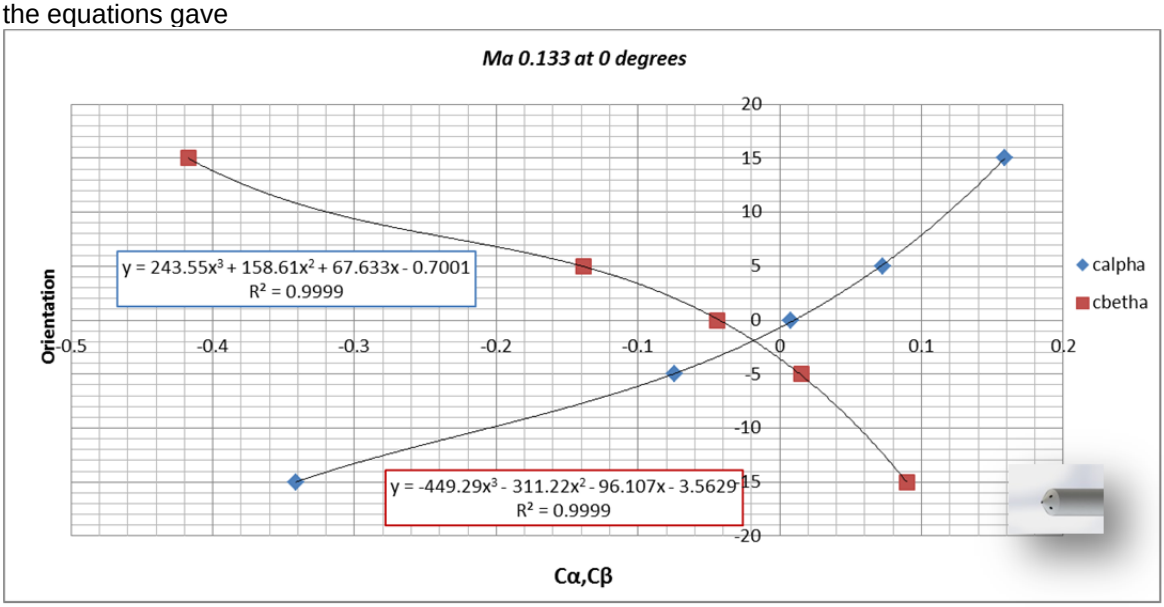

Figure 132. orientation versus Calpha and Cbetha at Mach 0.133 and 0 degrees

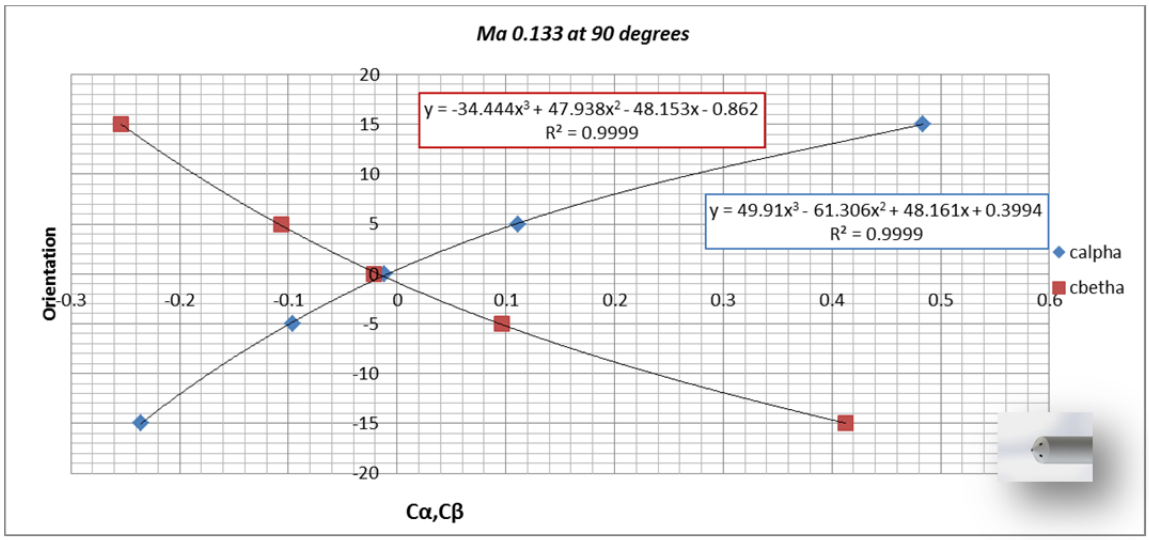

Figure 133.- orientation versus Calpha and Cbetha at Mach 0.133 and 90degrees

	a_3	a_2	a_1	a_0	Mach
C_alpha_0133_0	243.55	158.61	67.633	-0.7001	0.133
C_betha_0133_90	-34.444	47.938	-48.153	-0.862	0.133
C_betha_0133_0	-449.29	-311.22	-96.107	-3.5629	0.133
C_alpha_0133_90	49.91	-61.306	48.161	0.3994	0.133
C_alpha_0211_0	308.74	190.49	72.662	-0.5695	0.211
C_betha_0211_90	-25.329	49.497	-52.245	0.0195	0.211
C_betha_0211_0	-470.72	-302.04	-89.999	-2.145	0.211
C_alpha_0211_90	45.982	-64.503	50.829	0.5913	0.211
C_alpha_0235_0	329.11	199.01	73.438	-0.6507	0.235
C_betha_0235_90	-7.7551	44.918	-54.001	0.2608	0.235
C_betha_0235_0	-478.47	-304.1	-89.35	-1.8555	0.235
C_alpha_0235_90	36.607	-61.297	51.642	0.5913	0.235
C_alpha_0284_0	374.27	213.86	73.374	-0.8829	0.284
C_betha_0284_90	-7.7551	44.918	-54.001	0.2608	0.284
C_betha_0284_0	-613.5	-359.84	-91.326	-1.5796	0.284
C_alpha_0284_90	36.607	-61.297	51.642	0.5913	0.284

Figure 134.- Table with the resulting coefficients

$$C_{\alpha,\beta} = a_3 \cdot x^3 + a_2 \cdot x^2 + a_1 \cdot x^1 + a_0 \cdot x^0$$

It can be seen in the equations and graphs that there are 4 zones depending on the angle of the pitot. At 0 degrees, changing the sign of cbetha seems that both graphs are coincident

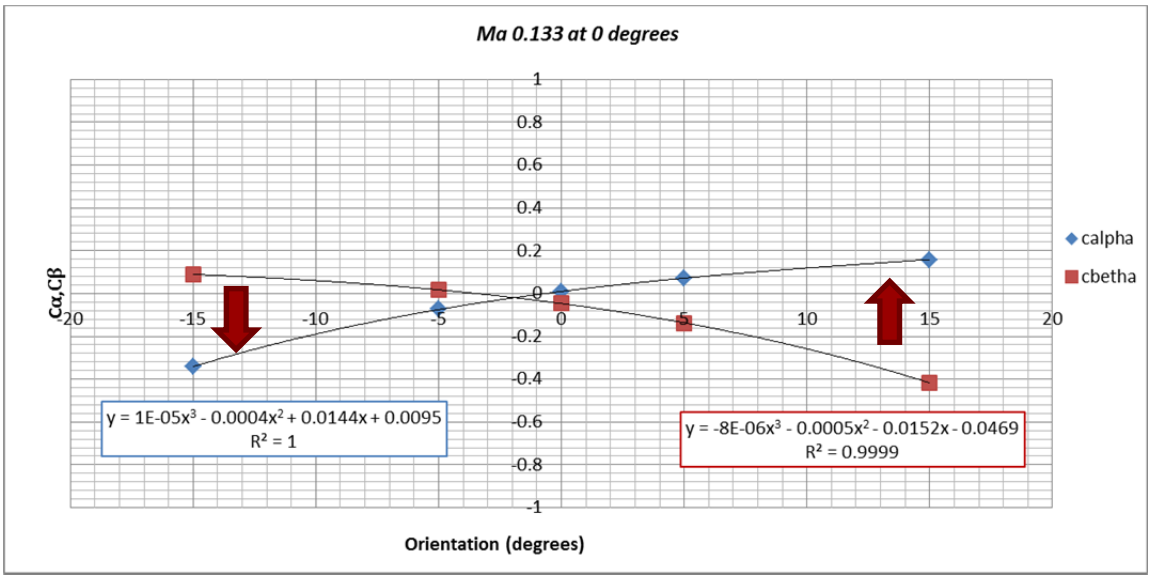

Figure 135.- Polarity change in Cbetha

As a result the pitot seems to have a linear behaviour in the negative area for this configuration

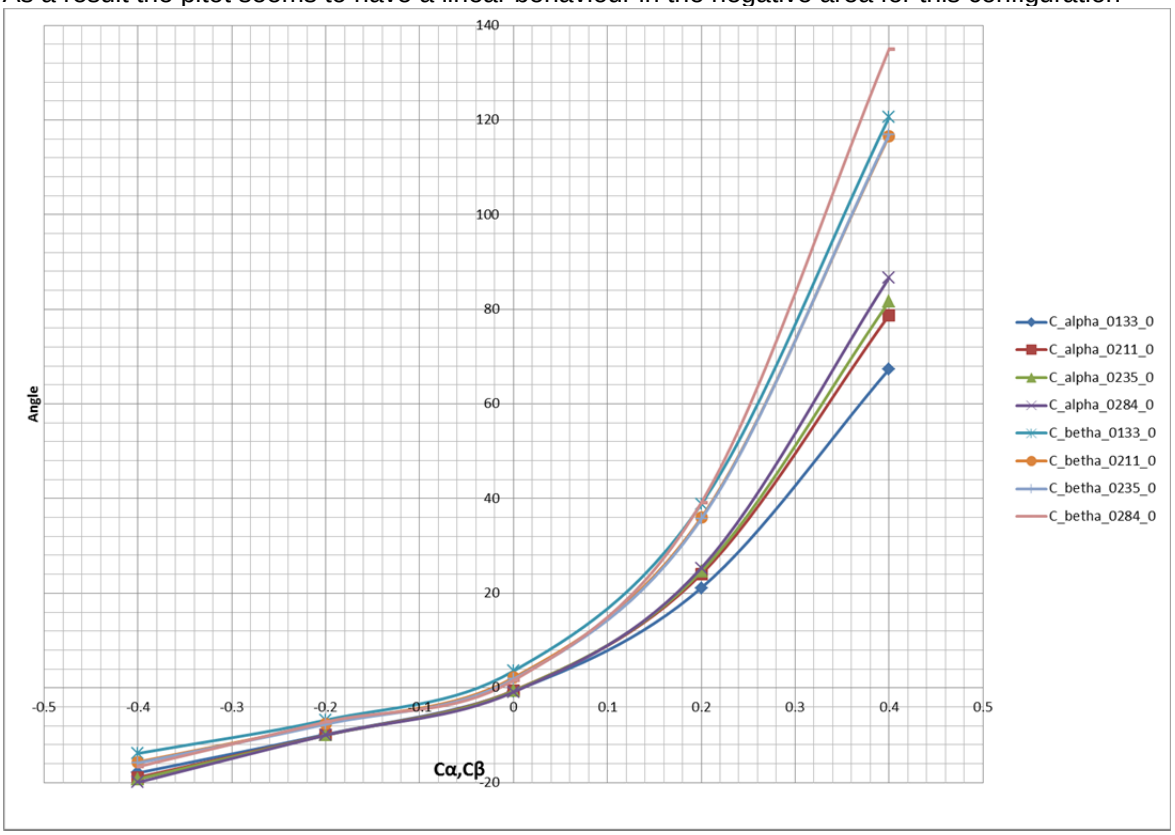

Figure 136 Solutions at 0 degrees having changed the polarity of Cbetha

At 90 degrees the behaviour seems different

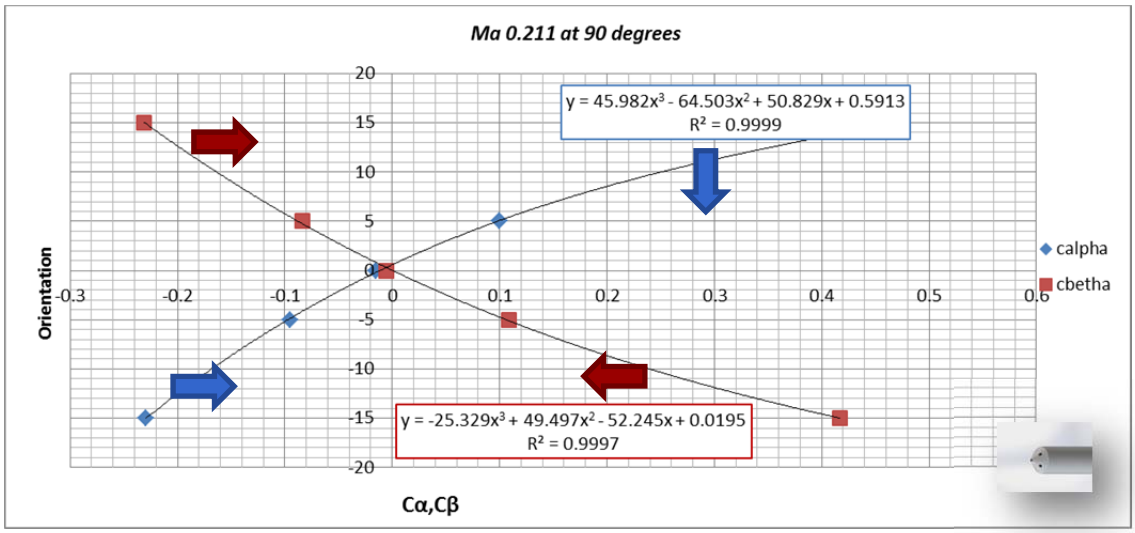

Figure 137.- polarity and sign changed in C alpha and polarity changed in cbetha

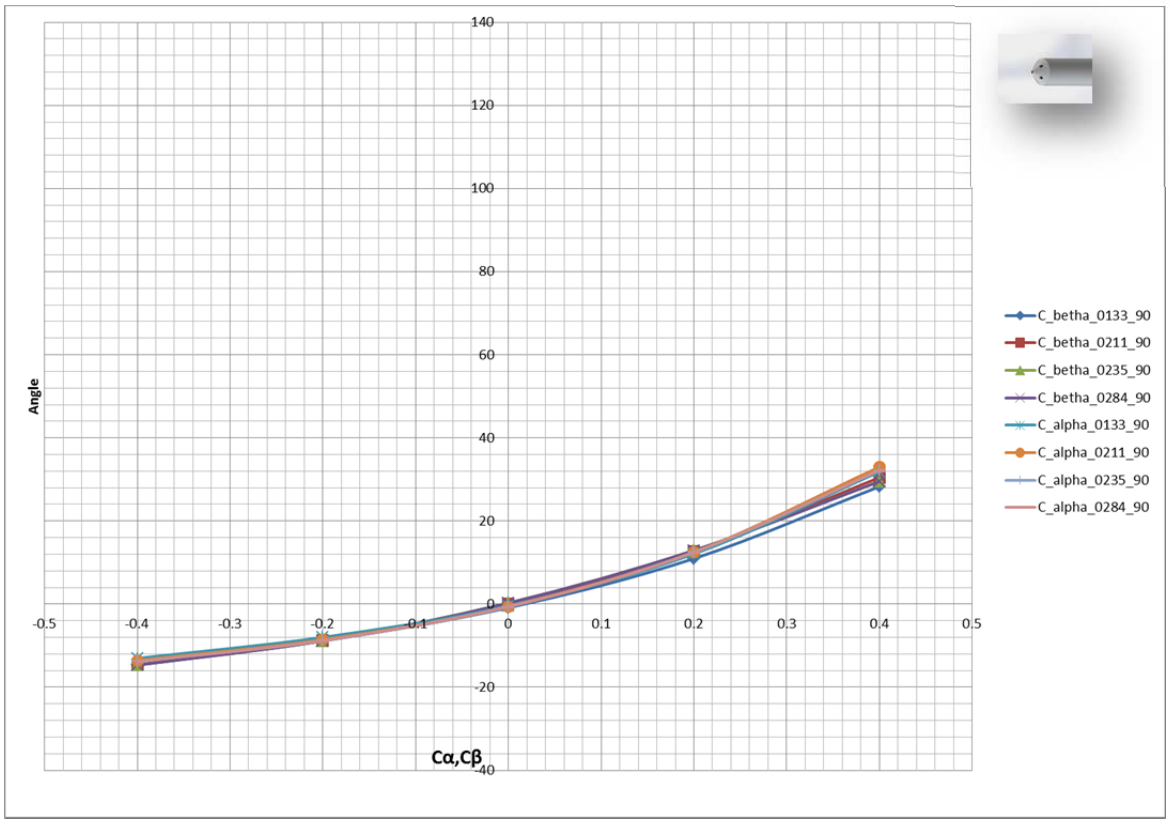

Figure 138.- Solutions at 90 degrees

So it seems that in a specific region the dynamic behaviour is linear. Therefore the first thing to do is to identify in which position the pitot head is and then get the belonging angle

Conclusions

It seems that the pitot head is not behaving linear in one region, this could be due to several reasons:

- Rod stiffness
- Alignment of the pitot rod against the flow

4. Measurement campaign

4.1 Description of the measurements campaign, turbine, location and site description

For convenience the measurement campaigns were performed on the on the Nordtank 500 kW wind turbine at the test field of DTU Campus Risø situated close to Roskilde fjord Figure 139. Where DTU can carry out a full measurement campaign on this turbine such as fulfilling power curve- or loads measurements, there meteorological masts are instrumented with cup anemometers, temperature transmitters and sonic wind speed measurement devices.

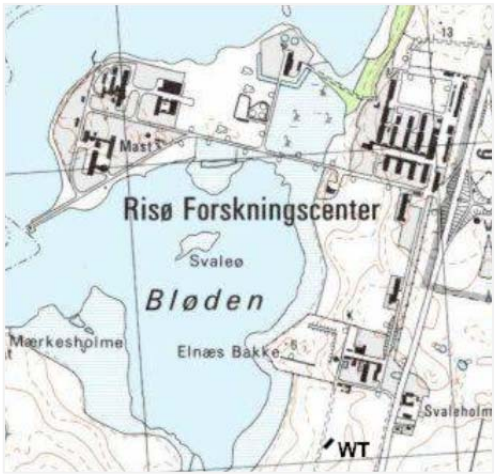

Figure 139 Wind turbine location (WT)

An overview of the possibilities for measuring on this wind turbine can be found in (Helgesen, Hansen, Schmidt Paulsen, & Sørensen, 2008) in overall three parts of the measurement system are taken in account:

- Turbine measurements(status signals, power, eventual strain gauge signals from tower or blades)
- Meteorological measurements (wind speed, wind direction, air temperature, air barometric pressure)
- Pitot Measurements (see annexure on transducers linked to this system)

The pitot measurements were recorded in a separate system device which will be shown in the next sections, in parallel the measurements of the met mast and turbine were recorded with a standard data acquisition system.

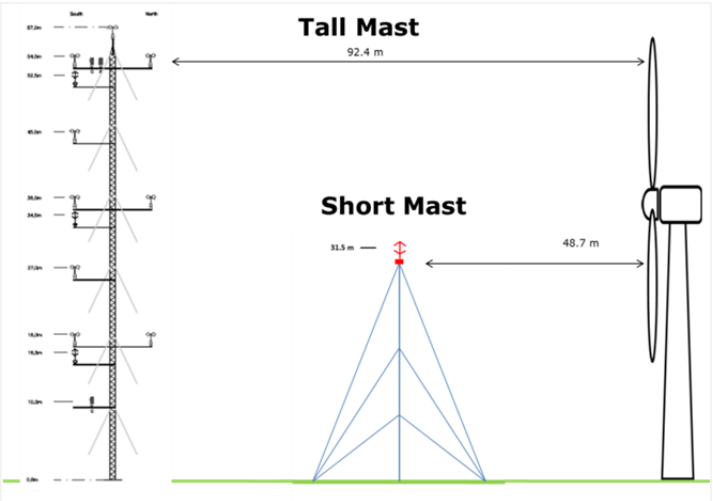

Figure 140 Instrumentation layout

In overall two measurement campaigns have being performed in 2014 and 2015:

i) 2014-Nov-03 from 13:00 to 15:10
ii) 2015-Sep-01 from 18:40 to 20:30

The results from the measurements are organized in databases which will be described in the next sections.

4.1.1 Turbine description

The sensor including the mount was installed on one of the Nordtank rotor blades as shown in the next picture. The wind turbine has the following characteristics shown in the Table 20

Figure 141. Photograph of the turbine with the encircled pitot measurement device

Table 20.- Characteristics of the turbine

Rotor Diameter	41.1m
Rotational Speed	27.1 rpm
Tilt angle	2º
Cone angle	0º
Blade type	LM 19.1
Blade profile[s]	NACA 63-4xx & NACA FF-W3, equipped with vortex generators
Blade length	19.04 m
Blade chord	0.265 – 1.630 m
Blade twist	0.02 – 20.00 degrees
Generator	Siemens 500 kW
Hub height	36.0 m
Blade weight	1960 kg (2249 kg incl. Extender and bolts)

4.1.2 Met Mast description

As previously described the meteorological mast is located at 92 meters to the turbine west .

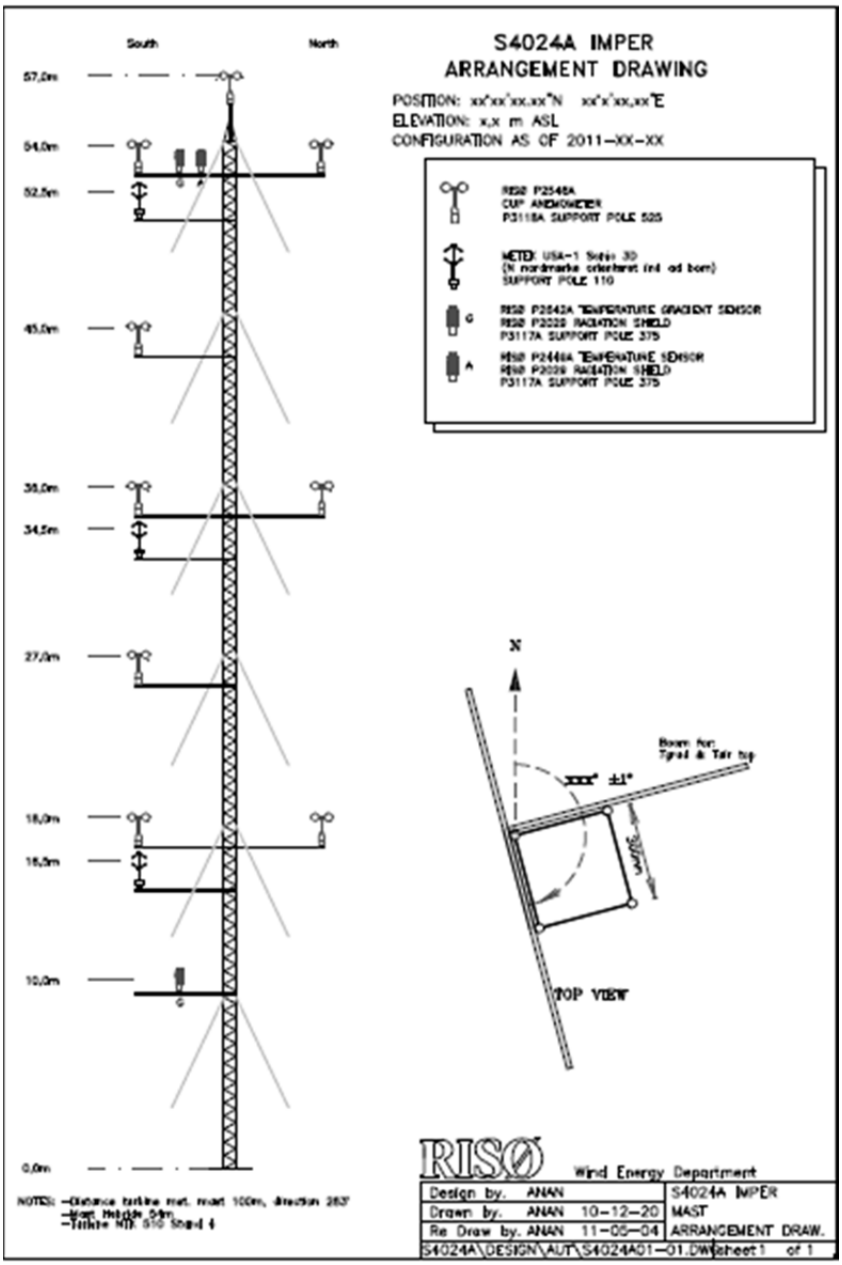

Figure 142 Met Mast arrangement

4.1.3 Pitot measurement description

The pitot measurements for both campaigns have being realized with the myRio setup as explained in the Hardware components section. The system was attached with gluing screws on the blade surface

and the setup was attached with a crane(that created a problem because the location of the system was not completely known, so this is why an extra measurement was needed to assess the location of the pitot's head).

Measured distance to the position of the pitot

The distance to the measurement device form the wind turbine rotating shaft centre has not being measured directly, therefore a theodolite in front of the turbine was used to determine it. Following Figure 143 different points were measured in three spatial coordinates (north, east and height). The locations were the center of the hub, the blade root, pitot and tip locations in the blade. The Table 20 Table 21 shows the values

Table 21 Table with the values and distances measured by the theodolite, the righter column is derived distance to the center

Position	N	E	Height	$\sqrt{(x-x_c)^2+(y-y_c)^2+(z-z_c)^2}$
	m	m	m	m
Center	-36.648	16.056	35.301	0
Pitot	-45.490	6.450	42.529	14.923
Tip	-48.323	2.622	45.699	20.613
Root	-38.589	16.010	35.369	1.943

As being shown in the next graph, the difference is that in total it seems that follows the cosine theorem

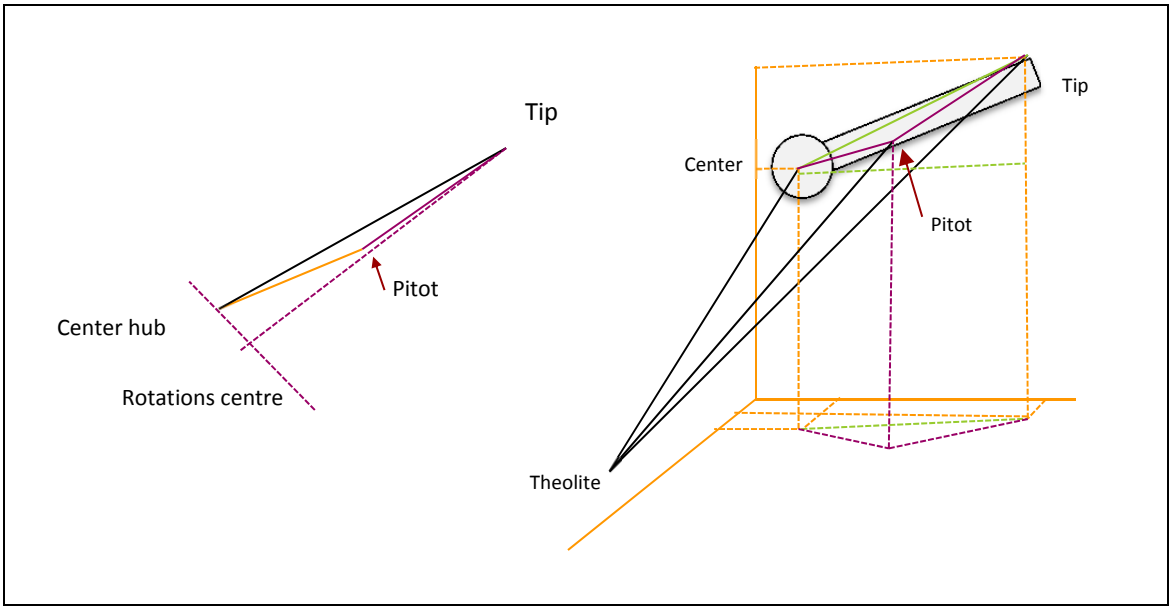

Figure 143. Geometrical condition for determining actual sensor distance. The angles represented are exaggerated for a better understanding

In this particular case the conus angle for the Nordtank turbine is 0. However it shall not be forgotten to be taken into account

The distance between pitot and tip is of 5.72 m and the distance between the center and the tip 20.61. The distance between pitot and center is 14.92. Therefore:

$$cos\alpha = \frac{{pitot_{tip}}^2 + {Tip_{center}}^2 - {pitot_{center}}^2}{2 * pitot_{tip} * Tip_{center}} = 0.996$$

This gives 5.07 degrees. Therefore the radius is

$$R = Tip_{center} * cos\alpha - pitot_{tip} = 14.81m \pm 0.3\ \mathrm{m}$$

Then the speed should be around 27 rpm, 41.84 m/s. The uncertainty is purely an estimation thought the atmospheric conditions on the measurement day were completely unfavorable and the blade was moving due to the wind influence.

Pitot's blade speed

The hub height is 36 meters and the position thereby of the pitot was found at 14.81m to the centre. So, thereby the height of the pitot measurement will vary following the next equation:

$$\boldsymbol{Height(t)_{Pitot} = 36 + 14.81 \cdot \sin(pos_{rotor} + phi)}$$

Being phi the phase gap between the marked 0 rotor position and the position of the blade where the pitot is located

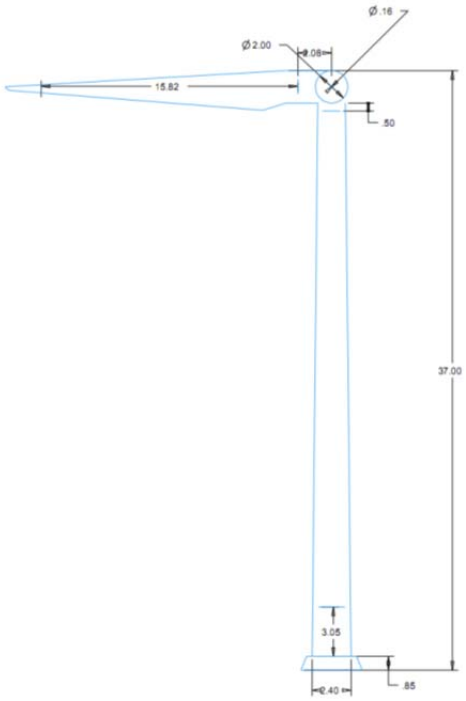

Figure 144 Sketch with dimensions of the Nordtank turbine

The approx. speed characteristics in the location of the pitot are the next:

Table 22.- Kinematic values for the pitot position

Quantity	value	units
Rotational speed	**27.1**	**Rpm**
	0.451667	**rev/seg**
	2.837905	**rads/seg**
Linear speed	**42.02937**	**m/s**
Centripetal acceleration	**119.2754**	**m/s2**

Photographs for the installation

Figure 145 Pitot sensor view from below

Figure 146 Pitot view from front of the turbine

4.1.4 Database

The measurement campaign has being provided two different independent databases:

Pitot with:

- Sampling rate: 100Hz
- Data files length: 600 seconds
- Data files format: .tim
- Duration of the measurements: from 12:00 to 14:10 (incomplete) every 10 minutes, without stop
- Naming: Rover_20141103_120000

Nordtank:

- Sampling rate: 35Hz
- Data files length: 600 seconds
- Data files format: .tim
- Duration of the measurements: continuous
- Naming: PowerCurveDemo_20141103_1200

The pitot itself had not file header but the channels were recorded without calibration. The Nordtank channels description can be found in the annexes.

4.1.5 Synchronization

The timestamp of the measurements performed by pitot do not have the same timestamp as Nordtank

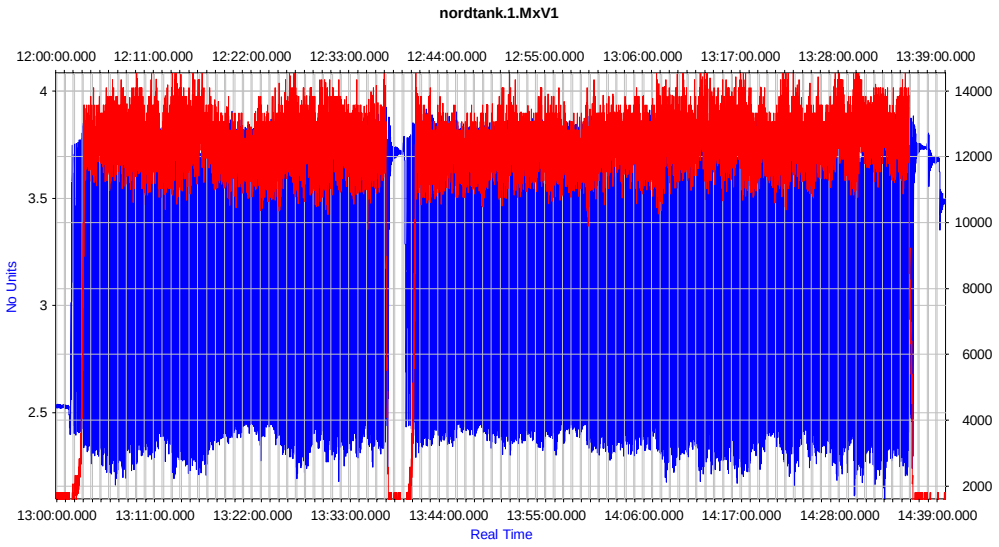

Figure 147 plot showing on blue the Nordtank blade edgewise bending moment signal and in red the uncalibrated dynamic pressure on pitot's head on the first measurement campaign. The Nordtank measurements have a time difference of +1 hour in reference with myRio measurements.

The difference in time for the first measurement campaign was of 1 hour, being the Nordtank timestamp 1 hour later than the pitot's measurement on the same event.

4.2 First Measurement campaign

This measurement campaign deals shows selected signals from the measurement systems: from the wind turbine, from the met mast, and from the pitot measurement device.

4.2.1 Turbine Measurements

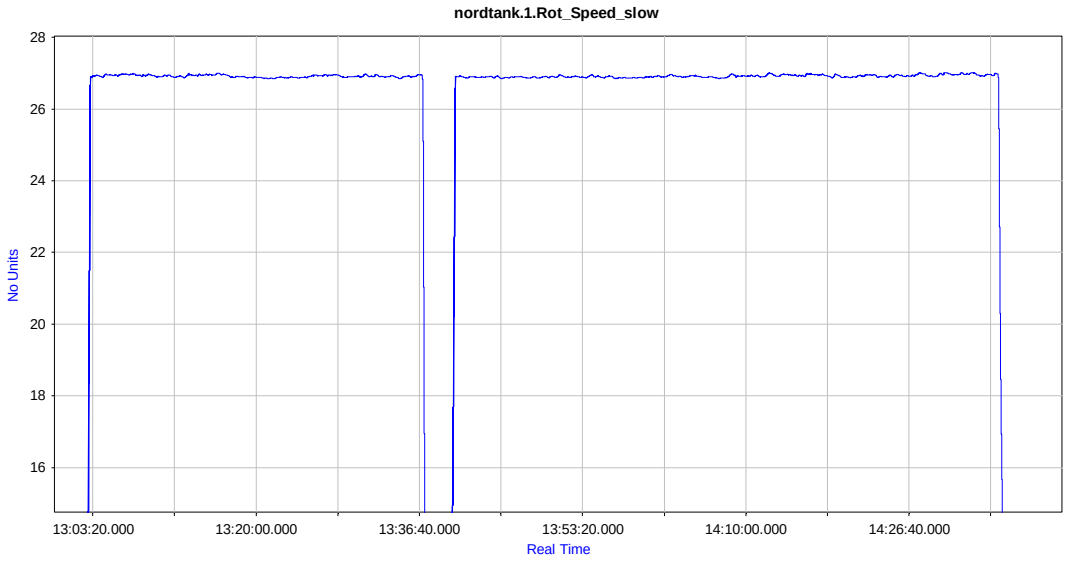

Figure 148 Rotor speed

4.2.2 Met Mast Measurements

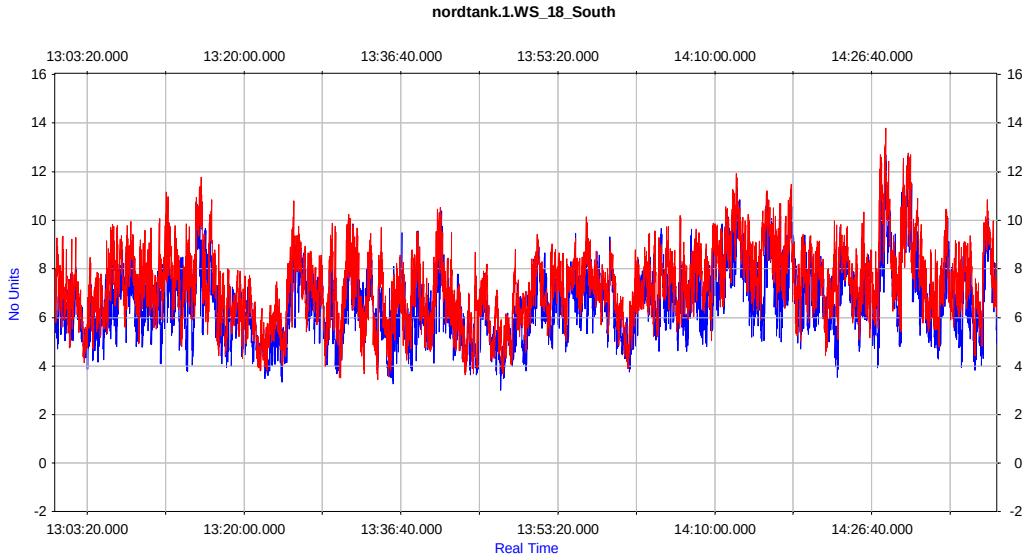

Figure 149 Wind speeds at two heights (18m and 36 m)

Atmospheric conditions

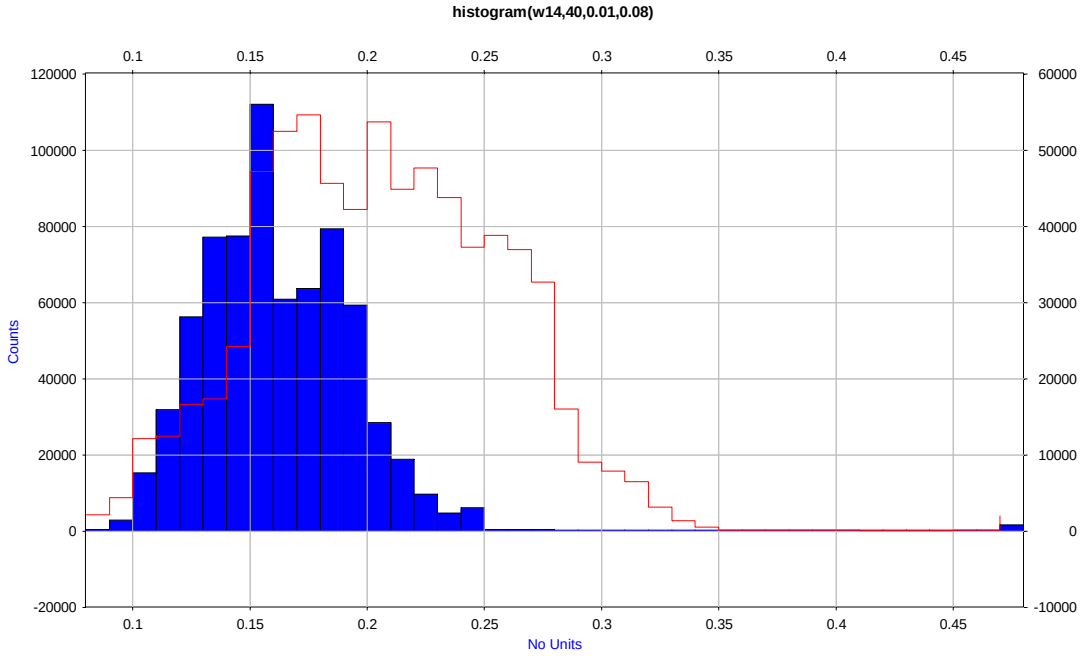

Figure 150 Distribution of the wind shear factors in the met mast at two heights 18 magl and 36magl, and between 36magl and 54 magl

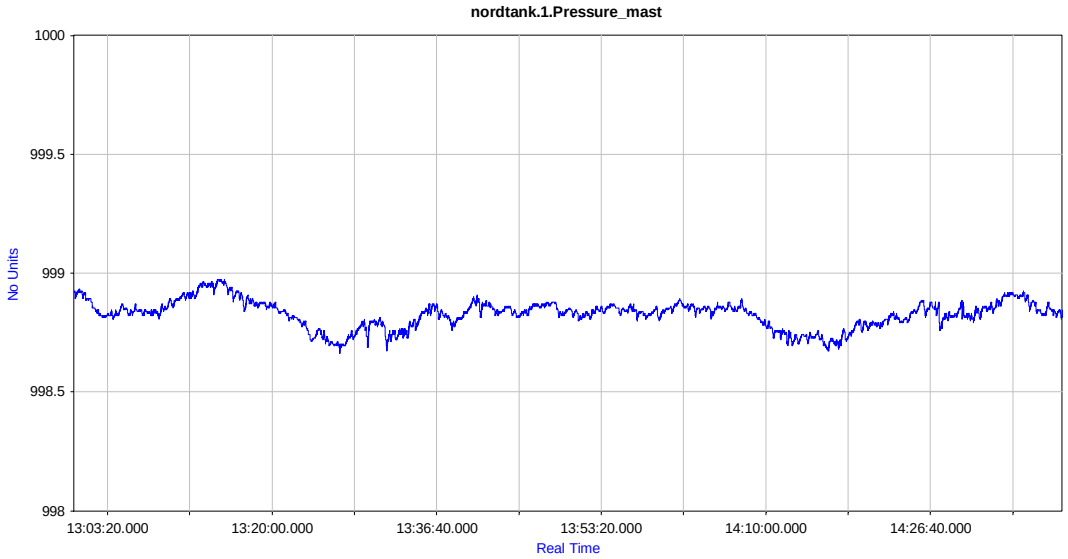

Figure 151 Air barometric pressure , xx magl Mean value: 998.8 hPa

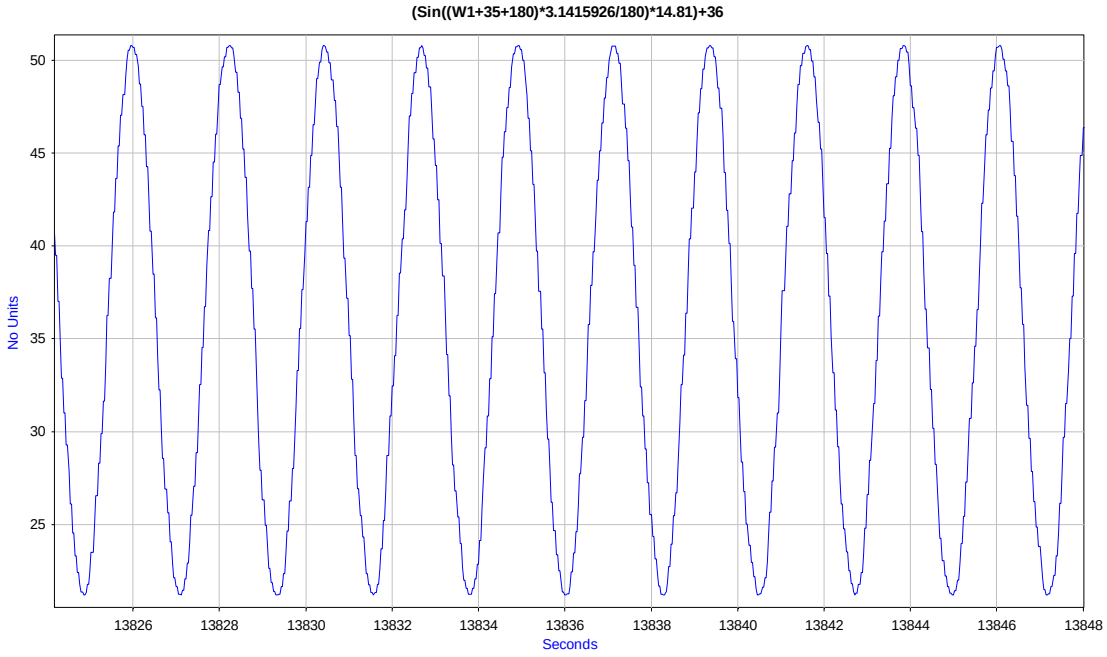

Figure 152 Rotating Height from the azimuth rotor position

The correction has being done as expressed in the previous formula to determine the height of the sensor. This correction will be used to get an estimation of the temperature on the first measurement campaign on the temperature and air density. The temperature sensors of the met mast can be seen on the

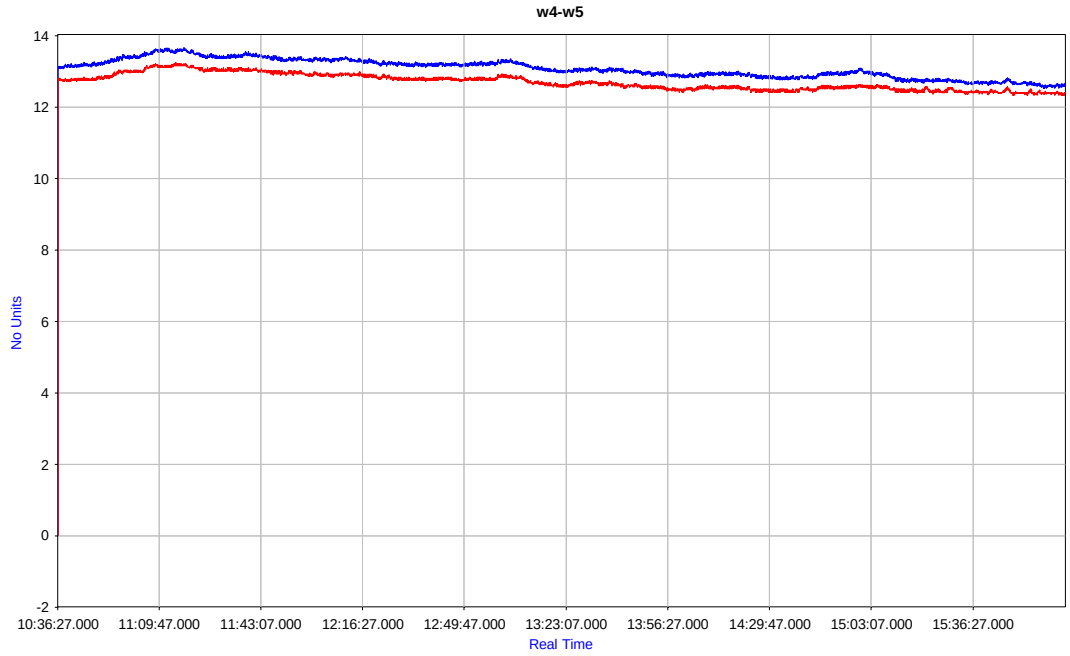

Figure 153 Temperature in the meteorological mast at 54 and 44 meters.

Assuming linearity a correction of temperature showed as follows:

$$T_{36} = \frac{T_{54-44}}{10} \cdot (54 - 36) + T_{54}$$

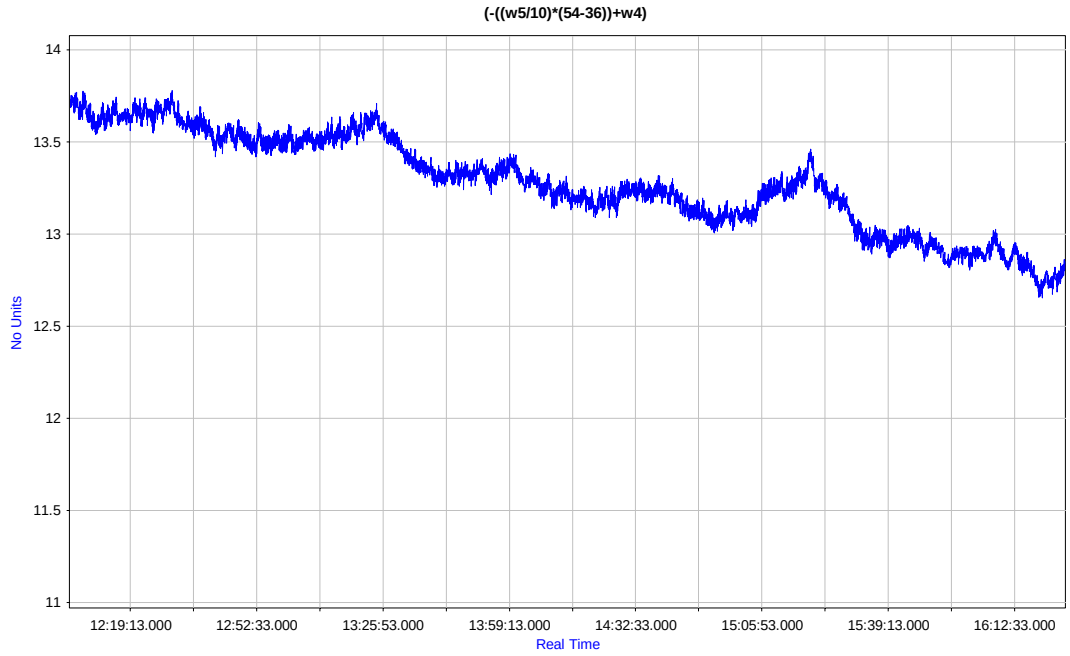

Figure 154 Assumed temperature at 36m

If will be extracted the next amount of data for the Nordtank

Assuming the pressure as constant, the air density should be:

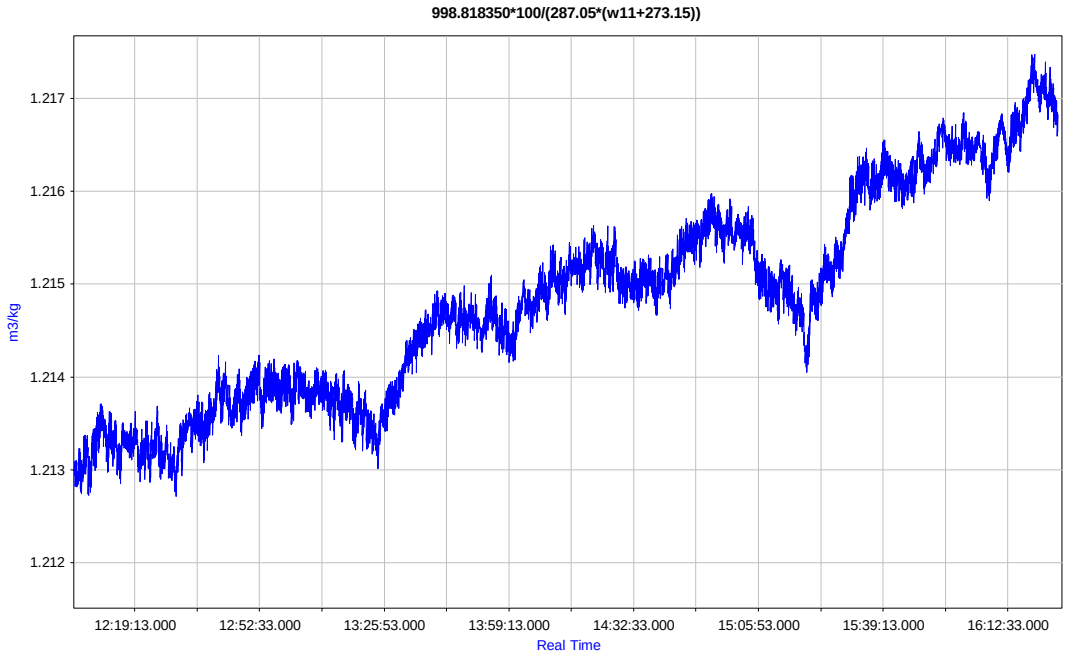

Figure 155 Rho

4.2.3 Pitot Measurements original signals

Raw signals overview

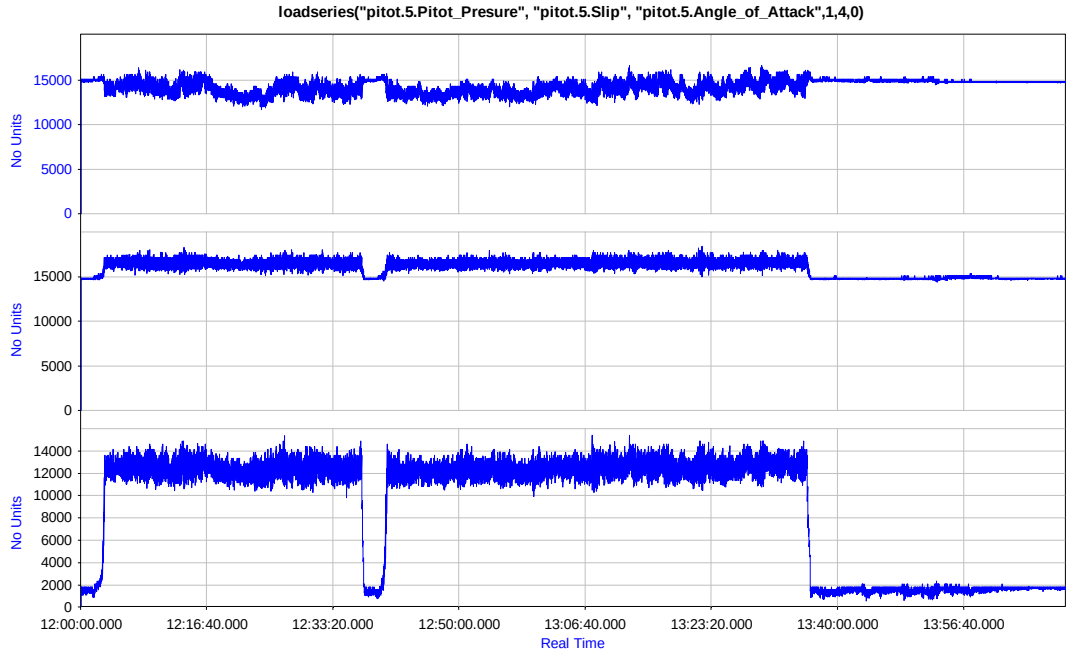

Figure 156 Pitot uncalibrated signals: pitot's pressures from up to bottom Angle of Attack, Slip and dynamic pressure

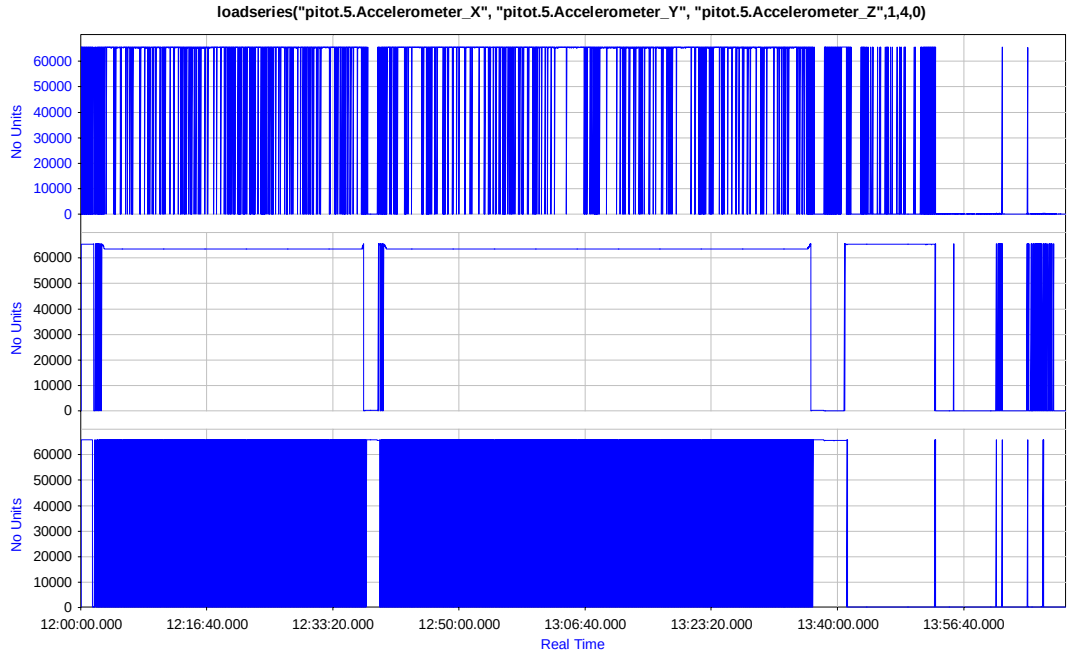

Figure 157 Accelerometers in the NI MyRio Data acquisition system, from top to bottom Z, Y and X

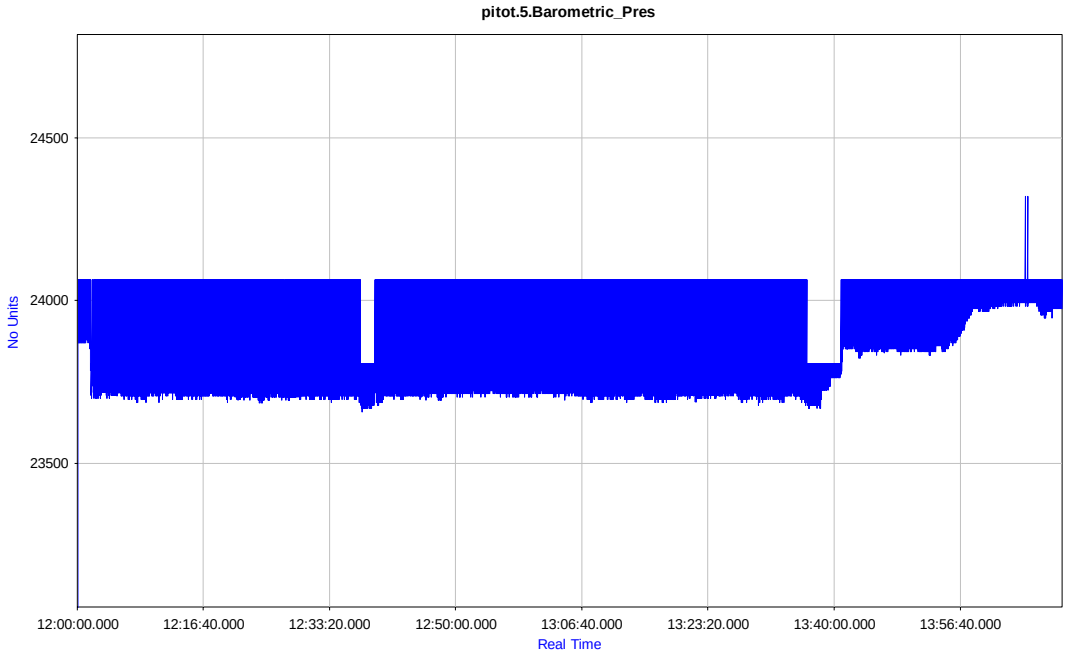

Figure 158 Barometric Pressure

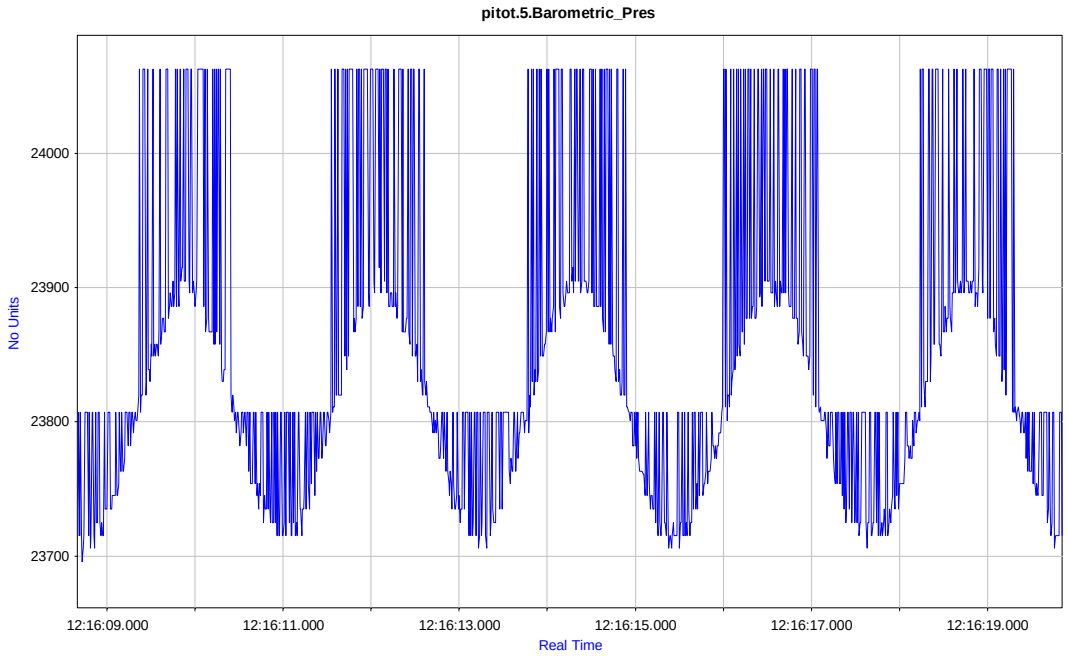

Figure 159 Zoom in the Barometric Pressure

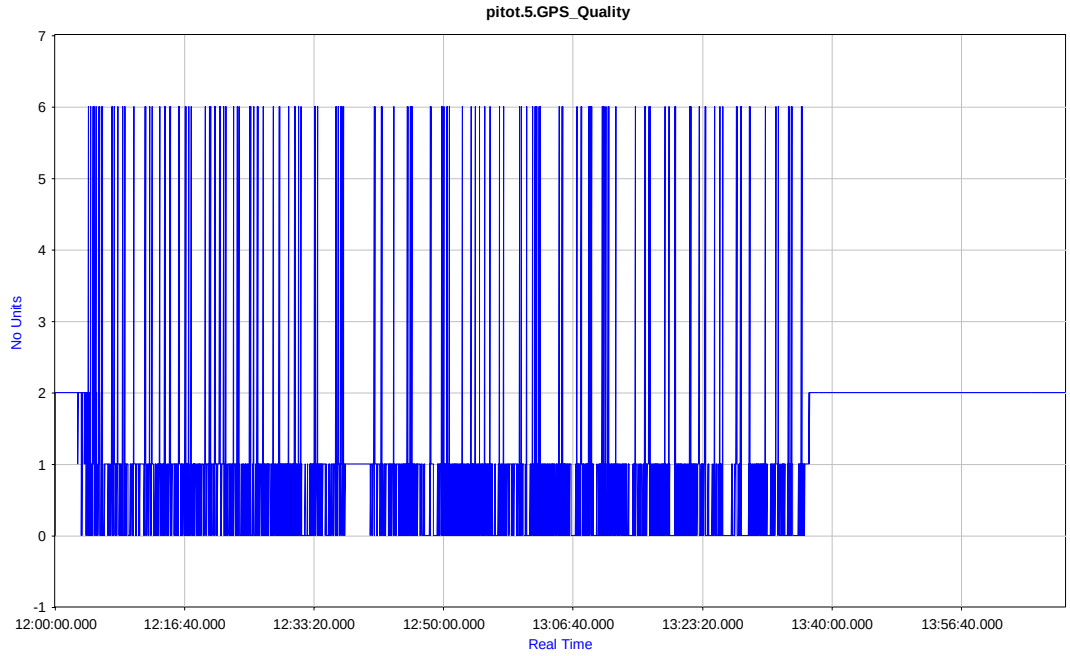

Figure 160 GPS quality signals

4.2.4 Pitot Measurements processed and calibrated signals

The signals have being treated, calibrated and checked with a post processing which is detailed in the annexure. The results are here shown

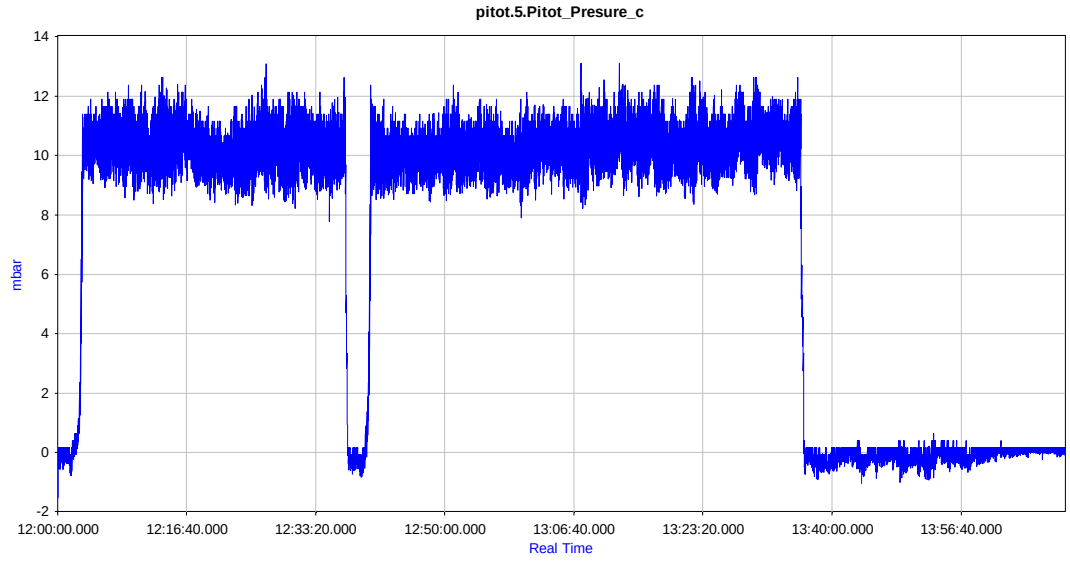

Figure 161 P16 pressure

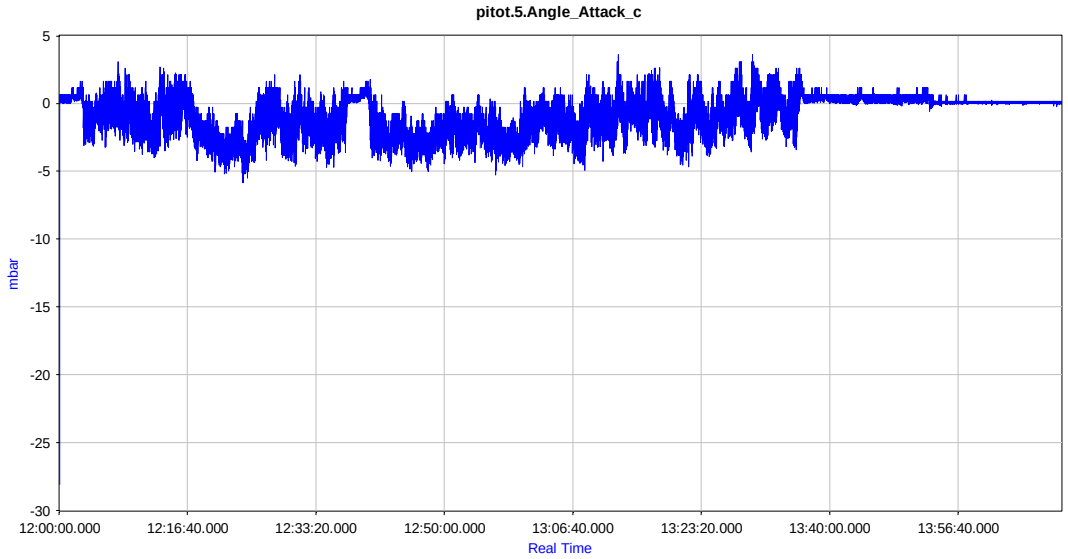

Figure 162 P23 pressure defined as angle of attack

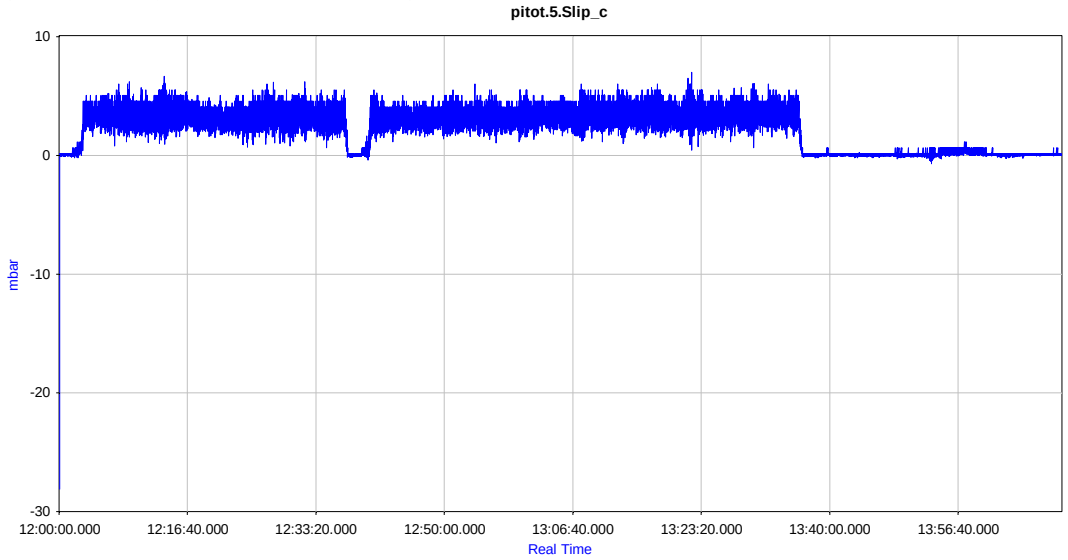

Figure 163 P45 Slip

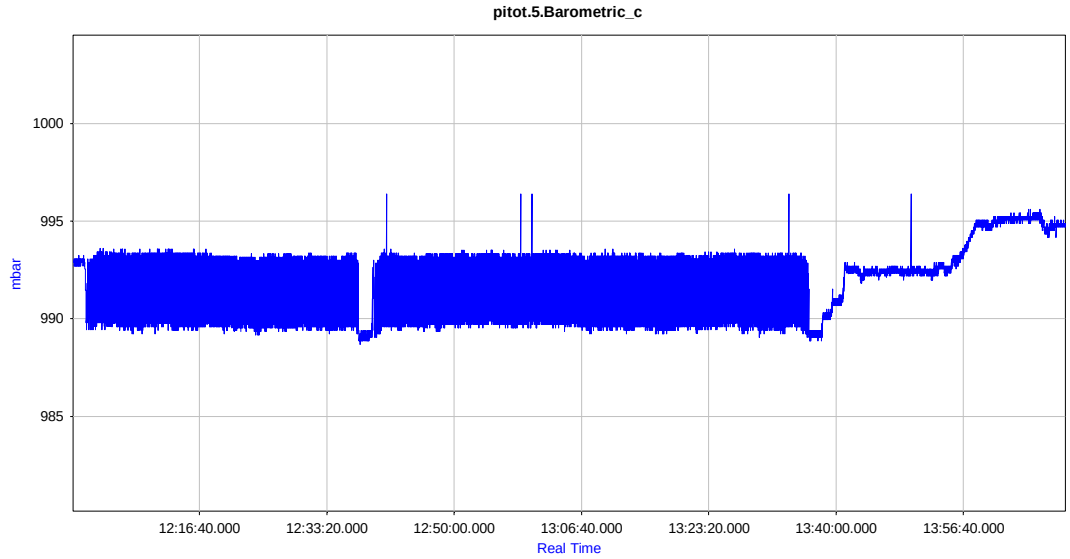

Figure 164 Barometric pressure among the cycles and when demounted

4.2.5 Results

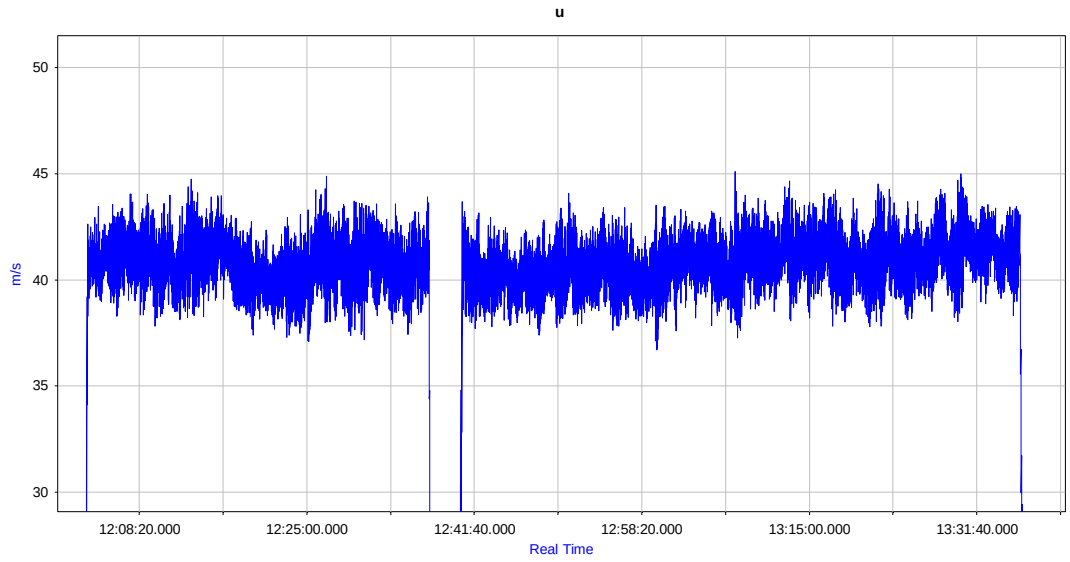

Figure 165 horizontal speed “u”

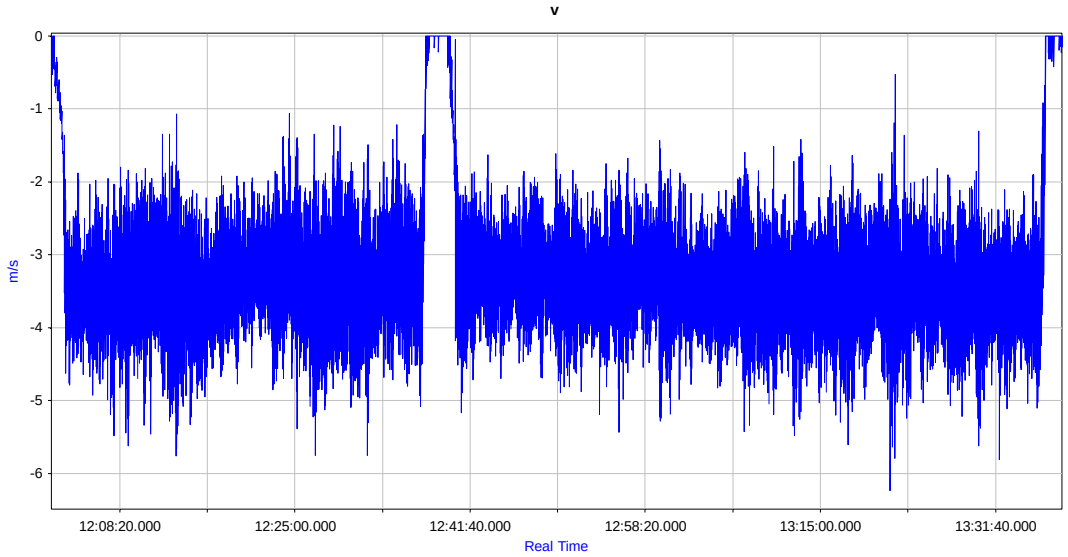

Figure 166 Speed in V direction

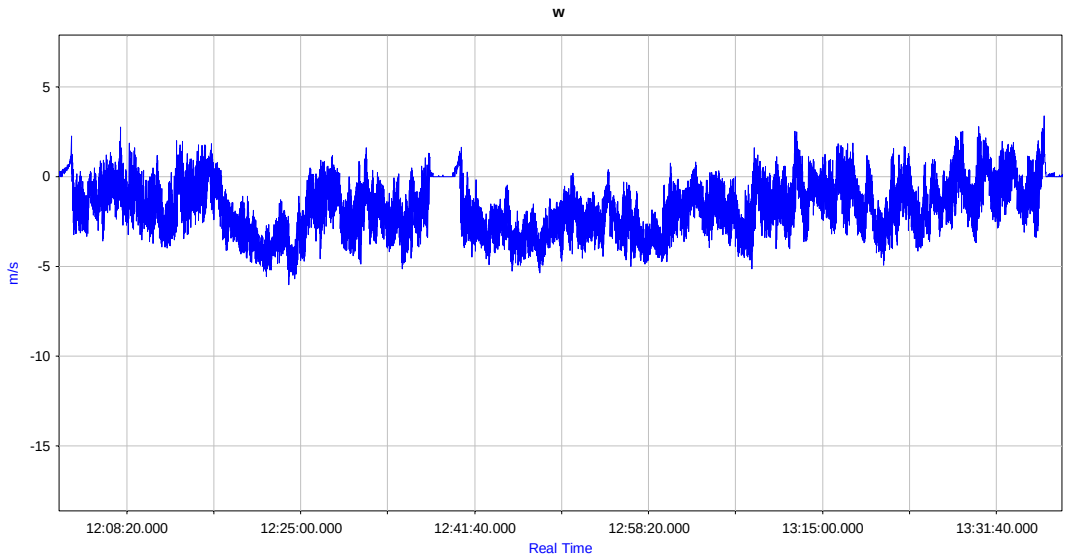

Figure 167 Speed in w direction

The angle of attack shows the characteristics sinusoidal behaviour, indeed getting an fft of the angle of attack shows there are more influences.

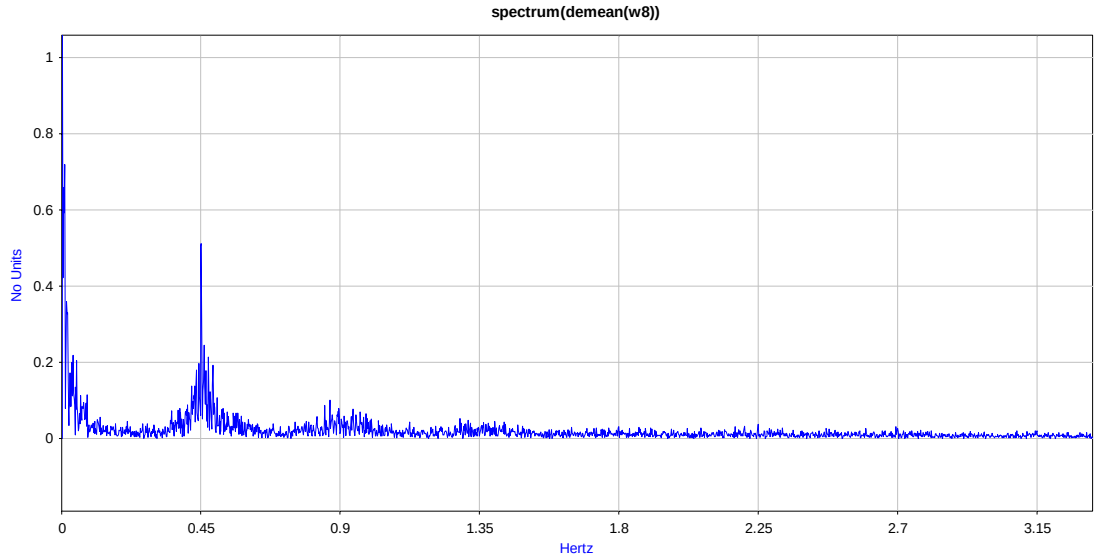

Figure 168 FFT from the alpha angle

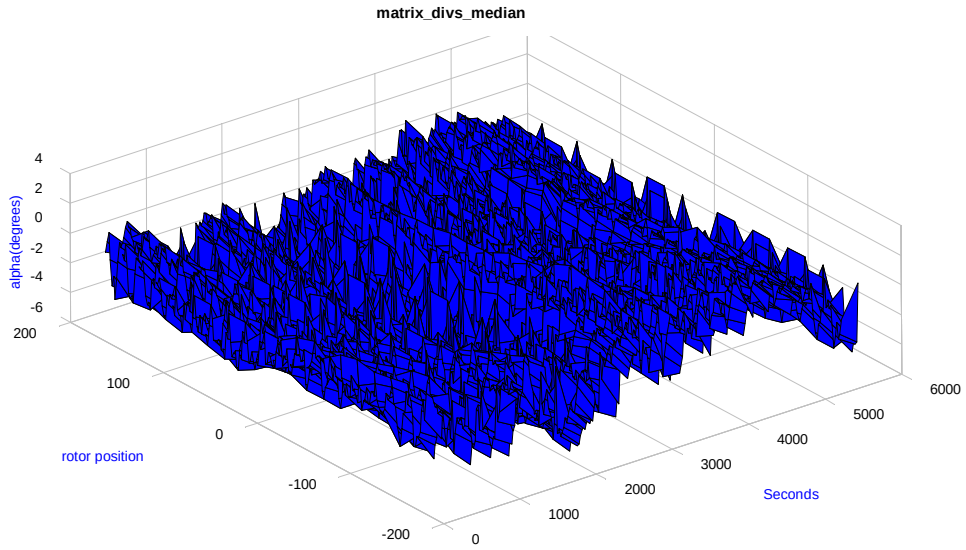

Figure 169 median result of the alpha value among several revolutions

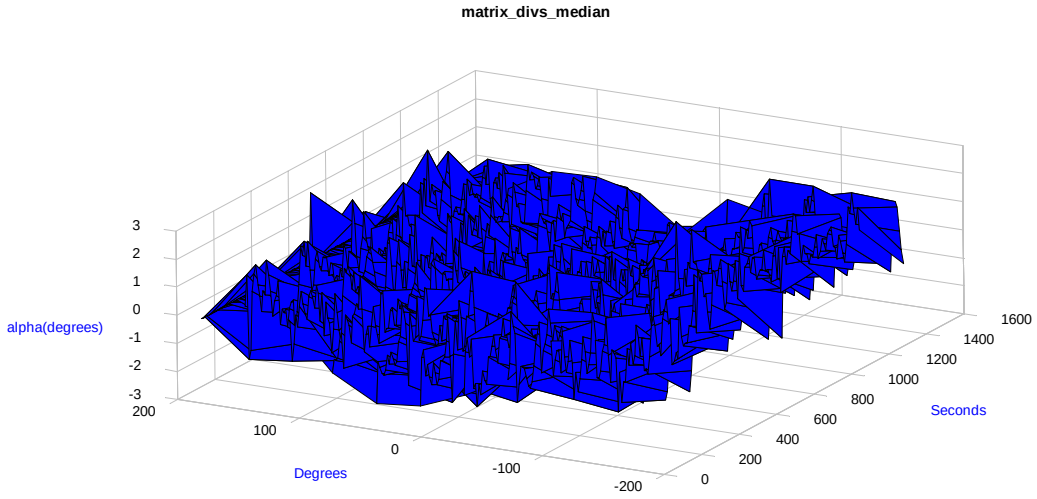

Figure 170 median result of the alpha de-trending the mean value per cycle. A sinusoidal shape seems to follow the rotor position

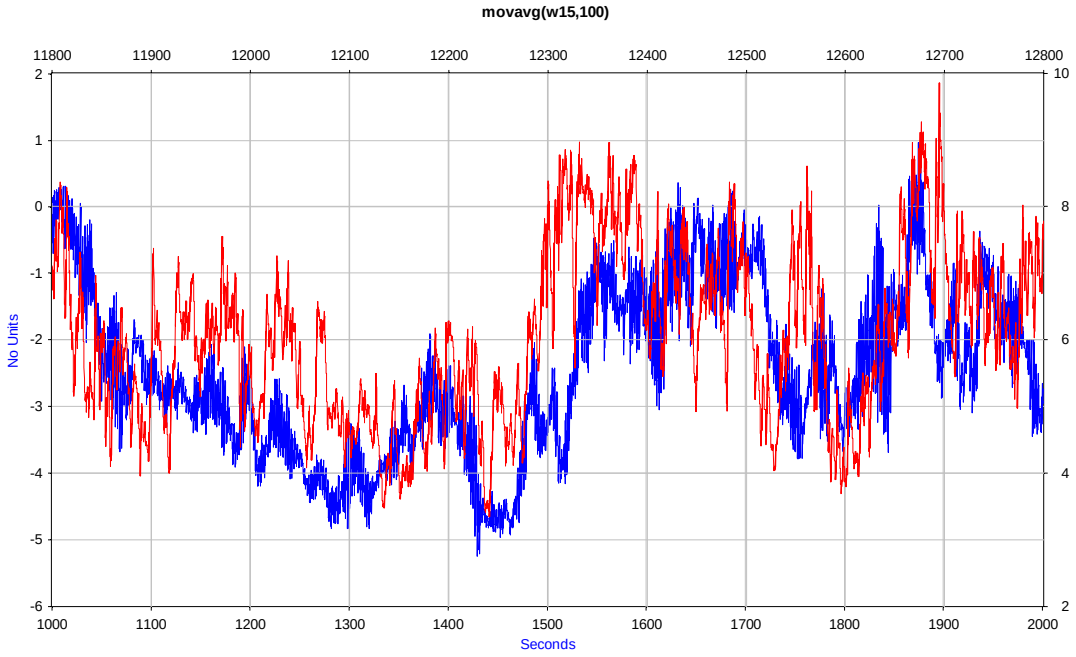

Figure 171 Comparisson of the w speed (blue) against the speed in the mast applying (red) in both terms a moving average of 1 second

Assuming a fixed rotor speed and a fixed angle of 15 degrees plues 10 degrees of misalignment.

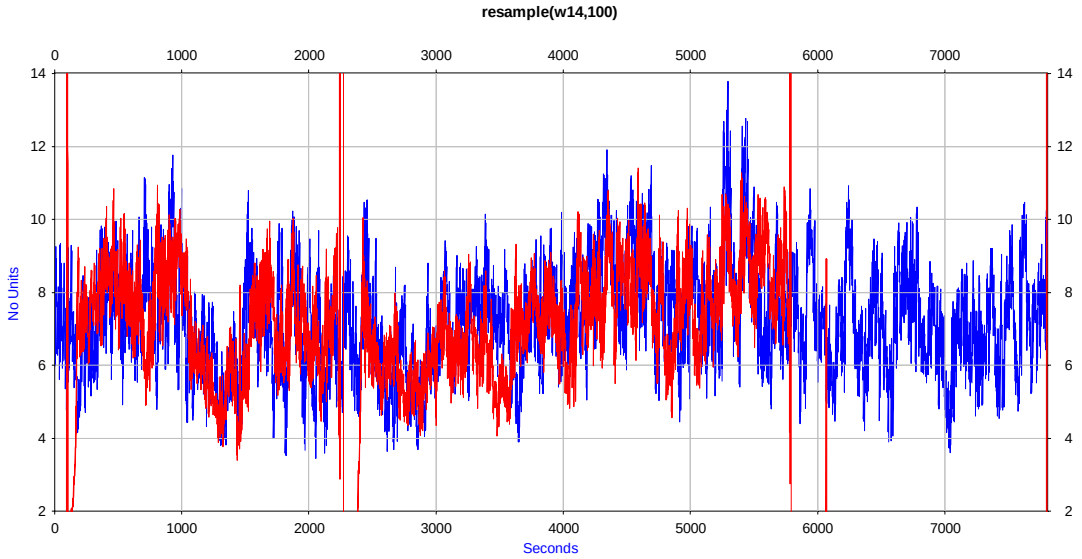

Figure 172 Comparison of the wind speed assuming certain parameters against the speed in the mast applying (blue). Both signals averaged to 1 second

4.3 Second Measurement campaign

The timing in this measurement campaign does not fit with the real time and besides did save in different timing among the measurement campaign per se. This was caused by a hardware error already corrected. Therefore on this measurement campaign is almost impossible to combine met mast measurements with on board measurements.

4.3.1 Turbine Measurements

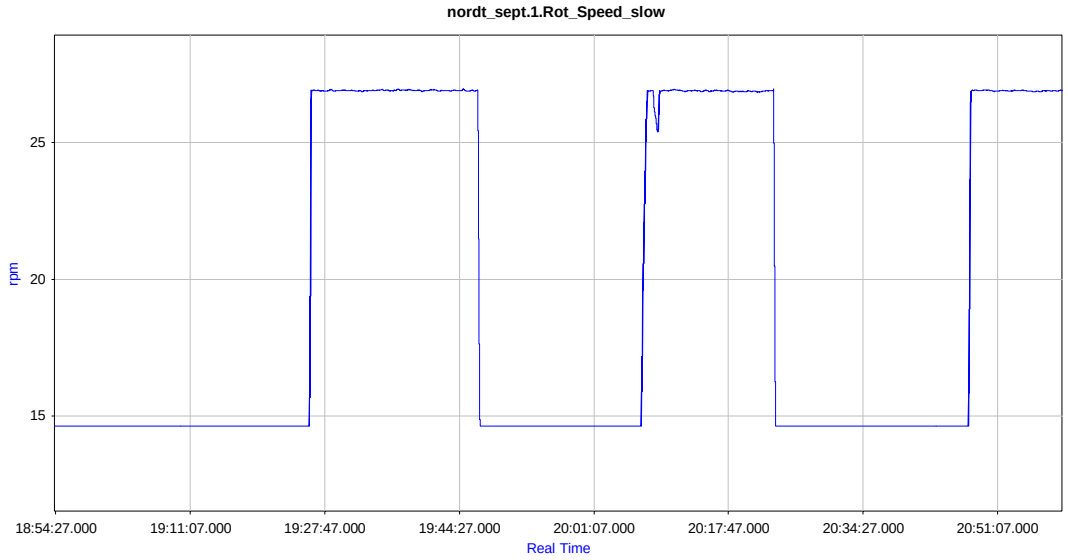

Figure 173 Rotor speed

4.3.2 Met Mast Measurements

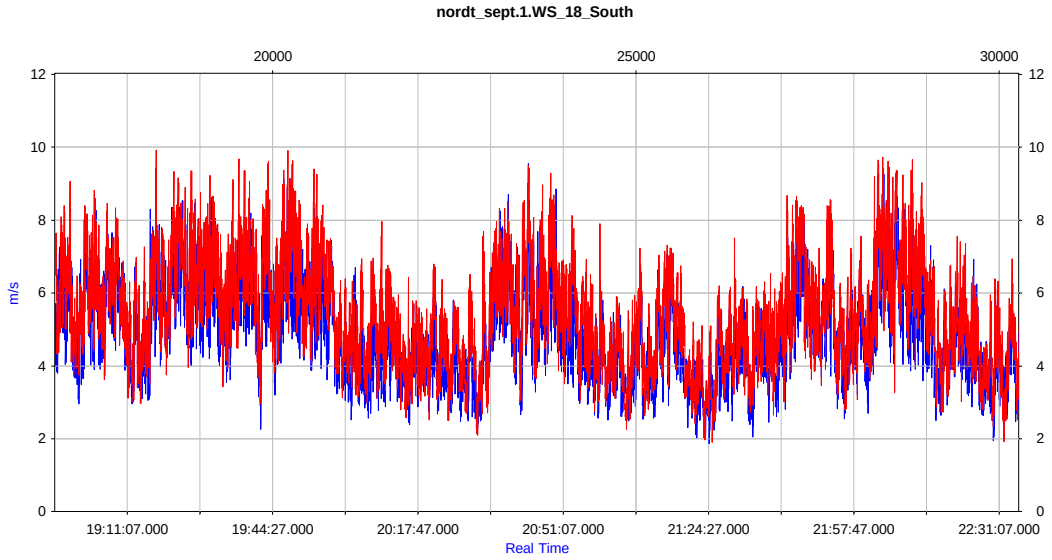

Figure 174 Wind speeds at two heights (18m and 36 m)

Atmospheric conditions

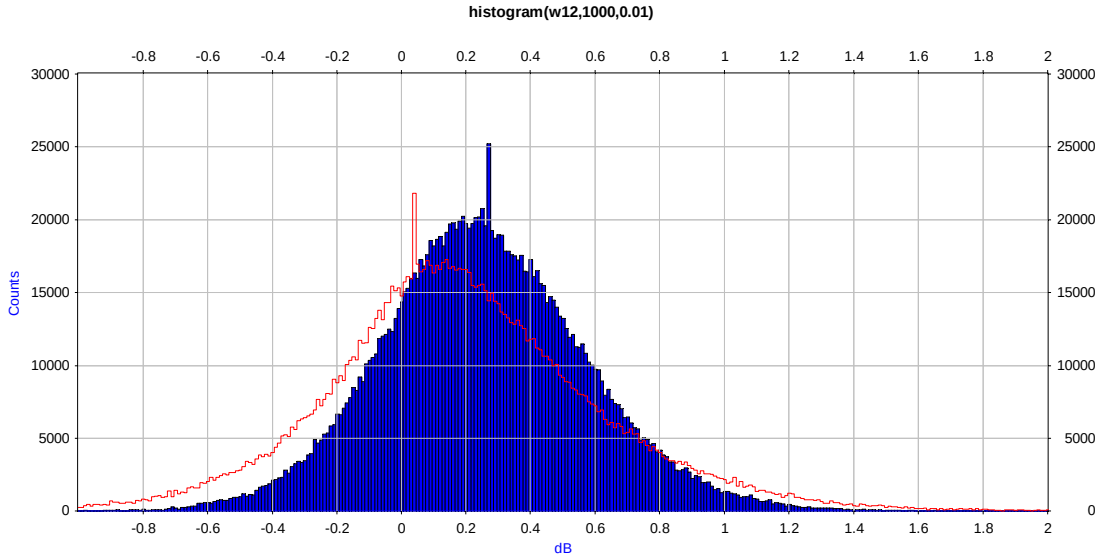

Figure 175 Distribution of the wind shear factors in the met mast at two heights 18 magl and 36magl, and between 36 magl and 54 magl

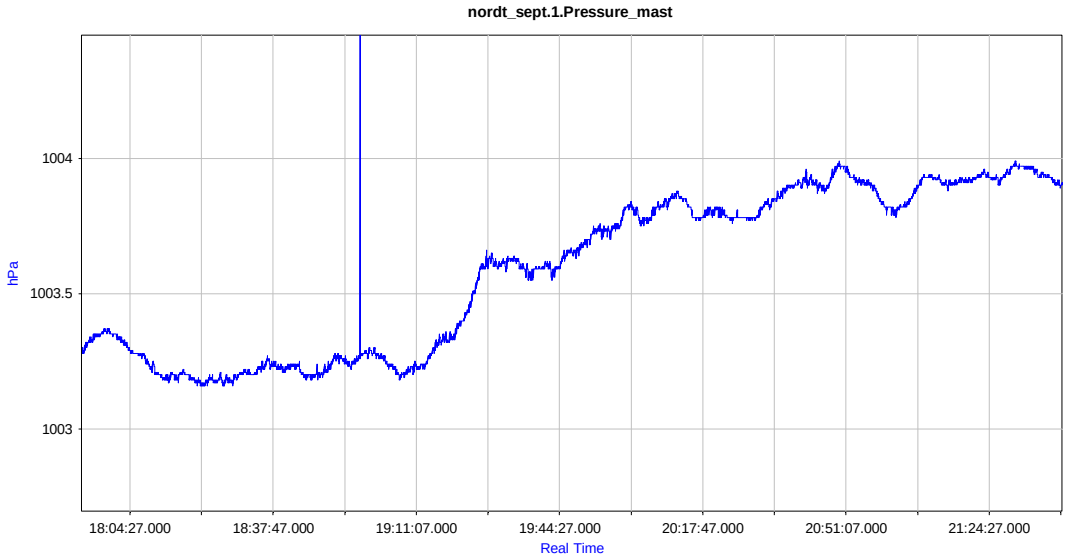

Figure 176 Air barometric pressure , Mean value: 1003.6 hPa

4.3.3 Pitot Measurements original signals

Raw signals overview

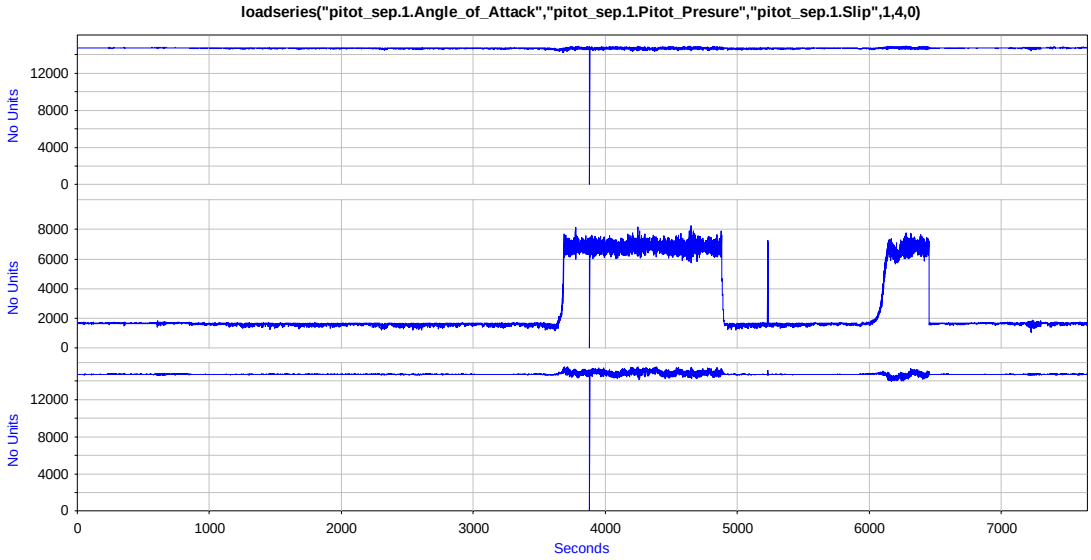

Figure 177 Pitot uncalibrated signals: pitot's pressures from up to bottom Angle of Attack, Slip and dynamic pressure

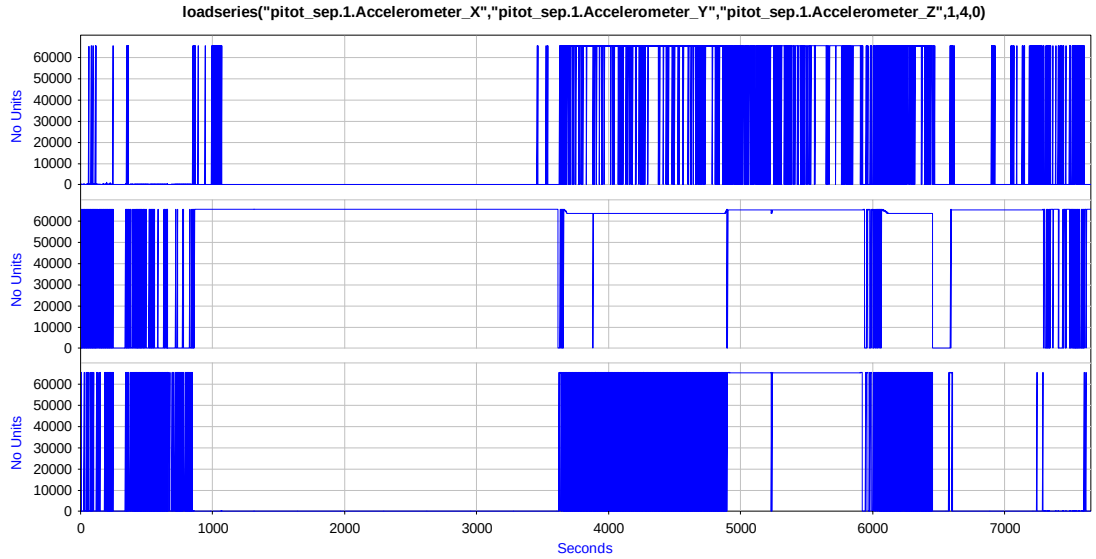

Figure 178 Accelerometers in the NI MyRio Data acquisition system, from top to bottom Z, Y and X

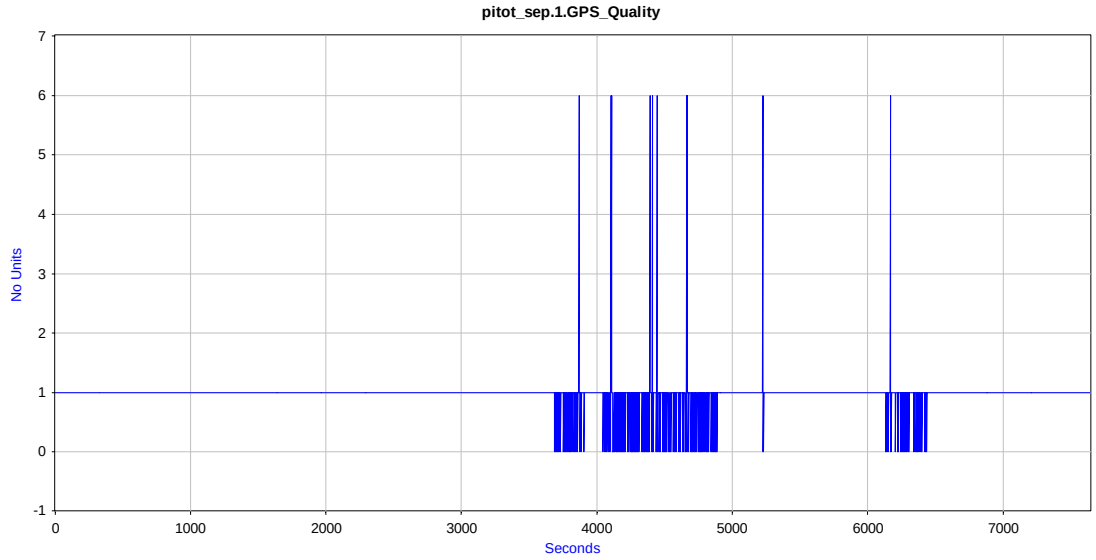

Figure 179 GPS quality signals

In the measurement campaign, the first period has being analysed.

4.3.4 Pitot Measurements processed and calibrated signals

The signals have being calibrated and checked with a post processing which is detailed in the annexure. The results are shown in the following plots.

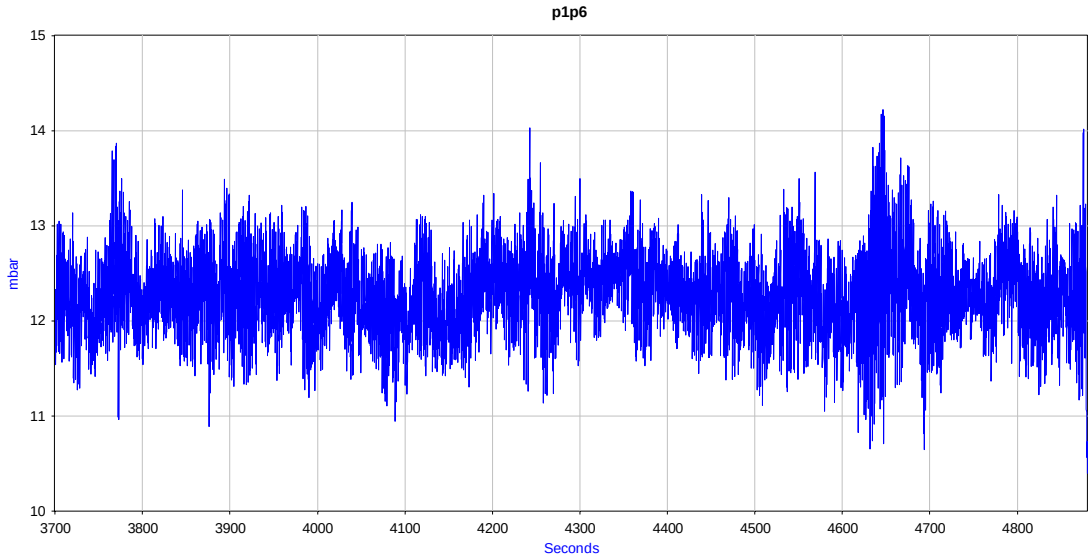

Figure 180 P16 pressure

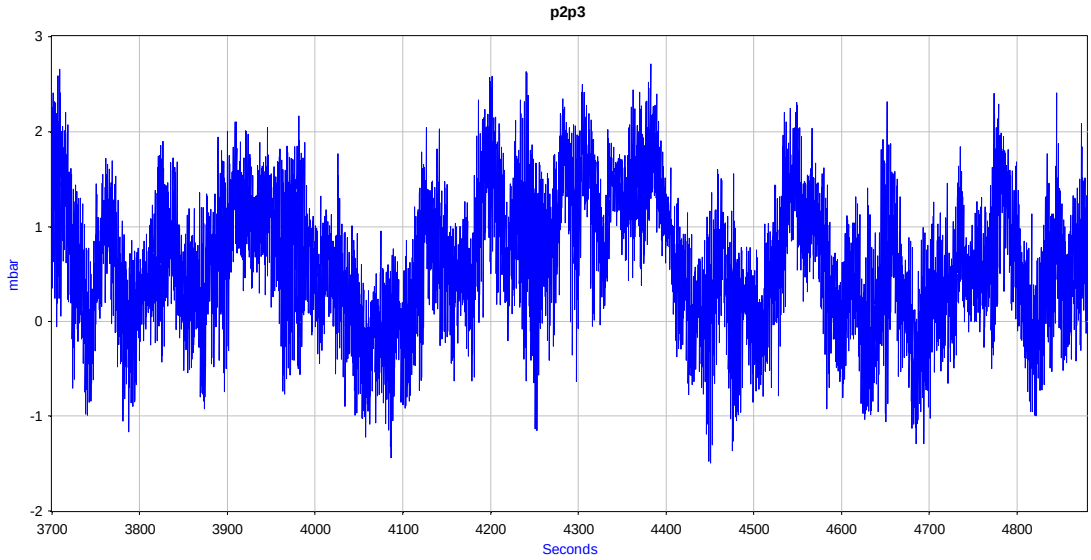

Figure 181 P23 pressure defined as angle of attack

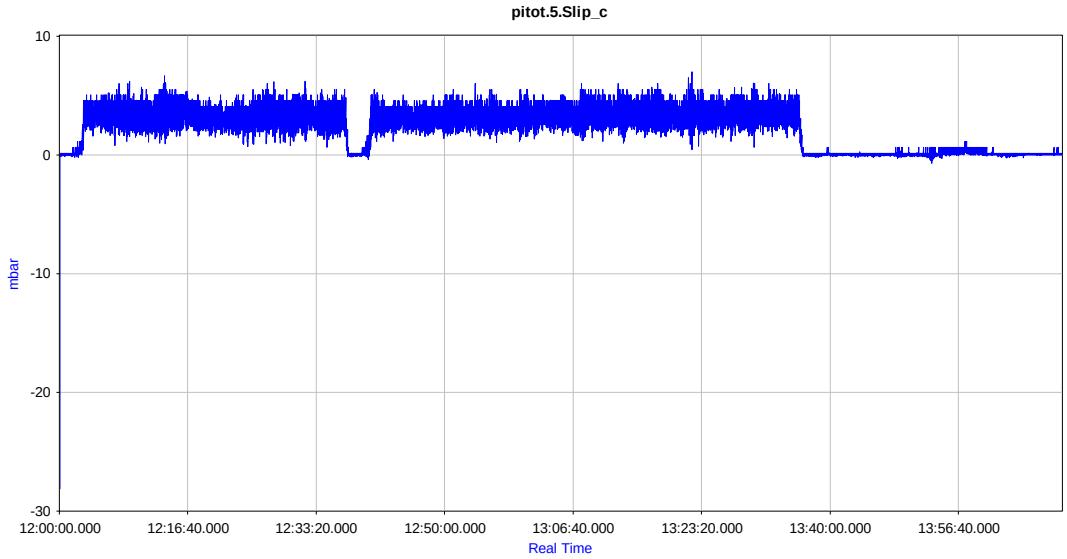

Figure 182 P45 Slip

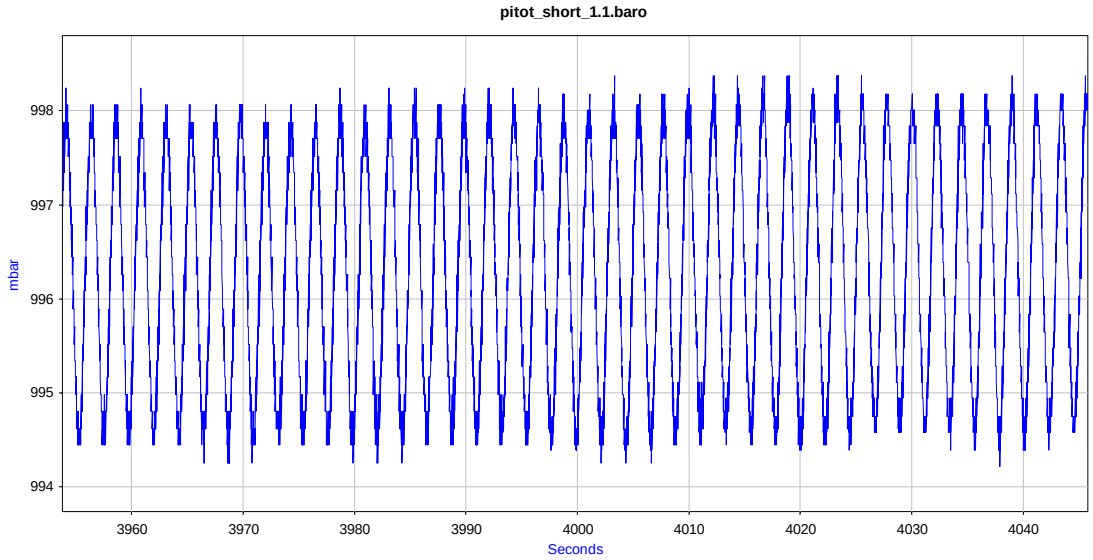

Figure 183 barometric pressure zoom

4.3.5 Results

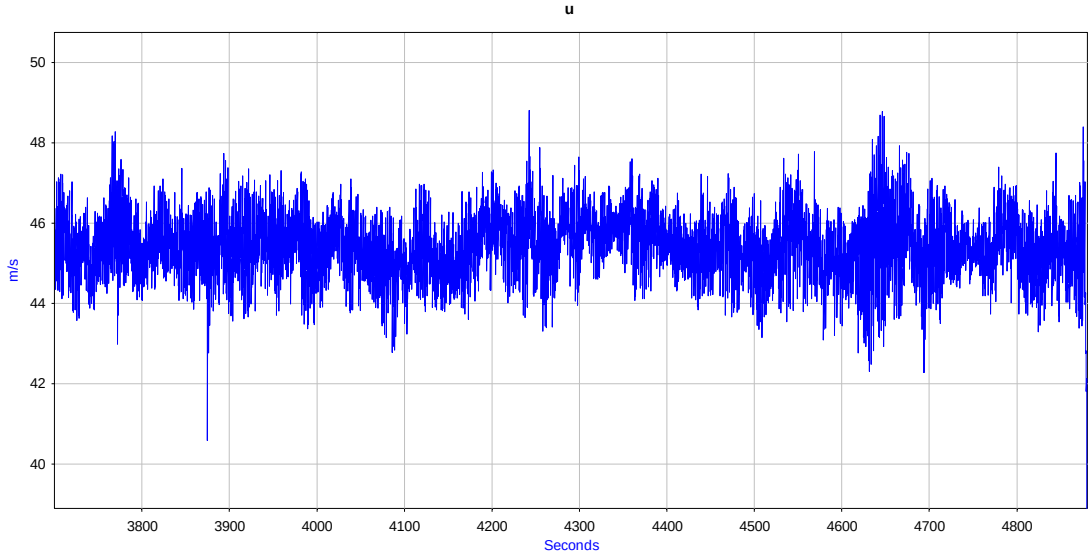

Figure 184 pitot speed Vx

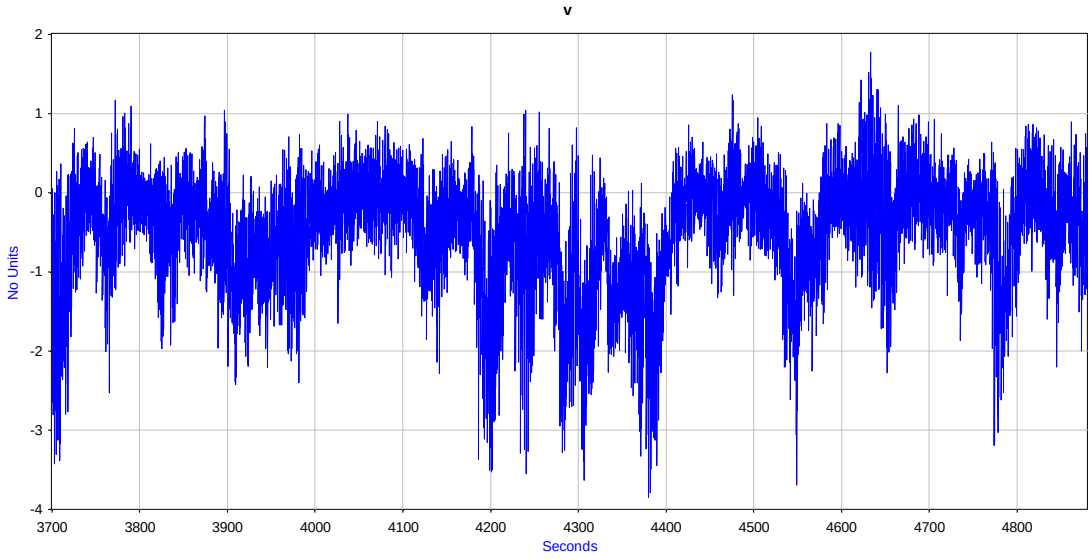

Figure 185 pitot speed Vy

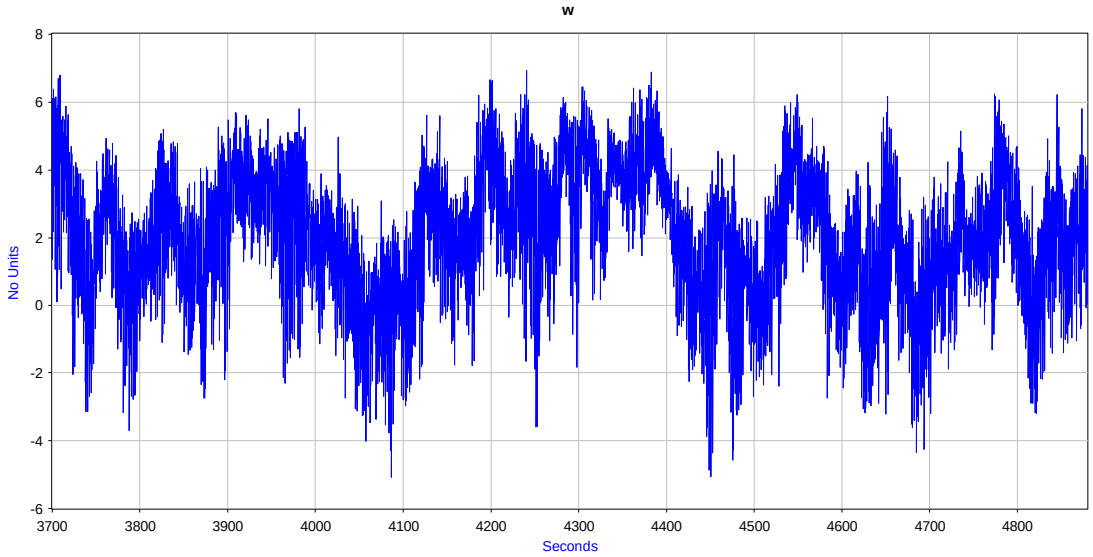

Figure 186 pitot speed Vz

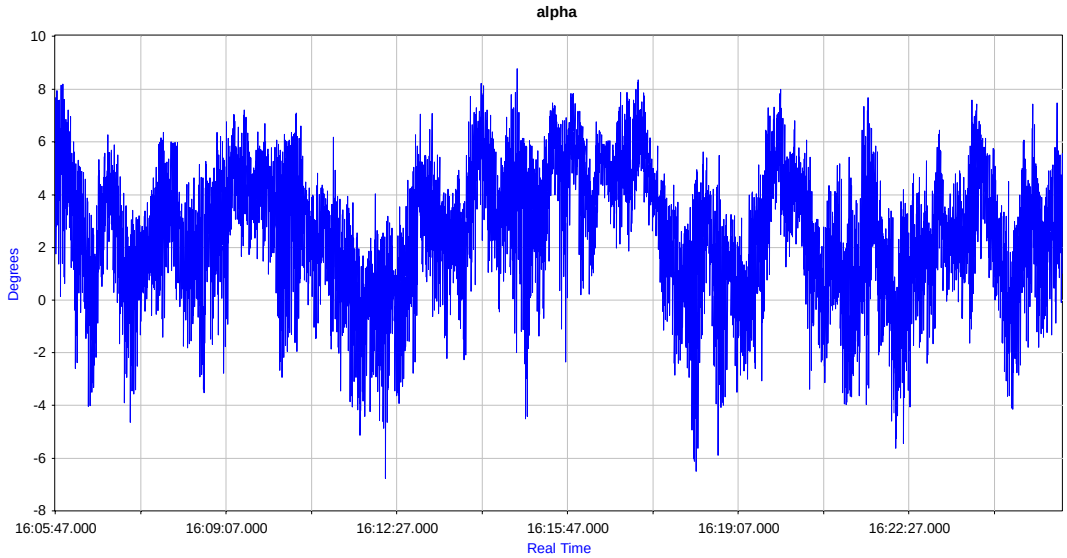

Figure 187 alpha

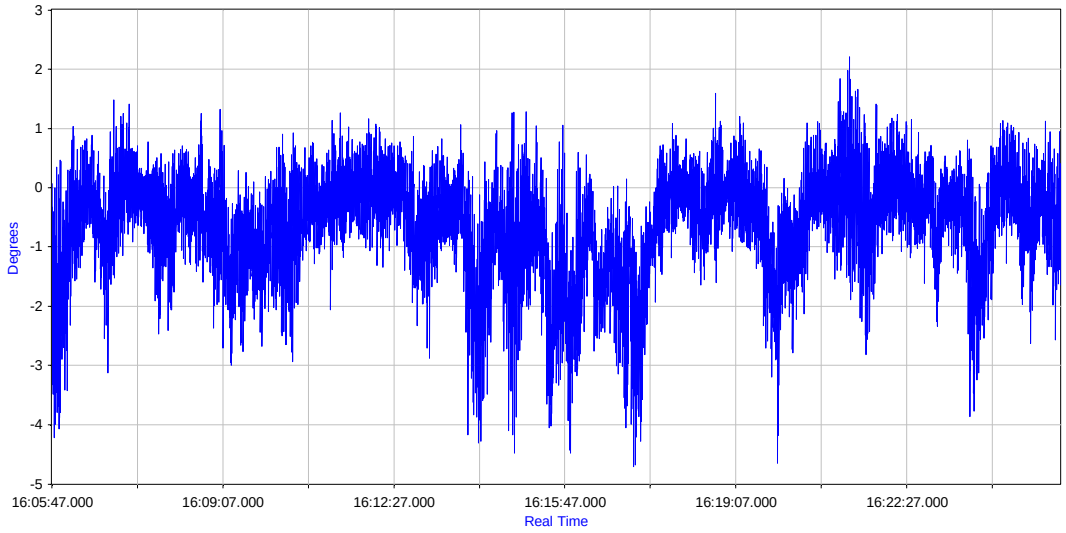

Figure 188 beta angle

Histograms

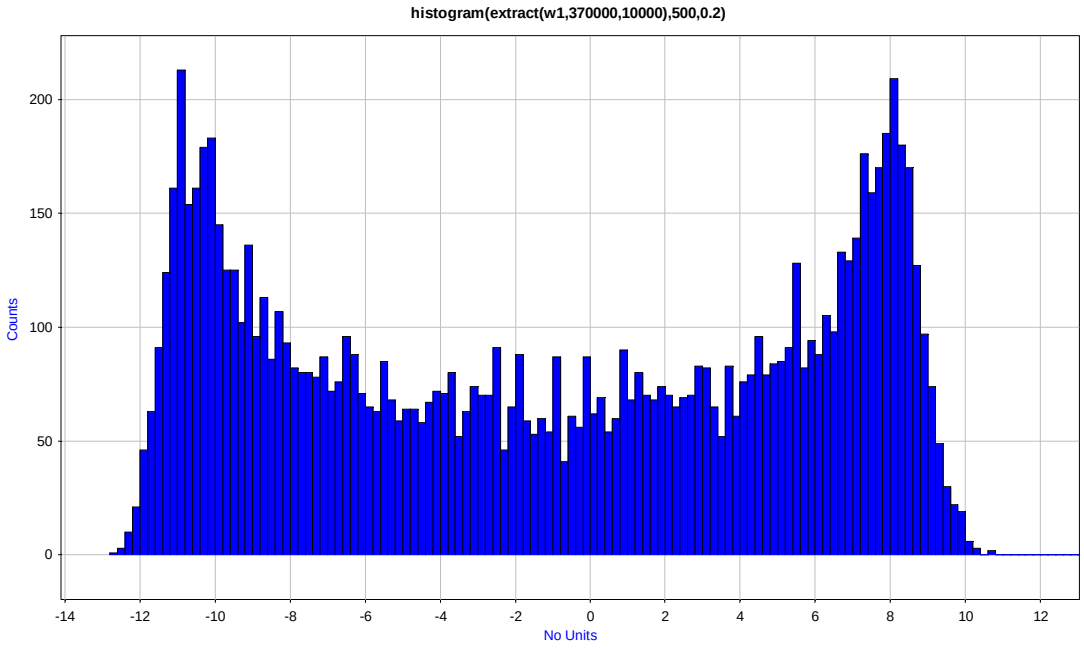

Figure 189 Distribution of the acceleration in x

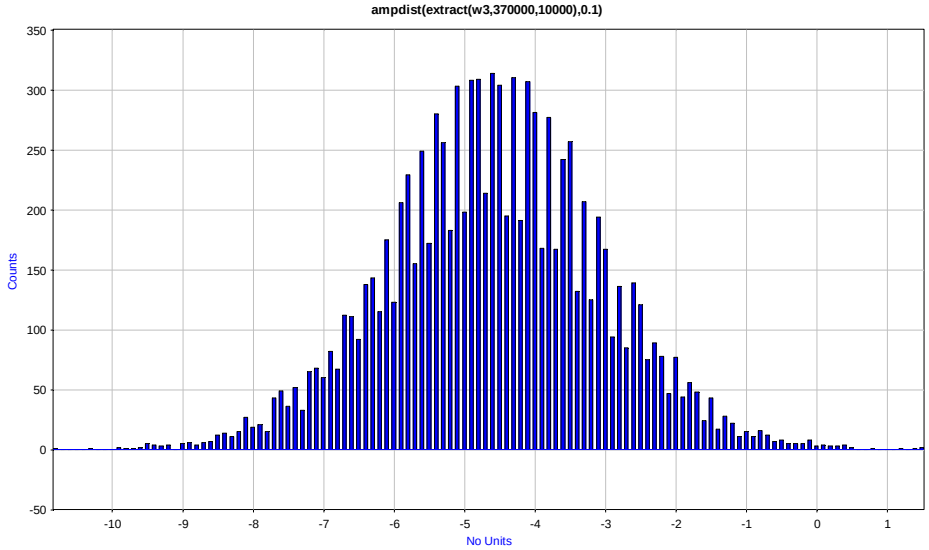

Figure 190 Distribution of the acceleration in z

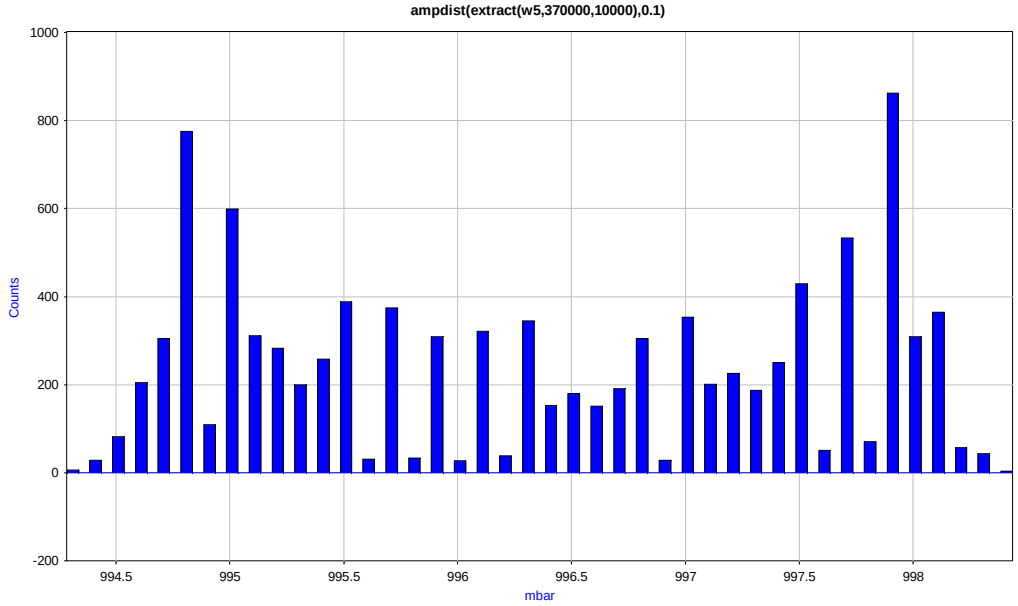

Figure 191 Distribution of the acceleration with barometric pressure

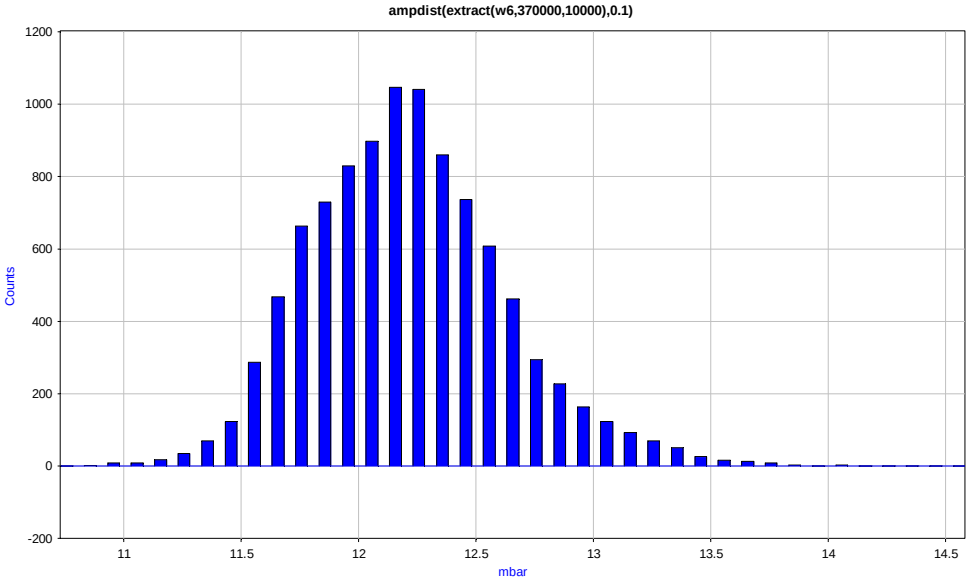

Figure 192 Distribution of the pitot pressure, median 12.24 mBar

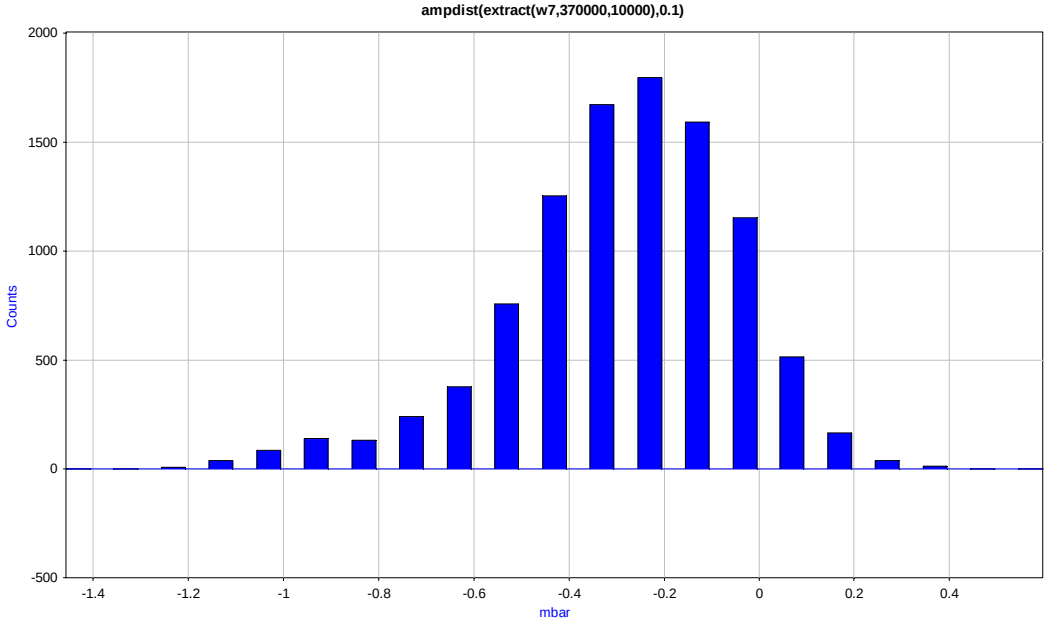

Figure 193 Slip, median -0.202189

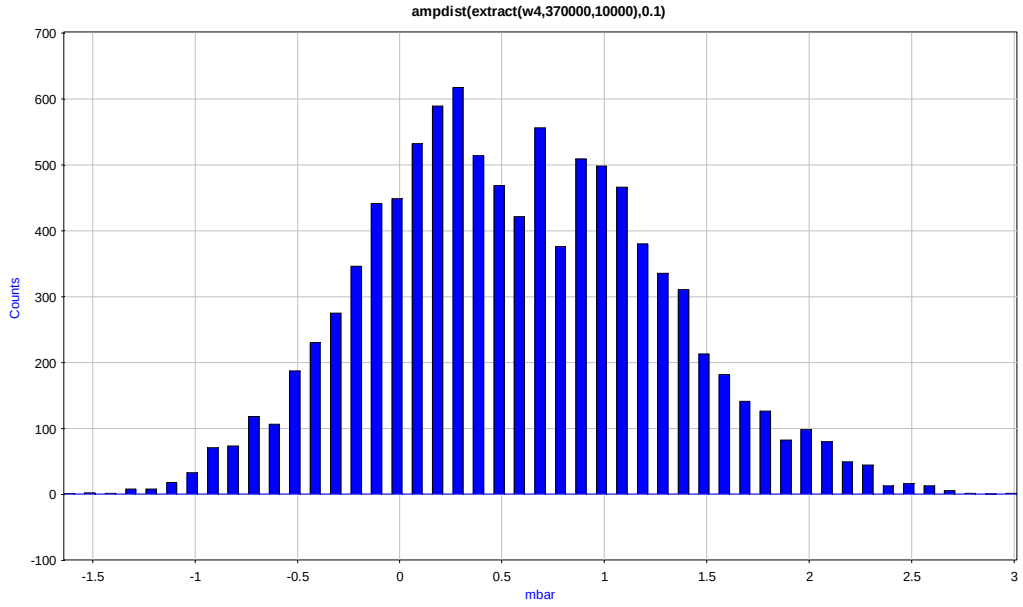

Figure 194 angle of attack, with median 0.568

In order to check the behavior of the speed on some divisions per cycle has being taken. On the vertical axis is represented the maximum peak found in a histogram of the mentioned series. In the y axis is represented the cycle in radians and in the x is the time. On this approach 10 seconds approach has being taken

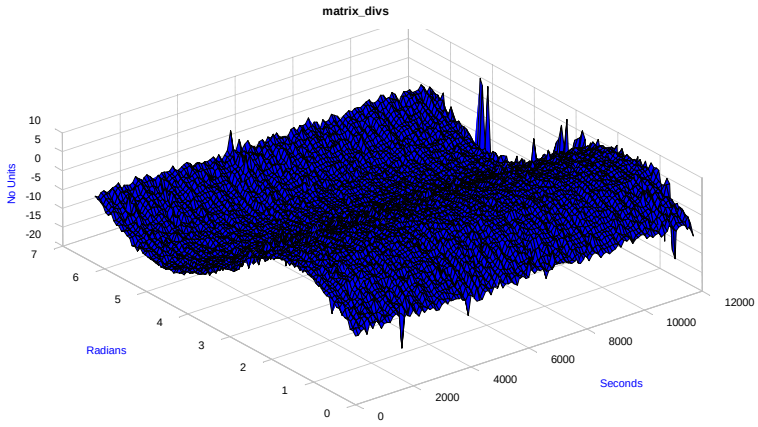

Figure 195 Maximum occurrence of the acceleration at value (Z) versus time (X) and position of the rotor (Y)

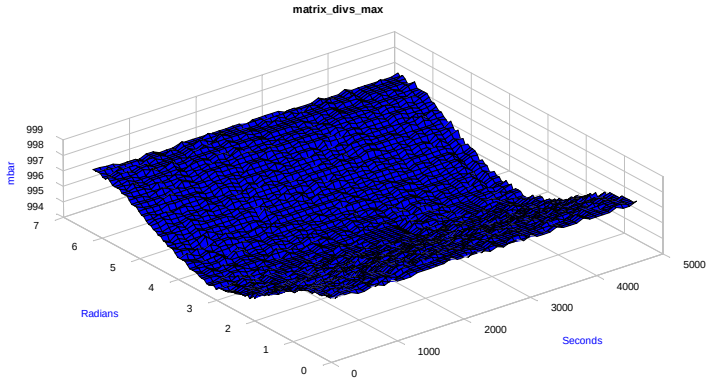

Figure 196 Same as before but with the barometric pressure

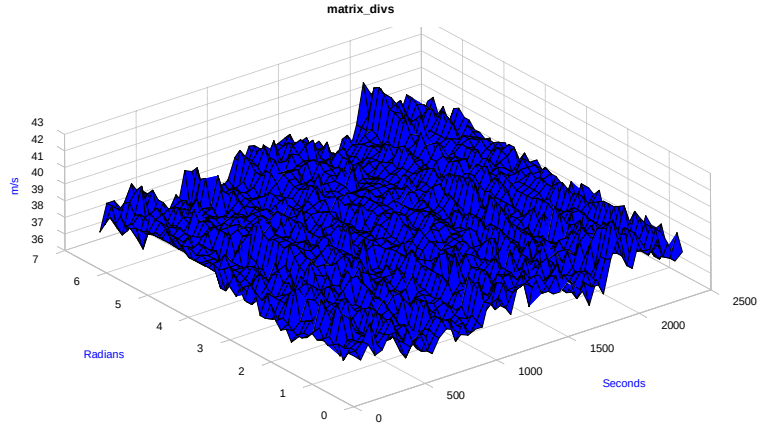

Figure 197 Maximum amplitude of the total speed (Z) versus time (X) and cycle (Y)

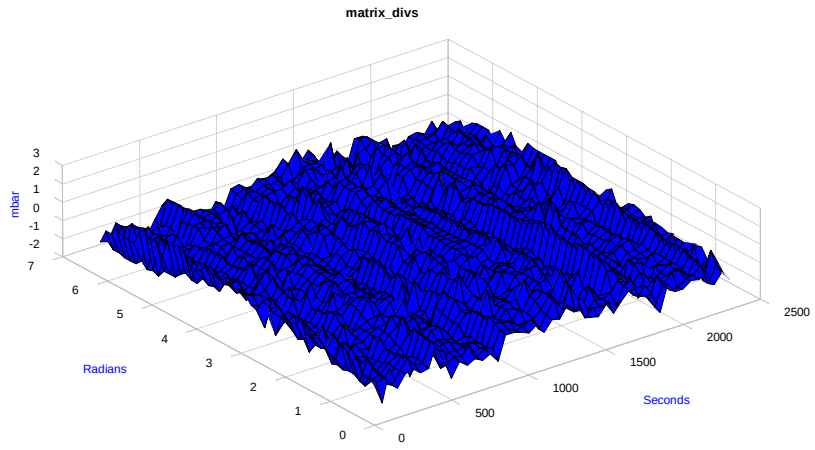

Figure 198 angle of attack

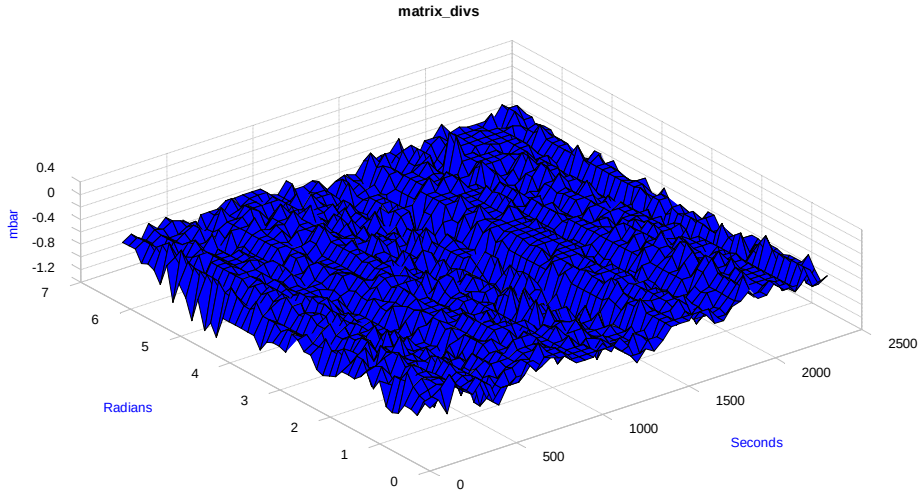

Figure 199 slip angle

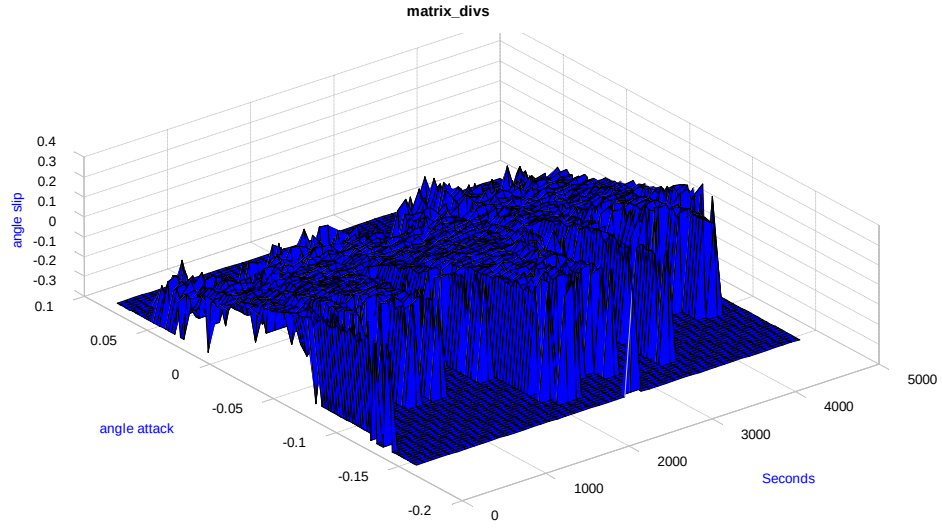

Figure 200 Relation between slip angle and angle of attack in time

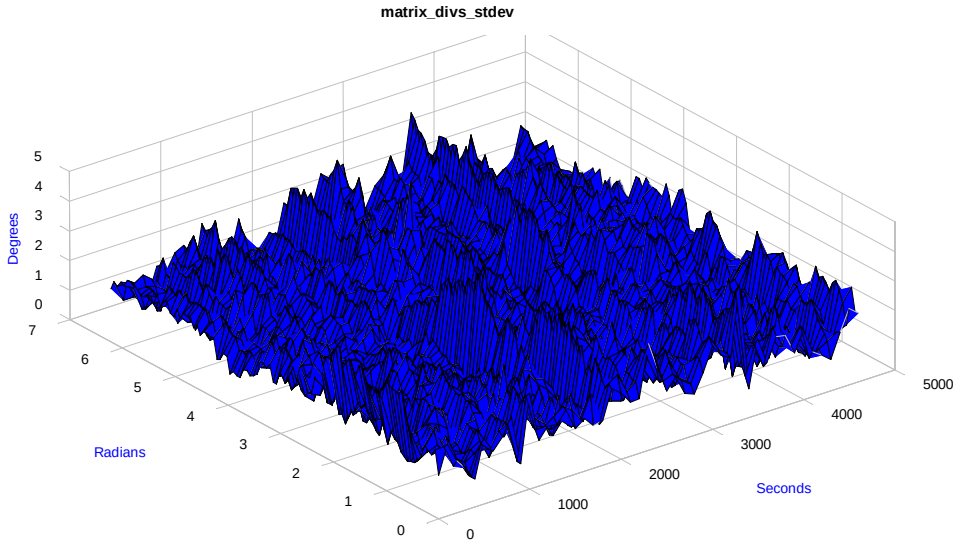

Figure 201 Standard deviation of the angle ρ

5. Evaluation on the results

5.1 Evaluation of the aerial sensor, installation, operation and maintenance

We have built and calibrated a special purpose wind tunnel for dry and non-dry air flow conditions, allowing us to calibrate the 5-hole pitot tube in dry air flows up to 90 m/s. The wedge type pitot head was calibrated, and it was found that the tube structure was rather flexible at 90 m/s, and therefore too soft. The tube was afterwards stiffened with a circular tube over the existing, so to be at least 10 times less flexible, but the redesigned tube was not calibrated in the wind tunnel. We made good experiences with the current flexible setup, which demonstrated an estimated uncertainty of about 1 deg(which was 10 times larger than expected, but we believe that 0.1 deg is reachable with the stiffer rod structure design).

We realised early in the project that the DELTA boards were delayed considerably, and that is why we used the NI MyRio data logger. The data logger takes measurements at a regular interval and immediately appends the time-stamped record to a file to ensure that data records are not lost in case of a power failure during the data logging session. The interfacing to the data logger was accomplished, and we operated the system with a battery power supply. With quite high power consumption of the Ni system, some 3 hours of data recordings were performed and saved on a memory stick.

We have investigated a robust system that is flexible and portable. We looked into the use of solar panels to be applied on the turbine blades without interfering with aerodynamics. The panels were found feasible for the purpose and available as on-the-shelf products, and we did not chase the idea for further development in this project. We also designed and built a small silent wind turbine for charging the on-board batteries and tested in the wind tunnel. We did not operate it on the wind turbine, because it was not weight optimised and hence it would likely cause a large centripetal force, and in the end safety issues for operation.

The NI data logger and interface system was installed in an aerial board enclosure, easily mounted with screws onto anchors glued to the rotor blade airfoil suction surface. The mounting requires normally a lift for access to the downward pointing rotor blade, or climbing gear so for the technician to reach the 75% blade span area and mount the board. The anchors can each hold shear up to 200 kg and can be easily grinded off surface, but the mounting and installation has to be further developed. Practical difficulties were experienced for the exercise of referencing the orientation and position of the sensors mounted on the board. The board was set in operation several times, and after taking it down and charging batteries, we had no difficulties in mounting and getting it into run in a new campaign.

Time synchronisation issue is non-trivial and remains a potential risk for no data if malfunction. The synchronisation works if the GPS (mounted on a wind turbine blade- it has to point with the signal active face towards the sky) can enable a satellite signal for time synchronisation. Experience shows difficulties in finding an on-the-shelf solution; the issue could be solved with a special purpose antenna enabling signals from several satellites. However the synchronisation has importance when we have to correlate signals from different positions in space, and study phenomena that vary over short time, e.g. variations within 10 degrees blade sector. One rotor revolution for the NTK 500 kW takes about 2.2 seconds, corresponding to a blade passage speed of 162 deg/s. By gathering 100 data per second, we can achieve to see variations. If now the time stamping jitters a second or even more when starting a new run,

causalities are hard to find. If we base our observations on a more statistical basis, for time periods of 10 minutes, a second or several does not matter for the precision. However, for the implementation of the idea of synchronisation, exact timing matters. The NI MyRio specs states exact timing within 0.1 seconds should be possible; however we did not implement 'exact' time stamping of the runs because of the arguments given before.

The delays experienced with manufacture and proof checking the DELTA data loggers did not give us enough time changing the data logger with the intended one, test it and operate this aerial sensor on the NTK 500 kW wind turbine.

5.2 Evaluation of the inflow wind vector (speed and angles)

The wind speed vector shown in Figure 179 gives a variation between 11 to 14 mBar, in Figure 180 the angle of attack varies between -1.5 mBar and + 2.5 mBar, in Figure 181 the Slip angle is recorded between roughly 3-7 mBar. The transducer show acceptable resolution of pressures in the 12bit analogue output resolution, if we consider also larger wind turbines to be tested. The 50 mbar pressure ranges of the pressure transducers are 2-2.5 times too large for capturing very details of the NTK 500 kW turbine inflow.

The calibrated signals reveal, that for the local speeds obtained in the pitot reference system, Vx the projection of the relative wind in the direction parallel to the pitot tube, is in the range 43-49 m/s, and Vy varies between -1 to +4 m/s, Vz between -5 and +7 m/s. As result, angle of attack varies in between -7° to +8°, and beta between -4.5 and +2, and beta between -4.5° and +2°. Further analysed were restricted, mainly due to uncertainties in determining angles. Additional analyses for deriving free wind were not made within this demonstration.

During the field campaigns, 71 10-minutes of data (118 hours) were collected in total-however a complete analysis was limited to some hours. The plot shown in Figure 45 on inflow demonstrates good correlation with wind turbine power and meets the expected outcome.

A statistical evaluation obtained on a database, say at least 3 weeks' time, would have been useful for plotting the power curve with the method.

6. Conclusion

Conclusion and recommendations

The acceleration experienced by the board is closely linked to the blade length and operating conditions of the wind turbine. In the present case, the NI inbuilt sensors are not adequate to monitor the sensor direction co-parallel with the board centripetal acceleration. Someone could place the board more inward to the hub of the turbine, allowing a lesser centripetal acceleration at the expense of less correlated rotor loading with inflow detected. The acceleration sensors experience in the flap and edgewise directions of the blade are monitoring combined effects such as motion differences as well as vibrations, and interpretation of wind and structural effects are hard to distinguish. For the accelerometer in the span wise blade direction, the NI on-board accelerometers are to be extended ±16g capability for NTK500 kW measurements.

The acceleration setup also allowed during installation of the board on the blade for a local dis-orientation of the sensors relative to the blade orientation planes. The difficult exercise of finding the position was done in this exercise, but it is complicated and needs further instrumentation with sensors to facilitate automatic position and orientation finding of the board and the pitot tube.

It is recommended to install a local, reference system on-board inertial sensor to supplement with directions and position of the sensor board and assist tracking the board.

For wind speeds 4-25 m/s, the speed range for a local observer at the 75% blade span Vx is about 40-50 m/s, which for the pitot dynamic pressure range requires about 1500 Pa(15 mBar). A formula for calculating inflow angles for a sphere shaped pitot head shows in this case, that the pressure range would ideally be ±6mBar. For other turbine sizes, at 90 m/s speed range, the pressure range would correspond to ±20mBar. For other shapes, no exact relations hold and calibration has to be done, as demonstrated here. We decided to adapt the transducers to the wind tunnel capacity of 90 m/s, and changed the pressure transducers setup from 25mBar to 50 mBar. The angle of attack measured ± 2.5 mBar and with the observed weather window, it was 1/20 of the setup pressure range. This has as shown some consequences on the resolution for our 500 kW test wind turbine, and less for MW wind turbines.

6.1 Summary

Several milestones mentioned in chapter 1 are achieved, with results on wind tunnel realisation and testing, and results from the aerial sensor board are reported in this report.
The board seems to be feasible for further development. Recommendations include adding functionalities such as monitoring tube position and orientations with blade, acceleration sensors orientation add on and a motion reference(INS) would improve the functionality and ease the use of the boards technology for operating the system in remote areas.
Exceptions for not meeting milestones are:
i)the new boards were not tested on the turbine as intended
ii)a data base capturing satisfactory statistics were not achieved, due to budgetary limitations and lift expenses

iii)the accuracy of the inflow device was approximately 1 deg instead of target uncertainty 0.1 deg
iv)Correlation of inflow with electric power of the wind turbine was made
vi)The use of SyncBoards are intended to be followed up in another ongoing project about noise from the NTK500 test wind turbine

In conclusion and with the exception for 2) as described by the project coordinator summarised in the following (https://nanosync.wordpress.com/2016/07/01/successful-field-test/):
"..
The nanosync demonstration board has been tested:
1. Against existing off-the-shelf precision synchronized systems provided by CIM A/S and has shown excellent absolute time alignment.
2. Successfully operated on an operating the Nordtank 500 test turbine blade at the DTU Department of Wind Energy in Risø, Denmark.
3. And validated the synchronization capabilities in practical (potato) field measurements using five microphones as seen above.
.."

6.2 Recommendations

The work here comprised has involved several areas of expertise. On each some recommendations needs to be addressed to improve the quality of the results for the future

6.2.1 System Hardware

The hardware can be considered in two terms: mechanical and electrical

Mechanical

Whenever the design of the casing changes it has to be considered several main characteristics:

- Casing:
  - It needs an aerodynamic profile
  - It should be allocated in the suction side of the blade.
  - The pitot would be allocated outside positioning the angle of attack that must be estimated for the range of speeds of the turbine and within ±10 degrees
- Heat conduction:
  - The design must allow an easy heat exchange with the outside
- Shield
  - The GPS positioning system should be tested with the casing
- Weight
  - It should not over exceeded a limit of 2 Kgs

Electrical

On the hardware side it will be beneficial to get the data transfer via wireless. The system is a complete electrical system without noise interference. The challenge of limited time on power supply needs development /implementation of power harvesting.

Pressure transducers

There is a need of pressure upscaling, i.e. incrementing the range, if the device will measure on a VAWT. It shall be reached at least 35 mBar, pressure measurement which belongs to a speed of ~70m/s. Nevertheless this range will be never covered by the p23 and p45 pressure transducers which may be adjusted to smaller ranges

Whenever used i2c protocol, configure the hardware in order to have different addresses. Nowadays in the second phase the i2C protocol was implemented through the Field Programmable Gate array avoiding this particular problem.

GPS

The GPS signal should be acquired with the same sensor. But it shall be foreseen that whenever the signal is lost, the system will use a parallel timing. If this happens an internal trigger must be activated.

Temperature

The temperature signal must be inside of the casing and if possible must be calibrated on different speeds. It is important to check the signal in the laboratory prior to perform any test.

Protocol signals

It would be beneficial to have the I2C port architecture for the hardware

6.2.2 System Energy Harvesting

It is recommended to use solar panels as main system. In case it is not possible the Archimedes screw or some other element can be installed, but redesigned for lesser weight. Whenever possible it is recommended to extract the energy from the turbine via cabling.

6.2.3 System pitot

It is recommended to increase the stiffness of the bar, using a parallel carbon rod or either changing the profile. This was done towards the end of project time, but we could not perform a new calibration with this design in the wind tunnel. The 5 hole pitot is definitively good for stall turbines and it can reach the goal for most regimes in pitch controlled turbines. Nevertheless it could be convenient for other turbines, vertical, or either in other operational mode, to get a wider range for the angle of attack. On this specific subject using a 7 hole pitot could be definitely beneficial.

6.2.4 Software

Dadisp™ software package v6.7was used to analyse the time series

6.2.5 Calibration procedures: blower

The wind tunnel facility has showed to provide results in agreement with objectives. However the instrumentation used for monitoring and investigating flow quality (temperature and pressure) has to be designed and implemented as a stationary system. For rods, vertical and horizontal reference planes this stationary rule also has to be applied.

References

Bak, C. H. (2010). *DANAERO MW: Measurement campaigns on the NM80 2.3MW wind turbine at Tjæreborg 2009.* Risø Na-tional Laboratory for Sustainable Energy, Technical University of Denmark, Roskilde, Denmark.

Doolan, C. J. (2007). Numerical Evaluation of Contemporary Low-Speed Wind Tunnel Contraction Designs. *Journal of fluids Engineering*.

Gracey, W. (1980). *Measurement of Aircraft Speed and Altitude.* NASA.

Giebel G., Paulsen U. S. (May 2009). Autonomous Aerial Sensors for Wind Power Meteorology. *researchgate* .

Madsen H, A. (1988). Experimental Investigation of Horizontal-Axis Wind Turbine Aerodynamics in Natural Conditions. *Brussels: Commission of the European Communities.*

Helgesen, K. O., Hansen, K. S., Paulsen, U. S., & Sørensen, P. E. (2008). Wind Turbine Measurement Technique—an Open Laboratory for Educational Purposes. *Wind Energy, Vol. 11*, 281-295.

Christensen L. S., M. J. (2007, November). GPS Synchronized high voltage measuring system.

Appendix A

A.1. Uncertainties: Blower uncertainty calculation

Blower pressure uncertainty

The wind speed calibration of the 5-hole pitot is performed by carrying out a measurement of the dynamic pressure with the reference of the pressure obtained over the contraction. The sensor with sensor head is installed at the position in the symmetry line of the flow 1.5 D behind the nozzle exit.

The speed obtained at this point is assumed to be the same as measured with the Prandtl tube at the same position at the different contraction pressure differences, providing a linear function equivalent to

$$\zeta_{x,y,z,frequency} = \frac{q_{prandtl}}{q_{contraction}}(x, y, z, frequency) + \zeta_{offset}$$

Here it can be also extracted that $\zeta_{x,y,z,frequency}$ is a dimensionless term normalized that can be decomposed in two different terms

$$\zeta_{x,y,z,frequency} = \zeta_{x,y,z} * \zeta_{frequency} + \zeta_{offset}$$

The point where the system was calibrated: 1.5D at a converter frequency of 70Hz
Then the standard deviation is this expression (variables are correlated) and taking the uncertainty based on the point per se measured:

$$u^2_{\zeta_{x,y,z,frequency}} = \sum_{i=x,y,z....}^{N} \left(\frac{\partial \zeta_{x,y,z,frequency}}{\partial x_i}\right)^2 + 2 \cdot \sum_{i=x,y,z....}^{N} \sum_{i=x,y,z....}^{N} \left(\frac{\partial \zeta_{x,y,z,frequency}}{\partial x_i}\right) \cdot \left(\frac{\partial \zeta_{x,y,z,frequency}}{\partial x_i}\right) \cdot u^1_{x_i} \cdot u^1_{x_j} \cdot r_{ij}$$

There are no correlation between x, y and z in positions, and this is mainly why the terms have not being given, thus $r_{x,y} = 0$;
$r_{z,y} = 0; r_{z,x} = 0; r_{frequency,x} = 0; r_{frequency,y} = 0; r_{frequency,z} = 0; r_{x,qcontraction} = 0; r_{y,qcontraction} = 0; r_{z,qcontraction} = 0$

Then

$$u^2_{\zeta_{x,y,z,frequency}} = \left(\frac{\partial \zeta_{x,y,z,frequency}}{\partial q_{prandtl}}\right)^2 \cdot u^2_{q_{prandtl}} + \left(\frac{\partial \zeta_{x,y,z,frequency}}{\partial x}\right)^2 \cdot u^2_x + \left(\frac{\partial \zeta_{x,y,z,frequency}}{\partial y}\right)^2 \cdot u^2_y + \left(\frac{\partial \zeta_{x,y,z,frequency}}{\partial z}\right)^2 \cdot u^2_z + \left(\frac{\partial \zeta_{x,y,z,frequency}}{\partial freq}\right)^2 \cdot u^2_{freq} +$$

$$\left(\frac{\partial \zeta_{x,y,z,frequency}}{\partial q_{contraction}}\right)^2 \cdot u^2_{q_{contraction}} + 2 \cdot \left(\frac{\partial \zeta_{x,y,z,frequency}}{\partial q_{prandtl}}\right) \cdot \left(\frac{\partial \zeta_{x,y,z,frequency}}{\partial x}\right) \cdot u^1_x \cdot u^1_{q_{prandtl}}$$
$$\cdot r_{x,qprandtl} + 2 \cdot \left(\frac{\partial \zeta_{x,y,z,frequency}}{\partial q_{prandtl}}\right) \cdot \left(\frac{\partial \zeta_{x,y,z,frequency}}{\partial y}\right) \cdot u^1_y \cdot u^1_{q_{prandtl}} \cdot r_{y,qprandtl}$$
$$+ 2 \cdot \left(\frac{\partial \zeta_{x,y,z,frequency}}{\partial q_{prandtl}}\right) \cdot \left(\frac{\partial \zeta_{x,y,z,frequency}}{\partial z}\right) \cdot u^1_z \cdot u^1_{q_{prandtl}} \cdot r_{z,qprandtl} + 2$$
$$\cdot \left(\frac{\partial \zeta_{x,y,z,frequency}}{\partial q_{contraction}}\right) \cdot \left(\frac{\partial \zeta_{x,y,z,frequency}}{\partial freq}\right) \cdot u^1_{contraction} \cdot u^1_{frequency}$$
$$\cdot r_{contraction,frequency} + 2 \cdot \left(\frac{\partial \zeta_{x,y,z,frequency}}{\partial q_{prandtl}}\right) \cdot \left(\frac{\partial \zeta_{x,y,z,frequency}}{\partial freq}\right) \cdot u^1_{prandtl}$$
$$\cdot u^1_{frequency} \cdot r_{prandtl,frequency} + 2 \cdot \left(\frac{\partial \zeta_{x,y,z,frequency}}{\partial q_{prandtl}}\right) \cdot \left(\frac{\partial \zeta_{x,y,z,frequency}}{\partial q_{contraction}}\right)$$
$$\cdot u^1_{q_{contraction}} \cdot u^1_{q_{prandtl}} \cdot r_{prandtl,contraction}$$

Positive correlations will be assumed =1 and negative -1, i.e. wort case scenario

- As far away for the center the pressure will be reduced:

  - $r_{x,qprandtl} = -1$
  - $r_{y,qprandtl} = -1$
  - $r_{z,qprandtl} = -1$

As higher is the frequency or the contraction pressure, much higher will be the pressure in the Prandtl tube:

  - $r_{prandtl,frequency} = 1$
  - $r_{contraction,frequency} = 1$
  - $r_{prandtl,contraction} = 1$

At 1.5D, the functions were also determined:

$$\zeta_{x,y,1.5D} = 1.066 - 0.01466 \cdot x - 0.026 \cdot x^2 - 0.006584 \cdot y - 0.0232 \cdot y^2$$

And

$$\zeta_{0,0,zD} = 0.9927 - 0.0002327z - 0.0006238 \cdot z^2$$

Then

$$\left(\frac{\partial \zeta_{x,y,z,frequency}}{\partial y}\right) = -0.006584 - 0.0464 \cdot y$$
$$\left(\frac{\partial \zeta_{x,y,z,frequency}}{\partial x}\right) = -0.01466 - 0.053 \cdot x$$
$$\left(\frac{\partial \zeta_{x,y,z,frequency}}{\partial z}\right) = -0.0002327 - 0.0012476 \cdot z$$

The converter has a quite accurate frequency conversion i.e.

$$u^2_{freq} \approx 0$$

Then it is clear

$$u^2_{\zeta_{x,y,z,frequency}} = \left(\frac{1}{q_{contraction}}\right)^2 \cdot u^2_{q_{prandtl}} + (-0.01466 - 0.053 \cdot x)^2 \cdot u_x^2 + (-0.006584 - 0.0464 \cdot y)^2 \cdot u_y^2 + (-0.0002327 - 0.0012476 \cdot z)^2 \cdot u_z^2 + \left(-\frac{q_{prandtl}}{q_{contraction}{}^2}\right)^2 \cdot u^2_{q_{contraction}} + 2 \cdot \left(\frac{1}{q_{contraction}}\right) \cdot (-0.01466 - 0.053 \cdot x) \cdot u_x^1 \cdot u^1_{q_{prandtl}} \cdot r_{x,qprandtl} + 2 \cdot \left(\frac{1}{q_{contraction}}\right) \cdot (-0.006584 - 0.0464 \cdot y) \cdot u_y^1 \cdot u^1_{q_{prandtl}} \cdot r_{y,qprandtl} + 2 \cdot \left(\frac{1}{q_{contraction}}\right) \cdot (-0.0002327 - 0.0012476 \cdot z) \cdot u_z^1 \cdot u^1_{q_{prandtl}} \cdot r_{z,qprandtl} - \frac{2 \cdot q_{prandtl}}{q_{contraction}{}^3} \cdot u^1_{q_{contraction}} \cdot u^1_{q_{prandtl}} \cdot r_{contraction,prandtl}$$

This should be calculated per each value, making quite different, but it can be assumed that the maximum we want to measure is at 70Hz ~75 m/s, and we can take that uncertainty as a maximum value and this is the standard deviation per se of the blower taking the reference of the dynamic pressure in the contraction, so

$$u^2_{\zeta_{x,y,z,frequency}} = u^2_{\zeta_{0,0,1.5D,frequency}}$$

Table 23.- Mean, max, min and standard deviation for the measured period

N	traversal	vertical	ζmean	qprandtlmean	qprandtlstd	qprandtlmax	qprandtlmin	qcontractionmean	qcontractionstd	qcontractionmax	qcontractionmin
				mbar	mbar	mbar	mbar	mbar	mbar	mbar	mbar
11550	-4	0	0.715650591	28.22223301	0.924614885	36.76015038	23.75965338	39.43577126	0.169732722	40.15323538	38.73721938
10150	-2	0	0.993146655	39.13344538	0.17850517	40.15370938	38.46913538	39.4034911	0.167723318	40.10440638	38.74942638
11550	0	0	0.993791785	39.15906807	0.175732891	39.88515438	38.51796338	39.40369468	0.166806953	40.06778538	38.73721938
11900	2	0	0.995157167	39.21187358	0.182795136	39.89736138	38.49354938	39.40269426	0.168915019	40.14102838	38.79825438
7700	4	0	0.567997025	22.37253065	0.825379235	25.59070938	19.25525438	39.38846447	0.168722484	40.07999238	38.78604738
3850	0	4	0.655365447	25.83452965	0.801434281	28.56922738	23.11268038	39.42003619	0.169914086	40.04337138	38.82266838
6300	0	2	0.993698219	39.16012488	0.223756703	39.87294738	36.71132238	39.40846843	0.167367109	40.07999238	38.83487538
3150	0	-2	0.98405851	38.76545582	0.616999608	39.79970538	33.39100638	39.39344604	0.165524837	40.03116438	38.88370338
3150	0	-4	0.72602437	28.60855293	1.503626643	32.84169038	20.42713138	39.4043976	0.170258373	39.99454338	38.74942638

Table 24.- Mean, max, min and standard deviation for the measurements

N	traversal	vertical	ζmean	poprandtl	poprandtlstd	poprandtlmax	poprandtlmin
				mbar	mbar	mbar	mbar
11550	-4	0	0.715650591	1043.170319	0.928608742	1045.73275	1040.713077
10150	-2	0	0.993146655	1055.138389	0.172101317	1055.671294	1054.623549
11550	0	0	0.993791785	1055.250543	0.168583197	1055.761944	1054.74415
11900	2	0	0.995157167	1055.163959	0.177105452	1055.69335	1054.633709
7700	4	0	0.567997025	1037.302847	0.820445366	1039.80298	1034.895625
3850	0	4	0.655365447	1040.737616	0.796750743	1043.096253	1038.353934
6300	0	2	0.993698219	1054.987188	0.175871576	1055.488747	1054.485419
3150	0	-2	0.98405851	1054.920317	0.17904654	1055.405702	1054.409169
3150	0	-4	0.72602437	1043.451457	1.462880629	1046.314847	1040.650847

The standard specifications for the PMP series are ±0.08% FS and ±1% FS from 0 to 50 degrees. And the DAU has an absolute accuracy of ±2.3mV over the range. The conversion from analog to digital is considered to be inside the accuracy. The coverage factor here is assumed to be 1, 0.08% BSL is the lowest accuracy in the products and then the temperature effect is 1%

$$u^2_{instrument\_range} = q^2 * u^2_{accuracy\_instrument} = (39.15 * 0.0004)^2 = 2.45 * 10 - 4\ mbar^2$$

On the temperature it will be assumed the maximum value that can be reached with the minimum range (i.e. 35mBar) (1%/2)

$$u^2_{instrument\_range} = q^2 * u^2_{temperature} = (39.15 * 0.005)^2 = 3.83 * 10 - 2\ mbar^2$$
$$u^2_{dau} = V^2 * u^2_{accuracy_{instrument}} = \frac{35^2}{5} * 0.00232^2 = 2.64 * 10 - 4\ mbar^2$$

The total uncertainty for the Prandtl tube is

$$u_{contraction} = \sqrt{u^2_{instrument\_accuracy} + u^2_{instrument\_temperature} + u^2_{measurement} + u^2_{dau}}$$
$$= \sqrt{0.0383 + 0.000245 + (0.167)^2 + 0.000264} = 0.258\ mbar$$
$$u_{prandtl} = \sqrt{u^2_{instrument\_accuracy} + u^2_{instrument\_temperature} + u^2_{measurement} + u^2_{dau}}$$
$$= \sqrt{3.83 * 10 - 2 + 2.45 * 10 - 4 + (0.176)^2 + 2.64 * 10 - 4} = 0.264\ mbar$$

Same approximation is applicable to the contraction

It will be assumed ±0.17cm and that the values are representative (rectangular distribution) i.e. 0.35/sqrt(12) = 0.1

$$u^2_{\zeta_{0,0,1.5D,frequency}} = \left(\frac{1}{q_{contraction}}\right)^2 \cdot (0.264)^2 + (0.01466)^2 \cdot 0.1 + (0.006584)^2 \cdot (0.1)^2$$
$$+ (0.0002327 + 0.0012476 \cdot 1.5)^2 \cdot (0.1/8.3)^2 +$$
$$\left(-\frac{q_{prandtl}}{{q_{contraction}}^2}\right)^2 \cdot (0.258)^2 + 2 \cdot \left(\frac{1}{q_{contraction}}\right) \cdot (0.01466) \cdot 0.1 \cdot 0.264 + 2 \cdot \left(\frac{1}{q_{contraction}}\right)$$
$$\cdot (0.006584) \cdot 0.1 \cdot 0.264 + 2 \cdot \left(\frac{1}{q_{contraction}}\right) \cdot (0.0002327) \cdot \left(\frac{0.1}{8.3}\right) \cdot 0.264$$
$$- \frac{2 \cdot q_{prandtl}}{{q_{contraction}}^3} \cdot 0.258 \cdot 0.264 = 3.07e - 5$$

$$\boldsymbol{u^1_{\zeta_{0,0,1.5D,frequency}} = 0.006}$$

The tunnel has around 0.6% of uncertainty at this position on these values. A sensitivity analysis of the uncertainty could be expressed in the measurement point

Sensitivity Analysis on the pressure uncertainty

On the previous analysis some facts have being chosen, but the uncertainty can be reduced whenever the distance or the accuracy are on a higher quality. Therefore a small analysis has being performed

$$u_{contraction} = \sqrt{u^2_{instrument\_accuracy} + u^2_{instrument\_temperature} + u^2_{measurement} + u^2_{dau}}$$
$$= \sqrt{x^2 + (0.167)^2}$$
$$u_{prandtl} = \sqrt{u^2_{instrument\_accuracy} + u^2_{instrument\_temperature} + u^2_{measurement} + u^2_{dau}} = \sqrt{x^2 + (0.176)^2}$$

$$u^2_{\zeta_{0,0,1.5D,frequency}} = \left(\frac{1}{39.403}\right)^2 * \left(\sqrt{x'^2 + (0.176)^2}\right)^2 + (0.01466)^2 * y' + (0.006584)^2 * (y')^2 + (0.0002327 + 0.0012476 * 1.5)^2 * (y'/8.3)^2 + \left(-\frac{39.156}{39.403^2}\right)^2 * \left(\sqrt{x'^2 + (0.167)^2}\right)^2 + 2 * \left(\frac{1}{39.403}\right) * (0.01466) * y' * \sqrt{x'^2 + (0.176)^2} + 2 * \left(\frac{1}{39.403}\right) * (0.006584) * y' * \sqrt{x'^2 + (0.176)^2} + 2 * \left(\frac{1}{39.403}\right) * (0.0002327) * \left(\frac{y'}{8.3}\right) * \sqrt{x'^2 + (0.176)^2} - \frac{2 * 39.156}{39.403^3} * \sqrt{x'^2 + (0.167)^2} * \sqrt{x'^2 + (0.176)^2}$$

$$= \left(\frac{1}{39.403}\right)^2 * \left(\sqrt{\left(x \cdot \frac{0.176}{100}\right)^2 + (0.176)^2}\right)^2 + (0.01466)^2 * \frac{y}{2\sqrt{12}} + (0.006584)^2 * \left(\frac{y}{2\sqrt{12}}\right)^2 + (0.0002327 + 0.0012476 * 1.5)^2 * \left(\frac{y}{2\sqrt{12}}/8.3\right)^2 + \left(-\frac{39.156}{39.403^2}\right)^2 * \left(\sqrt{\left(x \cdot \frac{0.176}{100}\right)^2 + (0.167)^2}\right)^2 + 2 * \left(\frac{1}{39.403}\right) * (0.01466) * \frac{y}{2\sqrt{12}} * \sqrt{\left(x \cdot \frac{0.176}{100}\right)^2 + (0.176)^2} + 2 * \left(\frac{1}{39.403}\right) * (0.006584) * \frac{y}{2\sqrt{12}} * \sqrt{\left(x \cdot \frac{0.176}{100}\right)^2 + (0.176)^2} + 2 * \left(\frac{1}{39.403}\right) * (0.0002327) * \left(\frac{\frac{y}{2\sqrt{12}}}{8.3}\right) * \sqrt{\left(x \cdot \frac{0.176}{100}\right)^2 + (0.176)^2} - \frac{2 * 39.156}{39.403^3} * \sqrt{\left(x \cdot \frac{0.176}{100}\right)^2 + (0.167)^2} * \sqrt{\left(x \cdot \frac{0.176}{100}\right)^2 + (0.176)^2}$$

Plotting this as a mathematical expression in

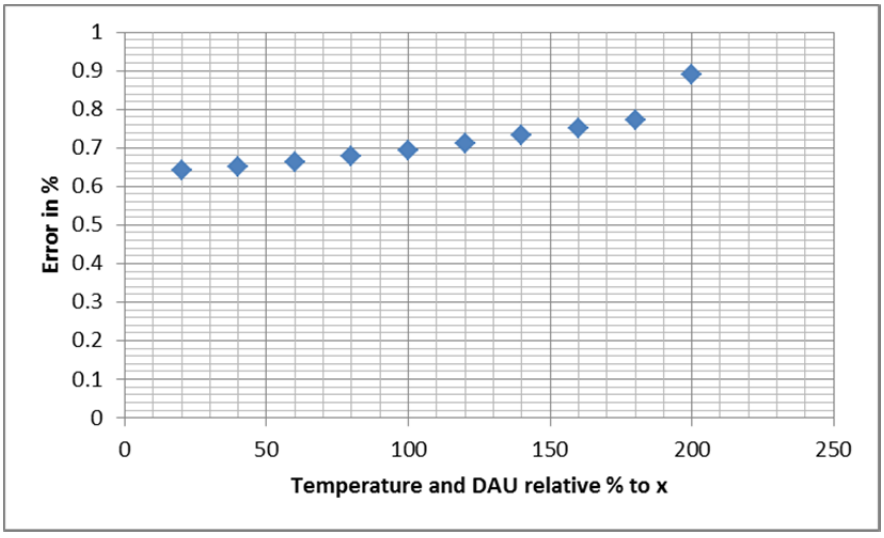

Figure 202.- Temperature and DAU influence

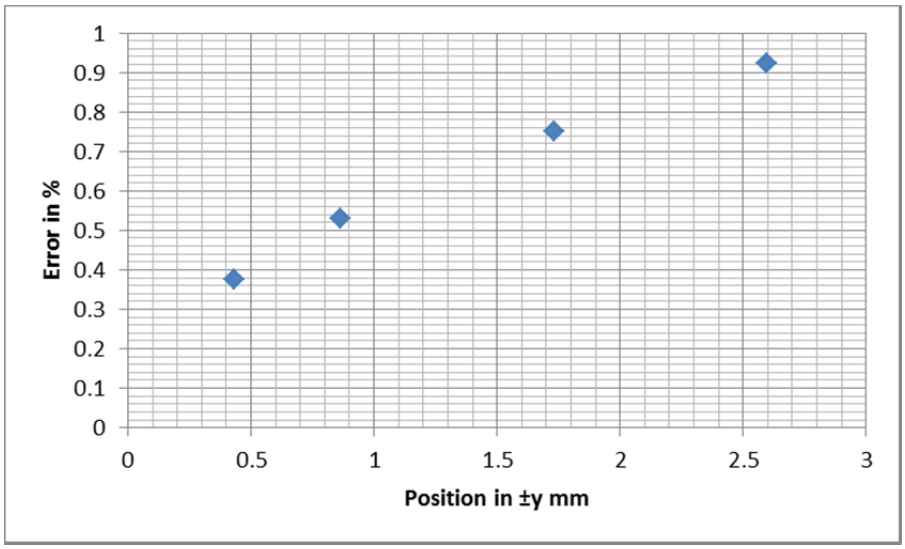

Figure 203.- Position influence in the error

As a result it can be seen that the effects in the positioning system have more influence that the uncertainty of the measurement on a reduced area

Blower coefficient Cα, Cβ uncertainty

Once we have the uncertainty of the wind tunnel the uncertainty of the values C_i

$$C_i = \frac{q_{lateral}}{q_{pitot}}$$

The coefficients depends on different parameters

$$C_i = C(q_{lateral}, q_{pitot}, x, y, z, \psi)$$

The value

$$u_{C_i}^2 = \left(\frac{\partial C_i}{\partial q_{pitot}}\right)^2 \cdot u_{q_{pitot}}^2 + \left(\frac{\partial C_i}{\partial q_{lateral}}\right)^2 \cdot u_{q_{lateral}}^2 + \left(\frac{\partial C_i}{\partial x}\right)^2 \cdot u_x^2 + \left(\frac{\partial C_i}{\partial y}\right)^2 \cdot u_y^2 + \left(\frac{\partial C_i}{\partial z}\right)^2 \cdot u_z^2 + \left(\frac{\partial C_i}{\partial \psi}\right)^2 \cdot u_\alpha^2 + 2 \cdot \left(\frac{\partial C_i}{\partial q_{pitot}}\right) \cdot \left(\frac{\partial C_i}{\partial q_{lateral}}\right) \cdot u_{q_{pitot}}^1 \cdot u_{q_{lateral}}^1 \cdot r_{pitot,lateral} + 2 \cdot \left(\frac{\partial C_i}{\partial q_{pitot}}\right) \cdot \left(\frac{\partial C_i}{\partial x}\right) \cdot u_{q_{pitot}}^1 \cdot u_x^1 \cdot r_{pitot,x} + 2 \cdot \left(\frac{\partial C_i}{\partial q_{pitot}}\right) \cdot \left(\frac{\partial C_i}{\partial y}\right) \cdot u_{q_{pitot}}^1 \cdot u_y^1 \cdot r_{pitot,y} + 2 \cdot \left(\frac{\partial C_i}{\partial q_{pitot}}\right) \cdot \left(\frac{\partial C_i}{\partial z}\right) \cdot u_{q_{pitot}}^1 \cdot u_z^1 \cdot r_{pitot,z} + 2 \cdot \left(\frac{\partial C_i}{\partial q_{lateral}}\right) \cdot \left(\frac{\partial C_i}{\partial x}\right) \cdot u_{q_{lateral}}^1 \cdot u_x^1 \cdot r_{lateral,x} + 2 \cdot \left(\frac{\partial C_i}{\partial q_{lateral}}\right) \cdot \left(\frac{\partial C_i}{\partial y}\right) \cdot u_{q_{lateral}}^1 \cdot u_y^1 \cdot r_{lateral,y} + 2 \cdot \left(\frac{\partial C_i}{\partial q_{lateral}}\right) \cdot \left(\frac{\partial C_i}{\partial z}\right) \cdot u_{q_{lateral}}^1 \cdot u_z^1 \cdot r_{lateral,z} + 2 \cdot \left(\frac{\partial C_i}{\partial q_{lateral}}\right) \cdot \left(\frac{\partial C_i}{\partial \psi}\right) \cdot u_{q_{lateral}}^1 \cdot u_\psi^1 \cdot r_{lateral,\alpha} + 2 \cdot \left(\frac{\partial C_i}{\partial q_{pitot}}\right) \cdot \left(\frac{\partial C_i}{\partial \psi}\right) \cdot u_{q_{pitot}}^1 \cdot u_\psi^1 \cdot r_{pitot,\psi}$$

And in the other way around the value that needs to be taken is the angle. So the uncertainty in this case must be rewritten

$$u_{\alpha_{Ci}}^2 = \left(\frac{\partial \alpha_{Ci}}{\partial q_{pitot}}\right)^2 \cdot u_{q_{pitot}}^2 + \left(\frac{\partial \alpha_{Ci}}{\partial q_{lateral}}\right)^2 \cdot u_{q_{lateral}}^2 + \left(\frac{\partial \alpha_{Ci}}{\partial x}\right)^2 \cdot u_x^2 + \left(\frac{\partial \alpha_{Ci}}{\partial y}\right)^2 \cdot u_y^2 + \left(\frac{\partial \alpha_{Ci}}{\partial z}\right)^2 \cdot u_z^2$$
$$+ \left(\frac{\partial \alpha_{Ci}}{\partial \psi}\right)^2 \cdot u_\psi^2 + 2 \cdot \left(\frac{\partial \alpha_{Ci}}{\partial q_{pitot}}\right) \cdot \left(\frac{\partial \alpha_{Ci}}{\partial q_{lateral}}\right) \cdot u_{q_{pitot}}^1 \cdot u_{q_{lateral}}^1 \cdot r_{pitot,lateral} + 2$$
$$\cdot \left(\frac{\partial \alpha_{Ci}}{\partial q_{pitot}}\right) \cdot \left(\frac{\partial \alpha_{Ci}}{\partial x}\right) \cdot u_{q_{pitot}}^1 \cdot u_x^1 \cdot r_{pitot,x} + 2 \cdot \left(\frac{\partial \alpha_{Ci}}{\partial q_{pitot}}\right) \cdot \left(\frac{\partial \alpha_{Ci}}{\partial y}\right) \cdot u_{q_{pitot}}^1 \cdot u_y^1 \cdot r_{pitot,y}$$
$$+ 2 \cdot \left(\frac{\partial \alpha_{Ci}}{\partial q_{pitot}}\right) \cdot \left(\frac{\partial \alpha_{Ci}}{\partial z}\right) \cdot u_{q_{pitot}}^1 \cdot u_z^1 \cdot r_{pitot,z} + 2 \cdot \left(\frac{\partial \alpha_{Ci}}{\partial q_{lateral}}\right) \cdot \left(\frac{\partial \alpha_{Ci}}{\partial x}\right) \cdot u_{q_{lateral}}^1 \cdot u_x^1$$
$$\cdot r_{lateral,x} + 2 \cdot \left(\frac{\partial \alpha_{Ci}}{\partial q_{lateral}}\right) \cdot \left(\frac{\partial \alpha_{Ci}}{\partial y}\right) \cdot u_{q_{lateral}}^1 \cdot u_y^1 \cdot r_{lateral,y} + 2 \cdot \left(\frac{\partial \alpha_{Ci}}{\partial q_{lateral}}\right) \cdot \left(\frac{\partial \alpha_{Ci}}{\partial z}\right)$$
$$\cdot u_{q_{lateral}}^1 \cdot u_z^1 \cdot r_{lateral,z} + 2 \cdot \left(\frac{\partial \alpha_{Ci}}{\partial q_{lateral}}\right) \cdot \left(\frac{\partial \alpha_{Ci}}{\partial \psi}\right) \cdot u_{q_{lateral}}^1 \cdot u_\psi^1 \cdot r_{lateral,\psi} + 2$$
$$\cdot \left(\frac{\partial \alpha_{Ci}}{\partial q_{pitot}}\right) \cdot \left(\frac{\partial \alpha_{Ci}}{\partial \psi}\right) \cdot u_{q_{pitot}}^1 \cdot u_\psi^1 \cdot r_{pitot,\psi}$$

It is assumed that:

$$r_{x,\psi} = 0$$
$$r_{y,\psi} = 0$$
$$r_{z,\psi} = 0$$
$$r_{x,z} = 0$$
$$r_{x,y} = 0$$
$$r_{z,y} = 0$$

The correlations

$$r_{pitot,lateral} = 1$$
$$r_{pitot,x} = -1$$
$$r_{pitot,y} = -1$$
$$r_{pitot,z} = -1$$
$$r_{lateral,x} = 1$$

$$r_{lateral,y} = 1$$
$$r_{lateral,z} = 1$$
$$r_{lateral,\psi} = 1$$
$$r_{pitot,\psi} = -1$$

$$u_{\alpha_{Ci}}^2 = \left(\frac{\partial \alpha_{Ci}}{\partial q_{pitot}}\right)^2 \cdot u_{q_{pitot}}^2 + \left(\frac{\partial \alpha_{Ci}}{\partial q_{lateral}}\right)^2 \cdot u_{q_{lateral}}^2 + \left(\frac{\partial \alpha_{Ci}}{\partial x}\right)^2 \cdot u_x^2 + \left(\frac{\partial \alpha_{Ci}}{\partial y}\right)^2 \cdot u_y^2 + \left(\frac{\partial \alpha_{Ci}}{\partial z}\right)^2 \cdot u_z^2 + \left(\frac{\partial \alpha_{Ci}}{\partial \psi}\right)^2 \cdot u_\alpha^2 + 2 \cdot \left(\frac{\partial \alpha_{Ci}}{\partial q_{pitot}}\right) \cdot \left(\frac{\partial \alpha_{Ci}}{\partial q_{lateral}}\right) \cdot u_{q_{pitot}}^1 \cdot u_{q_{lateral}}^1 - 2 \cdot \left(\frac{\partial \alpha_{Ci}}{\partial q_{pitot}}\right) \cdot \left(\frac{\partial \alpha_{Ci}}{\partial x}\right) \cdot u_{q_{pitot}}^1 \cdot u_x^1 - 2 \cdot \left(\frac{\partial \alpha_{Ci}}{\partial q_{pitot}}\right) \cdot \left(\frac{\partial \alpha_{Ci}}{\partial y}\right) \cdot u_{q_{pitot}}^1 \cdot u_y^1 - 2 \cdot \left(\frac{\partial \alpha_{Ci}}{\partial q_{pitot}}\right) \cdot \left(\frac{\partial \alpha_{Ci}}{\partial z}\right) \cdot u_{q_{pitot}}^1 \cdot u_z^1 + 2 \cdot \left(\frac{\partial \alpha_{Ci}}{\partial q_{lateral}}\right) \cdot \left(\frac{\partial \alpha_{Ci}}{\partial x}\right) \cdot u_{q_{lateral}}^1 \cdot u_x^1 + 2 \cdot \left(\frac{\partial \alpha_{Ci}}{\partial q_{lateral}}\right) \cdot \left(\frac{\partial \alpha_{Ci}}{\partial y}\right) \cdot u_{q_{lateral}}^1 \cdot u_y^1 + 2 \cdot \left(\frac{\partial \alpha_{Ci}}{\partial q_{lateral}}\right) \cdot \left(\frac{\partial \alpha_{Ci}}{\partial z}\right) \cdot u_{q_{lateral}}^1 \cdot u_z^1 + 2 \cdot \left(\frac{\partial \alpha_{Ci}}{\partial q_{lateral}}\right) \cdot \left(\frac{\partial \alpha_{Ci}}{\partial \psi}\right) \cdot u_{q_{lateral}}^1 \cdot u_\psi^1 - 2 \cdot \left(\frac{\partial \alpha_{Ci}}{\partial q_{pitot}}\right) \cdot \left(\frac{\partial \alpha_{Ci}}{\partial \psi}\right) \cdot u_{q_{pitot}}^1 \cdot u_\psi^1$$

If

$$\alpha = a_3 \cdot {C_\alpha}^3 + a_2 \cdot {C_\alpha}^2 + a_1 \cdot {C_\alpha}^1 + a_0 \cdot {C_\alpha}^0 = a_3 \cdot \left(\frac{q_{lateral}}{q_{pitot}}\right)^3 + a_2 \cdot \left(\frac{q_{lateral}}{q_{pitot}}\right)^2 + a_1 \cdot \left(\frac{q_{lateral}}{q_{pitot}}\right)^1 + a_0$$

Then

$$\frac{\partial \alpha_{Ci}}{\partial q_{pitot}} = \frac{-a_3 \cdot 3}{q_{pitot}} \cdot \left(\frac{q_{lateral}}{q_{pitot}}\right)^3 + \frac{-a_2 \cdot 2}{q_{pitot}} \cdot \left(\frac{q_{lateral}}{q_{pitot}}\right)^2 + \frac{-a_1}{q_{pitot}} \cdot \left(\frac{q_{lateral}}{q_{pitot}}\right)^1 = {a_3}' \cdot \left(\frac{q_{lateral}}{q_{pitot}}\right)^3 + {a_2}' \cdot \left(\frac{q_{lateral}}{q_{pitot}}\right)^2 + {a_1}' \cdot \left(\frac{q_{lateral}}{q_{pitot}}\right)^1 + {a_0}'$$

With

$$a_3' = \frac{-a_3 \cdot 3}{q_{pitot}}$$
$$a_2' = \frac{-a_2 \cdot 2}{q_{pitot}}$$
$$a_1' = \frac{-a_1}{q_{pitot}}$$
$$a_0' = 0$$

$$\frac{\partial \alpha_{Ci}}{\partial q_{lateral}} = \frac{a_3 \cdot 3}{q_{lateral}} \cdot \left(\frac{q_{lateral}}{q_{pitot}}\right)^3 + \frac{a_2 \cdot 2}{q_{lateral}} \cdot \left(\frac{q_{lateral}}{q_{pitot}}\right)^2 + \frac{a_1}{q_{lateral}} \cdot \left(\frac{q_{lateral}}{q_{pitot}}\right)^1 = {a_3}'' \cdot \left(\frac{q_{lateral}}{q_{pitot}}\right)^3 + {a_2}'' \cdot \left(\frac{q_{lateral}}{q_{pitot}}\right)^2 + {a_1}'' \cdot \left(\frac{q_{lateral}}{q_{pitot}}\right)^1 + {a_0}''$$

$$a_3'' = \frac{a_3 \cdot 3}{q_{lateral}}$$
$$a_2'' = \frac{a_2 \cdot 2}{q_{lateral}}$$
$$a_1'' = \frac{a_1}{q_{lateral}}$$
$$a_0'' = 0$$

Other parameters will be estimated as a constant though in the wind tunnel it has being proven than on small distances (~0.2cm) the flow is almost the same

$$\zeta_{\frac{0,0,x+0.2}{8D}} - \zeta_{0,0,xD} = -0.9927 + 0.0002327x - 0.0006238 \cdot x^2 + 90.9927 - 0.0002327 \cdot \left(x + 0.2 \cdot \frac{0.125}{D}\right) + 0.0006238 \cdot \left(x + 0.2 \cdot \frac{0.125}{D}\right)^2$$
$$= -0.0002327 \cdot \left(0.2 \cdot \frac{0.125}{D}\right) + 0.0006238 \cdot \left(0.2 \cdot \frac{0.125}{D} \cdot 2 \cdot x + \left(0.2 \cdot \frac{0.125}{D}\right)^2\right)$$
$$= 4.88e - 6\ (when\ x = 1.5)$$

So in overall the result is 99.999%, which is completely neglectible for this range

$$\frac{\partial \alpha_{Ci}}{\partial z} \approx 0$$

$$\zeta_{x,y,1.5D} - \zeta_{0.2,0.2,1.5D} = 1.066 - 0.01466 \cdot 0 - 0.026 \cdot 0^2 - 0.006584 \cdot 0 - 0.0232 \cdot 0^2 - 1.066 + 0.01466 \cdot 0.2 + 0.026 \cdot 0.2^2 + 0.006584 \cdot 0.2 + 0.0232 \cdot 0.2^2 = 0.0054$$

So in overall the result is 99.4%, Which is not negible but with the combined uncertainty

$$\zeta_{x,y,1.5D} - \zeta_{x,x,1.5D} = 0.01466 \cdot x + 0.026 \cdot x^2 + 0.006584 \cdot x + 0.0232 \cdot x^2 = 0.0492 \cdot x^2 + 0.021244 \cdot x$$

Then if

$$\alpha = a_3 \cdot {C_\alpha}^3 + a_2 \cdot {C_\alpha}^2 + a_1 \cdot {C_\alpha}^1 + a_0 \cdot {C_\alpha}^0 = a_3 \cdot \left(\frac{q_{lateral}}{q_{pitot} \cdot (1 - 0.0492 \cdot x^2 - 0.021244 \cdot x)}\right)^3 + a_2 \cdot \left(\frac{q_{lateral}}{q_{pitot} \cdot (1 - 0.0492 \cdot x^2 - 0.021244 \cdot x)}\right)^2 + a_1 \cdot \left(\frac{q_{lateral}}{q_{pitot} \cdot (1 - 0.0492 \cdot x^2 - 0.021244 \cdot x)}\right)^1 + a_0$$

The holes are 0.7 cm from each one

$$\zeta_{-0.35,-0.35,1.5D} - \zeta_{0.35+x,0.35+x,0,1.5D} = 0.021244 \cdot (x - 0.125) + 0.0492 \cdot (x^2 - 0.125)$$

$$\alpha = a_3 \cdot {C_\alpha}^3 + a_2 \cdot {C_\alpha}^2 + a_1 \cdot {C_\alpha}^1 + a_0 \cdot {C_\alpha}^0 = a_3 \cdot \left(\frac{q_{lateral} \cdot \left(0.021244 \cdot (x - 0.125) + 0.0492 \cdot (x^2 - 0.125)\right)}{q_{pitot} \cdot (1 - 0.0492 \cdot x^2 - 0.021244 \cdot x)}\right)^3 + a_2 \cdot \left(\frac{q_{lateral} \cdot \left(0.021244 \cdot (x - 0.125) + 0.0492 \cdot (x^2 - 0.125)\right)}{q_{pitot} \cdot (1 - 0.0492 \cdot x^2 - 0.021244 \cdot x)}\right)^2 + a_1 \cdot \left(\frac{q_{lateral} \cdot \left(0.021244 \cdot (x - 0.125) + 0.0492 \cdot (x^2 - 0.125)\right)}{q_{pitot} \cdot (1 - 0.0492 \cdot x^2 - 0.021244 \cdot x)}\right)^1 + a_0$$
$$= a_3 \cdot \left(\frac{q_{lateral}}{q_{pitot}}\right)^3 \cdot \frac{[0.021244 \cdot (x - 0.125) + 0.0492 \cdot (x^2 - 0.125)]^3}{(1 - 0.0492 \cdot x^2 - 0.021244 \cdot x)^3} + a_2 \cdot \left(\frac{q_{lateral}}{q_{pitot}}\right)^2 \cdot \frac{[0.021244 \cdot (x - 0.125) + 0.0492 \cdot (x^2 - 0.125)]^2}{(1 - 0.0492 \cdot x^2 - 0.021244 \cdot x)^2} + a_1 \cdot \left(\frac{q_{lateral}}{q_{pitot}}\right)^1 \cdot \left(\frac{\left(0.021244 \cdot (x - 0.125) + 0.0492 \cdot (x^2 - 0.125)\right)}{(1 - 0.0492 \cdot x^2 - 0.021244 \cdot x)}\right)^1 + a_0$$

Then it will be assumed that

$$\frac{\partial \alpha_{Ci}}{\partial x} = \frac{\partial \alpha_{Ci}}{\partial y}$$

$$\frac{\partial \alpha_{Ci}}{\partial x} + \frac{\partial \alpha_{Ci}}{\partial y}$$
$$= a_3 \cdot \left(\frac{q_{lateral}}{q_{pitot}}\right)^3$$
$$\cdot \left\{ \frac{3 * [0.021244 \cdot (x - 0.125) + 0.0492 \cdot (x^2 - 0.125)]^2 * (0.021244 + 0.0492 * 2 * x) * (1 - 0.0492 \cdot x^2 - 0.021244 \cdot x)^3}{(1 - 0.0492 \cdot x^2 - 0.021244 \cdot x)^6} \right.$$
$$\left. - \frac{3 * [(1 - 0.0492 \cdot x^2 - 0.021244 \cdot x)]^2 * (-0.021244 - 0.0492 * 2 * x) * [0.021244 \cdot (x - 0.125) + 0.0492 \cdot (x^2 - 0.125)]^3}{(1 - 0.0492 \cdot x^2 - 0.021244 \cdot x)^6} \right\}$$
$$+ a_2 \cdot \left(\frac{q_{lateral}}{q_{pitot}}\right)^2$$
$$\cdot \left\{ \frac{2 * [0.021244 \cdot (x - 0.125) + 0.0492 \cdot (x^2 - 0.125)]^1 * (0.021244 + 0.0492 * 2 * x) * (1 - 0.0492 \cdot x^2 - 0.021244 \cdot x)^2}{(1 - 0.0492 \cdot x^2 - 0.021244 \cdot x)^4} \right.$$
$$\left. - \frac{2 * [(1 - 0.0492 \cdot x^2 - 0.021244 \cdot x)]^1 * (-0.021244 - 0.0492 * 2 * x) * [0.021244 \cdot (x - 0.125) + 0.0492 \cdot (x^2 - 0.125)]^2}{(1 - 0.0492 \cdot x^2 - 0.021244 \cdot x)^4} \right\}$$
$$+ a_1 \cdot \left(\frac{q_{lateral}}{q_{pitot}}\right)^1$$
$$\cdot \left\{ \frac{(0.021244 + 0.0492 * 2 * x) * (1 - 0.0492 \cdot x^2 - 0.021244 \cdot x)}{(1 - 0.0492 \cdot x^2 - 0.021244 \cdot x)^2} \right.$$
$$\left. - \frac{(-0.021244 - 0.0492 * 2 * x) * [0.021244 \cdot (x - 0.125) + 0.0492 \cdot (x^2 - 0.125)]}{(1 - 0.0492 \cdot x^2 - 0.021244 \cdot x)^2} \right\}$$

$$\frac{\partial \alpha_{Ci}}{\partial x} + \frac{\partial \alpha_{Ci}}{\partial y} = a_3 \cdot \left(\frac{q_{lateral}}{q_{pitot}}\right)^3 \cdot 0.000201 - a_2 \cdot \left(\frac{q_{lateral}}{q_{pitot}}\right)^2 \cdot 0.000214 + a_1 \cdot \left(\frac{q_{lateral}}{q_{pitot}}\right)^1 \cdot 0.0412$$
$$\approx a_1 \cdot \left(\frac{q_{lateral}}{q_{pitot}}\right)^1 \cdot 0.0412$$

Then

$$u_x^1 = u_y^1$$

$$\frac{\partial \alpha_{Ci}}{\partial x} \approx \frac{\frac{\partial \alpha_{Ci}}{\partial x} + \frac{\partial \alpha_{Ci}}{\partial y}}{2} = a_1 \cdot \left(\frac{q_{lateral}}{q_{pitot}}\right)^1 \cdot 0.0206$$

$$^2_{\alpha_{Ci}} = \left(\frac{\partial \alpha_{Ci}}{\partial q_{pitot}}\right)^2 \cdot u^2_{q_{pitot}} + \left(\frac{\partial \alpha_{Ci}}{\partial q_{lateral}}\right)^2 \cdot u^2_{q_{lateral}} + 2 \cdot \left(\frac{\partial \alpha_{Ci}}{\partial x}\right)^2 \cdot u_x^2 + \left(\frac{\partial \alpha_{Ci}}{\partial \psi}\right)^2 \cdot u_\psi^2 + 2 \cdot \left(\frac{\partial \alpha_{Ci}}{\partial q_{pitot}}\right)$$
$$\cdot \left(\frac{\partial \alpha_{Ci}}{\partial q_{lateral}}\right) \cdot u^1_{q_{pitot}} \cdot u^1_{q_{lateral}} - 2 \cdot \left[\left(\frac{\partial \alpha_{Ci}}{\partial q_{lateral}}\right) \cdot u^1_{q_{lateral}} - \left(\frac{\partial \alpha_{Ci}}{\partial q_{pitot}} u^1_{q_{pitot}}\right)\right]$$
$$* \left[\frac{\partial \alpha_{Ci}}{\partial x} + \frac{\partial \alpha_{Ci}}{\partial y}\right] \cdot u_x^1 + 2 \cdot \left(\frac{\partial \alpha_{Ci}}{\partial q_{lateral}}\right) \cdot \left(\frac{\partial \alpha_{Ci}}{\partial \psi}\right) \cdot u^1_{q_{lateral}} \cdot u_\psi^1 - 2 \cdot \left(\frac{\partial \alpha_{Ci}}{\partial q_{pitot}}\right) \cdot \left(\frac{\partial \alpha_{Ci}}{\partial \psi}\right)$$
$$\cdot u^1_{q_{pitot}} \cdot u_\psi^1$$

if

$$\alpha = a_3 \cdot {C_\alpha}^3 + a_2 \cdot {C_\alpha}^2 + a_1 \cdot {C_\alpha}^1 + a_0 \cdot {C_\alpha}^0$$

It is clear that the real position is ψ, so α is the resulting

$$\alpha = a_3 \cdot {C_\psi}^3 + a_2 \cdot {C_\psi}^2 + a_1 \cdot {C_\psi}^1 + a_0 \cdot {C_\psi}^0$$

$$\partial\alpha = a_3 \cdot 3 \cdot {C_\psi}^2 \cdot \partial\psi + 2 \cdot a_2 \cdot {C_\psi}^1 \cdot \partial\psi + a_1 \cdot \partial\psi$$

$$\frac{\partial\alpha_{Ci}}{\partial\psi} = a_3 \cdot 3 \cdot {C_\psi}^2 + 2 \cdot a_2 \cdot {C_\psi}^1 + a_1 = a_3 \cdot 3 \cdot \left(\frac{q_{lateral}}{q_{pitot}}\right)^2 + 2 \cdot a_2 \cdot \left(\frac{q_{lateral}}{q_{pitot}}\right) + a_1$$

then

$$\begin{aligned}
u_{\alpha_{Ci}}^2 = {} & \left(a_3' \cdot \left(\frac{q_{lateral}}{q_{pitot}}\right)^3 + a_2' \cdot \left(\frac{q_{lateral}}{q_{pitot}}\right)^2 + a_1' \cdot \left(\frac{q_{lateral}}{q_{pitot}}\right)^1\right)^2 \cdot u_{q_{pitot}}^2 \\
& + \left(a_3'' \cdot \left(\frac{q_{lateral}}{q_{pitot}}\right)^3 + a_2'' \cdot \left(\frac{q_{lateral}}{q_{pitot}}\right)^2 + a_1'' \cdot \left(\frac{q_{lateral}}{q_{pitot}}\right)^1\right)^2 \cdot u_{q_{lateral}}^2 + 2 \cdot \left(a_1 \cdot \left(\frac{q_{lateral}}{q_{pitot}}\right)^1 \cdot 0.0206\right)^2 \\
& \cdot u_x^2 + \left(a_3 \cdot 3 \cdot \left(\frac{q_{lateral}}{q_{pitot}}\right)^2 + 2 \cdot a_2 \cdot \left(\frac{q_{lateral}}{q_{pitot}}\right) + a_1\right)^2 \cdot u_\psi^2 + 2 \\
& \cdot \left(a_3' \cdot \left(\frac{q_{lateral}}{q_{pitot}}\right)^3 + a_2' \cdot \left(\frac{q_{lateral}}{q_{pitot}}\right)^2 + a_1' \cdot \left(\frac{q_{lateral}}{q_{pitot}}\right)^1\right) \\
& \cdot \left(a_3'' \cdot \left(\frac{q_{lateral}}{q_{pitot}}\right)^3 + a_2'' \cdot \left(\frac{q_{lateral}}{q_{pitot}}\right)^2 + a_1'' \cdot \left(\frac{q_{lateral}}{q_{pitot}}\right)^1 + a_0''\right) \cdot u_{q_{pitot}}^1 \cdot u_{q_{lateral}}^1 - 2 \\
& \cdot \left[\left(a_3'' \cdot \left(\frac{q_{lateral}}{q_{pitot}}\right)^3 + a_2'' \cdot \left(\frac{q_{lateral}}{q_{pitot}}\right)^2 + a_1'' \cdot \left(\frac{q_{lateral}}{q_{pitot}}\right)^1\right) \cdot u_{q_{lateral}}^1\right. \\
& \left. - \left(\left(a_3' \cdot \left(\frac{q_{lateral}}{q_{pitot}}\right)^3 + a_2' \cdot \left(\frac{q_{lateral}}{q_{pitot}}\right)^2 + a_1' \cdot \left(\frac{q_{lateral}}{q_{pitot}}\right)^1\right) * u_{q_{pitot}}^1\right)\right] * \left[a_1 \cdot \left(\frac{q_{lateral}}{q_{pitot}}\right)^1 \cdot 0.0412\right] \cdot u_x^1 \\
& + 2 \cdot \left(a_3'' \cdot \left(\frac{q_{lateral}}{q_{pitot}}\right)^3 + a_2'' \cdot \left(\frac{q_{lateral}}{q_{pitot}}\right)^2 + a_1'' \cdot \left(\frac{q_{lateral}}{q_{pitot}}\right)^1\right) \\
& \cdot \left(a_3 \cdot 3 \cdot \left(\frac{q_{lateral}}{q_{pitot}}\right)^2 + 2 \cdot a_2 \cdot \left(\frac{q_{lateral}}{q_{pitot}}\right) + a_1\right) \cdot u_{q_{lateral}}^1 \cdot u_\psi^1 - 2 \\
& \cdot \left(a_3' \cdot \left(\frac{q_{lateral}}{q_{pitot}}\right)^3 + a_2' \cdot \left(\frac{q_{lateral}}{q_{pitot}}\right)^2 + a_1' \cdot \left(\frac{q_{lateral}}{q_{pitot}}\right)^1\right) \cdot \left(a_3 \cdot 3 \cdot \left(\frac{q_{lateral}}{q_{pitot}}\right)^2 + 2 \cdot a_2 \cdot \left(\frac{q_{lateral}}{q_{pitot}}\right) + a_1\right) \\
& \cdot u_{q_{pitot}}^1 \cdot u_\psi^1
\end{aligned}$$

Then

$$
\begin{aligned}
{}^{2}_{\alpha_{Ci}} = &\left(3a_3\cdot\left(\frac{q_{lateral}}{q_{pitot}}\right)^3+2a_2\cdot\left(\frac{q_{lateral}}{q_{pitot}}\right)^2+a_1\cdot\left(\frac{q_{lateral}}{q_{pitot}}\right)^1\right)^2\cdot\frac{u^2_{q_{pitot}}}{{q_{pitot}}^2}\\
&+\left(3a_3\cdot\left(\frac{q_{lateral}}{q_{pitot}}\right)^3+2a_2\cdot\left(\frac{q_{lateral}}{q_{pitot}}\right)^2+a_1\cdot\left(\frac{q_{lateral}}{q_{pitot}}\right)^1\right)^2\cdot\frac{u^2_{q_{lateral}}}{{q_{lateral}}^2}+2\cdot\left(a_1\cdot\left(\frac{q_{lateral}}{q_{pitot}}\right)^1\cdot 0.0206\right)^2\\
&\cdot u_x^2+\left(3a_3\cdot\left(\frac{q_{lateral}}{q_{pitot}}\right)^3+2a_2\cdot\left(\frac{q_{lateral}}{q_{pitot}}\right)^2+a_1\cdot\left(\frac{q_{lateral}}{q_{pitot}}\right)^1\right)^2\cdot\frac{u_\psi^2}{\left(\frac{q_{lateral}}{q_{pitot}}\right)^2}+2\\
&\cdot\left({a_3}'\cdot\left(\frac{q_{lateral}}{q_{pitot}}\right)^3+{a_2}'\cdot\left(\frac{q_{lateral}}{q_{pitot}}\right)^2+{a_1}'\cdot\left(\frac{q_{lateral}}{q_{pitot}}\right)^1\right)\\
&\cdot\left({a_3}''\cdot\left(\frac{q_{lateral}}{q_{pitot}}\right)^3+{a_2}''\cdot\left(\frac{q_{lateral}}{q_{pitot}}\right)^2+{a_1}''\cdot\left(\frac{q_{lateral}}{q_{pitot}}\right)^1+{a_0}''\right)\cdot u^1_{q_{pitot}}\cdot u^1_{q_{lateral}}-2\\
&\cdot\left[\left({a_3}''\cdot\left(\frac{q_{lateral}}{q_{pitot}}\right)^3+{a_2}''\cdot\left(\frac{q_{lateral}}{q_{pitot}}\right)^2+{a_1}''\cdot\left(\frac{q_{lateral}}{q_{pitot}}\right)^1\right)\cdot u^1_{q_{lateral}}\right.\\
&\left.-\left(\left({a_3}'\cdot\left(\frac{q_{lateral}}{q_{pitot}}\right)^3+{a_2}'\cdot\left(\frac{q_{lateral}}{q_{pitot}}\right)^2+{a_1}'\cdot\left(\frac{q_{lateral}}{q_{pitot}}\right)^1\right)*u^1_{q_{pitot}}\right)\right]*\left[a_1\cdot\left(\frac{q_{lateral}}{q_{pitot}}\right)^1\cdot 0.0412\right]\cdot u_x^1\\
&+2\cdot\left({a_3}''\cdot\left(\frac{q_{lateral}}{q_{pitot}}\right)^3+{a_2}''\cdot\left(\frac{q_{lateral}}{q_{pitot}}\right)^2+{a_1}''\cdot\left(\frac{q_{lateral}}{q_{pitot}}\right)^1\right)\\
&\cdot\left(a_3\cdot 3\cdot\left(\frac{q_{lateral}}{q_{pitot}}\right)^2+2\cdot a_2\cdot\left(\frac{q_{lateral}}{q_{pitot}}\right)+a_1\right)\cdot u^1_{q_{lateral}}\cdot u^1_{\psi}-2\\
&\cdot\left({a_3}'\cdot\left(\frac{q_{lateral}}{q_{pitot}}\right)^3+{a_2}'\cdot\left(\frac{q_{lateral}}{q_{pitot}}\right)^2+{a_1}'\cdot\left(\frac{q_{lateral}}{q_{pitot}}\right)^1\right)\cdot\left(a_3\cdot 3\cdot\left(\frac{q_{lateral}}{q_{pitot}}\right)^2+2\cdot a_2\cdot\left(\frac{q_{lateral}}{q_{pitot}}\right)+a_1\right)\\
&\cdot u^1_{q_{pitot}}\cdot u^1_{\psi}
\end{aligned}
$$

$$a_3' = \frac{-a_3\cdot 3}{q_{pitot}}$$

$$a_2' = \frac{-a_2\cdot 2}{q_{pitot}}$$

$$a_1' = \frac{-a_1}{q_{pitot}}$$

$$a_0' = 0$$

$$
\begin{aligned}
\frac{\partial\alpha_{Ci}}{\partial q_{lateral}} &= \frac{a_3\cdot 3}{q_{lateral}}\cdot\left(\frac{q_{lateral}}{q_{pitot}}\right)^3+\frac{a_2\cdot 2}{q_{lateral}}\cdot\left(\frac{q_{lateral}}{q_{pitot}}\right)^2+\frac{a_1}{q_{lateral}}\cdot\left(\frac{q_{lateral}}{q_{pitot}}\right)^1\\
&= {a_3}''\cdot\left(\frac{q_{lateral}}{q_{pitot}}\right)^3+{a_2}''\cdot\left(\frac{q_{lateral}}{q_{pitot}}\right)^2+{a_1}''\cdot\left(\frac{q_{lateral}}{q_{pitot}}\right)^1+{a_0}''
\end{aligned}
$$

$$a_3'' = \frac{a_3\cdot 3}{q_{lateral}}$$

$$a_2'' = \frac{a_2\cdot 2}{q_{lateral}}$$

$$a_1'' = \frac{a_1}{q_{lateral}}$$

$$a_0'' = 0$$

Defining $\left(3a_3\cdot\left(\frac{q_{lateral}}{q_{pitot}}\right)^3+2a_2\cdot\left(\frac{q_{lateral}}{q_{pitot}}\right)^2+a_1\cdot\left(\frac{q_{lateral}}{q_{pitot}}\right)^1\right)^1 = A$

$$
\begin{aligned}
u^2_{\alpha_{Ci}} = &A^2\cdot\frac{u^2_{q_{pitot}}}{{q_{pitot}}^2}+A^2\cdot\frac{u^2_{q_{lateral}}}{{q_{lateral}}^2}+2\cdot\left(a_1\cdot\left(\frac{q_{lateral}}{q_{pitot}}\right)^1\cdot 0.0206\right)^2\cdot u_x^2+A^2\cdot\frac{u_\psi^2}{\left(\frac{q_{lateral}}{q_{pitot}}\right)^2}-2\cdot A^2\cdot\frac{u^1_{q_{pitot}}}{q_{pitot}}\cdot\frac{u^1_{q_{lateral}}}{q_{lateral}}-2\\
&\cdot\left[A\cdot\frac{u^1_{q_{lateral}}}{q_{lateral}}+A\cdot\frac{u^1_{q_{pitot}}}{q_{pitot}}\right]*\left[a_1\cdot\left(\frac{q_{lateral}}{q_{pitot}}\right)^1\cdot 0.0412\right]\cdot u_x^1-2\cdot\frac{A^2}{q_{lateral}}\cdot\frac{u^1_{q_{lateral}}\cdot u^1_{\psi}}{\frac{q_{lateral}}{q_{pitot}}}+2\cdot A^2\cdot\frac{u^1_{q_{pitot}}}{q_{pitot}}\cdot u^1_{\psi}
\end{aligned}
$$

$$u_{\alpha_{Ci}}^2 = A^2 \cdot \left[\frac{u_{q_{pitot}}^2}{{q_{pitot}}^2} + \frac{u_{q_{lateral}}^2}{{q_{lateral}}^2} + \frac{u_{\psi}^2}{\left(\frac{q_{lateral}}{q_{pitot}}\right)^2} - 2 \cdot \frac{u_{q_{pitot}}^1}{q_{pitot}} \cdot \frac{u_{q_{lateral}}^1}{q_{lateral}} - 2 \cdot \frac{1}{q_{lateral}} \cdot \frac{u_{q_{lateral}}^1 \cdot u_{\psi}^1}{\frac{q_{lateral}}{q_{pitot}}} + 2 \cdot \frac{u_{q_{pitot}}^1}{q_{pitot}} \cdot u_{\psi}^1 \right] + 2 \cdot \left(a_1 \cdot \left(\frac{q_{lateral}}{q_{pitot}} \right)^1 \cdot 0.0206 \right)^2 \cdot u_x^2 - 2 \cdot A \cdot \left[\frac{u_{q_{lateral}}^1}{q_{lateral}} + \frac{u_{q_{pitot}}^1}{q_{pitot}} \right] * \left[a_1 \cdot \left(\frac{q_{lateral}}{q_{pitot}} \right)^1 \cdot 0.0412 \right] \cdot u_x^1$$

This is equivalent to

$$u_{\alpha_{Ci}}^2 = A^2 \cdot \left[\frac{u_{q_{pitot}}^2}{{q_{pitot}}^2} + \frac{u_{q_{lateral}}^2}{{q_{lateral}}^2} + \frac{u_{\psi}^2}{\left(\frac{q_{lateral}}{q_{pitot}}\right)^2} - 2 \cdot \frac{u_{q_{pitot}}^1}{q_{pitot}} \cdot \frac{u_{q_{lateral}}^1}{q_{lateral}} - 2 \cdot \frac{1}{q_{lateral}} \cdot \frac{u_{q_{lateral}}^1 \cdot u_{\psi}^1}{\frac{q_{lateral}}{q_{pitot}}} + 2 \cdot \frac{u_{q_{pitot}}^1}{q_{pitot}} \cdot u_{\psi}^1 \right] + 2 \cdot \left(\frac{\partial \alpha_{Ci}}{\partial x} \right)^2 \cdot u_x^2 - 2 \cdot A \cdot \left[\frac{u_{q_{lateral}}^1}{q_{lateral}} + \frac{u_{q_{pitot}}^1}{q_{pitot}} \right] * \left[2 * \frac{\partial \alpha_{Ci}}{\partial x} \right] \cdot u_x^1$$

The angular misalignment is being estimated of 1mm for the length of the pitot (~250mm). This means to have as a maximum of 0.25 degrees of misalignment, which in radians is 0.0044 rad

$$u_{\psi}^1 = 0.0044 * \frac{2}{\sqrt{12}} = 0.144\ deg$$

Assuming that the maximum uncertainty can be found at 70 Hz (belonging to a Mach 0.24) in this specific turbine

$$A_{\alpha} = \left(3a_3 \cdot \left(\frac{q_{lateral}}{q_{pitot}} \right)^3 + 2a_2 \cdot \left(\frac{q_{lateral}}{q_{pitot}} \right)^2 + a_1 \cdot \left(\frac{q_{lateral}}{q_{pitot}} \right)^1 \right)^1 = \left(3 * 329.11 \cdot \left(\frac{q_{lateral}}{q_{pitot}} \right)^3 + 2 * 199.01 \cdot \left(\frac{q_{lateral}}{q_{pitot}} \right)^2 + 73.438 \cdot \left(\frac{q_{lateral}}{q_{pitot}} \right)^1 \right)$$

$$A_{\beta} = \left(3a_3 \cdot \left(\frac{q_{lateral}}{q_{pitot}} \right)^3 + 2a_2 \cdot \left(\frac{q_{lateral}}{q_{pitot}} \right)^2 + a_1 \cdot \left(\frac{q_{lateral}}{q_{pitot}} \right)^1 \right)^1 = \left(-3 * 7.7551 \cdot \left(\frac{q_{lateral}}{q_{pitot}} \right)^3 + 2 * 44.918 \cdot \left(\frac{q_{lateral}}{q_{pitot}} \right)^2 - 54.001 \cdot \left(\frac{q_{lateral}}{q_{pitot}} \right)^1 \right)$$

The values for Calpha and Cbetha can be found in the next table. It will be considered in both cases the maximum value

f	alpha	calpha	cbetha
Hz	degrees		
70	0	0.005746	
70	5	0.066274	
70	15	0.143487	
70	-5	-0.06977	
70	-15	-0.32924	
70	-15		0.416216
70	-5		0.10961
70	0		-0.00158
70	5		-0.07781
70	15		-0.22849

$$A_\alpha = \left(3a_3 \cdot \left(\frac{q_{lateral}}{q_{pitot}}\right)^3 + 2a_2 \cdot \left(\frac{q_{lateral}}{q_{pitot}}\right)^2 + a_1 \cdot \left(\frac{q_{lateral}}{q_{pitot}}\right)^1\right)^1$$
$$= (3 * 329.11 \cdot (0.143487)^3 + 2 * 199.01 \cdot (0.143487)^2 + 73.438 \cdot (0.143487)^1) = 21.47\ deg$$

$$A_\beta = \left(3a_3 \cdot \left(\frac{q_{lateral}}{q_{pitot}}\right)^3 + 2a_2 \cdot \left(\frac{q_{lateral}}{q_{pitot}}\right)^2 + a_1 \cdot \left(\frac{q_{lateral}}{q_{pitot}}\right)^1\right)^1$$
$$= (-3 * 7.7551 \cdot (0.416216)^3 + 2 * 44.918 \cdot (0.416216)^2 - 54.001 \cdot (0.416216)^1) = -8.59\ deg$$

Then

$$u_{\alpha_{Ci}}^2 = 468.67 \cdot \left[\frac{u_{q_{pitot}}^2}{{q_{pitot}}^2} + \frac{u_{q_{lateral}}^2}{{q_{lateral}}^2} + \frac{u_\psi^2}{\left(\frac{q_{lateral}}{q_{pitot}}\right)^2} - 2 \cdot \frac{u_{q_{pitot}}^1}{q_{pitot}} \cdot \frac{u_{q_{lateral}}^1}{q_{lateral}} - 2 \cdot \frac{1}{q_{lateral}} \cdot \frac{u_{q_{lateral}}^1 \cdot u_\psi^1}{\frac{q_{lateral}}{q_{pitot}}} + 2 \cdot \frac{u_{q_{pitot}}^1}{q_{pitot}} \cdot u_\psi^1\right] + 2$$
$$\cdot \left(a_1 \cdot \left(\frac{q_{lateral}}{q_{pitot}}\right)^1 \cdot 0.0206\right)^2 \cdot u_x^2 - 43.30 \cdot \left[\frac{u_{q_{lateral}}^1}{q_{lateral}} + \frac{u_{q_{pitot}}^1}{q_{pitot}}\right] * \left[a_1 \cdot \left(\frac{q_{lateral}}{q_{pitot}}\right)^1 \cdot 0.0412\right] \cdot u_x^1$$

$$u_{q_{pitot}}^2 = u_{q_{pitot}_{measured}}^2 + k * u_{q_{pitot}_{wind}}^2 + u_{q_{pitot}_{equipment}}^2$$
$$\approx u_{q_{pitot}_{measured}}^2 + {q_{range}_{pitot}}^2 * u_{\zeta_{0,0,1.5D,frequency}}^2 * k * u_{q_{pitot}_{wind}}^2 + u_{q_{pitot}_{equipment}}^2$$

K = 1; $u_{\zeta_{0,0,1.5D,frequency}}^2 = 0.006\text{^}2$; in a generic term temperature has the same influence as before

$$u_{q_{pitot}}^2 = 3.83 * 10 - 2 + 2.45 * 10 - 4\ + 0.100^2 * 0.006^2 + 2.64 * 10 - 4 + 0.0645^2 = 0.043$$

Then

$$u_{q_{pitot}}^1 = 0.207\ mbar$$

$$u_{q_{lateral}}^2 = 3.83 * 10 - 2 + 2.45 * 10 - 4\ + 0.100^2 * 0.006^2 + 2.64 * 10 - 4 + 0.0251^2 = 0.039$$

$$u_{q_{lateral}}^1 = 0.199\ mbar$$

$$u_\alpha^2 = 468.67 \cdot \frac{\pi * \pi}{180 * 180}\left[\frac{0.043}{38.18^2} + \frac{0.199}{5.48^2} + \frac{6.25e-6}{\left(\frac{5.48}{38.18}\right)^2} - 2 \cdot \frac{0.207}{38.18} \cdot \frac{0.199}{5.48} - 2 \cdot \frac{1}{5.48} \cdot \frac{0.199 \cdot 0.0025}{\frac{5.48}{38.18}} + 2 \cdot \frac{0.207}{38.18} \cdot 0.0025\right] + 2$$
$$\cdot \frac{\pi * \pi}{180 * 180} \cdot \left(73.438 \cdot \left(\frac{5.48}{38.18}\right)^1 \cdot 0.0206\right)^2 \cdot 0.01 - 43.30 \cdot \frac{\pi * \pi}{180 * 180} \cdot \left[\frac{0.199}{5.48} + \frac{0.207}{38.18}\right]$$
$$* \left[73.438 \cdot \left(\frac{5.48}{38.18}\right)^1 \cdot 0.0412\right] \cdot 0.1 = 0.000737008\ rad2$$

This is equivalent to **1.56 degrees in alpha which as being the maximum will be considered as the uncertainty in that direction**

A.2. Pitot configurations

Danaero has provided several schemes where different configurations can be made

Pneumatic Option #1

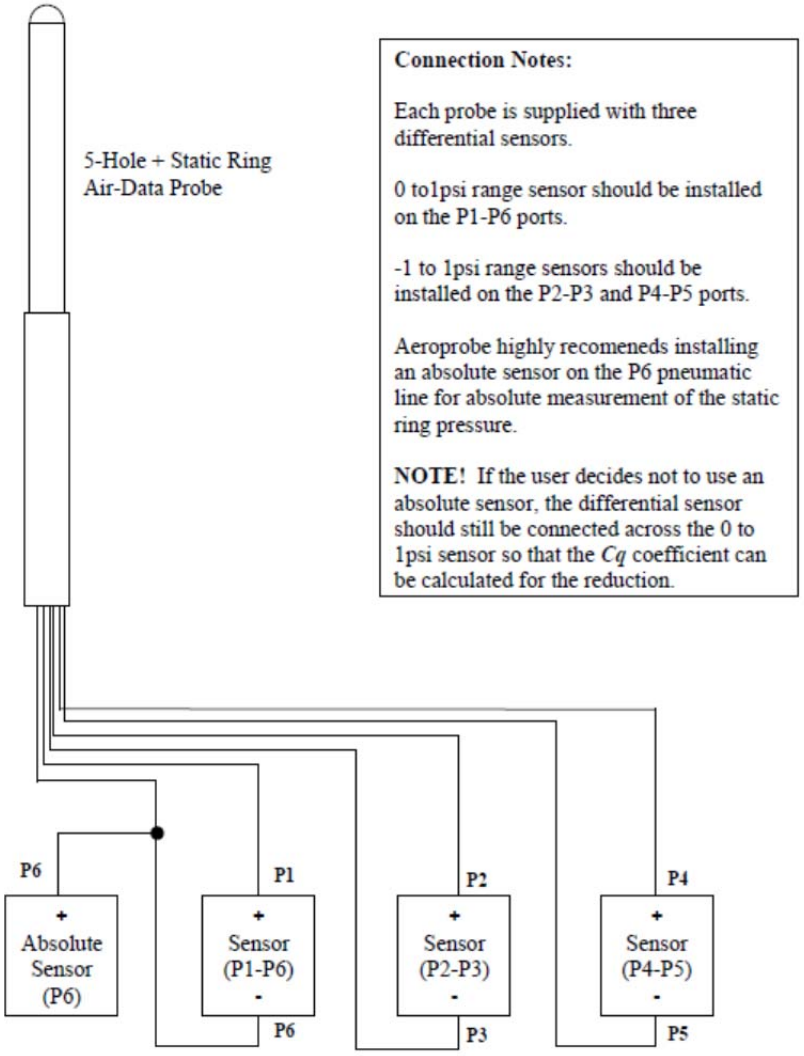

* The absolute sensor measures the probe static ring pressure directly. The user would use "Sample Reduction Method 2" directly.

Pneumatic Option #2

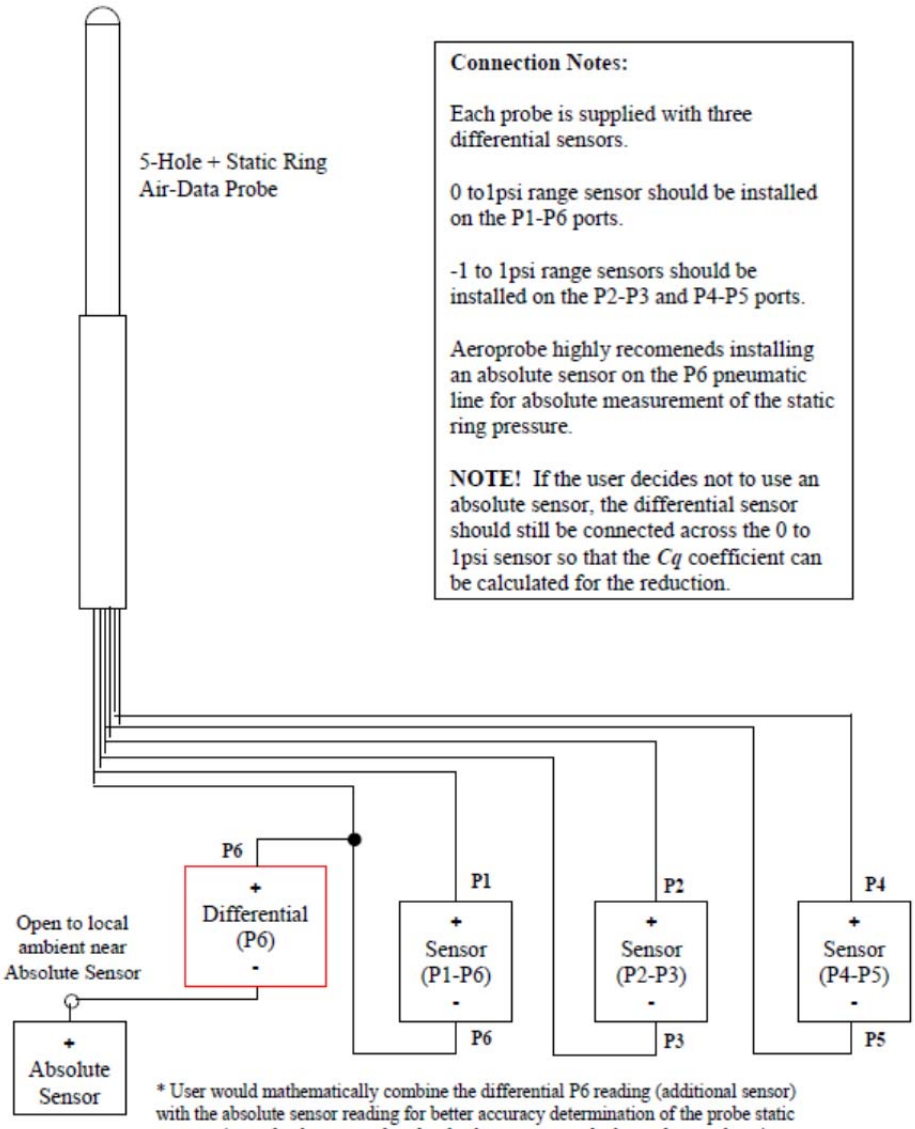

* User would mathematically combine the differential P6 reading (additional sensor) with the absolute sensor reading for better accuracy determination of the probe static pressure in an absolute sense, but the absolute sensor can be located at any location. For reduction, the user can use "Sample Reduction Method2" and insert the resultant pressure reading into the Ps column (Column D is not used), OR use "Sample Reduction Method3" and use the resultant pressure reading to calculate a density.

Probe Pneumatic Connection #3

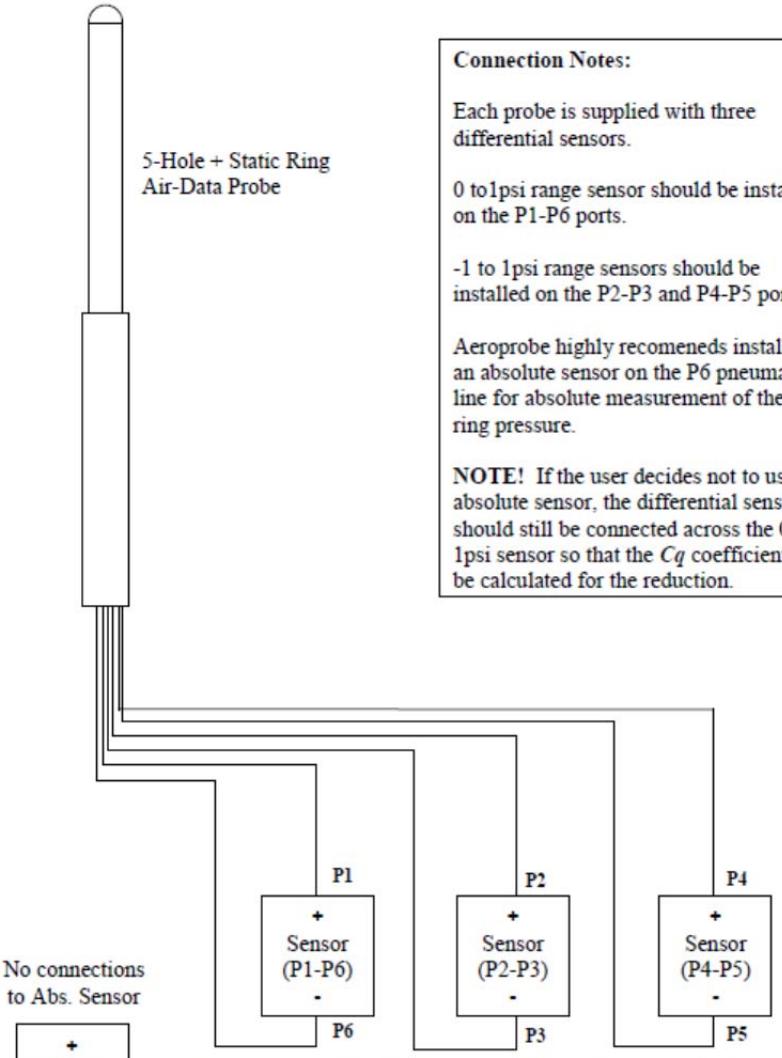

Connection Notes:

Each probe is supplied with three differential sensors.

0 to1psi range sensor should be installed on the P1-P6 ports.

-1 to 1psi range sensors should be installed on the P2-P3 and P4-P5 ports.

Aeroprobe highly recomeneds installing an absolute sensor on the P6 pneumatic line for absolute measurement of the static ring pressure.

NOTE! If the user decides not to use an absolute sensor, the differential sensor should still be connected across the 0 to 1psi sensor so that the *Cq* coefficient can be calculated for the reduction.

* The user measures the local ambient pressure near the hub or ground and assumes this pressure is the local static pressure at the location of the probe at all times. Then use "Sample Reduction Method2" and insert the absolute sensor reading into the Ps column manually (Column D is not used), OR use "Sample Reduction Method3" and calculate the density for the reduction using the measured absolute pressure. In this case, "Sample Reduction Method3" is recommended.

A.3. Nordtank full channel list

Ch#	Name	Gain	Offset	Unit	description
			Turbine		
	HH	–	–	–	Hour of measurement from windows clock
	MM	–	–	–	Minutes of measurement from windows clock
	SS	–	–	–	Seconds of measurement from windows clock
4	Mz_TT	1136.1	840	kNm	Tower top torsion, h=
5	MTBEW	1447.33	194.01	kNm	MyTB, tower bottom, EW
6	MTBNS	1341.09	195.01	kNm	MzTB, tower bottom, NS
7	Pe	1	0	kW	Active power
12	IO_tip	1	0	0/1	Tip activated (0/1)
13	IO_brk	1	0	0/1	Brake activated (0/1)
14	IO_gen	1	0	0/1	Generator grid conn. (0/1)
21	Yaw	1	0	Deg	NP- nacelle position
22	Rot_Azi_Pos	1	0	Deg	Azimuth, top=0
23	Rot_Speed_slow	1	0	rpm	Rotor speed main shaft
24	Rot_Speed_fast	1	0	rpm	Rotor speed generator shaft
25	WS_Nac	1	0	m/s	WSN - nacelle wind speed
37	WD_Nac	1	-180	Deg	WDN - nacelle wind direction
38	MxNR	193.2	-87	kNm	Torque, main shaft
39	MyNR	79.45	23	kNm	BM main shaft MYNR
40	MzNR	86.66	-245	kNm	BM main shaft MZNR
41	MxV1	-152.88	412	kNm	B1.Edgewise
42	MyV1	-114.5	77	kNm	B1.Flapwise
43	MxV2	-173.74	114	kNm	B2.Edgewise
44	MyV2	-117.17	287	kNm	B2.Flapwise
45	MxV3	-150.54	147	kNm	B3.Edgewise
46	MyV3	127.39	337	kNm	B3.Flapwise
	Acc_Gearx	2.212389	-4.86062	[g]	Acceleration Gearbox forth\back
	Acc_Geary	2.267574	-5.38549	[g]	Acceleration Gearbox sideway
	Acc_Gearz	2.257336	-5.17381	[g]	Acceleration Gearbox up\down
	Acc_Nacx	2.227171	-4.70379	[g]	Acceleration Nacelle forth\back
	Acc_Nacy	2.217295	-4.19734	[g]	Acceleration Nacelle sideways
	Acc_Nacz	2.309469	-4.65127	[g]	Acceleration Nacelle up\down
	TBAcc_x1	2.212389	-4.77655	[g]	Tower Acceleration 140 cm from top flange turbine-mast dir
	TBAcc_y1	2.227171	-7.34967	[g]	Tower Acceleration 140 cm from top flange transverse dir
	TBAcc_x2	2.207506	-5.85872	[g]	Tower Acceleration 80 cm from flange turbine-mast dir
	TBAcc_y2	2.325581	-5.97674	[g]	Tower Acceleration 80 cm from flange transverse dir
			Tall Mast		

112	WS_57	1	0	m/s	WS, h=57 m, windsensor cup anemometer, top mounted boom
	WS_54_North	1	0	m/s	WS-North, h=54 m , windsensor cup anemometer, boom in north direction
	WS_54_South	1	0	m/s	WS-South, h=54 m, , windsensor cup anemometer, boom in south direction
	Sstat _52_5	1	0	[-]	Status Sonic@52.5m
	SX _52_5	1	0	[m/s]	Speed Vector x-direction@52.5m
	SY _52_5	1	0	[m/s]	Speed Vector y-direction@52.5m
	SZ _52_5	1	0	[m/s]	Speed Vector z-direction@52.5m
	ST _52_5	1	0	[Deg C]	Air temperature Sonic@52.5m
	Sspd _52_5	1	0	[m/s]	Speed Sonic@52.5m
	Sdir _52_5	1	0	[Deg]	Horizontal wind Direction@52.5m
	Stilt _52_5	1	0	[Deg]	Tilt angle 52.5m
	WS_45_South	1	0	m/s	WS, h=45 m , windsensor cup anemometer, boom in south direction
115	WS_36_North	1	0	m/s	WS-North, h=36 m
116	WS_36_South	1	0	m/s	WS-South, h=36 m
	Sstat _34_5	1	0	[-]	Status Sonic@34.5m
	SX _34_5	1	0	[m/s]	Speed Vector x-direction@34.5m
	SY _34_5	1	0	[m/s]	Speed Vector y-direction@34.5m
	SZ _34_5	1	0	[m/s]	Speed Vector z-direction@34.5m
	ST _34_5	1	0	[Deg C]	Air temperature Sonic@34.5m
	Sspd _34_5	1	0	[m/s]	Speed Sonic@34.5m
93	Sdir _34_5	1	0	[Deg]	Horizontal wind Direction@34.5m
	Stilt _34_5	1	0	[Deg]	Tilt angle 34.5m
121	WS_18_North	1	0	m/s	WS-North, h=18 m
122	WS_18_South	1	0	m/s	WS-South, h=18 m
	Sstat_16_5	1	0	[-]	Status Sonic@16.5m
	SX_16_5	1	0	[m/s]	Speed Vector x-direction@16.5m
	SY_16_5	1	0	[m/s]	Speed Vector y-direction@16.5m
	SZ_16_5	1	0	[m/s]	Speed Vector z-direction@16.5m
	ST_16_5	1	0	[Deg C]	Air temperature Sonic@16.5m
	Sspd_16_5	1	0	[m/s]	Speed Sonic@16.5m
	Sdir_16_5	1	0	[Deg]	Horizontal wind Direction@16.5m
	Stilt_16_5	1	0	[Deg]	Tilt angle 16.5m
118	Tabs_54	1	0	deg C	Absolute Air Temp, h=54 m
	Tdiff_54_10	1	0	deg C	Differential Temp, 54m - 10m
119	Pressure_mast	1	0	hPa	Pressure 2m
			Short Mast		
	Sstat_M2_31_5	1	0	[-]	Status Sonic@31.5m - top mounted on short mast
	SX_M2_31_5	1	0	[m/s]	Speed Vector x-direction@31.5m - top mounted on short mast
	SY_M2_31_5	1	0	[m/s]	Speed Vector y-direction@31.5m - top mounted on short mast
	SZ_M2_31_5	1	0	[m/s]	Speed Vector z-direction@31.5m - top mounted on short mast
	ST_M2_31_5	1	0	[Deg C]	Air temperature Sonic@31.5m - top mounted on short mast
	Sspd_M2_31_5	1	0	[m/s]	Speed Sonic@31.5m - top mounted on short mast
	Sdir_M2_31_5	1	0	[Deg]	Horizontal wind Direction@31.5m - top mounted on short mast

	Stilt_M2_31_5	1	0	[Deg]	Tilt angle 31.5m - top mounted on short mast
16	Rain2	1	0	0/1	Rain short mast
			Spinner anemometer		
	gama_Av				yaw missalignment from spinner - 1 probe
	beta_Av				flow inclination from spinner -1 probe
	gama				yaw missalignment from spinner
	beta				flow inclination from spinner
	V1				Vspinner
	V2				Vspinner
	V3				Vspinner
	Temp_1				Tspinner
	Temp_2				Tspinner
	Temp_3				Tspinner
	Acc_1				Accelerometer Spinner
	Acc_2				Accelerometer Spinner
	Acc_3				Accelerometer Spinner
	Theta				Rotor position from spinner
	rotor_pos				Rotor position from spinner
	rotor_speed				Rotor speed from spinner
	Speed_Av				Horizontal speed Spinner - 1 probe
	speed				Horizontal speed Spinner
	Speed_Quality				Quality Spinner Data
	Acc_Quality				Quality Spinner Data
	Calculation_Quality				Quality Spinner Data
			Not working		
	Sstat				Sonic Nacelle
	Sheat				Sonic Nacelle
	SX				Sonic Nacelle
	SY				Sonic Nacelle
	SZ				Sonic Nacelle
	ST				Sonic Nacelle
	Sdir				Sonic Nacelle
	Sspeed				Sonic Nacelle
	Stilt				Sonic Nacelle
	WS_hh				Previous measurements on short mast
	T_Air				Previous measurements on short mast
	B_Air				Previous measurements on short mast
	Shaft_tors2				Shaft torsion in gearbox
	Shaft_tors3				Shaft torsion in generator

A.4. Raw signals corrections

A.4.1. Raw measurements:

Some strange noise affected the air barometric pressure signal as shown in **Error! Reference source not found.** as a negative replication of the signal itself. The maximum value of that shape was occurring at the digital value 24063, and the value where the mean was floating was 23807. The difference between them is 256, i.e. 2^8.

Table 25.- Change in the bits causing the error

Bits	14	13	12	11	10	9	8	7	6	5	4	3	2	1	0
23807	1	0	1	1	1	0	0	1	1	1	1	1	1	1	1
24063	1	0	1	1	1	0	1	1	1	1	1	1	1	1	1

However, the signal can be easily corrected by applying a 12-point moving minimum filter with a windowing of 0.12 seconds in Dadisp, equivalent to ~20 degrees of a rotor revolution.

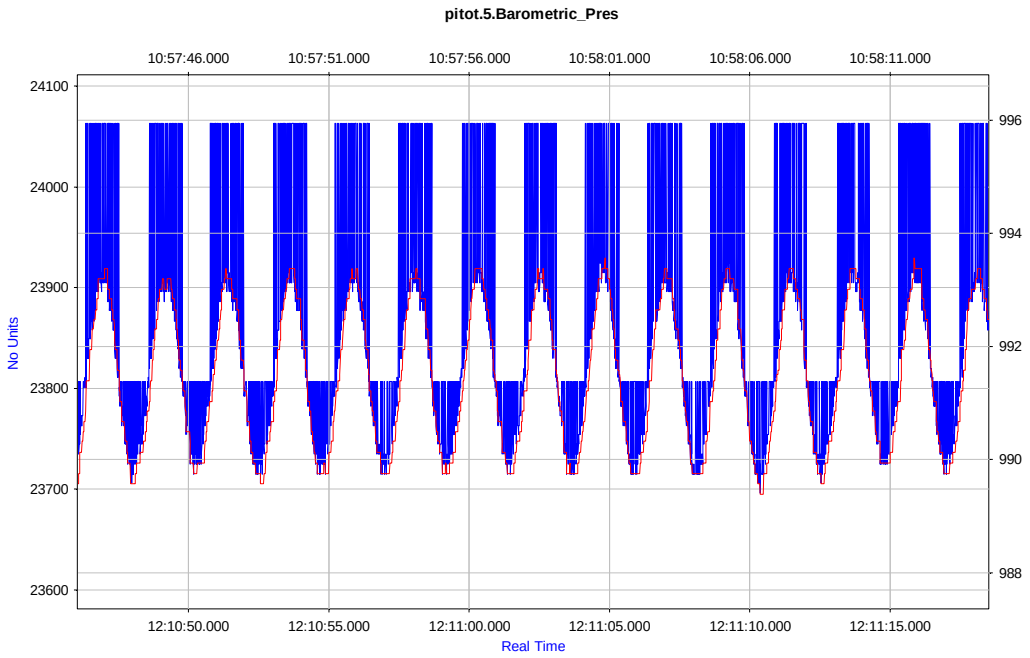

Figure 204 Cleaned signal and original signal (blue). On the vertical Axis on the left digital signal is represented (blue) and on the right, the vertical Axis are in hPa

The spectral analysis gave the rotational speed as expected (0.45 Hz).

This jump cannot be derived from gravity effects thus is not

Figure 205 non symmetrical error

symmetrical. Seems an activation of the bits 2^0 to the 2^7 periodically, which can be produced by several causes but seems more a protocol/hardware error

In 5000 seconds, there is an integration of app 4000 events, i.e. it happens every 400000/5000 = 80Hz or at a multiple of it

From the sinusoidal shape it can be derived in which blade was installed (if pressure higher at lower attitude and comparing with the edgewise of the blades the maximum of the edgewise should belong to the crossing zero point. In this case it fits for the second blade (MxV2)

Accelerometer X-axis

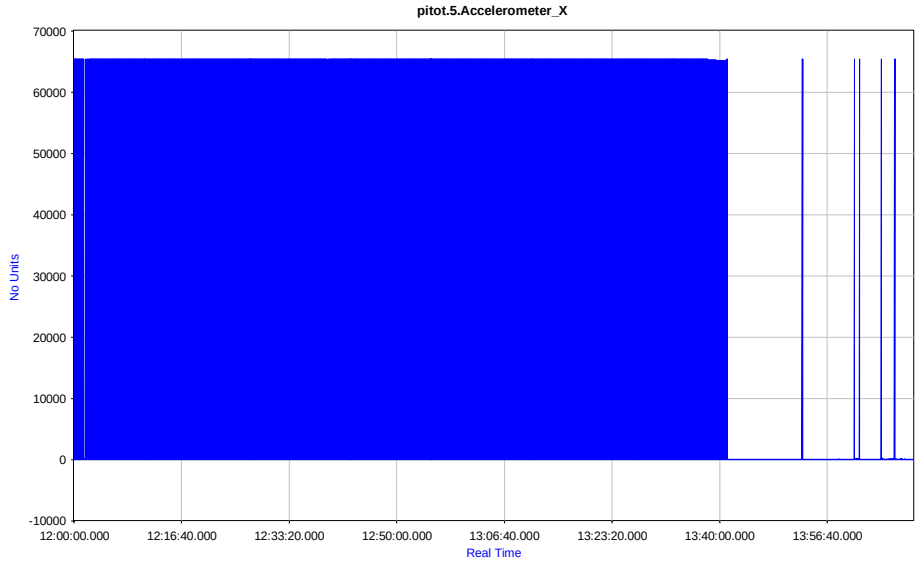

Figure 206 The acceleration in X is reaching saturation point

The signal varies jumping from 0 to 65536 continuously, which is the maximum value2^{16}. This is clear an error that can be corrected with product-array logic

$$acc_{x\_corr} = \left(\left(acc_x < \frac{65536}{2}\right) \cdot \left(acc_x + \frac{65536}{2}\right)\right) + \left(\left(acc_x > \frac{65536}{2}\right) \cdot \left(acc_x - \frac{65536}{2}\right)\right)$$

The result is shown as it follows:

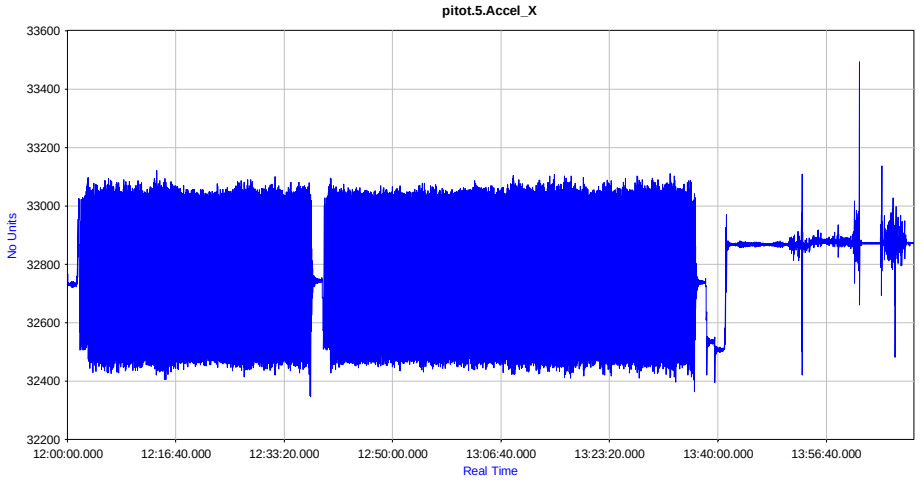

Figure 207 corrected Acceleration-X, yet uncalibrated

The point of equilibrium has being chosen in the mid-range assuming that this point belongs to 0, nevertheless this equilibrium point must be checked with the measurements in the Nordtank.

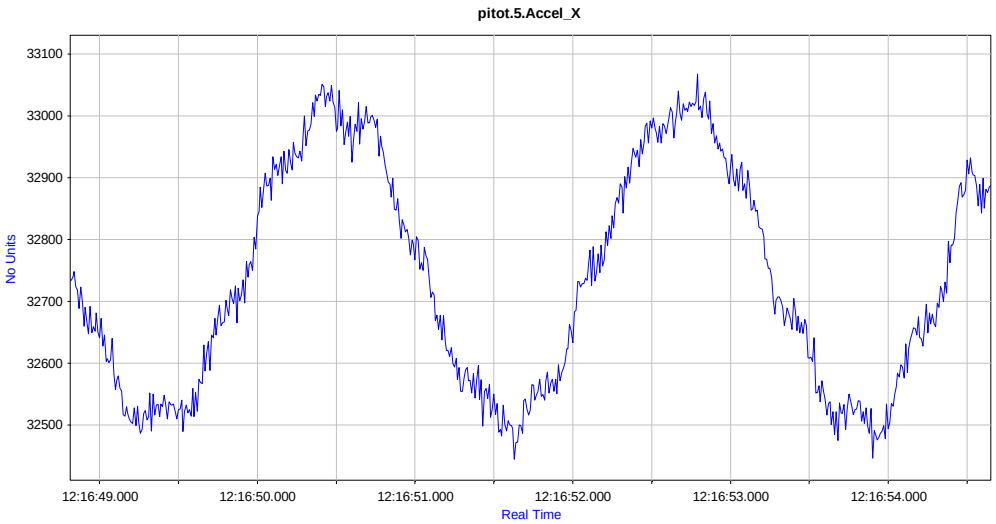

Figure 208 zoom in the signal

The constant value among a position just can be justified with the gravity force

Once the signal is “corrected”, a frequency analysis will be performed in normal operation

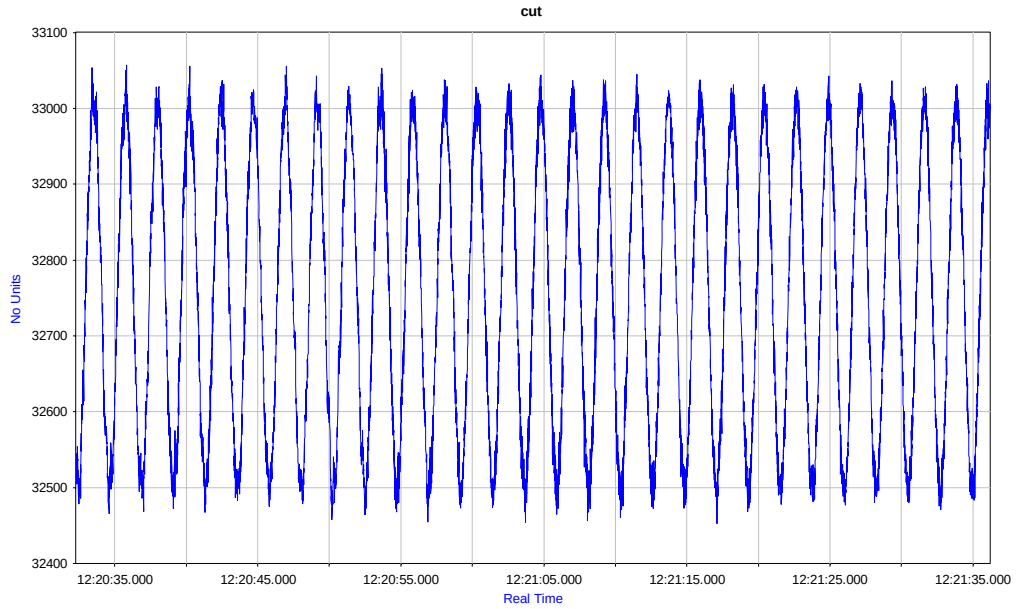

Figure 209 Extracted signal in NOP

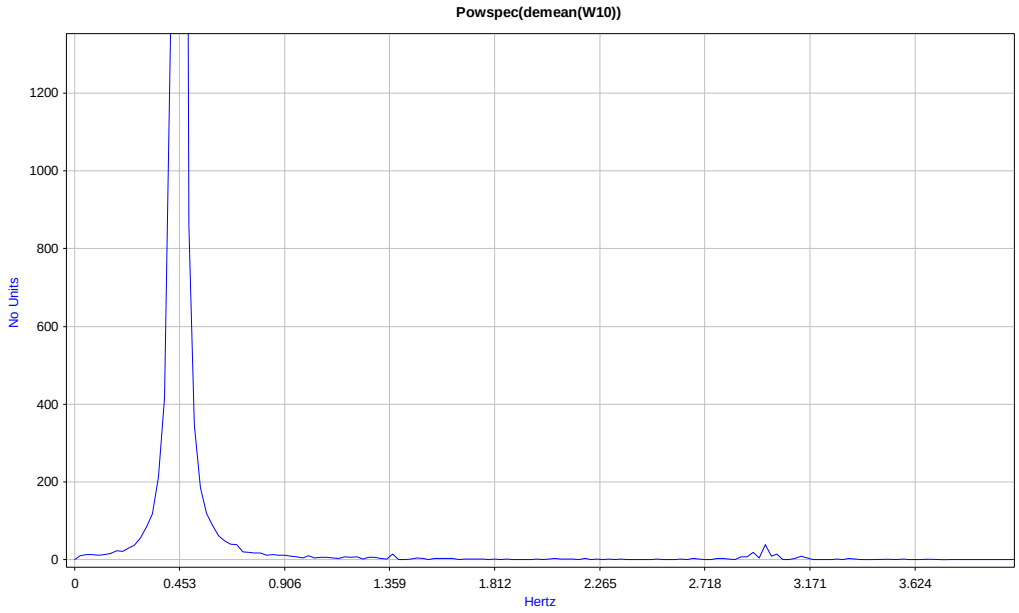

Figure 210 NOP peak value in Acc. X at 0.453Hz

Accelerometer Y-axis

On the signal it is clear that it has being reached a saturation limit in the lowest side

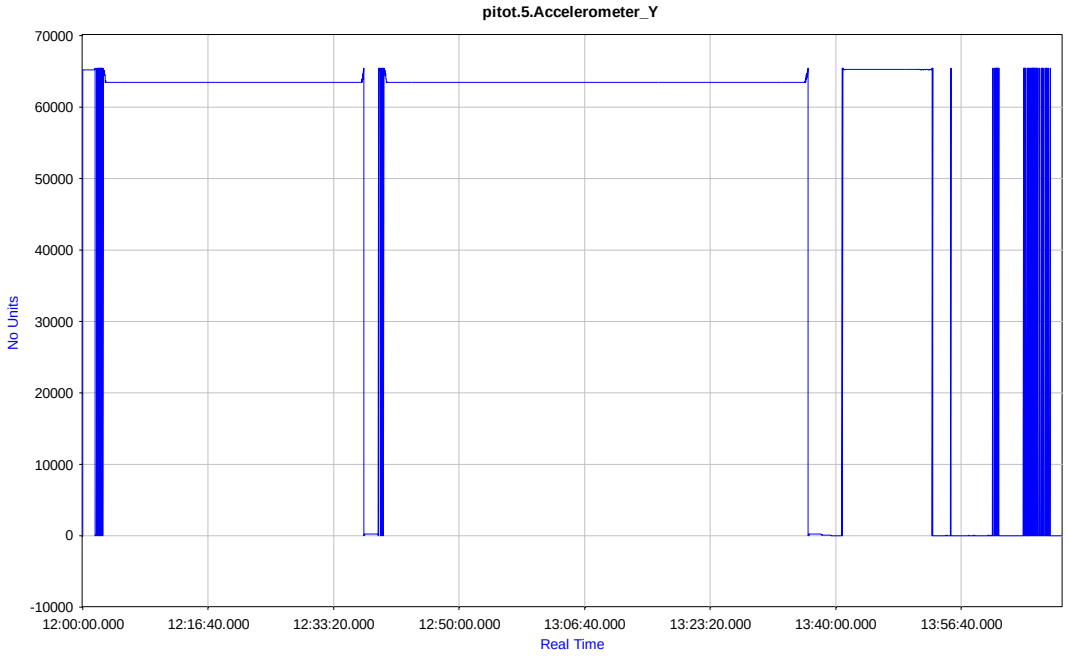

Figure 211 Acceleration Y

In this specific case it will not be considered the mean value of the range as the reference but the lowest limit of the upper section, i.e. the expected lower saturation limit. This reached negative saturation limit could indicate that the acceleration board had the Y axis in opposite direction of the maximum amplitude, i.e. It is clear that the Y is pointing in the centrifugal forces created by the normal operation but it does point in negative direction

$$acc_{y\_corr} = -\left(\left(acc_y - 63487 < 0\right) \cdot \left(acc_y - 63487 + \frac{65536}{2}\right)\right) + \left(\left(acc_y - 63487 > 0\right) \cdot \left(acc_y - 63487 - \frac{65536}{2}\right)\right)$$

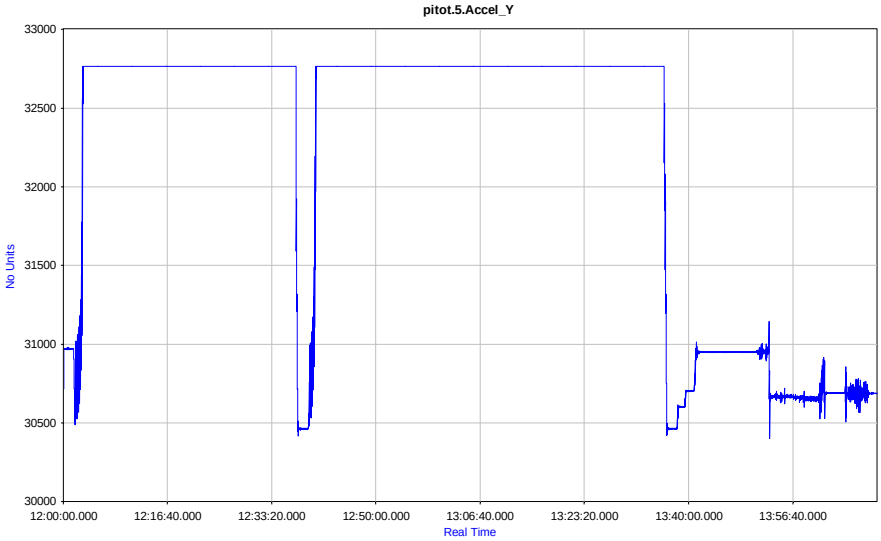

Figure 212 Recovered signal (the sign has being inverted)

The constant value among a position just can be justified with the gravity force

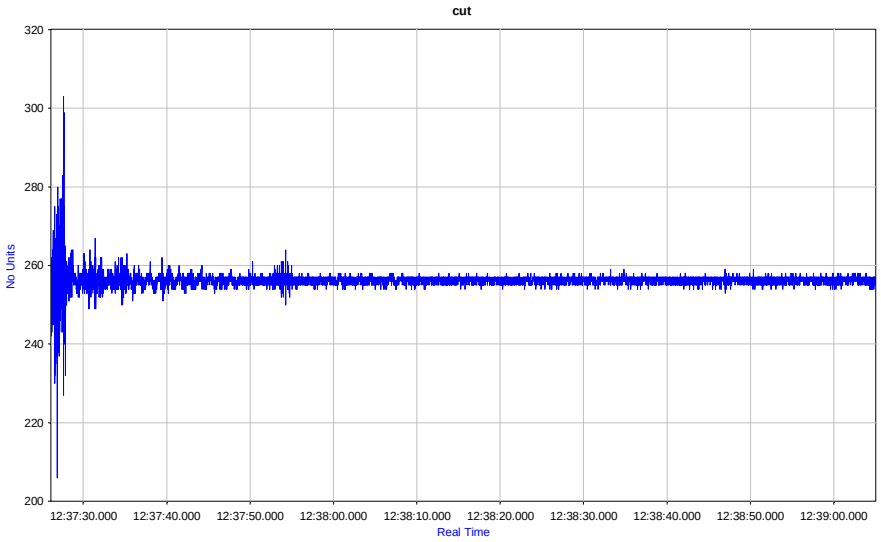

Figure 213 Manual stop

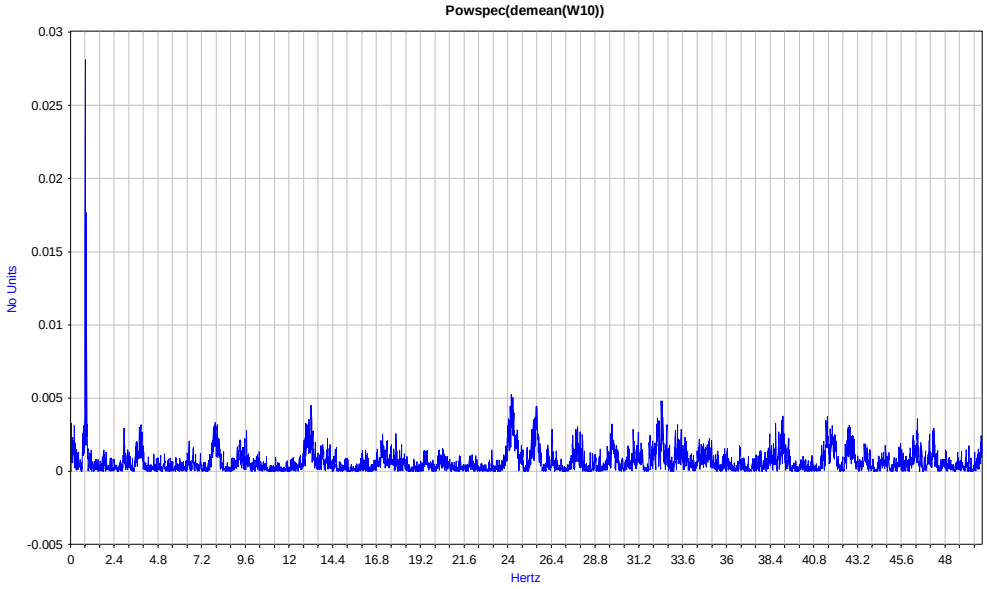

Figure 214 peak at 0.8Hz

On saturation reached (NOP) did not make any sense to get the signal.

6.2.6 Accelerometer Z-axis

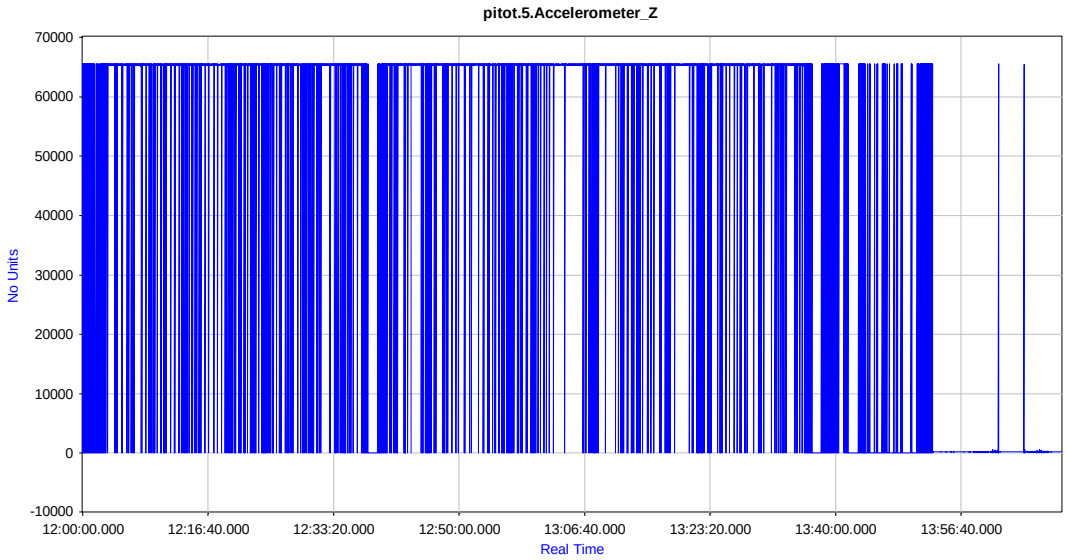

Figure 215 In Z same problem as in X does occur

$$acc_{z\_corr} = \left(\left(acc_z < \frac{65536}{2}\right) \cdot \left(acc_z + \frac{65536}{2}\right)\right) + \left(\left(acc_z > \frac{65536}{2}\right) \cdot \left(acc_z - \frac{65536}{2}\right)\right)$$

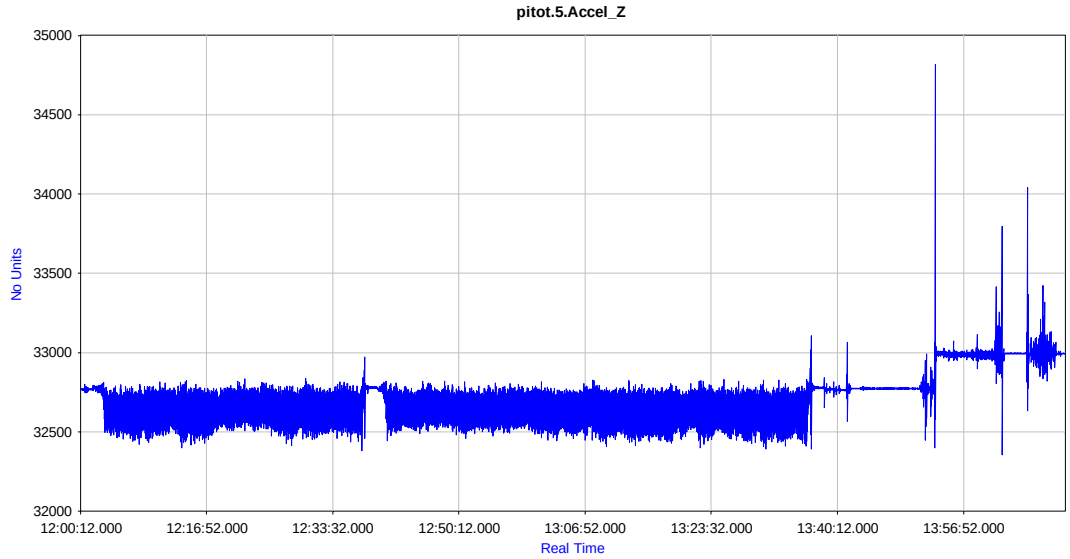

Figure 216 Recovered acceleration in Z

The constant value among a position just can be justified with the gravity force

Once the signal is “corrected”, a frequency analysis will be performed in normal operation

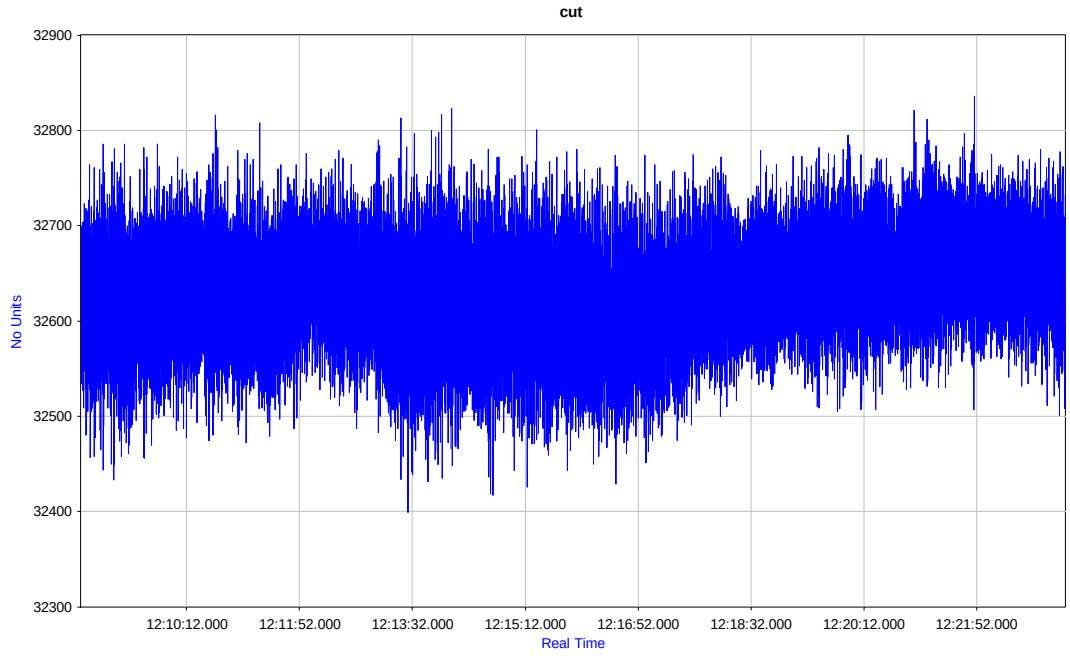

Figure 217 Acceleration Z in NOP

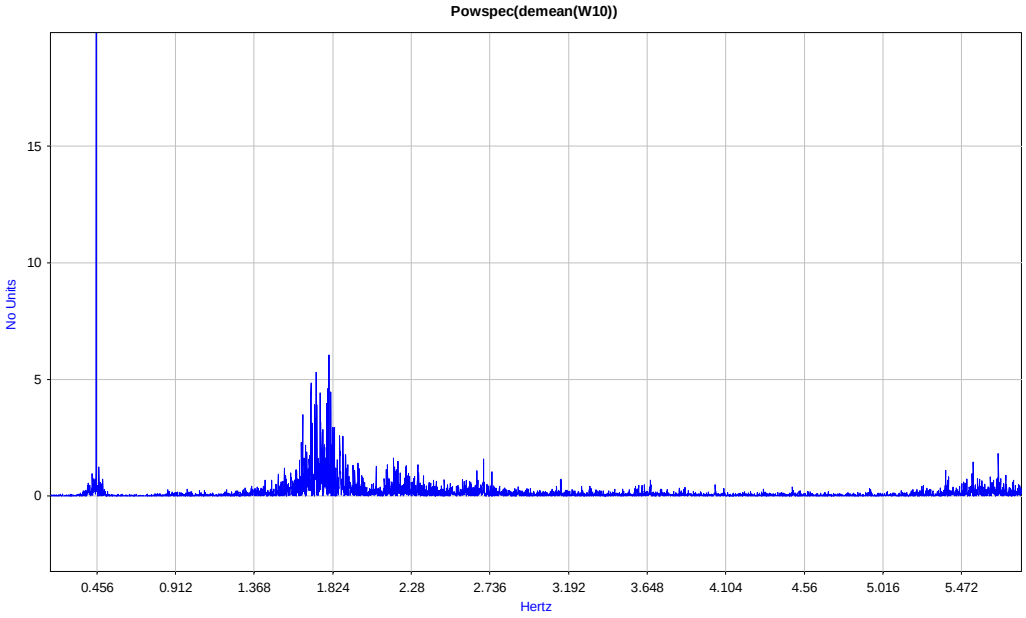

Figure 218 Frequency analysis. Maximum peak at 0.45 Hz

Calibration factors from spreadsheets

It has being applied some calibration factors on the previous design which will be hereby described. The following factors are extracted from the original code

Pressure transducers

On the pressure transducers the output belongs to:

Table 26.- Digital values for the pressure transducers

	Decimal	**Pressure**
	HLCA0025…B	
Max	27852	25mBar
Min	1638	-25mBar
	HLCA0025…U	
Max	27852	25mBar
Min	0	0
	HDI0611ARZ8P5	
Max	29490	1100mBar
Min	3277	600mBar

This expressed in equations is determined in

$$P_{3-5_{25mbar}} = 0.0019 \cdot x - 28.0155$$

$$P_{1-6_{25mbar}} = 0.0008976 \cdot x$$

$$P_T = 0.01907 \cdot x + 537.5076$$

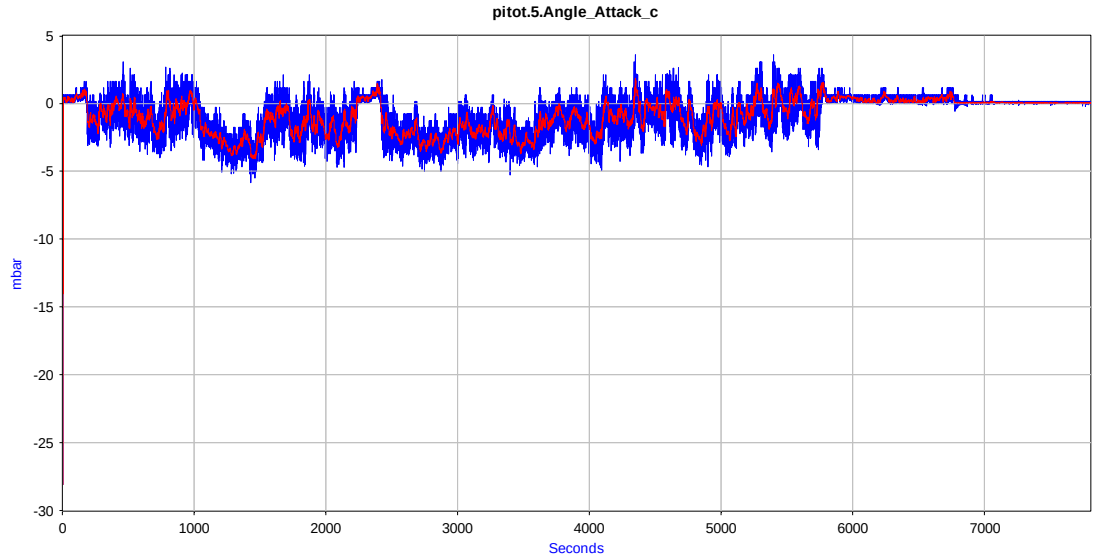

Figure 219 angle of attack pressure (blue) with its average in red of 222 samples (i.e. 0.45Hz)

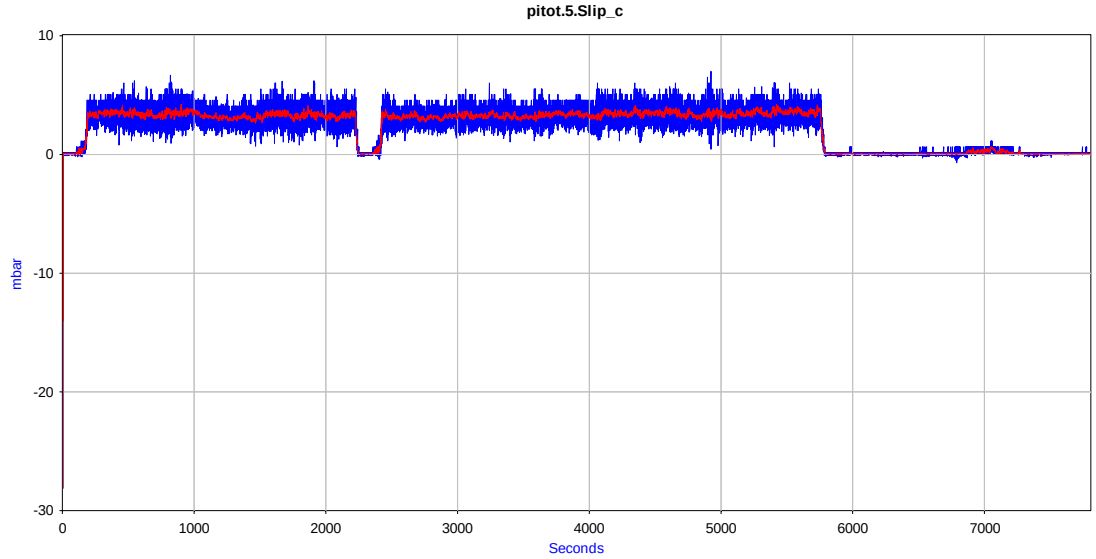

Figure 220 slip pressure (blue) with its average in red of 222 samples (i.e. 0.45Hz)

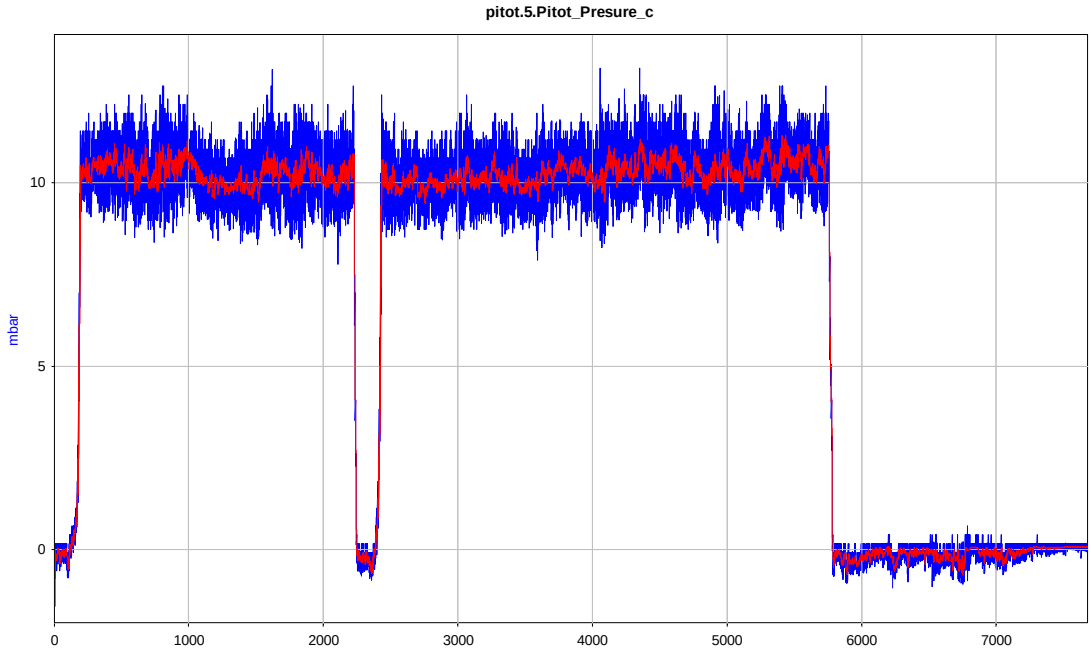

Figure 221 pitots pressure (blue) with its average in red of 222 samples (i.e. 0.45Hz)

After applying the calibration the result when rotating is the shown in Figure 222

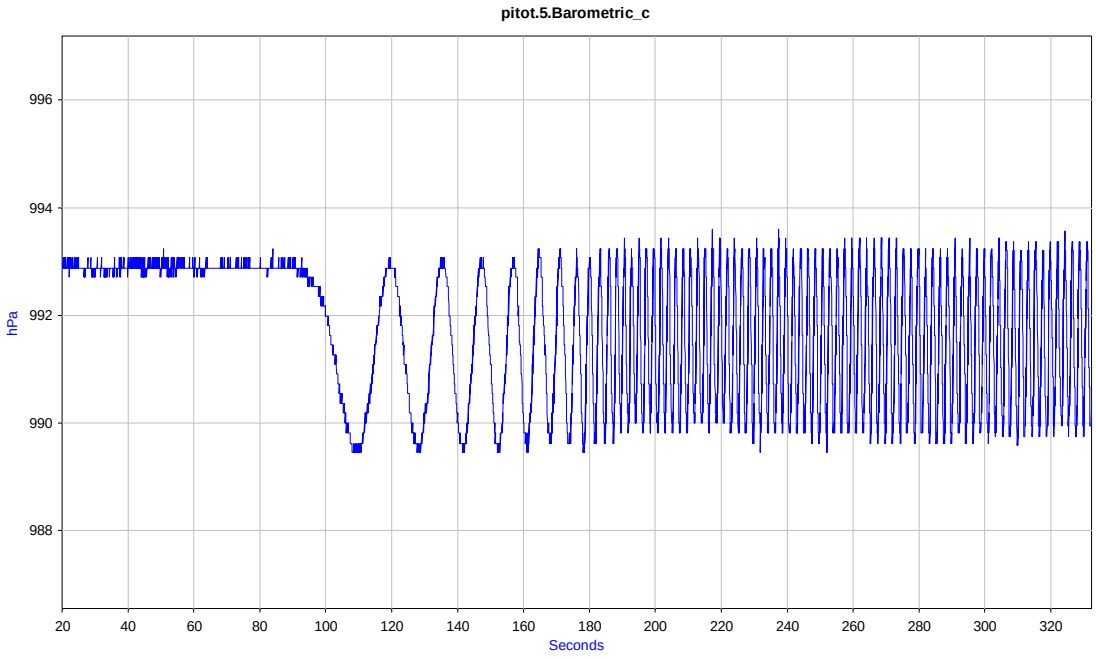

Figure 222 Barometric Pressure

Accelerometers

The accelerometers have two limits on two sides:

Max positive range: 7,996
Min positive range: -8

The accelerometer in this case has a saturation limit which does not fit with the specified 2^{12}. but with 2^{16}. Nevertheless it is proven that the real factor to be applied on 2^{12}. rather than 2^{16}., taking the gravity cycle and making a fast comparison

Assuming that all the accelerations have the same factors, it has being derived from the $\mathrm{acc_x}$ the value following the gravity force should be as shown in **Error! Reference source not found.**

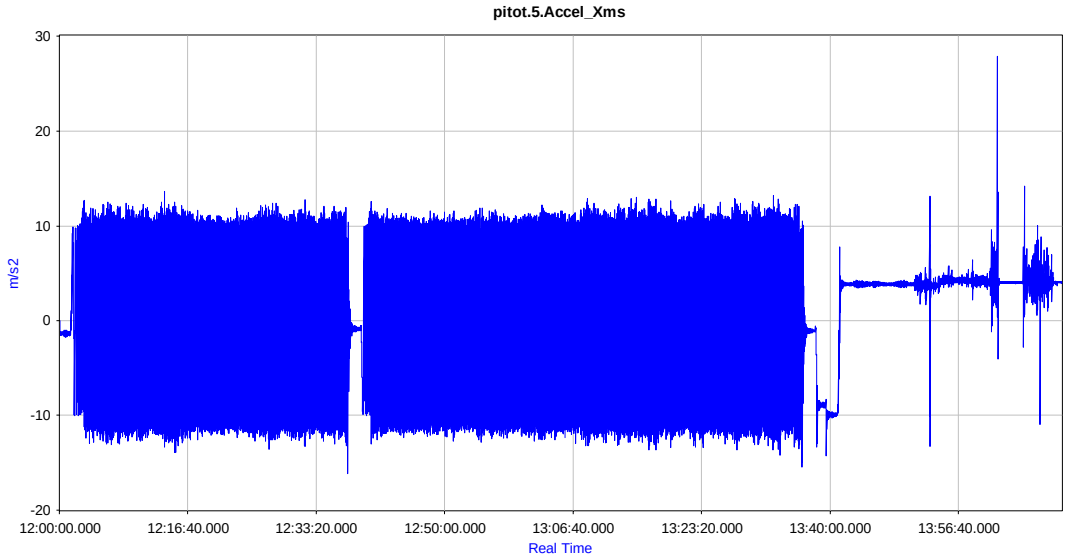

Figure 223 First approximation for the signal acc_x

This with an approximation belongs to: 9.8*(w15-32735)/313

In order to crosscheck the values it is done the same with the signal acc_y taking in account the maximum saturation limit, i.e. 8g, and then derive if truly the saturation limit belongs to the scale factor of 2^{12}.

Comparing both values seems more appropriate to adapt the saturation range to the final value, i.e. 0.03832 as slope. This value fits with

$$0.03832 = 9.81 \cdot \frac{(8 - -8)}{2^{12}}$$

So to sum up:

- the slope is 0.03832 m/s2
- saturation limit of 8 g is proven

- The offset belongs to -0.03832*2^16/2, i.e. -1255.7 m/s2. On the Y acceleration a correction of +8*9.81 must be done in addition to this amount

Combined signals

Accelerations

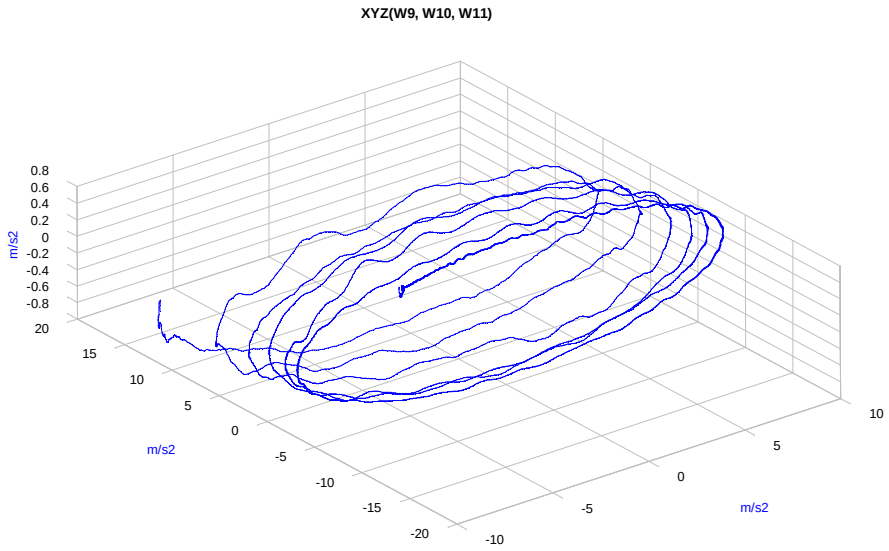

Figure 224 3D averaged plot of the accelerometers when starting wind turbine

The vertical axis belongs to Z. The X-Z plane describes an ellipsoidal figure and Y is slowly accelerating, this was clear before that the Y-axis coincided with the centripetal acceleration. From low speed signals it can be derived that the X-Y plane is the same plane as the blade and Z is perpendicular to the blade gyroscope.

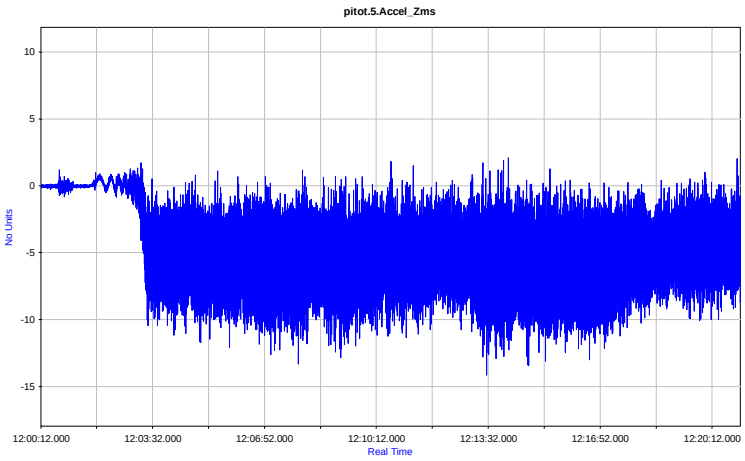

Figure 225 acceleration in Z axis.

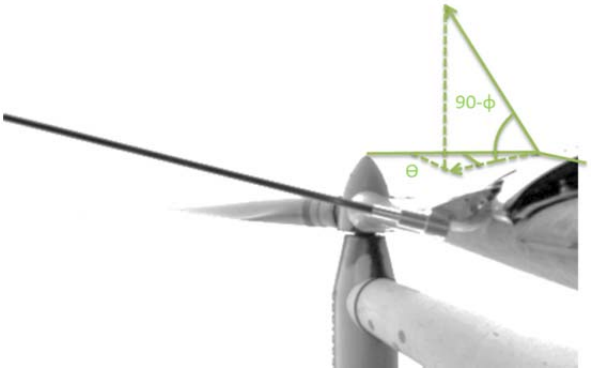

The acceleration in Z-axis indicates that the angle derived from the absence of acceleration due to gravity should be close to 0

The variation of the flatwise among the blade is

Having the blade a length of 19.4 meters, and assuming as an estimation a linear thrust distribution along the blade the acceleration in the tip could vary

Figure 226. Position of the Accelerometer in the Z-Axis

$$\Delta acc_z = \sqrt{\frac{2 * Mb_f}{m * l^2}}$$

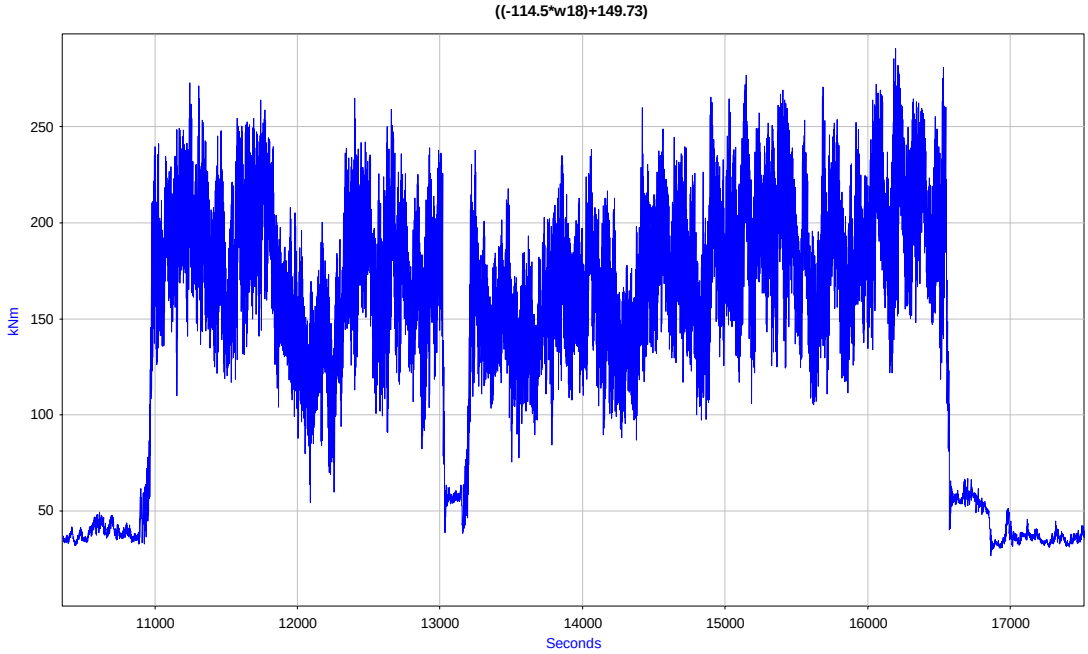

Figure 227.- Variation of the flatwise within operation and stop. The calibration is extracted from another report.

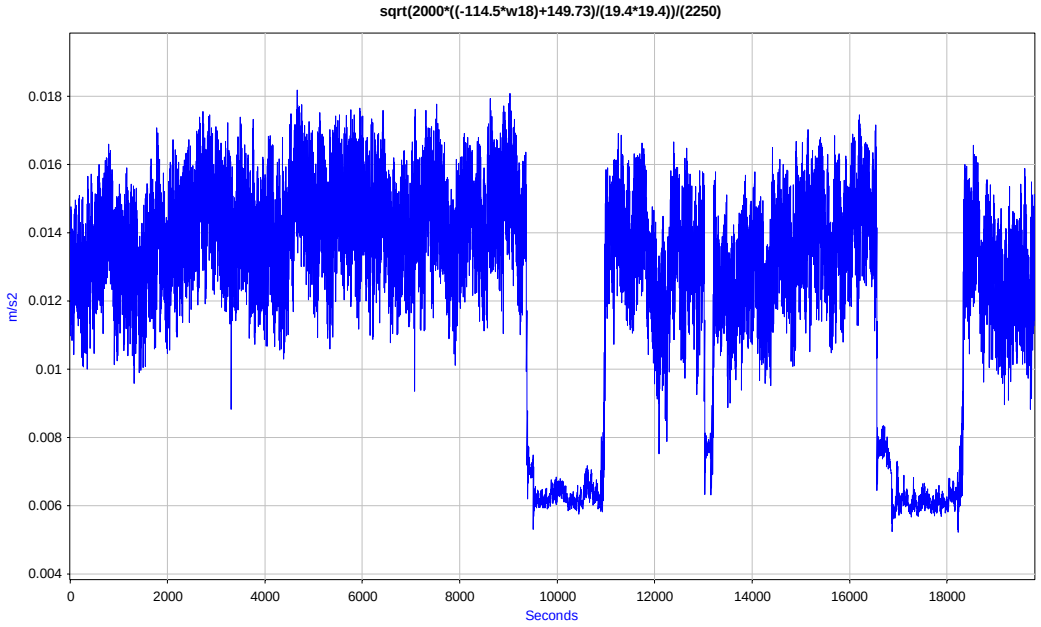

Figure 228.- Increment of acceleration from stop to NOP

The acceleration in Z axis is giving around 5m/s2 on NOP. There is no reason to believe that it is not real, and that imply two different reasons explained in the next equation.

$$acc_z = g * cos\emptyset \pm \Delta acc_z * sin\emptyset \pm 14.8 * w^2 * sin\theta$$

a) There is an influence of the tilt angle: and the blade is deforming up to an extent that the accelerometer sees that effect. This seems an influence due to the gravity and wind would have being describing sinusoidal shapes and stochastic changes which is indeed what it happens around the signal

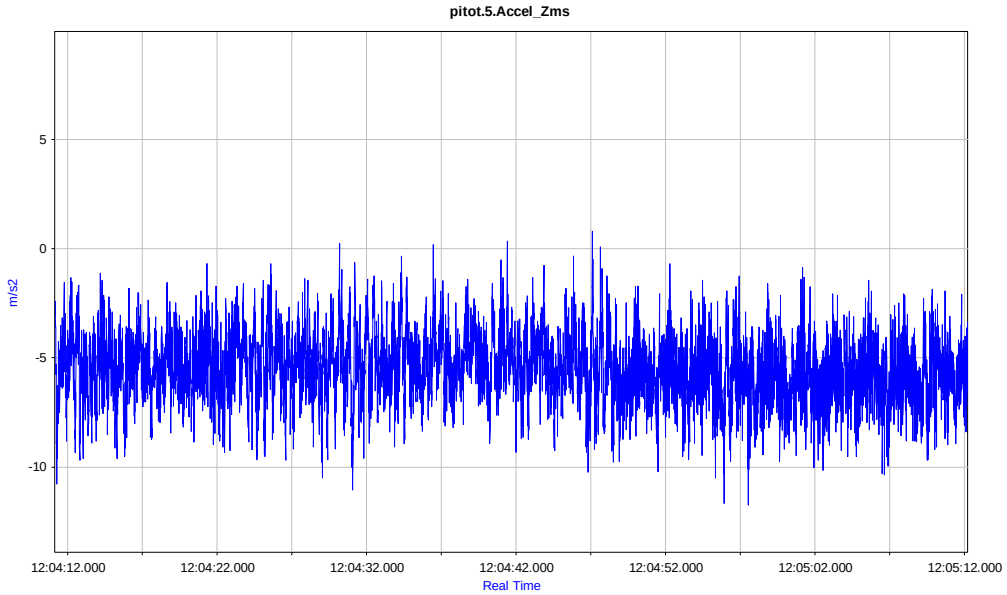

Figure 229 Detail of the centripetal forces on the Z axis

b) Centripetal forces, that seems to be in this case more realistic

The constant value of acc_z is fluctuating around 119.2754 m/s2, thereby applying

$$\theta \approx \operatorname{asin}\left(\frac{acc_z}{14.8 * w^2}\right) = 2.5$$

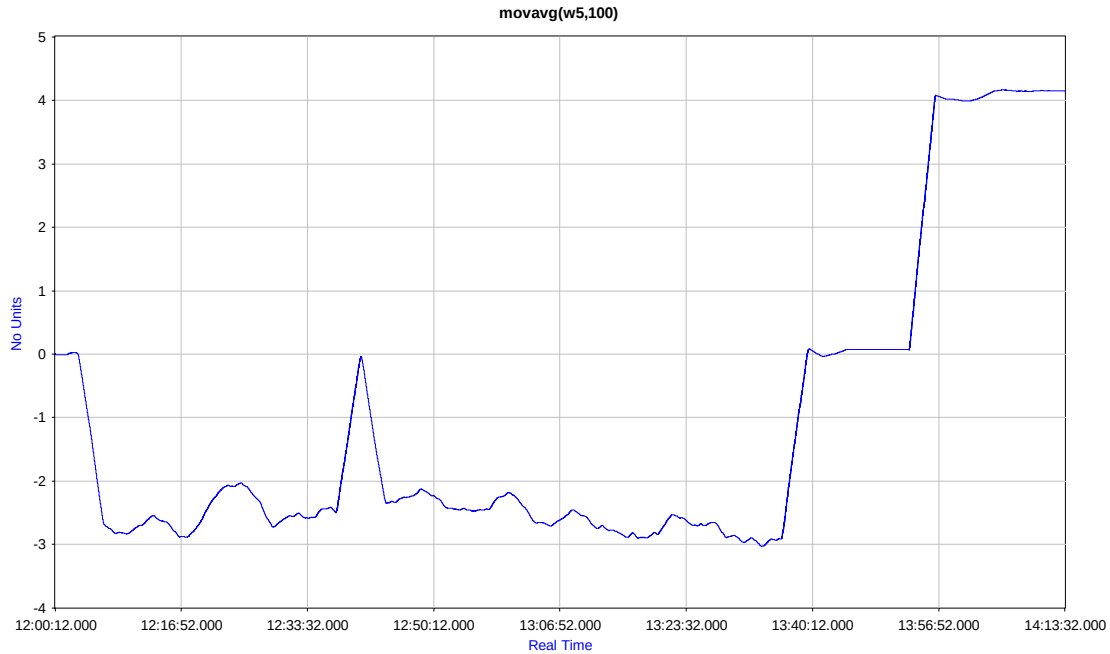

Figure 230 deviation in Z, 2.5 degrees in horizontal

A.5. Hardware scheme

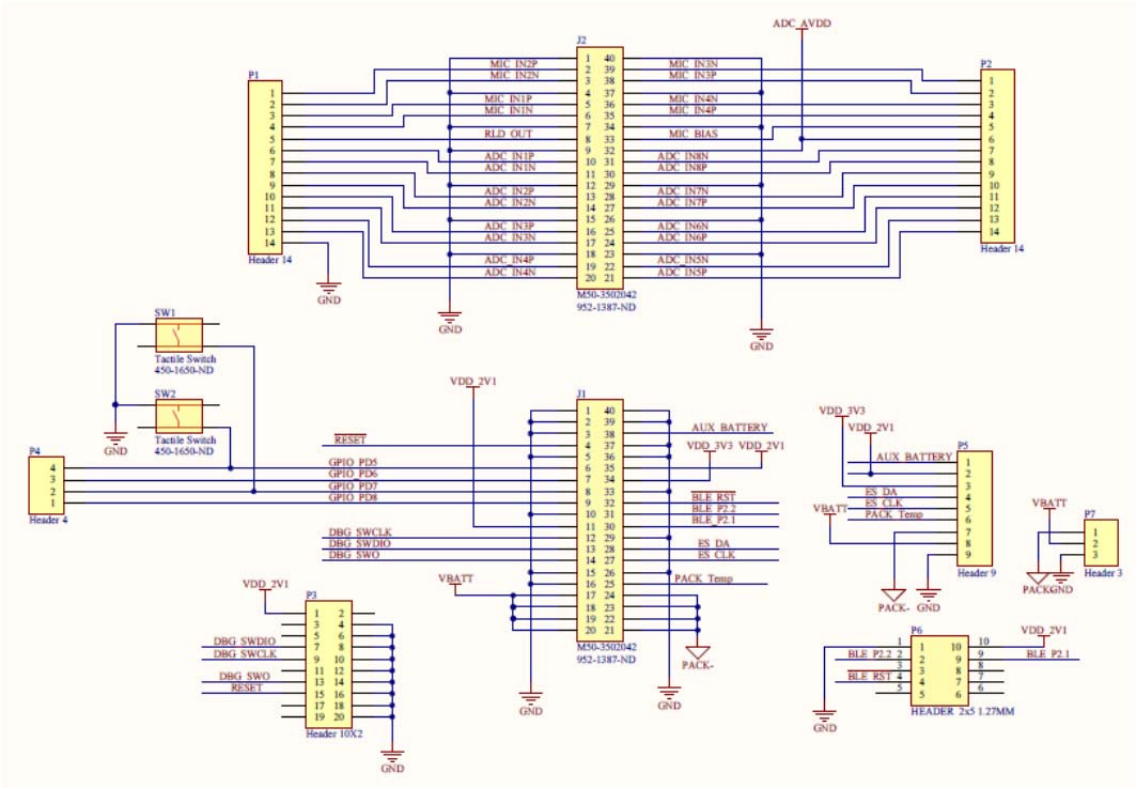

A.6. Pressure transducers list and calibrations

The pressure transducers from the blower

used in pitot	P	sensor	serial number	conected to	pressure	voltage	pressure 2	voltage2	sensitivity	formula	Theoretic slope	Pressure by formula			observations
									mbar/V		mbar/V	Pa (val1)	Pa (val2)	diff(%)	
1	p6		2377		atmosph	1.06				(2.9V+11.6)*6894	1999260	101162.556			
3	p6		2378		atmosph	1.065				(2.9V+11.6)*6894	1999260	101262.519			
2	p6		2379		atmosph	1.061				(2.9V+11.6)*6894	1999260	101182.5486			
NO	NO		2381	ve	5										pressure drops in Ve+.... some escape
2	p2-p3	1 psi	2382	ve	7.47	1.108	-4.96	0.933	71.02857143	(V-1)*6894	68.94	744.552	-461.898	3.029549505	leackage in ve and ve-. Need to be change the pressure adapters, can be quite probably solved
NO	NO		2383												different colours. Not tested
2	p4-p5	1 psi	2384	ve	4	1.085	-6.7	0.934	70.86092715	(V-1)*6894	68.94	585.99	-455.004	2.78637533	blue cable for signal is not attached. It has to be demounted. Small leakage in both ends
1	p2-p3	1 psi	2385	ve	7.15	1.12	-2.5	0.985	71.48148148	(V-1)*6894	68.94	827.28	-103.41	3.686512158	
1	p4-p5	1 psi	2386	ve-	7.61	0.912	-3.9	1.078	69.3373494	(V-1)*6894	68.94	606.672	-537.732	0.576369883	
2	p1-p6	1 psi d	2387	ve	7.68	0.262	-3.6	-0.064	34.60122699	(0.5*V)*6894	34.47	903.114	-220.608	0.380699141	small leackage in both ends
NO	NO	1 psi d	2388	p3/ve-	3.97	-0.064	-1.17	0.079	35.94405594	(0.5*V)*6894	34.47	220.608	-272.313	4.276344485	ok
3	p1-p6	1 psi d	2389	ve	4.53	0.182	-5.12	-0.095	34.83754513	(0.5*V)*6894	34.47	627.354	-327.465	1.066275388	
3	p2-p3	8 kpa	2390	ve	4.2	1.057	-4.1	0.954	80.58252427	8000*V-8000	80	456	-368	0.72815534	
3	p4-p5	8kpa	2391	ve	5	1.08	-4.26	0.964	79.82758621	8000*V-8000	80	640	-288	0.215517241	small leakage in ve+, maybe can be solved but was stubborn and difference is big. Better not to use it this time
1	p1-p6	8kpa	2392	ve	6.75	1.08	-3.8	0.949	80.53435115	8000*V-8000	80	640	-408	0.667938931	drop. Conectors must be changed

Figure 231 . Observations from the pressure transducers

A.6.1. Pressure transducers on the 2nd-12-2014

It was realized a test on the system where the linearity was proven. Here are the results on the pressure transducers

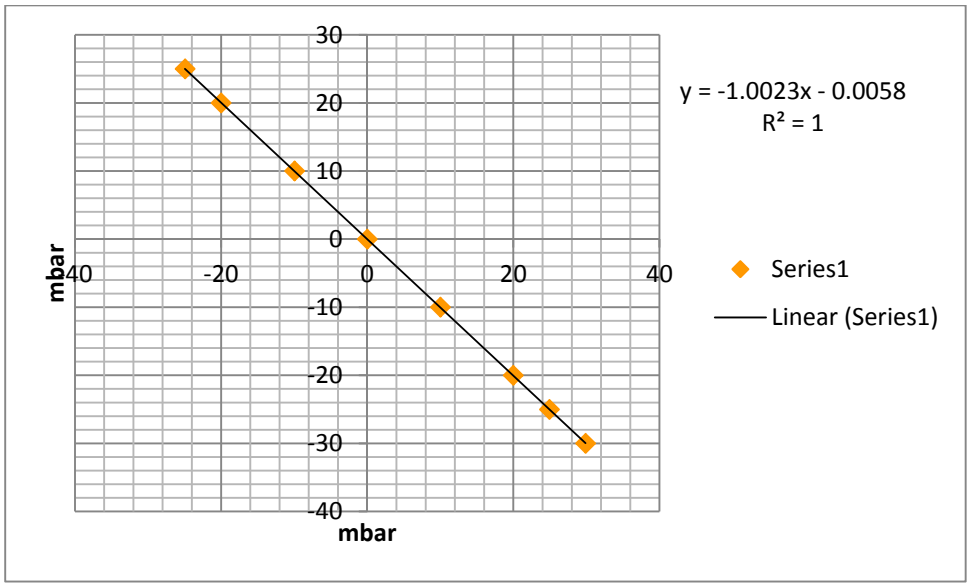

Figure 232 Angle of attack (mBar to mBar)

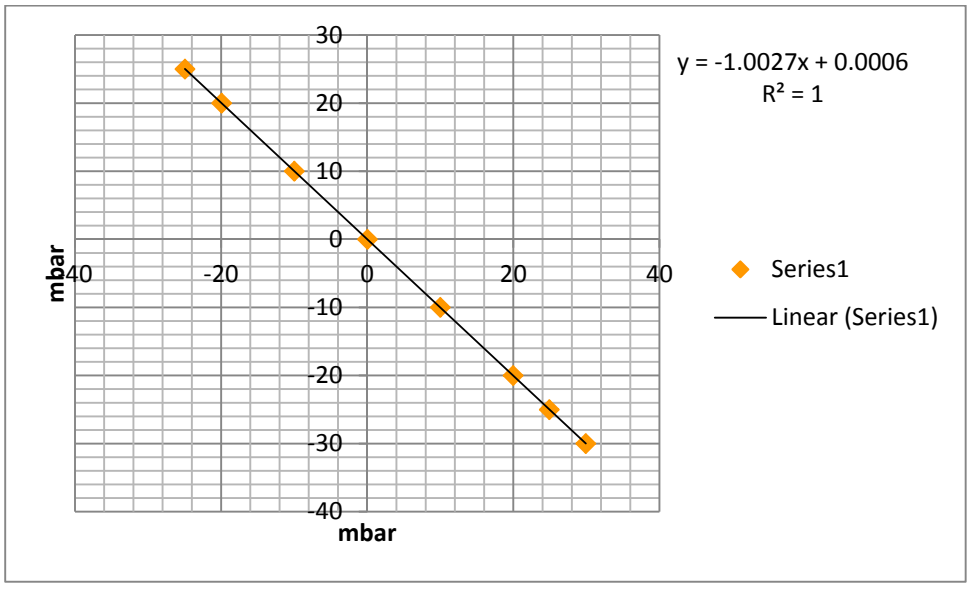

Figure 233 slip (mBar to mBar)

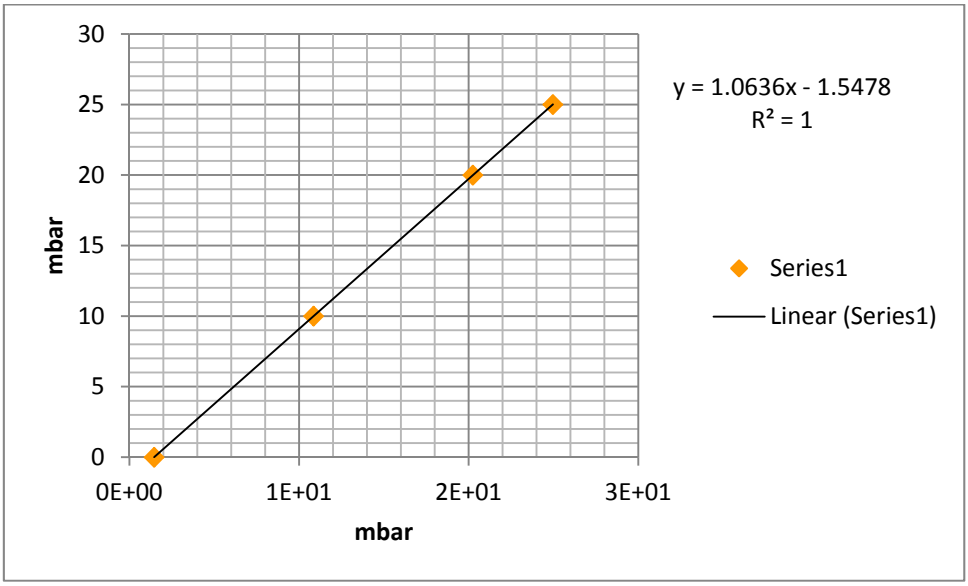

Figure 234 pitot pressure (mBar to mBar)

A.6.2. Hardware Certificates

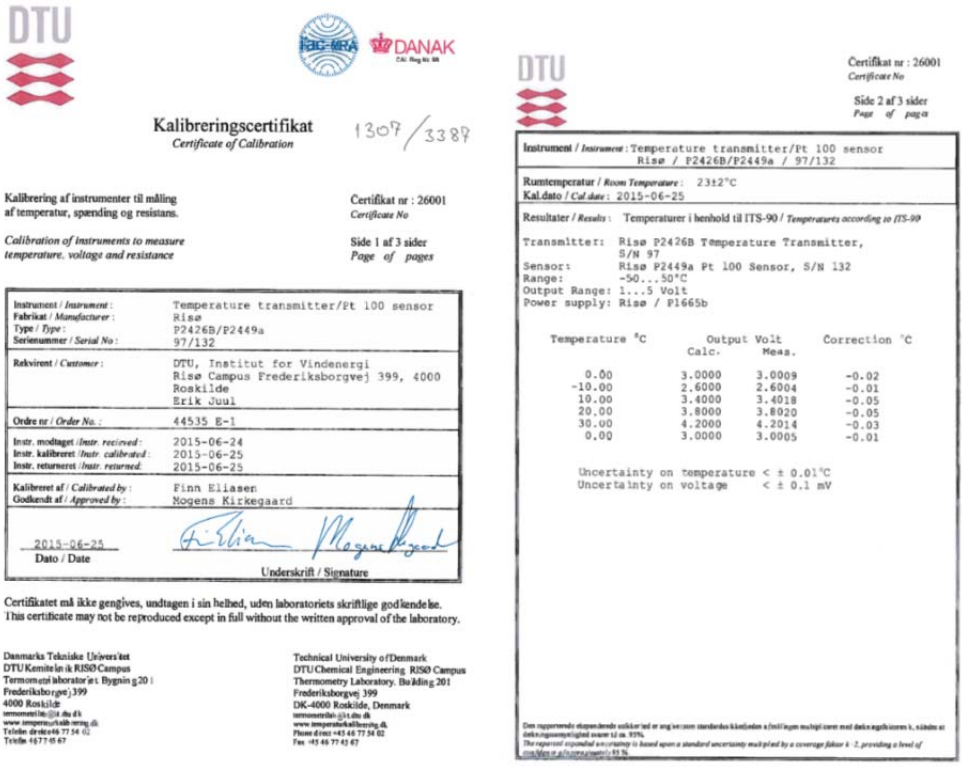

Kalibreringscertifikat
Certificate of Calibration
1307/3387

Kalibrering af instrumenter til måling af temperatur, spænding og resistans.
Calibration of instruments to measure temperature, voltage and resistance

Certifikat nr : 26001
Certificate No
Side 1 af 3 sider
Page of pages

Instrument / *Instrument* :	Temperature transmitter/Pt 100 sensor
Fabrikat / *Manufacturer* :	Risø
Type / *Type* :	P2426B/P2449a
Serienummer / *Serial No* :	97/132
Rekvirent / *Customer* :	DTU, Institut for Vindenergi Risø Campus Frederiksborgvej 399, 4000 Roskilde Erik Juul
Ordre nr / *Order No.* :	44535 E-1
Instr. modtaget /*Instr. received* :	2015-06-24
Instr. kalibreret /*Instr. calibrated* :	2015-06-25
Instr. returneret /*Instr. returned*:	2015-06-25
Kalibreret af / *Calibrated by* :	Finn Eliasen
Godkendt af / *Approved by* :	Mogens Kirkegaard

2015-06-25
Dato / Date
Underskrift / Signature

Certifikatet må ikke gengives, undtagen i sin helhed, uden laboratoriets skriftlige godkendelse.
This certificate may not be reproduced except in full without the written approval of the laboratory.

Danmarks Tekniske Universitet
DTU Kemiteknik RISØ Campus
Termometrilaboratoriet. Bygning 201
Frederiksborgvej 399
4000 Roskilde

Technical University of Denmark
DTU Chemical Engineering RISØ Campus
Thermometry Laboratory. Building 201
Frederiksborgvej 399
DK-4000 Roskilde, Denmark

Certifikat nr : 26001
Certificate No
Side 2 af 3 sider
Page of pages

Instrument / *Instrument* : Temperature transmitter/Pt 100 sensor
Risø / P2426B/P2449a / 97/132

Rumtemperatur / *Room Temperature* : 23±2°C
Kal.dato / *Cal.date* : 2015-06-25

Resultater / *Results* : Temperaturer i henhold til ITS-90 / *Temperatures according to ITS-90*

Transmitter: Risø P2426B Temperature Transmitter, S/N 97
Sensor: Risø P2449a Pt 100 Sensor, S/N 132
Range: -50...50°C
Output Range: 1...5 Volt
Power supply: Risø / P1665b

Temperature °C	Output Volt Calc.	Output Volt Meas.	Correction °C
0.00	3.0000	3.0009	-0.02
-10.00	2.6000	2.6004	-0.01
10.00	3.4000	3.4018	-0.05
20.00	3.8000	3.8020	-0.05
30.00	4.2000	4.2014	-0.03
0.00	3.0000	3.0005	-0.01

Uncertainty on temperature < ± 0.01°C
Uncertainty on voltage < ± 0.1 mV

Figure 235 Temperature calibration certificate pages 1 and 2

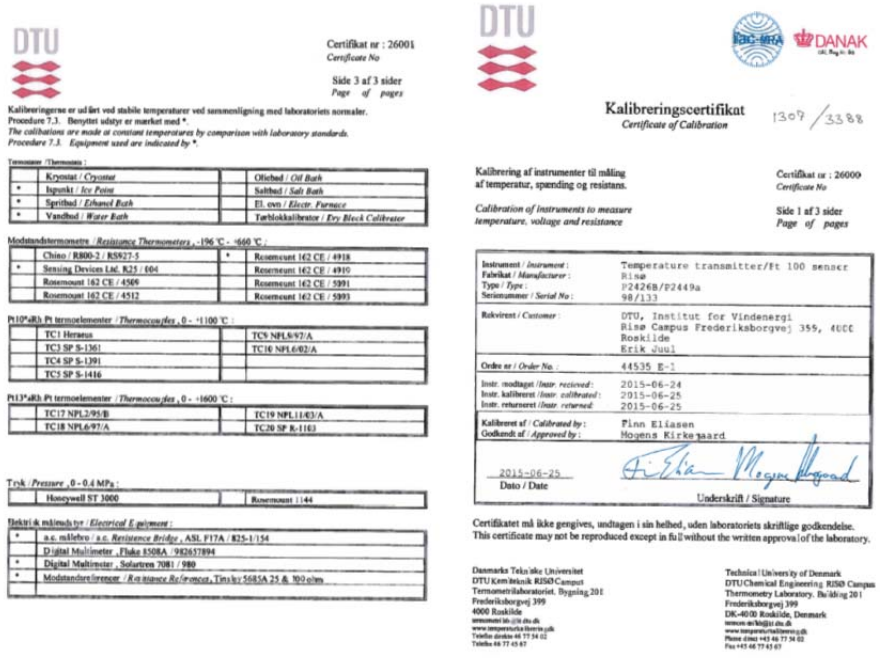

Certifikat nr : 26001
Certificate No
Side 3 af 3 sider
Page of pages

Kalibreringerne er udført ved stabile temperaturer ved sammenligning med laboratoriets normaler.
Procedure 7.3. Benyttet udstyr er markeret med *.
The calibrations are made at constant temperatures by comparison with laboratory standards.
*Procedure 7.3. Equipment used are indicated by *.*

Termometre / *Thermometers* :

	Kryostat / *Cryostat*		Oliebad / *Oil Bath*
*	Ispunkt / *Ice Point*		Saltbad / *Salt Bath*
*	Sprithad / *Ethanol Bath*		El. ovn / *Electr. Furnace*
*	Vandbad / *Water Bath*		Tørblokkalibrator / *Dry Block Calibrator*

Modstandstermometre / *Resistance Thermometers* , -196 °C - +660 °C :

	Chino / R800-2 / RS927-5	*	Rosemount 162 CE / 4918
*	Sensing Devices Ltd. RJ5 / 004		Rosemount 162 CE / 4910
	Rosemount 162 CE / 4509		Rosemount 162 CE / 5091
	Rosemount 162 CE / 4512		Rosemount 162 CE / 5093

Pt10%Rh Pt termoelementer / *Thermocouples* , 0 - +1100 °C :

	TC1 Heraeus		TC9 NPL8/97/A
	TC3 SP S-1361		TC10 NPL6/02/A
	TC4 SP S-1391		
	TC5 SP S-1416		

Pt13%Rh Pt termoelementer / *Thermocouples* , 0 - +1600 °C :

	TC12 NPL2/95/B		TC19 NPL11/03/A
	TC18 NPL6/97/A		TC20 SP K-1103

Tryk / *Pressure* , 0 - 0.4 MPa :

	Honeywell ST 3000		Rosemount 1144

Elektrisk måleudstyr / *Electrical Equipment* :

*	a.c. målebro / *a.c. Resistence Bridge* , ASL F17A / 825-1/154
	Digital Multimeter , Fluke 8508A / 98265789 4
*	Digital Multimeter , Solartron 7081 / 980
*	Modstandsreferencer / *Resistance References*, Tinsley 5685A 25 & 100 ohm

Kalibreringscertifikat
Certificate of Calibration
1307/3388

Kalibrering af instrumenter til måling af temperatur, spænding og resistans.
Calibration of instruments to measure temperature, voltage and resistance

Certifikat nr : 26000
Certificate No
Side 1 af 3 sider
Page of pages

Instrument / *Instrument* :	Temperature transmitter/Pt 100 sensor
Fabrikat / *Manufacturer* :	Risø
Type / *Type* :	P2426B/P2449a
Serienummer / *Serial No* :	98/133
Rekvirent / *Customer* :	DTU, Institut for Vindenergi Risø Campus Frederiksborgvej 355, 4000 Roskilde Erik Juul
Ordre nr / *Order No.* :	44535 E-1
Instr. modtaget /*Instr. received*:	2015-06-24
Instr. kalibreret /*Instr. calibrated* :	2015-06-25
Instr. returneret /*Instr. returned*:	2015-06-25
Kalibreret af / *Calibrated by* :	Finn Eliasen
Godkendt af / *Approved by* :	Mogens Kirkegaard

2015-06-25
Dato / Date
Underskrift / Signature

Certifikatet må ikke gengives, undtagen i sin helhed, uden laboratoriets skriftlige godkendelse.
This certificate may not be reproduced except in full without the written approval of the laboratory.

Danmarks Tekniske Universitet
DTU Kemiteknik RISØ Campus
Termometrilaboratoriet. Bygning 201
Frederiksborgvej 399
4000 Roskilde

Technical University of Denmark
DTU Chemical Engineering RISØ Campus
Thermometry Laboratory. Building 201
Frederiksborgvej 399
DK-4000 Roskilde, Denmark

Figure 236 Temperature calibration certificates

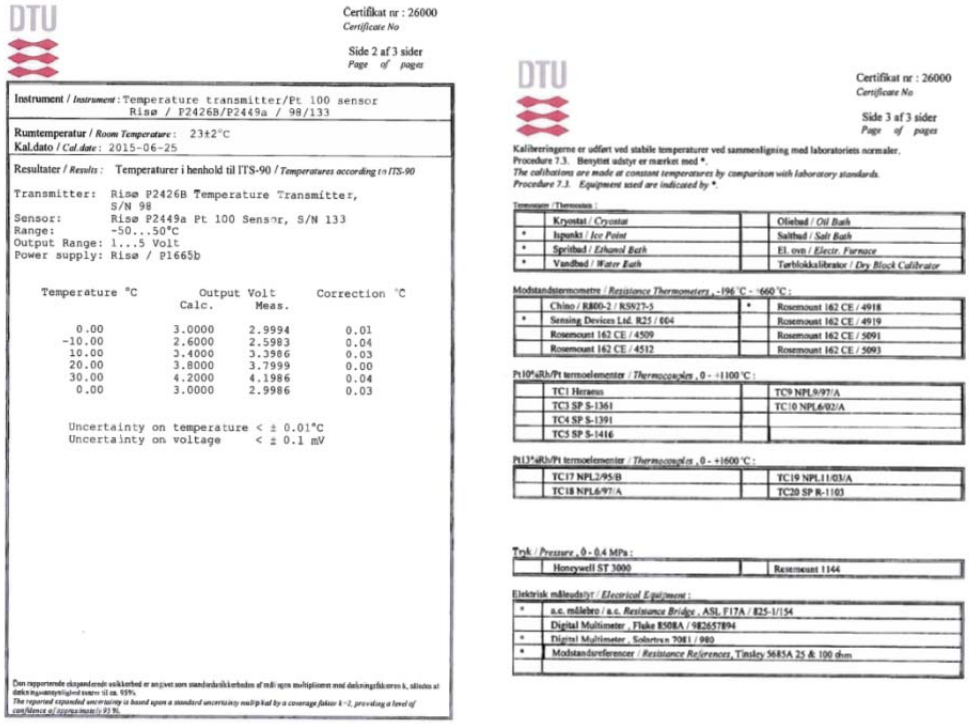

DTU

Certifikat nr : 26000
Certificate No

Side 2 af 3 sider
Page of pages

Instrument / *Instrument* : Temperature transmitter/Pt 100 sensor
Risø / P2426B/P2449a / 98/133

Rumtemperatur / *Room Temperature* : 23±2°C
Kal.dato / *Cal.date* : 2015-06-25

Resultater / *Results* : Temperaturer i henhold til ITS-90 / *Temperatures according to ITS-90*

Transmitter: Risø P2426B Temperature Transmitter, S/N 98
Sensor: Risø P2449a Pt 100 Sensor, S/N 133
Range: -50...50°C
Output Range: 1...5 Volt
Power supply: Risø / P1665b

Temperature °C	Output Volt Calc.	Meas.	Correction °C
0.00	3.0000	2.9994	0.01
-10.00	2.6000	2.5983	0.04
10.00	3.4000	3.3986	0.03
20.00	3.8000	3.7999	0.00
30.00	4.2000	4.1986	0.04
0.00	3.0000	2.9986	0.03

Uncertainty on temperature < ± 0.01°C
Uncertainty on voltage < ± 0.1 mV

Den rapporterede udvidede usikkerhed er angivet som standardusikkerheden af måling multipliceret med dækningsfaktoren k, således at den kan antages at svare til ca. 95%.
The reported expanded uncertainty is based upon a standard uncertainty multiplied by a coverage factor k=2, providing a level of confidence of approximately 95 %.

DTU

Certifikat nr : 26000
Certificate No

Side 3 af 3 sider
Page of pages

Kalibreringerne er udført ved stabile temperaturer ved sammenligning med laboratoriets normaler.
Procedure 7.3. Benyttet udstyr er mærket med *.
The calibations are made at constant temperatures by comparison with laboratory standards.
*Procedure 7.3. Equipment used are indicated by *.*

Temperatur /Thermostats :

	Kryostat / *Cryostat*		Oliebad / *Oil Bath*
*	Ispunkt / *Ice Point*		Saltbad / *Salt Bath*
*	Spritbad / *Ethanol Bath*		El. ovn / *Electr. Furnace*
*	Vandbad / *Water Bath*		Tørblokkalibrator / *Dry Block Calibrator*

Modstandstermometre / *Resistance Thermometers* , -196 °C - +660 °C :

	Chino / R800-2 / RS927-5	*	Rosemount 162 CE / 4918
*	Sensing Devices Ltd. R25 / 004		Rosemount 162 CE / 4919
	Rosemount 162 CE / 4509		Rosemount 162 CE / 5091
	Rosemount 162 CE / 4512		Rosemount 162 CE / 5093

Pt10%Rh/Pt termoelementer / *Thermocouples* , 0 - +1100 °C :

	TC1 Heraeus	TC9 NPL9/97/A
	TC3 SP S-1361	TC10 NPL6/02/A
	TC4 SP S-1391	
	TC5 SP S-1416	

Pt13%Rh/Pt termoelementer / *Thermocouples* , 0 - +1600 °C :

	TC17 NPL2/95/B	TC19 NPL11/03/A
	TC18 NPL6/97/A	TC20 SP R-1103

Tryk / *Pressure* , 0 - 0.4 MPa :

Honeywell ST 3000	Rosemount 1144

Elektrisk måleudstyr / *Electrical Equipment* :

*	a.c. målebro / a.c. *Resistance Bridge* , ASL F17A / 825-1/154
	Digital Multimeter , Fluke 8508A / 9826578?4
*	Digital Multimeter , Solartron 7081 / 980
*	Modstandsreferencer / *Resistance References*, Tinsley 5685A 25 & 100 ohm

Figure 237 Temperature calibration certificate

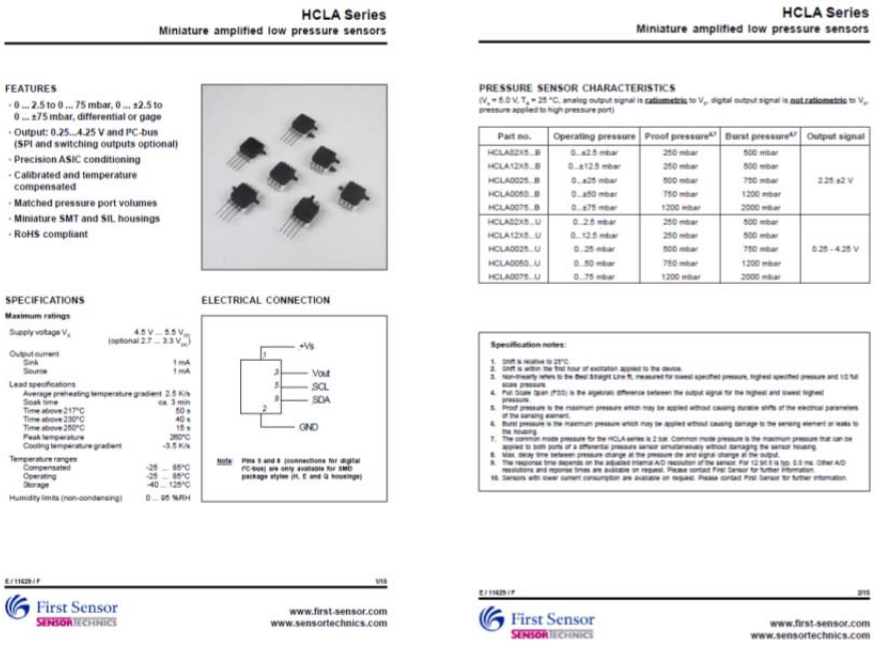

HCLA Series
Miniature amplified low pressure sensors

FEATURES

- 0 ... 2.5 to 0 ... 75 mbar, 0 ... ±2.5 to 0 ... ±75 mbar, differential or gage
- Output: 0.25...4.25 V and I²C-bus (SPI and switching outputs optional)
- Precision ASIC conditioning
- Calibrated and temperature compensated
- Matched pressure port volumes
- Miniature SMT and SIL housings
- RoHS compliant

SPECIFICATIONS

Maximum ratings

Supply voltage V_S 4.5 V ... 5.5 V_{DC} (optional 2.7 ... 3.3 V_{DC})

Output current
Sink 1 mA
Source 1 mA

Lead specifications
Average preheating temperature gradient 2.5 K/s
Soak time ca. 3 min
Time above 217°C 50 s
Time above 230°C 40 s
Time above 250°C 15 s
Peak temperature 260°C
Cooling temperature gradient -3.5 K/s

Temperature ranges
Compensated -25 ... 85°C
Operating -25 ... 85°C
Storage -40 ... 125°C

Humidity limits (non-condensing) 0 ... 95 %RH

ELECTRICAL CONNECTION

Note: Pins 5 and 8 (connections for digital I²C-bus) are only available for SMD package styles (H, E and G housings)

E / 11629 / F 1/15

First Sensor SENSORTECHNICS

www.first-sensor.com
www.sensortechnics.com

HCLA Series
Miniature amplified low pressure sensors

PRESSURE SENSOR CHARACTERISTICS

(V_S = 5.0 V, T_A = 25 °C, analog output signal is ratiometric to V_S, digital output signal is not ratiometric to V_S, pressure applied to high pressure port)

Part no.	Operating pressure	Proof pressure[A2]	Burst pressure[A2]	Output signal
HCLA02X5...B	0...±2.5 mbar	250 mbar	500 mbar	2.25 ±2 V
HCLA12X5...B	0...±12.5 mbar	250 mbar	500 mbar	
HCLA0025...B	0...±25 mbar	500 mbar	750 mbar	
HCLA0050...B	0...±50 mbar	750 mbar	1200 mbar	
HCLA0075...B	0...±75 mbar	1200 mbar	2000 mbar	
HCLA02X5...U	0...2.5 mbar	250 mbar	500 mbar	0.25 - 4.25 V
HCLA12X5...U	0...12.5 mbar	250 mbar	500 mbar	
HCLA0025...U	0...25 mbar	500 mbar	750 mbar	
HCLA0050...U	0...50 mbar	750 mbar	1200 mbar	
HCLA0075...U	0...75 mbar	1200 mbar	2000 mbar	

Specification notes:

1. Shift is relative to 25°C.
2. Shift is within the first hour of excitation applied to the device.
3. Non-linearity refers to the Best Straight Line fit, measured for lowest specified pressure, highest specified pressure and 1/2 full scale pressure.
4. Full Scale Span (FSS) is the algebraic difference between the output signal for the highest and lowest highest pressure.
5. Proof pressure is the maximum pressure which may be applied without causing durable shifts of the electrical parameters of the sensing element.
6. Burst pressure is the maximum pressure which may be applied without causing damage to the sensing element or leaks to the housing.
7. The common mode pressure for the HCLA series is 2 bar. Common mode pressure is the maximum pressure that can be applied to both ports of a differential pressure sensor simultaneously without damaging the sensor housing.
8. Max. delay time between pressure change at the pressure die and signal change at the output.
9. The response time depends on the adjusted internal A/D resolution of the sensor. For 12 bit it is typ. 0.6 ms. Other A/D resolutions and reponse times are available on request. Please contact First Sensor for further information.
10. Sensors with lower current consumption are available on request. Please contact First Sensor for further information.

E / 11629 / F 2/15

First Sensor SENSORTECHNICS

www.first-sensor.com
www.sensortechnics.com

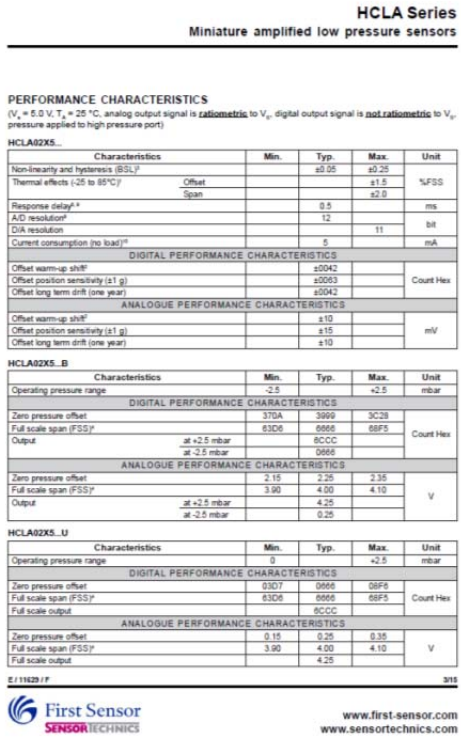

HCLA Series
Miniature amplified low pressure sensors

PERFORMANCE CHARACTERISTICS

(V_s = 5.0 V, T_A = 25 °C, analog output signal is ratiometric to V_s, digital output signal is not ratiometric to V_s, pressure applied to high pressure port)

HCLA02X5...

Characteristics		Min.	Typ.	Max.	Unit
Non-linearity and hysteresis (BSL)[2]			±0.05	±0.25	%FSS
Thermal effects (-25 to 85°C)[7]	Offset			±1.5	
	Span			±2.0	
Response delay[2,3]			0.5		ms
A/D resolution[4]			12		bit
D/A resolution				11	
Current consumption (no load)[10]			5		mA
DIGITAL PERFORMANCE CHARACTERISTICS					
Offset warm-up shift[8]			±0042		Count Hex
Offset position sensitivity (±1 g)			±0063		
Offset long term drift (one year)			±0042		
ANALOGUE PERFORMANCE CHARACTERISTICS					
Offset warm-up shift[8]			±10		mV
Offset position sensitivity (±1 g)			±15		
Offset long term drift (one year)			±10		

HCLA02X5...B

Characteristics		Min.	Typ.	Max.	Unit
Operating pressure range		-2.5		+2.5	mbar
DIGITAL PERFORMANCE CHARACTERISTICS					
Zero pressure offset		370A	3999	3C28	Count Hex
Full scale span (FSS)[9]		63D6	6666	68F5	
Output	at +2.5 mbar		6CCC		
	at -2.5 mbar		0666		
ANALOGUE PERFORMANCE CHARACTERISTICS					
Zero pressure offset		2.15	2.25	2.35	V
Full scale span (FSS)[9]		3.90	4.00	4.10	
Output	at +2.5 mbar		4.25		
	at -2.5 mbar		0.25		

HCLA02X5...U

Characteristics		Min.	Typ.	Max.	Unit
Operating pressure range		0		+2.5	mbar
DIGITAL PERFORMANCE CHARACTERISTICS					
Zero pressure offset		03D7	0666	08F6	Count Hex
Full scale span (FSS)[9]		63D6	6666	68F5	
Full scale output			6CCC		
ANALOGUE PERFORMANCE CHARACTERISTICS					
Zero pressure offset		0.15	0.25	0.35	V
Full scale span (FSS)[9]		3.90	4.00	4.10	
Full scale output			4.25		

E / 11629 / F 3/15

First Sensor SENSORTECHNICS www.first-sensor.com www.sensortechnics.com

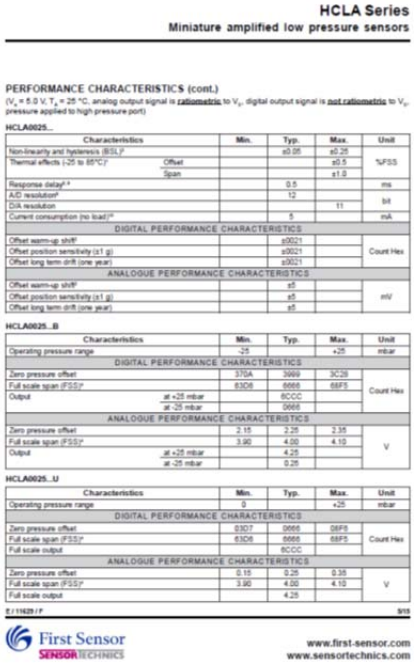

HCLA Series
Miniature amplified low pressure sensors

PERFORMANCE CHARACTERISTICS (cont.)

(V_s = 5.0 V, T_A = 25 °C, analog output signal is ratiometric to V_s, digital output signal is not ratiometric to V_s, pressure applied to high pressure port)

HCLA0025...

Characteristics		Min.	Typ.	Max.	Unit
Non-linearity and hysteresis (BSL)[2]			±0.05	±0.25	%FSS
Thermal effects (-25 to 85°C)[7]	Offset			±0.5	
	Span			±1.0	
Response delay[2,3]			0.5		ms
A/D resolution[4]			12		bit
D/A resolution				11	
Current consumption (no load)[10]			5		mA
DIGITAL PERFORMANCE CHARACTERISTICS					
Offset warm-up shift[8]			±0021		Count Hex
Offset position sensitivity (±1 g)			±0021		
Offset long term drift (one year)			±0021		
ANALOGUE PERFORMANCE CHARACTERISTICS					
Offset warm-up shift[8]			±5		mV
Offset position sensitivity (±1 g)			±5		
Offset long term drift (one year)			±5		

HCLA0025...B

Characteristics		Min.	Typ.	Max.	Unit
Operating pressure range		-25		+25	mbar
DIGITAL PERFORMANCE CHARACTERISTICS					
Zero pressure offset		370A	3999	3C28	Count Hex
Full scale span (FSS)[9]		63D6	6666	68F5	
Output	at +25 mbar		6CCC		
	at -25 mbar		0666		
ANALOGUE PERFORMANCE CHARACTERISTICS					
Zero pressure offset		2.15	2.25	2.35	V
Full scale span (FSS)[9]		3.90	4.00	4.10	
Output	at +25 mbar		4.25		
	at -25 mbar		0.25		

HCLA0025...U

Characteristics		Min.	Typ.	Max.	Unit
Operating pressure range		0		+25	mbar
DIGITAL PERFORMANCE CHARACTERISTICS					
Zero pressure offset		03D7	0666	08F6	Count Hex
Full scale span (FSS)[9]		63D6	6666	68F5	
Full scale output			6CCC		
ANALOGUE PERFORMANCE CHARACTERISTICS					
Zero pressure offset		0.15	0.25	0.35	V
Full scale span (FSS)[9]		3.90	4.00	4.10	
Full scale output			4.25		

E / 11629 / F 3/15

First Sensor SENSORTECHNICS www.first-sensor.com www.sensortechnics.com

Figure 238

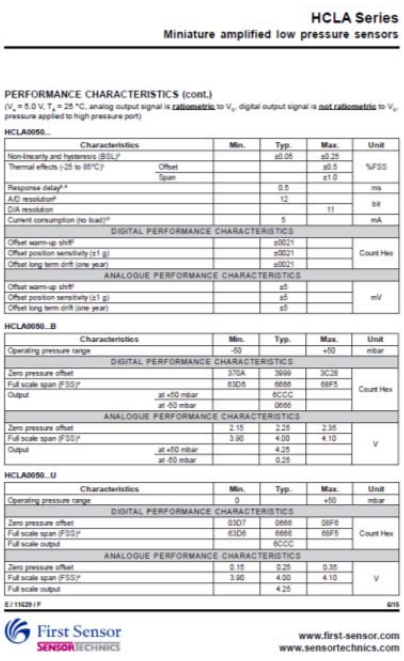

HCLA Series
Miniature amplified low pressure sensors

PERFORMANCE CHARACTERISTICS (cont.)

(V_s = 5.0 V, T_A = 25 °C, analog output signal is ratiometric to V_s, digital output signal is not ratiometric to V_s, pressure applied to high pressure port)

HCLA0050...

Characteristics		Min.	Typ.	Max.	Unit
Non-linearity and hysteresis (BSL)[2]			±0.05	±0.25	%FSS
Thermal effects (-25 to 85°C)[7]	Offset			±0.5	
	Span			±1.0	
Response delay[2,3]			0.5		ms
A/D resolution[4]			12		bit
D/A resolution				11	
Current consumption (no load)[10]			5		mA
DIGITAL PERFORMANCE CHARACTERISTICS					
Offset warm-up shift[8]			±0021		Count Hex
Offset position sensitivity (±1 g)			±0021		
Offset long term drift (one year)			±0021		
ANALOGUE PERFORMANCE CHARACTERISTICS					
Offset warm-up shift[8]			±5		mV
Offset position sensitivity (±1 g)			±5		
Offset long term drift (one year)			±5		

HCLA0050...B

Characteristics		Min.	Typ.	Max.	Unit
Operating pressure range		-50		+50	mbar
DIGITAL PERFORMANCE CHARACTERISTICS					
Zero pressure offset		370A	3999	3C28	Count Hex
Full scale span (FSS)[9]		63D6	6666	68F5	
Output	at +50 mbar		6CCC		
	at -50 mbar		0666		
ANALOGUE PERFORMANCE CHARACTERISTICS					
Zero pressure offset		2.15	2.25	2.35	V
Full scale span (FSS)[9]		3.90	4.00	4.10	
Output	at +50 mbar		4.25		
	at -50 mbar		0.25		

HCLA0050...U

Characteristics		Min.	Typ.	Max.	Unit
Operating pressure range		0		+50	mbar
DIGITAL PERFORMANCE CHARACTERISTICS					
Zero pressure offset		03D7	0666	08F6	Count Hex
Full scale span (FSS)[9]		63D6	6666	68F5	
Full scale output			6CCC		
ANALOGUE PERFORMANCE CHARACTERISTICS					
Zero pressure offset		0.15	0.25	0.35	V
Full scale span (FSS)[9]		3.90	4.00	4.10	
Full scale output			4.25		

E / 11629 / F 4/15

First Sensor SENSORTECHNICS www.first-sensor.com www.sensortechnics.com

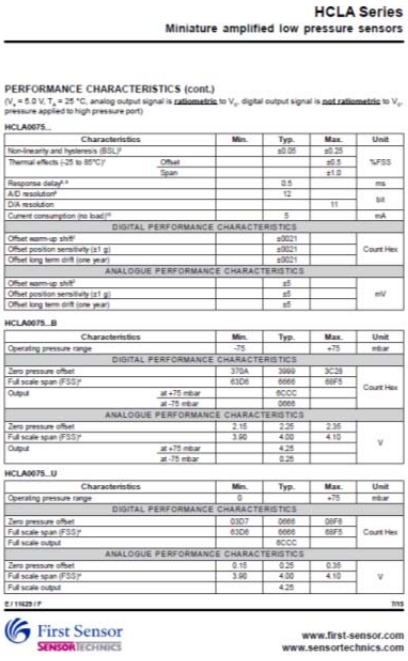

HCLA Series
Miniature amplified low pressure sensors

PERFORMANCE CHARACTERISTICS (cont.)

(V_s = 5.0 V, T_A = 25 °C, analog output signal is ratiometric to V_s, digital output signal is not ratiometric to V_s, pressure applied to high pressure port)

HCLA0075...

Characteristics		Min.	Typ.	Max.	Unit
Non-linearity and hysteresis (BSL)[2]			±0.05	±0.25	%FSS
Thermal effects (-25 to 85°C)[7]	Offset			±0.5	
	Span			±1.0	
Response delay[2,3]			0.5		ms
A/D resolution[4]			12		bit
D/A resolution				11	
Current consumption (no load)[10]			5		mA
DIGITAL PERFORMANCE CHARACTERISTICS					
Offset warm-up shift[8]			±0021		Count Hex
Offset position sensitivity (±1 g)			±0021		
Offset long term drift (one year)			±0021		
ANALOGUE PERFORMANCE CHARACTERISTICS					
Offset warm-up shift[8]			±5		mV
Offset position sensitivity (±1 g)			±5		
Offset long term drift (one year)			±5		

HCLA0075...B

Characteristics		Min.	Typ.	Max.	Unit
Operating pressure range		-75		+75	mbar
DIGITAL PERFORMANCE CHARACTERISTICS					
Zero pressure offset		370A	3999	3C28	Count Hex
Full scale span (FSS)[9]		63D6	6666	68F5	
Output	at +75 mbar		6CCC		
	at -75 mbar		0666		
ANALOGUE PERFORMANCE CHARACTERISTICS					
Zero pressure offset		2.15	2.25	2.35	V
Full scale span (FSS)[9]		3.90	4.00	4.10	
Output	at +75 mbar		4.25		
	at -75 mbar		0.25		

HCLA0075...U

Characteristics		Min.	Typ.	Max.	Unit
Operating pressure range		0		+75	mbar
DIGITAL PERFORMANCE CHARACTERISTICS					
Zero pressure offset		03D7	0666	08F6	Count Hex
Full scale span (FSS)[9]		63D6	6666	68F5	
Full scale output			6CCC		
ANALOGUE PERFORMANCE CHARACTERISTICS					
Zero pressure offset		0.15	0.25	0.35	V
Full scale span (FSS)[9]		3.90	4.00	4.10	
Full scale output			4.25		

E / 11629 / F 5/15

First Sensor SENSORTECHNICS www.first-sensor.com www.sensortechnics.com

Figure 239

Acknowledgements

The Danish Energy Agency has under the Danish Energy Research Programme EUDP funded this project. We would also like to thank our partners DELTA Dansk Elektronik, Lys & Akustik, G.R.A.S. Sound & Vibration A/S, CIM A/S, SIEMENS WP for cooperation in doing this demonstration.